UNICA UNIVERSITÀ DEGLI STUDI DI CAGLIARI

uniss UNIVERSITÀ DEGLI STUDI DI SASSARI

PhD Course in Chemical Sciences and Technologies

XXXV cycle

Development of innovative mesostructured catalysts for CO_2 conversion to dimethyl ether

Scientific Disciplinary Sectors

CHIM/02 - CHIM/04

PhD Student: Fausto Secci

Supervisor: Prof. Carla Cannas

Co-supervisors:

Dr. Mauro Mureddu (Sotacarbo S.p.A.)

Prof. Nicola Pinna (Humboldt University of Berlin)

Coordinator of the PhD Programme

Prof. Carla Cannas

Final exam Academic Year 2021– 2022

Table of contents

Foreword

The present thesis is focused on the development of mesostructured catalysts, catalysts featuring well-defined ordered porous structure on mesoscopic (2-50 nm) length scales, for the one-pot transformation of CO_2 into dimethyl ether (DME). The increasing levels of CO_2 emissions have been widely and unanimously acknowledged by the scientific community as the main cause of anthropogenic climate change. With the aim of reducing the emissions of CO_2, several measures are being adopted by many countries, like the use of renewable power sources (*e.g.* solar and wind power) and the replacement of traditional fossil fuels with green fuels. One of the most prominent technologies in this field is the Carbon Capture and Utilization (CCU), consisting in the capture of CO_2 at its main emission points in order to use it as it is or to transform it into chemicals and fuels. Several technologies are proposed to capture CO_2, but the most widespread ones are post-combustion technologies, consisting in the sequestration of CO_2 from flue gases of combustion processes (*e.g.* in thermal power plants). The fuels obtained from the chemical conversion of CO_2 (*e.g.* methane, methanol and dimethyl ether) are called electro-fuels, or e-fuels. To convert CO_2 into these fuels, it needs to be reduced with hydrogen using appropriate catalysts; when the hydrogen used for the reaction is obtained from water splitting using renewable power, the combustion of e-fuels does not give rise to net CO_2 emissions. Among e-fuels, DME represents a good choice: it can be indeed used as an additive for diesel fuel and, after some proper modification to the engines, it can even completely replace diesel fuel, providing better performances, due to its higher cetane number. DME can also be stored and transported using the same technologies used nowadays for LPG (liquefied petroleum gas) like pipelines, gas tanker ships and trucks. Furthermore, DME is non-toxic and non-carcinogenic, and its combustion does not produce sulfur or aromatic compounds; compared to diesel, it also gives rise to lower emissions of SO_x and NO_x.

CO_2 is transformed into DME via two subsequent reactions:

$CO_2 + 3H_2 \leftrightarrows CH_3OH + H_2O$ Redox reaction

$2CH_3OH \leftrightarrows CH_3OCH_3 + H_2O$ Dehydration reaction

The first reaction is catalyzed by Cu-based redox catalysts; in these systems Cu, the active phase of the catalyst, is usually paired with a promoter (ZnO), which increases the dispersion of Cu, and a third phase (Al_2O_3 or ZrO_2) which enhances the chemical and thermal stability of the catalyst.

For the second reaction, solid acidic dehydration catalysts are used, mainly zeolites and γ-Al_2O_3. Regarding the dehydration catalysts, γ-Al_2O_3, a widely used catalyst for the syngas-to-DME process, has a low cost but, since it presents only Lewis acid sites on its surface, it loses performances over time; the water formed during both CO_2 reduction and methanol dehydration, indeed, adsorbs on Lewis sites by forming an acid-base adduct, thus hampering methanol adsorption. Zeolites, on the other hand, show a much higher water resistance, due to the presence of Brønsted sites, that do not deactivate over time; the presence of Brønsted acid sites on zeolites is due to the insertion of Al into the SiO_2 framework.

CO_2 conversion to DME can be performed by following both an indirect (two-step) route or a direct (one-step) one. In the two-step process the two reactions are carried out in two separate reactor beds, each one with its catalyst. In the one-step process, on the other hand, both reactions are performed simultaneously inside the same reactor, using a mixture of the two catalytic systems. The one-step route presents some intrinsic advantages, like a higher CO_2 conversion and a lower cost related to the management on a single reactor rather than two. For these reasons, the attention of the scientists is mainly focused on the one-step (also known as one-pot) process. In the literature, the one-pot conversion of CO_2 to DME is usually carried out using physical mixtures of the two catalysts; however, recently, an increasing attention is being focused on composite bifunctional (redox-acidic) catalysts, presenting an intimate contact between the two phases. These catalysts, differently from physical mixtures, are obtained by dispersing a redox Cu-based phase onto an acidic support through chemical methods like coprecipitation or impregnation. In this context, the use of zeolites as scaffolds to support the redox phase, only allows the deposition of the redox phase on the external surface, being the dispersion inside the pores hampered by the reduced pore diameter (microporous systems). As a consequence, the size and the morphology of the particles of the redox phase cannot be controlled and, during the thermal treatment to convert the metal precursors to the corresponding oxides and during the reaction, sintering phenomena could occur. For these reasons, in this thesis work mesostructured acidic systems are proposed; the larger size of mesopores, compared to micropores, should render the mesostructured acidic catalysts able to confine the redox phase inside the pores in form of very small nanoparticles and to control the particle size by tuning the mesochannel size. The high surface area of the mesostructured acidic scaffold, together with the highly dispersed confined redox nanophase, might also allow to improve the accessibility of the sites to the gaseous reactants, enhancing the reactivity. Furthermore, the mesochannels walls should hamper sintering phenomena during thermal treatments and reaction assuring the stability and the possible regeneration of the catalysts.

In this study several mesostructured acidic catalysts with different compositions (Al-SiO_2, γ-Al_2O_3, TiO_2 and Zr-TiO_2) and different textural properties have been developed and characterized to assess their structural, morphological, textural, and acidic properties; particular attention has been focused on the characterization of the acidic sites of the catalysts in terms of amount, strength and surface density. The catalysts have been then tested for the CO_2-to-DME process in form of physical mixtures with a commercial Cu-based redox catalyst (CZA) and their catalytic performances have been correlated with their acidic properties, in order to understand which acidic features lead to a good catalytic activity for methanol dehydration. The mesostructured acidic catalysts have been subsequently used as supports to obtain bifunctional composite catalysts by dispersing a Cu-based redox phase inside their mesopores. These composites have been eventually tested for the one-pot CO_2 conversion to DME and their performances have been compared with those of physical mixtures consisting of the same redox and acidic phases present in the composite catalysts, in order to properly compare the effect of the two different types of mixing (*i.e.* physical or chemical) on the catalytic performances.

The PhD thesis is organized in five chapters organized as follows:

- Chapter 1 provides an overview on the different carbon capture technologies and on the use of captured CO_2. Particular attention has been focused on the syngas-to-DME and CO_2-to-DME processes and on the catalytic systems used for these processes.
- Chapter 2 gives an introduction on siliceous and non-siliceous mesostructured materials, on their synthesis and on their applications, as well as on their use as supports for composite systems.
- Chapter 3 focuses on the development on mesostructured TiO_2, Zr-TiO_2 mixed oxides and Al-SiO_2 (Al-MCM-41) describing their synthesis process, their structural, textural and morphological characterization and the correlation of their acidic features with their catalytic performances.

- Chapter 4 is dedicated to the development of several mesostructured aluminosilicates (Al-MCM-41, Al-SBA-16, and Al-SBA-15) with the same Si/Al ratio but different textural properties as well as on mesostructured γ-Al_2O_3. The main focus is the correlation of their textural properties with their acidic features and the understanding of how these different properties can influence catalytic activity.
- Chapter 5 describes the development of bifunctional (redox + acidic) composite catalysts by dispersing a redox phase onto the mesostructured catalysts synthesized in Chapter 4. The composite catalysts have been characterized and tested for the CO_2-to-DME process, to understand how the chemical composition, the textural properties and the intimate contact between the two catalytic phases affect the catalytic properties by comparing them with physical mixtures of the two catalysts (redox + acidic).

At the end, the conclusions about the results achieved in this thesis are given, with the possible future perspectives of this project.

An appendix describes the technical details of the characterization techniques and the instruments used in this work, as well as on the bench-scale plant used for the catalytic tests.

Chapter 1

Carbon Capture and Utilization (CCU) technologies and DME production from syngas and CO_2

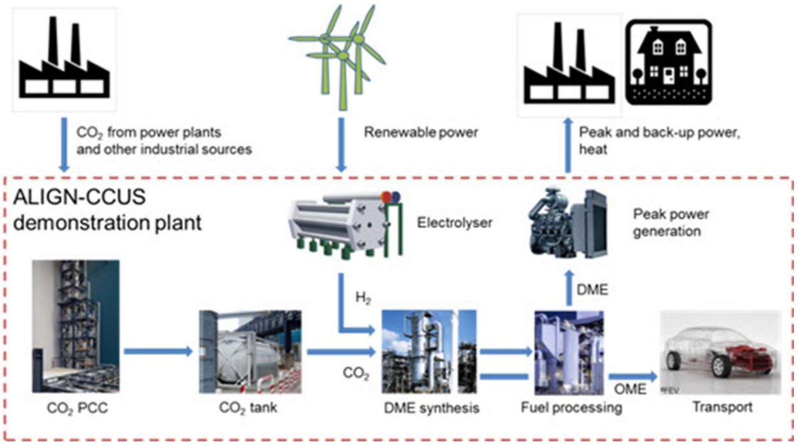

1.1 CCU: an overview

During the latest decades, the increasing levels of CO_2 emission have strongly gathered the attention of most of the governments all around the globe, as well as the concern of the whole scientific community. CO_2, due to its greenhouse effect, is indeed unanimously recognized as the major responsible of current global warming, leading to climate change, with severe effects on the environment, on marine and terrestrial ecosystems as well as on human life and activities. Due to this fact, many governments have taken several actions aimed to the reduction of CO_2 emissions; the Intergovernmental Panel on Climate Change (IPCC), has indeed established the goal of zero global net carbon emissions for 2050, in order to keep the temperature rise below +1.5 °C by 2100 [1][2]. With the aim of reducing the global carbon emissions, several strategies need to be implemented, like energy saving, use of renewable energy sources and Carbon Capture, Utilization and Storage (CCUS). The last emission reduction approach is based on the capture of CO_2 at its main emission points, like thermoelectric power plants and industrial plants and either its storage into underground deposits or its utilization with the aim of obtaining various useful products like fuels, chemicals and materials. [3]–[7]

1.1.1 Capture of CO_2

Despite being still an expensive and complex process, CO_2 capture is constantly gaining more attention, due to its potential in reducing anthropogenic CO_2 emissions into the atmosphere.

Nowadays, several technologies for CO_2 capture are available, at different levels of price, feasibility and technology readiness level (TRL). [4], [5], [8]–[10]

Pre-combustion capture

Pre-combustion CO_2 capture consists in removing the CO_2 from the fuel before its combustion; this is usually done through a partial oxidation of the feedstock in presence of water and oxygen, to obtain syngas, a mixture mainly consisting of CO and H_2, with minor and variable amount of CO_2. The obtained syngas then undergoes the water-gas shift process, leading to a mixture of CO_2 and H_2; CO_2 can be then separated from hydrogen which can be used as fuel in power plants such as gas turbines. [4][5]

Post-combustion capture

The vast majority of CO_2 capture pathways are however based on post-combustion processes, in which CO_2 is separated from the flue gases after the combustion of the fuel with air. The most mature and available technology for post-combustion CO_2 capture is the absorption from flue gases using amines; in this process the exhaust gas containing CO_2 in high concentration is sent into an absorption column containing amines in aqueous phase. When the flue gas comes into contact with the absorption solution, CO_2 bonds with the amine molecules; the resulting solution is subsequently sent into a stripper column to separate the CO_2 and regenerate the amine solution, which is then ready to perform the absorption process again. Besides amines, also metal bases, like hydroxides, can be used to absorb CO_2 forming carbonates; however, their high prices and the high energy requirements to separate CO_2 from carbonates limit their use. A significant drawback of CO_2 capture via amine absorption is the deterioration of the equipment, due to corrosion, gradual degradation of the amines and the energy requirements to perform the desorption of the absorbed CO_2; particularly, this last aspect, can lower the global efficiency of the power plant by up to 30% of the original efficiency. Another route to perform the post-combustion CO_2 capture involves the use of membranes; this technique is currently in an earlier stage of development, compared to amine separation, but has demonstrated to be much more environmentally friendly, requiring significantly less amounts of energy, and thus more promising in a future perspective. Membrane separation requires the CO_2 concentration in the flue gas to be higher than 10%, ideally at about 20%. Polymeric membranes are among the most promising types of membranes for CO_2 separation, due to their cheapness and ease of handling; however, their main drawback is their low resistance to degradation, mainly induced by high temperatures or high pressures; particularly the former one causes the membranes to swell, increasing their permeability to all type of gases and thus losing their selectivity. The use of low values of pressure in the inlet gas also poses a significant problem in the use of membranes, since their working principle is based on the difference of pressure between the flue gas and the outlet, and a low CO_2 partial pressure in the flue gas would result in low separation efficiency. Also, in case of flue gases rich in acidic species (like SOx and NOx) the degradation process of membranes can be further accelerated. On the other hand, hybrid membranes consisting of both polymers and inorganic materials, such as zeolites and ceramic materials, present a much higher temperature resistance, but they are at an earlier development stage [4][8].

Oxyfuel combustion

Another CO_2 capture route is the oxyfuel combustion, which consists in burning the fuel using pure oxygen, in absence of nitrogen, resulting in an exhaust mainly consisting of CO_2 and H_2O; the latter product can be simply removed by condensation, obtaining almost pure CO_2. The main issues related to oxyfuel combustion is the intrinsic cost related to the use of pure O_2, that needs to be produced by using an air separation unit (ASU), requiring a parasitic energy consumption. Also, combustion processes in pure oxygen reach much higher temperature compared with the same process performed using air as oxidizing agent; as a consequence, different materials, with a higher temperature resistance must be used in power plants that perform oxyfuel combustion [4].

Chemical looping combustion

CO_2 capture can also be performed via chemical looping combustion (CLC); this process uses an oxygen carrier, usually metal oxide particles (Fe_2O_3, NiO, Mn_2O_3), that is circulated between a fuel reactor and an air reactor. Into the fuel reactor, the oxygen carrier is reduced to its metal form by reacting with the fuel which, on the other hand, undergoes a combustion process; the carrier is subsequently introduced into the air reactor, where it is oxidized again to its oxide form by contact with air. Since the fuel combustion process is carried out without direct contact with air, and therefore in absence of nitrogen, the flue gas mainly consists of CO_2 and H_2O, which can be easily separated by condensation, obtaining almost pure CO_2. The CLC process can be used using natural gas, gasified biomass or even solid fuels in form of powder; the main issues consist in the formation of carbonaceous residues (particularly in case of solid fuels) and deterioration of the plant due to mechanical attrition caused by the circulation of the oxygen carrier [4].

Direct air capture

Another process that involves separation of CO_2 from a mixture of gases is the direct air capture (DAC); this process consists in the sequestration of CO_2 from air, rather than from flue gases resulting from a combustion process. In this case, the concentration of CO_2 is much lower and, as a consequence, it cannot be separated using the same technologies employed for post-combustion capture, as the process would be thermodynamically unfavored. DAC is usually performed using an aqueous solution of a strong base, like NaOH, KOH or $Ca(OH)_2$, which reacts with CO_2 forming carbonates; these carbonates are subsequently calcined at high temperatures (800 °C) releasing high-purity CO_2 and regenerating the metal oxide, which can be easily converted to its hydroxide form and used to perform the process again. The separation of CO_2 from the air has also been performed using bulk solid alkaline species (mainly calcium and sodium oxides and hydroxides); also in this case the process results in the formation of carbonates which are thermally treated to release CO_2 and regenerate the system. Another option for DAC is the use of solid amines, on which CO_2 is initially adsorbed and subsequently desorbed with a thermal treatment; in this case lower temperatures are required, due to the lower energy of the bond between CO_2 and amines, compared with the carbonate systems. The main issue associated with DAC is the high cost, mainly related to the high energy requirements; also, the energy used to separate CO_2 from the sorbents must necessarily be obtained from renewable sources, otherwise the use of energy from fossil fuels would compromise the aim of the whole process, for obvious reasons [4][5].

1.2 Utilization of CO_2

As of the utilization after its separation, captured CO_2 possess a wide range of use in the industrial sector and can be used either as it is or with the final aim to transform it into a wide range of useful products.

1.2.1 Usage of CO_2 as solvent, refrigerant and fertilizer

An important application of CO_2 as it is consists in its use as a solvent [3][4]. Nowadays, the chemical industry makes large use of solvents for many of its processes; in this context, the use of organic solvents poses a serious hazard for both the environment and the human health, besides the costs and the energy usage involved in the processes of separation of the solvents from the final product.

That is the reason that pushed towards the use of CO_2 as a solvent, mainly in its supercritical state, which presents chemical-physical properties similar to those of n-hexane; CO_2, compared to most organic solvents, is indeed much cheaper, more environmentally friendly and non-toxic for both human life and environment. The use of captured CO_2 for this purpose, indeed, does not give rise to net carbon emissions; the only drawback to take into account is the amount of energy required to bring CO_2 to its supercritical state, at a temperature and pressure value of 304.1 K and 7.4 MPa, respectively. Supercritical CO_2 is mainly used to extract natural flavors, spices and essential oils from their vegetal sources, as well as for the decaffeination of coffee and tea and the extraction of hops; besides all the advantages linked to the use of a non-toxic and cheap solvent, it has to be pointed out that the amount of supercritical CO_2 required to perform such processes is much lower (3 to 20 times lower) than the amount that would be necessary with the use of organic solvents. Also, since the waste materials resulting from the process have not been into contact with a toxic solvent, such wastes can be used for other purposes, rather than discarded with a significant cost for their disposal. The only minor drawback in using supercritical CO_2 for extraction processes is the higher cost of the equipment; but this is largely compensated by all the other advantages that strongly lower the price of the process [3][4].

Supercritical CO_2 can also be used as a solvent for several reactions of industrial interest; in the case of reactions involving gaseous reagents, the use of supercritical CO_2 as solvent allows to carry out the reaction in single-phase conditions avoiding the formation of a gas-liquid interface, and thus increasing its kinetics. Hydroformylation, the synthesis process of aldehydes starting from olefins and syngas, is one of the industrial reactions that can be performed using supercritical CO_2 as solvent; this synthesis can be carried out either in homogeneous- or heterogeneous-phase catalysis. In the former case the separation of the catalyst from the reaction medium can be difficult when traditional solvents are used; however, the use of supercritical CO_2 allows a much easier and cheaper catalyst recovery. Hydrogenation is another reaction industrially carried out, in some cases, using supercritical CO_2; it has been demonstrated, indeed, that the use of CO_2 as solvent allows to increase the selectivity and yields of several hydrogenation reactions, such as the transformation of nitrile to primary amines, avoiding the formation of undesired byproducts, and the hydrogenation of oleic acid. Since CO_2 is chemically stable and cannot be further oxidized, it has proven to be a good solvent to perform partial oxidation reactions of organic species; a solvent inert to oxidation, indeed, does not cause the formation of byproducts and, not being consumed with time, does not need to be replaced. One example is the oxidation of cyclohexane to cyclohexanol, for which supercritical CO_2 has shown better performances in terms of selectivity compared to other solvents like acetonitrile and ionic liquids. Similar results have been found for the oxidation of benzyl alcohol to benzaldehyde. Similarly to what exposed above, CO_2 can be used as solvent also for the synthesis of some polymers, like PTFE, replacing the hazardous traditional organic solvents; the only drawback is the low solubility of most polymers, especially those with a high molecular weight, in CO_2 [3][4].

CO_2 can also be used as refrigerant, replacing the hydrofluorocarbons used nowadays. Its use in this context implies dealing with much higher pressures, but grants superior performances and minor consequences due to potential leaks, since the Global Warming Potential (GWP) of CO_2 is much lower than that of hydrofluorocarbons [4].

Another use of captured CO_2 involves its application as a greenhouse fertilizer in agriculture, enhancing plant growth and thus reducing the usage of chemical fertilizers and water [4][10]. Furthermore, CO_2 can be captured by algae to produce bio-fertilizers, more environmentally friendly than chemical ones, and biomass, which can be in turn used to produce energy, biofuels, carbohydrates, protein extracts and organic chemicals to be used in cosmetic and pharmaceutical industries. Regarding biofuels, they mainly consist in biodiesel (obtained through transesterification), methane and hydrogen (obtained through anaerobic digestion), alcohols and acetone (obtained through fermentation) and bio-oil (obtained through thermochemical processes) [4][10].

1.2.2 Chemical conversion of CO_2

Besides its utilization as it is, CO_2 can be chemically converted into valuable products like bulk chemicals, polymers and electrofuels. Its transformation in such products is usually performed through carboxylation or reduction reactions: during the carboxylation the existing C=O bonds are not completely broken, while during the reduction one or both C=O bonds are broken by reaction with reducing agents like hydrogen. The main limit of CO_2 chemical conversion, and particularly its reduction, consists in its high thermodynamic stability and kinetic inertness, as indicated by its highly negative value of $\Delta_f G^0$ (= -394.38 kJ/mol). For this reason, for the transformation of CO_2, highly active catalysts are required, as well as an external energy input [11]. Regarding the obtainable products, the bulk chemicals mainly consist in urea, inorganic carbonates, propylene carbonates and salicylic acid; among polymers, the most relevant are polycarbonate and polyurethane [4], [10].

However, the most important products in the contest of this work are electrofuels. Electrofuels represent a way to store excess electric energy in form of chemical energy; particularly, captured CO_2 is converted into fuels by reduction with hydrogen obtained by electrolysis using energy from renewable sources. The combustion of the obtained fuels obviously produces CO_2, but with zero net carbon emissions, since the fuels themselves are entirely obtained from captured CO_2 [4], [10]. Methane is one of the most important fuels that can be obtained from CO_2 and finds large use as industrial and domestic fuel. CO_2 methanation, also called Sabatier reaction, consists in the reduction of CO_2 with hydrogen, using a H_2/CO_2 ratio of 4; the most used catalysts for this reaction are usually based on Ru, Fe, Ni, Co, Rh, Pd or Pt. Nickel is the most used one and is often dispersed onto various supports like γ-Al_2O_3, SiO_2, TiO_2, CeO_2, ZrO_2, hydrotalcites, zeolites, and carbon nanotubes to improve the efficiency of the catalyst [12]. Formic acid is another fuel that can be obtained from CO_2 and finds application in low temperature fuel cells; it is obtained with a H_2/CO_2 ratio of 1 using homogeneous catalysts that, compared to heterogeneous ones, present higher efficiency and require milder reaction conditions [10].

CO_2 conversion to methanol and dimethyl ether (DME)

Methanol and dimethyl ether (DME) are other two important electrofuels obtainable from CO_2 conversion as both have large applications mainly in the transportation sector. Methanol is obtained by using a H_2/CO_2 ratio of 3 over Cu-based catalysts and DME is obtained from methanol by its dehydration [4]. Compared to the synthesis of hydrocarbons, like methane, CO_2 conversion to methanol and DME (usually called oxygenates due to the presence of an oxygen atom in their structure) results to be preferable since it requires less hydrogen and has a higher atom efficiency [13]. Particularly, methanol, despite its toxicity, can be used as a fuel in fuel cells and in transportation, as a substitute of gasoline due to its high octane number [6]. DME, on the other hand, is non-toxic, non-carcinogenic, non-corrosive and has a low global warming potential; for these reasons, it is used as a propellant in cosmetic products and as a refrigerant. Furthermore, it can be used as an additive or even substitute of diesel fuel in internal combustion engines [14]–[16]. Diesel compression ignition engines have various advantages compared to gasoline engines, like a longer working life, higher power performance, and lower fuel consumption. However, they also show several drawbacks, mainly related to the higher combustion temperature and the chemical-physical properties of diesel fuel; particularly, diesel engines emit various pollutants like nitrogen oxides (NO_x), sulfur oxides (SO_x), CO, particulate and hydrocarbons. If diesel is replaced with DME in compression ignition engines sulfur emission are completely absent, and emissions of CO and hydrocarbons are lower [15]. Also, since DME does not have C-C bonds, the formation of particulate is significantly reduced, and therefore, the engine does not require the use of an anti-particulate filter, thus facilitating the installation of a catalyst to further decrease the CO and hydrocarbons emissions. Regarding NO_x emissions, a direct comparison between DME and diesel is not easy, since NO_x emissions are significantly influenced by external parameters such as the engine conditions; however, since DME combustion gives rise to lower emissions than diesel, a high exhaust gas recirculation can be used, allowing to reduce NO_x emissions. All these advantages are due to the different chemical-physical properties of DME and diesel as reported in Table 1 [15].

Table 1 Physicochemical properties of DME and diesel, adapted from [15], distributed under the terms and conditions of the Creative Commons Attribution (CC BY) license.

Property	**DME**	**Diesel**
Carbon content (mass%)	52.2	86
Hydrogen content (mass%)	1-3	14
Oxygen content (mass%)	34.8	0
Carbon-to-hydrogen ratio	0.337	0.516
Liquid density (kg/m^3)	667	831
Cetane number	>55	40-50
Autoignition temperature (K)	508	523
Stoichiometric air/fuel mass ratio	9.6	14.6
Normal boiling point (K)	248.1	450-643
Enthalpy of vaporization (kJ/kg)	467.1	300
Lower heating value (MJ/kg)	27.6	42.5
Ignition limits (vol% in air)	3.4/18.6	0.6/6.5
Elastic modulus (N/m^2)	$6.37 \cdot 10^8$	$14.86 \cdot 10^8$
Liquid kinematic viscosity (cSt)	<0.1	3
Surface tension at 298 K (N/m)	0.012	0.027
Vapour pressure at 298 K (kPa)	530	<10

Particularly, the lower boiling point of DME leads to a faster evaporation when the fuel is injected into the engine, improving the combustion. DME, compared to diesel, also has a higher cetane number, due to its lower auto-ignition temperature, leading to a cleaner combustion and a reduced noise [15]. Furthermore, in view of a potential large scale usage of DME as transportation fuel, it has to be pointed out that, due to its chemical-physical properties similar to those of Liquified Petroleum Gas (LPG), DME can be stored and transported using the same technologies used nowadays for LPG, with only minor modifications [14][16]. However, the substitution of diesel fuel with DME also presents some disadvantages. DME has a lower LHV (Lower Heating Value) than diesel, requiring a higher amount of fuel to obtain the same amount of energy; also, the utilization of DME in place of diesel requires to adopt important modification to the engines, like modified gaskets to avoid leakage and replacement of some plastic parts which can be degraded by DME [15]. Nowadays, several automotive companies like Volvo, Isuzu, Hino, Nissan, Shanghai Automotive, Navistar, and Ford are testing DME as an alternative to diesel fuel. Particularly, Volvo has been working on DME engines since the mid-90s, building a large fleet of test vehicles, including 10 heavy-duty trucks [17]. In the perspective of a gradual replacement of conventional fossil fuels with green fuels, DME is considered one of the most promising green fuels and could lead to an important development of a DME economy in the near future [13] [14]. Despite not being still a widespread technology, DME synthesis from CO_2 is currently performed in some demonstration plants. One of them is the ALIGN-CCUS demonstration plant, located at Niederaussem, in Germany, and is co-funded by the European Horizon 2020 program ACT. This demonstration plant produces 50 kg of DME per day using the CO_2 captured from a 1000 MW power plant and the hydrogen produced from an alkaline electrolyser. In this plant, DME is produced by the direct synthesis method, consisting of the direct conversion of CO_2 and H_2 into DME [18]. The indirect route, on the other hand consists of the transformation of CO_2 and H_2 into methanol and its subsequent dehydration to DME. Regarding DME production from CO_2 by the indirect process, one of the production plants currently in activity belongs to the Oberon Fuels company and is located in San Diego, USA, and produces about 22 m^3 of DME from CO_2 per day; in this case, however, the reduction of CO_2 is not performed using electrolytic hydrogen but biogas or natural gas [17]. The details on the direct and indirect synthesis methods will be described in the following paragraphs (1.2 and 1.3), with particular attention on the used catalytic systems.

1.3 Syngas-to-DME process

As mentioned above, one of the most promising electrofuels that can be obtained from the transformation of CO_2 is dimethyl ether. However, it needs to be pointed out as the original process used for the production of DME is based on the hydrogenation of syngas. The synthesis of DME from syngas can be carried out following a two-step process (also known as indirect route) or a one-step process (also known as direct route). In the first case CO is first reduced to methanol with an hydrogenation process, following the reaction reported below [16], [19]:

$$CO + 2H_2 \leftrightarrows CH_3OH \qquad \Delta H^0_{298k} = -90.6\ kJ/mol$$

The methanol obtained from the hydrogenation of CO is subsequently dehydrated to dimethyl ether, with the following reaction:

$$2CH_3OH \leftrightarrows CH_3OCH_3 + 2H_2O \qquad \Delta H^0_{298k} = -23.4\ kJ/mol$$

Each of these steps requires the use of solid catalysts: a redox phase for the CO hydrogenation and an acidic one for the dehydration.

1.3.1 Redox catalysts for CO hydrogenation to methanol

For the hydrogenation of CO to methanol, a wide number of catalysts has been reported in the literature. The first catalyst that has been reported for this reaction was a ZnO-Cr_2O_3-based catalyst developed by BASF in 1920s; however, this system works only under high pressure (240-350 bar) and high temperature (350-400 °C) and is highly susceptible to poisoning from sulfur and chlorine, which are impurities often present in syngas. [19]

Nowadays, the vast majority of catalysts reported for the hydrogenation of CO are Cu-based systems (Figure 1); the first Cu-based catalyst for this purpose was developed by Imperial Chemical Industries in 1960s, and, besides Cu, which is the active phase of the catalyst, also featured the presence of ZnO, which acts as a promoter by increasing the dispersion of Cu particles, acting as a spacer between such particles and thus increasing the number of Cu-based sites active towards methanol synthesis [19], [20].

Cu/ZnO-based catalysts are often paired with a third phase, usually Al_2O_3 or, less commonly, ZrO_2; this species increases the chemical and thermal stability as well as the dispersion of the active sites and the surface area of the catalyst, allowing to carry out the methanol synthesis reaction at relatively low values of pressure (50-100 bar) and temperature (250 °C). [19][21], [22]

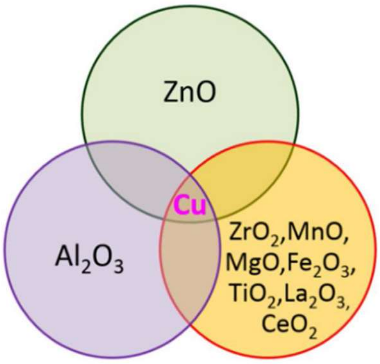

Figure 1 Promoters and modifiers used in combination with Cu for methanol synthesis from syngas. Reprinted with permission from [19]*, license number 5470430040707.*

1.3.2 Acidic catalysts for methanol dehydration to DME

As of the second reaction, the dehydration of methanol to dimethyl ether, the most widely used catalysts are solid acidic systems; ideally, a good dehydration catalyst for methanol dehydration, should show, besides the presence of acidic sites, high performances in terms of both activity and selectivity towards DME, a hydrophobic surface and, in a large-scale production scenario, a low cost. As observed by several authors, methanol dehydration is catalyzed by both Brønsted and Lewis acid sites [19]. Lewis sites, however, gradually deactivate due to the adsorption of water, which forms an acid-base Lewis adducts by donating one of its lone electron pairs to the Lewis electron-accepting site. Brønsted sites, on the other hand, have shown better performances in terms of activity. Due to their nature, consisting in a proton-donating Si-O-Al group, these sites do not give rise to water adsorption, thus showing a higher water resistance [23][19]. A graphical representation of Brønsted and Lewis acid sites is given in Figure 2.

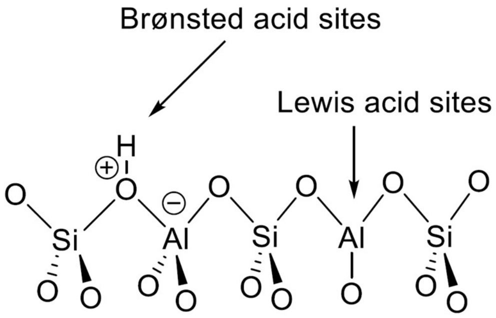

Figure 2 Brønsted and Lewis acid sites on aluminosilicates, reprinted from [24].

Regarding the strength of the acidic sites involved in the reaction, those with weak and moderate strength are preferred, since high strength could lead to the formation of undesired by-products, such as olefins, through the methanol-to olefins (MTO) process, and the deactivation of the catalyst due to coke deposition. γ-Al_2O_3 is the most widely reported catalyst for this reaction; this system is the most active one among all the polymorph species of Al_2O_3, like k-Al_2O_3 and α-Al_2O_3, the latter being completely inactive towards methanol dehydration. γ-Al_2O_3, as evidenced by several authors, shows high selectivity to DME in methanol dehydration, without giving rise to the formation of undesired byproducts; this catalyst, indeed, only features the presence of Lewis acidic sites, which are highly selective to DME. However, Lewis acidic sites, as mentioned before, are prone to deactivation due to water adsorption. This catalyst, however, is still vastly used due to its cheapness [19].

Besides γ-Al_2O_3, zeolites have been widely proposed as methanol dehydration catalysts (particularly, ferrierite, ZSM-5 and mordenite) and are, nowadays, the most active systems reported in the literature. Zeolites, indeed, due to the lower hydrophilicity of their surface, compared to γ-Al_2O_3, and due to the presence of Brønsted sites, showed significantly higher activity than γ-Al_2O_3; Brønsted sites, indeed, present a much higher resistance to water adsorption than Lewis sites, giving zeolites a higher water tolerance [19][25]. However, the presence of strong Brønsted acidic sites needs to be pointed out leading to those processes already described above (MTO process and coke deposition) [19].

The mechanism of methanol dehydration depends on the complex (and not fully understood) interaction of methanol with the acid sites. For DME formation both an associative Langmuir-Hinshelwood (L-H) mechanism, involving the reaction of two surface species, and a dissociative Rideal-Eley (R-E) mechanism, involving the reaction of a surface species and a gas-phase methanol molecule, have been reported [26][27]. However, an agreement about the real mechanism of methanol dehydration has not been reached in the literature, and the debate is still in progress. A graphical representation of the two proposed mechanisms is given in Figure 3.

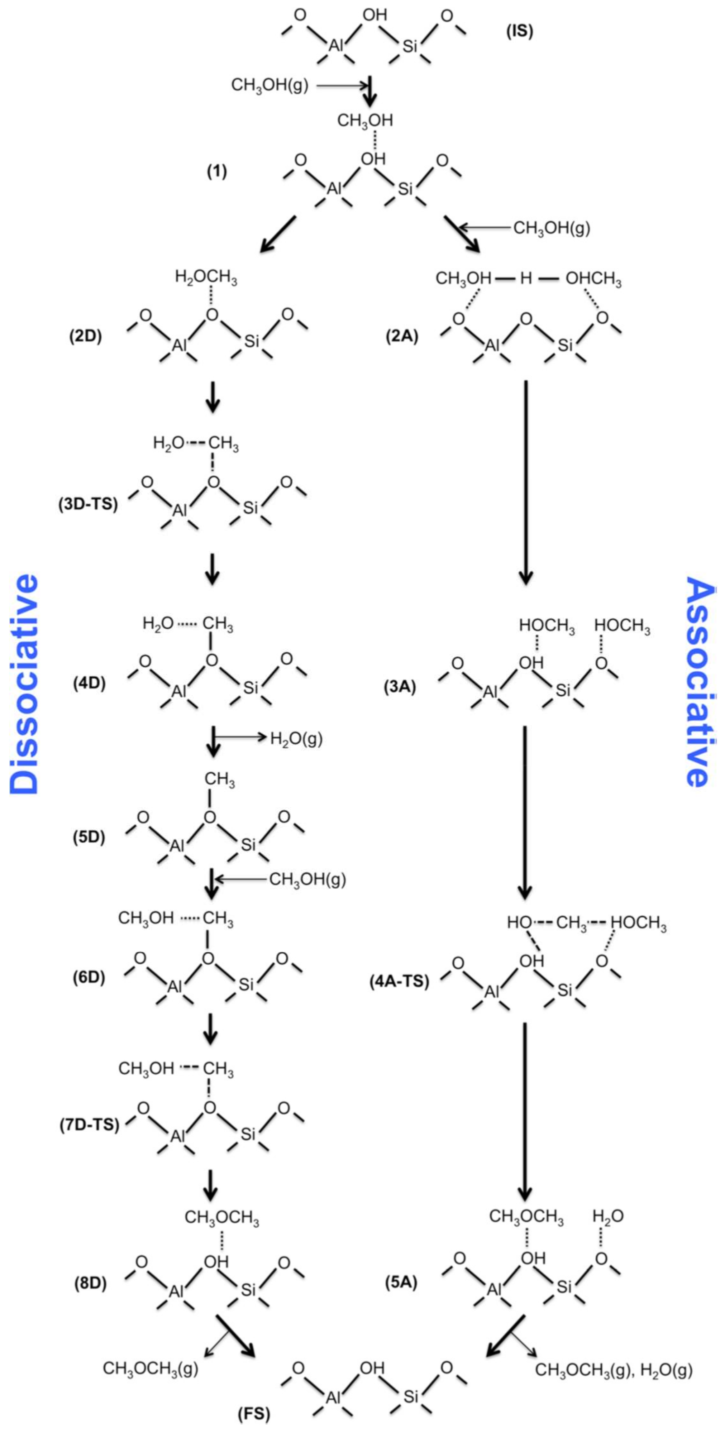

Figure 3 Dissociative (left) and associative (right) mechanism for methanol dehydration to DME. Reprinted with permission from [26]*. Copyright 2016 American Chemical Society.*

There are substantial differences in the details of specific surface species involved. The L-H mechanism requires the adsorption of two molecules of methanol on an acid site and on an adjacent oxygen site; these surface species subsequently react to give one molecule of DME and H_2O. The R-E mechanism requires only an acid site, which adsorbs a methanol molecule; a water molecule is then released, leaving a surface -CH_3 species which eventually reacts with a methanol molecule in gas phase. In this context, both mechanisms are bimolecular, since both of them involve two molecular species, either in adsorbed or gas form. It is worth of note that, in both the articles here reported, the associative L-H mechanism is suggested as the most prominent one; particularly, in the most recent work [26], a computational study performed on the Brønsted acid sites of a zeolite, suggest that the associative mechanism is predominant at temperatures lower than 600 °C at all pressures. Furthermore, high values of pressure favor the L-H mechanism, so, in our case, it can be assumed that this mechanism is the most predominant one.

1.3.3 One-step syngas-to-DME process

Besides the two-step syngas-to-DME process, in which the two reactions are carried out in two different reactors, much attention is currently focused on the one-step (or one-pot) process, which consists in the two reactions being performed simultaneously into the same reactor. This process has drawn so much attention due to its intrinsic advantages like the lower complexity and cost associated with the management of a single reactor rather than two. To carry out the one-pot process it is necessary to have both catalytic functions into the reactor; in the literature the most widely used method to obtain such two-function catalyst consists in the simple physical mixing of the redox and the acidic catalysts. However, the two catalytic functions can also be put together by obtaining what in the context of this dissertation is defined as "bifunctional catalyst", called “hybrid catalyst” by some other authors [14]; in these systems the redox phase is usually deposited onto the acidic phase by chemical methods, rather than by physical mixing, obtaining bifunctional catalysts with an intimate contact between the two catalytic phases. Such catalysts have been obtained by several synthesis methods like coprecipitation [28], impregnation, coprecipitation-impregnation, coprecipitation-sedimentation, sol-gel, sol-gel impregnation, liquid-phase synthesis [21] and, more recently, colloidal approach, ultrasound-assisted coprecipitation, and flame spray pyrolysis [19]. Bifunctional catalysts should ideally grant superior performances due to various features like a higher dispersion of the redox phase, which should maximize the contact area with the reagents, and a prompt dehydration of the formed methanol, due to the close proximity of the redox Cu-based sites and the acidic sites.

γ-Al_2O_3-based catalysts

Cu/ZnO/Al_2O_3-based redox catalysts (CZA) are often paired with γ-Al_2O_3 for the one pot syngas-to-DME process either in form of physical mixtures or as bifunctional catalysts; the reaction is usually carried out in a temperature range comprised between 240 and 290 °C with a pressure range of 30-60 bar. With these reaction parameters CO conversions up to 95% and DME yields up to 61% have been reported. Regarding the nature of the contact between the redox and the acidic catalyst, different results were reported in the literature; some authors reported a positive effect of the intimate contact between the two phases in composite catalysts, which showed better performances then physical mixtures [19]. On the other hand, other authors reported a detrimental interaction between the two catalysts and observed higher performances in physical mixtures [19][29]. In addition to this, the lack of systematical studies and the significant differences in both synthesis methods and reaction conditions make difficult to establish if the best way to combine the two catalytic functions is physical mixing or "chemical" mixing. Due to the intrinsic limits of the Lewis sites present on γ-Al_2O_3 mentioned above, several efforts have been focused on the optimization of γ-Al_2O_3 for the syngas-to-DME process, modifying it by the insertion of heteroatoms [19] like Si [30] and Nb [31] and anions like F^- [32], SO_4^{2-} [33] and PO_4^{3-} [34]. In the literature, several modifications to the redox phase in γ-Al_2O_3-based catalysts have been reported. Besides Al_2O_3, other species have been investigated [19], namely Zr [35]–[37], Ga [35], [36], Mn [38], [39], Pd [40], La [36], [41], Y [36], Mg [42], Ga-Cr [30] and carbon nanotubes [43]. Taking into account the peculiar properties of mesoporous/mesostructured materials, such as the high surface area and the relatively large pore size, some cases of bifunctional catalysts based on mesoporous [44] and mesostructured [45][46][47] γ-Al_2O_3 have also been reported. Mesostructured γ-Al_2O_3 is usually synthesized by an Evaporation-Induced Self-Assembly (EISA) approach and used as support to disperse the Cu-based redox phase inside the mesopores, which is usually done with impregnation methods using copper nitrate. The composite catalysts obtained by dispersing Cu on mesostructured γ-Al_2O_3 [46] showed homogeneous and fine dispersion of the redox phase inside the mesopores (Figure 4), resulting in better performances due to the improved mass transfer and the high dispersion of Cu. Interestingly, in the few cases reported for mesostructured γ-Al_2O_3, the authors only used Cu as active phase, excluding ZnO, despite the positive effect of this species on the catalytic performances observed by many researchers; despite the absence of the promoter, these catalysts showed good activities for the syngas-to-DME process, presumably due to the high dispersion of copper in form of nanoparticles mentioned above [46][19]. Although the results obtained using mesostructured γ-Al_2O_3 were promising, the use of ordered mesoporous systems to obtain bifunctional catalysts for DME synthesis is still not deeply investigated.

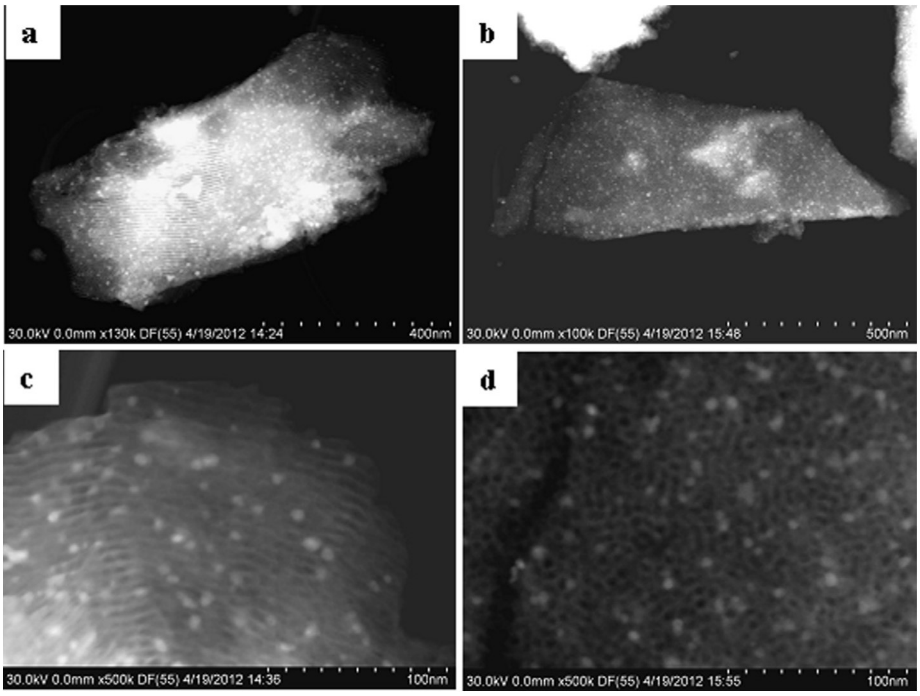

Figure 4 STEM dark-field images of Cu nanoparticles dispersed on mesostructured γ-Al_2O_3. Reprinted with permission from [46]*, license number 5463180021656.*

Zeolite-based catalysts

Due to the intrinsic limits of γ-Al_2O_3, deriving from the low water resistance of its Lewis sites and their consequent lower activity towards methanol dehydration, many examples of either physical mixtures or bifunctional catalysts based on zeolites as dehydration catalysts have been reported for the syngas-to-DME process. Zeolites are crystalline microporous aluminosilicates with a framework consisting of tetrahedral silicate groups (SiO_4^{4-}) and intra-framework aluminate groups (AlO_4^{5-}); like in the structure of pure silica, metal atoms are interconnected to each other by oxygen atoms and the presence of Al^{3+} species in place of Si^{4+} gives rise to the formation of a negative charge, which is compensated by the presence of a cation like H^+ or Na^+. Acidic form of zeolites (zeolites featuring the presence of H^+ as cation) are the most used for methanol dehydration. Zeolites, contrary to γ-Al_2O_3, have a much higher water resistance, not only due to the presence of Brønsted acid sites, deriving from the tetrahedrally coordinated aluminum atoms in the crystal framework, but also due to their higher surface hydrophobicity; furthermore, γ-Al_2O_3 shows its maximum activity for methanol dehydration at higher temperature than the ideal working temperature of Cu-based redox catalysts (~250 °C). Zeolites, on the other hand, can work properly at lower temperatures, making them ideal dehydration systems to work as dehydration catalysts paired with Cu-based methanol synthesis catalysts [19]. The difference in terms of activity of Brønsted sites, compared to Lewis sites, was studied by Garcia-Trenco *et al.* [48] on H-ZSM-5 treated with both Na^+ and Co^{2+} in order to neutralize its Brønsted acid sites; namely, the addition of Na^+ decreased both the amount of Brønsted and Lewis sites, while Co^{2+} decreased the amount of Brønsted sites, increasing Lewis sites. By comparing the amount of both Brønsted and Lewis acid sites with the performances of the catalysts, the authors concluded that methanol dehydration is mostly driven by Brønsted sites, with a minor contribution from Lewis sites. However, it has to be pointed out that not all zeolites are ideal methanol dehydration catalysts; the presence of strong Brønsted sites, for example, must be avoided, for the occurrence of those processes previously mentioned [49][30], [50]. In order to reduce the amount of strong Brønsted sites in the structure of zeolites, several authors, beside the classical approach consisting in the modulation of Si/Al ratio, proposed their modification with the insertion of basic oxides like MgO, CaO, ZnO [51], [52] and Sb_2O_5 [53] or transition metals like Zr [54] and Fe [55]. The most used zeolites for methanol dehydration are ZSM-5, ferrierite, mordenite, and zeolite-Y; particularly, ZSM-5 is the zeolite most used in the literature for this reaction due to its intrinsic advantages like the medium size of its pores, which allows to prevent coke deposition without limiting the diffusion of the reagents. Also, the amount and strength of the acid sites present on ZSM-5, like on most zeolites, can be tuned by modifying the Si/Al ratio [56]. As expected, several authors observed that the best results are obtained with low Si/Al ratio (< 50) [57], [58], since the high amount of Al in the structure grants a high number of sites and a moderate acidic strength. It has also been observed that the crystallite size of zeolites strongly affects the catalytic activity for methanol dehydration and coke deposition; namely, zeolites in form of nanocrystals (crystallite size < 100 nm) showed better performances, due to the increased mass transfer, and less coke deposition [59]–[61]. Some authors, however, observed a detrimental effect of the intimate contact between the redox and acidic phase in ZSM-5-based bifunctional catalysts, due to sintering of the redox phase particles, their oxidation, and also ion-exchange phenomena with the zeolite, which also led to a deactivation of the acidic sites [59]. A negative interaction due to the close contact of the two phases was also observed by other authors which observed a decrease in the number of Brønsted acid sites of H-ZSM-5 zeolite when it was put into contact with the dehydration catalyst through mechanical mixing (grinding) and liquid phase mixing (slurry), resulting in a performance drop; this negative effect was not observed, on the other hand, when the two catalysts were separately pelletized and then mixed together [62].

Despite not being reported as often as ZSM-5, the zeolite ferrierite (FER) has attracted the attention of several researchers due to its high selectivity to DME and, particularly, its high stability over time, due to the extremely limited coke deposition. In a work of Montesano *et al*, ferrierite and theta-1, compared with other zeolites like ZSM-5 and mordenite, gave rise to smaller amounts of coke deposition, due to their structure, which does not allow the accumulation of large carbonaceous species, providing easier paths for molecular diffusion; FER and theta-1 also showed higher values of DME selectivity [63][19]. Similar results, highlighting the superior behavior of ferrierite compared to other zeolites, were also obtained by other authors [64][54].

1.4 CO_2-to-DME process

Starting from the production process of DME from syngas, the research has recently devoted efforts to the CO_2-to-DME process, which allows to obtain DME re-evaluating CO_2 as a reagent rather than as a waste [1][4][7][11]. This process can thus be considered as a part of the CCU framework previously described. CO_2 transformation into DME consists in two subsequent reactions [6], [14], [15], [65], [66]. The first one is the reduction of CO_2 to methanol in the presence of hydrogen:

$$CO_2 + 3H_2 \leftrightarrows CH_3OH + H_2O \qquad \Delta H^0_{298k} = -49.5\ kJ/mol$$

The second one consists in the dehydration of methanol to DME:

$$2CH_3OH \leftrightarrows CH_3OCH_3 + 2H_2O \qquad \Delta H^0_{298k} = -23.4\ kJ/mol$$

The global reaction, thus, results to be:

$$2CO_2 + 6H_2 \leftrightarrows CH_3OCH_3 + 3H_2O \qquad \Delta H^0_{298k} = -122\ kJ/mol$$

1.4.1 Thermodynamics of the CO_2-to-DME process

Despite its promising potential, the CO_2-to-DME process present some chemical and thermodynamic disadvantages, compared to the process starting from syngas. First, unlike the syngas-to-DME process, in the CO_2-to-DME process, CO_2 reduction to methanol competes with the Reverse Water-Gas Shift (RWGS) reaction, that gives rise to the formation of CO:

$$CO_2 + H_2 \leftrightarrows CO + H_2O \qquad \Delta H^0_{298k} = +41.2\ kJ/mol$$

Another disadvantage is that, as can be seen from the CO_2 hydrogenation reaction, the reduction of one molecule of CO_2 to methanol requires three molecules of hydrogen, compared to the two molecules required by the process starting from CO; as a consequence, the hydrogenation of CO_2 also gives rise to the production of water as by-product. Also, it has to be pointed out that CO_2 shows a much lower reactivity than CO; consequently, CO_2 hydrogenation results to be less thermodynamically favored than CO hydrogenation, as can be seen from the values of enthalpy, further lowering the yield to DME. Figure 5 reports the differences in terms of methanol yield and DME yield for the two processes (syngas-to-DME and CO_2-to-DME); as can be seen, the values of yield at the same conditions of temperature and pressure, are significantly higher for the process starting from syngas, due to the reasons stated above [66].

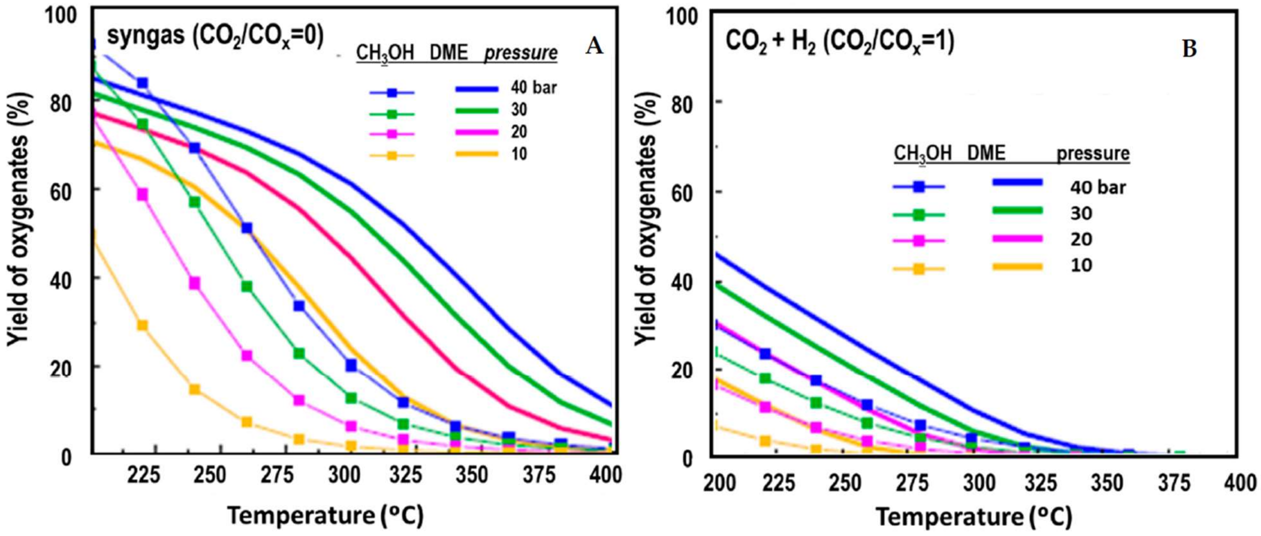

Figure 5 Methanol and DME yield for the syngas-to-DME and the CO_2-to-DME processes. Reprinted from [66]*, distributed under the terms and conditions of the Creative Commons Attribution (CC BY) license.*

As mentioned above, the CO_2-to-DME process gives rise to the production of significant amount of water as by-product. In the syngas-to-DME process water is only produced by methanol dehydration, giving rise to the formation of one molecule of water for each DME molecule formed; on the other hand, in the CO_2-to-DME process, besides methanol dehydration, water is also produced by CO_2 hydrogenation, for a total of three water molecules per DME molecule. Furthermore, the RWGS reaction is an additional source of water in the process. For this reason, considering that the catalytic systems used for the CO_2-to-DME process are similar to those used for the DME production from syngas, water formation could give rise to significant deactivation phenomena of both the redox and the acidic catalyst, blocking their active sites and causing growth and oxidation phenomena on the particles of the redox catalyst. [66]

As can be seen in Figure 6, that shows the change in CO_2 conversion by varying both temperature and pressure, the CO_2-to-DME process is favored by relatively low temperatures, due to the exothermic nature of both the CO_2 hydrogenation to methanol and the methanol dehydration to DME. Low values of temperature also allow to limit the endothermic RWGS reaction, that prevails at high temperatures. Another aspect that favors DME production from CO_2 are high pressure conditions, owing to the decrease in terms of number of moles between reactants and products [14], [15], [66].

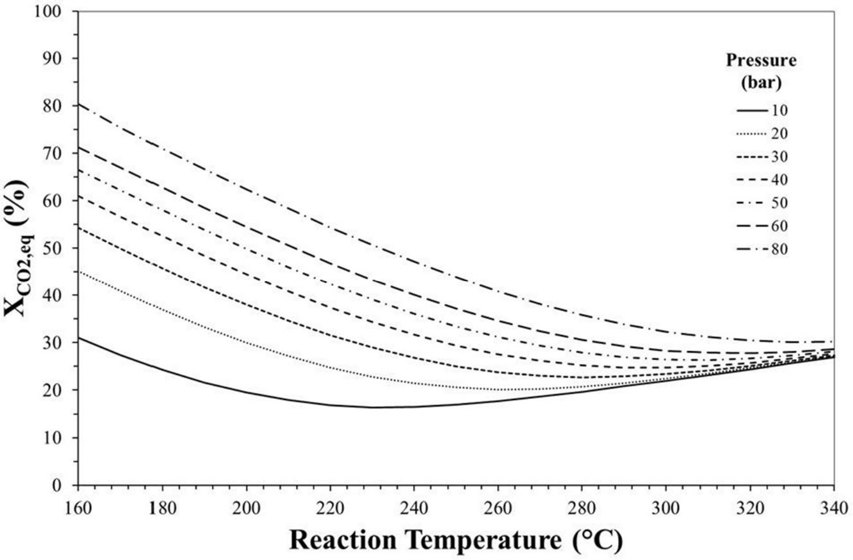

Figure 6 CO_2 conversion for the CO_2-to-DME process at various temperatures and pressures. Reprinted from [15]*, distributed under the terms and conditions of the Creative Commons Attribution (CC BY) license.*

Due to the exothermicity of methanol dehydration mentioned above, also DME selectivity (Figure 7) is positively influenced by relatively low temperatures and high pressures. On the contrary, the formation of CO, being originated from an endothermic reaction, is favored by high temperatures and low pressures (Figure 8) [15].

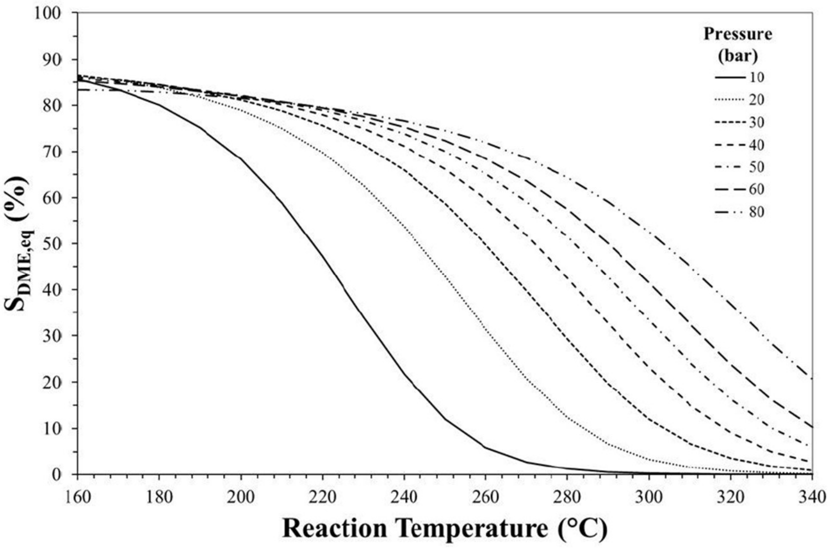

Figure 7 DME selectivity for the CO_2-to-DME process at various temperatures and pressures. Reprinted from [15]*, distributed under the terms and conditions of the Creative Commons Attribution (CC BY) license.*

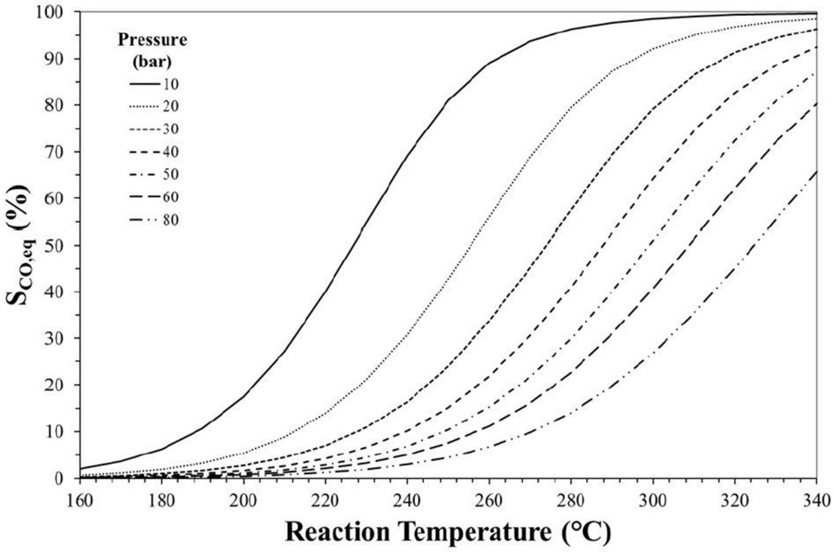

Figure 8 CO selectivity for the CO_2-to-DME process at various temperatures and pressures. Reprinted from [15]*, distributed under the terms and conditions of the Creative Commons Attribution (CC BY) license.*

Selectivity to methanol, being this molecule formed from a reaction that implies a decrease in the number of moles, is always positively influenced by an increase in pressure; however, since methanol is produced and consumed by two different exothermic reactions, its selectivity at lower temperatures is increased by increasing the temperature up to a maximum after which it starts decreasing (Figure 9) [15].

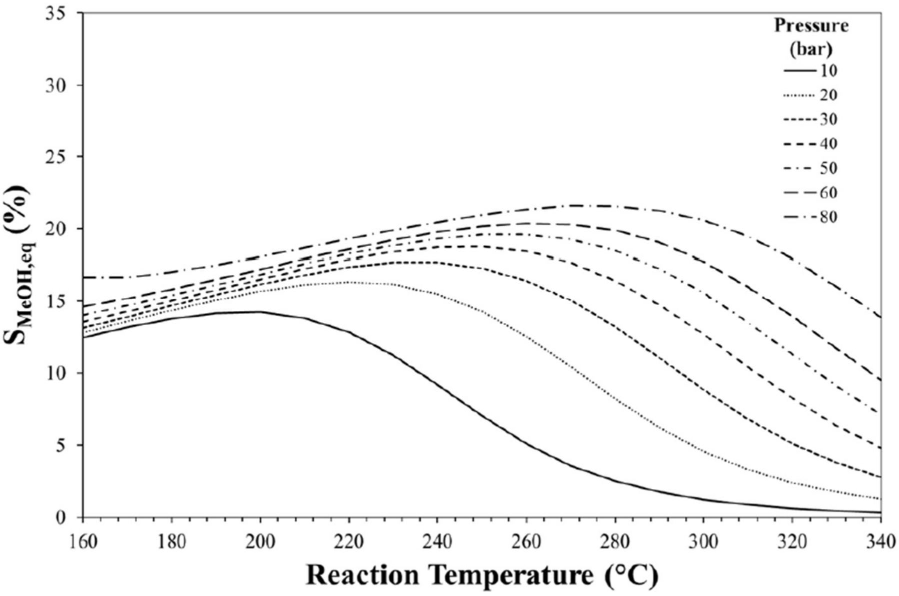

Figure 9 Methanol selectivity for the CO_2-to-DME process at various temperatures and pressures. Reprinted from [15]*, distributed under the terms and conditions of the Creative Commons Attribution (CC BY) license.*

Like for the syngas-to-DME process, the CO_2-to-DME process can be performed through both a two-step and a one-step route; however, the intrinsic benefits of the one-step process, like the reduced costs and the thermodynamic advantages, for the process from syngas are limited by the production of water during methanol dehydration, which could lead to the consumption of CO to form CO_2 through the water-gas shift (WGS) reaction. On the contrary, for the CO_2-to-DME process, this phenomenon is not a problem, since water is produced anyway during CO_2 hydrogenation. Particularly, the two-step CO_2-to-DME process features some advantages, like a higher purity of the produced DME, which can be easily separated from water (the only by-product in significant amounts), and an easier management of the water formed during the process. On the other hand, however, the one-step process presents important advantages, like the use of a single reactor that, compared to the use of two separate reactors, significantly decreases the building and management cost of the plant; another benefit of the one-step process consists in an increased conversion of CO_2, due to the subtraction of methanol by the dehydration reaction, which shifts the equilibrium of CO_2 hydrogenation towards the products. The thermodynamic advantage of the one-step process, consisting in the increased CO_2 conversion, can be quantified by using a parameter called CO_2 conversion gain (CPG) (Figure 10), calculated according to the equation:

$$CPG = \frac{X^{a}_{CO2,eq} - X^{b}_{CO\ \ ,eq}}{X^{b}_{CO\ \ ,eq}} * 100$$

where $X_{CO2,eq}$ is CO_2 conversion at equilibrium at given values of temperature and pressure for the one-step (a) and two-step (b) process. As can be seen (Figure 10), the one-step process always results to be advantageous.

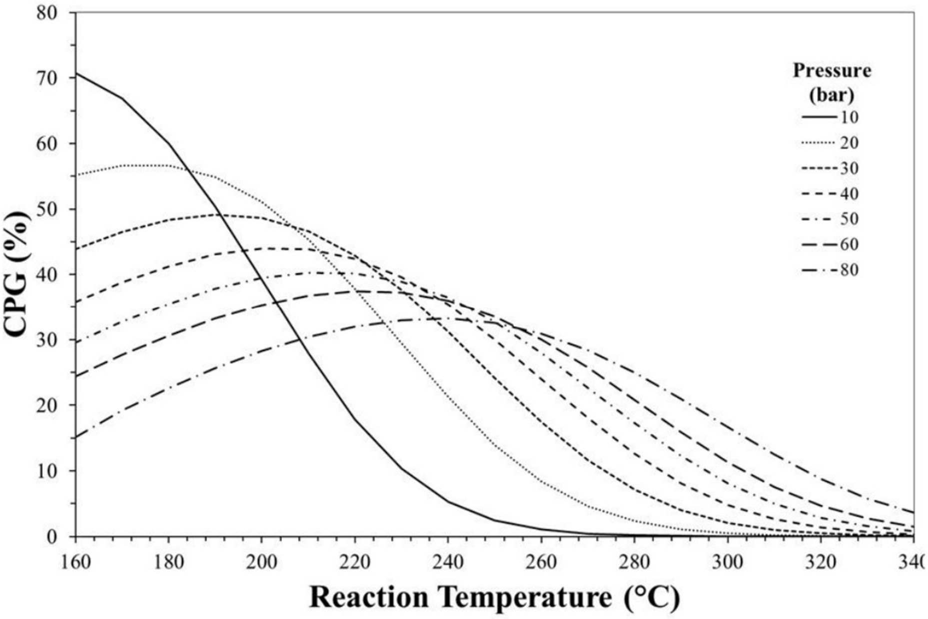

Figure 10 CO_2 conversion gain for the one-step CO_2-to-DME process over the two-step process. Reprinted from [15]*, distributed under the terms and conditions of the Creative Commons Attribution (CC BY) license.*

1.4.2 Redox catalysts for CO_2 hydrogenation

Cu-based catalysts

Similarly to what has been reported in the literature regarding the catalysts used for CO hydrogenation, Cu-based catalysts are, by far, the most widely reported systems for the promotion of the CO_2 reduction to methanol. In these catalysts, Cu is often paired with one or more promoters, among which ZnO is the most widely used. Also, several studies suggest the presence of a synergy between Cu and Zn to form the active sites for CO_2 hydrogenation; these sites consist in Cu^0 or partially reduced copper oxide and their formation is favored by the intimate contact with Zn species [11], [66]. To better understand this synergy, it must be pointed out that there are two main reaction mechanisms proposed for the CO_2 hydrogenation to methanol (Figure 11): the first one, called the “formate route”, consists in the initial formation of formate species which is then hydrogenated to form methoxy species that is finally hydrolyzed to methanol. The second reaction pathway first consists in the RWGS reaction, that converts CO_2 to CO; CO is then hydrogenated to methanol through formyl and formaldehyde as reaction intermediates [11], [66].

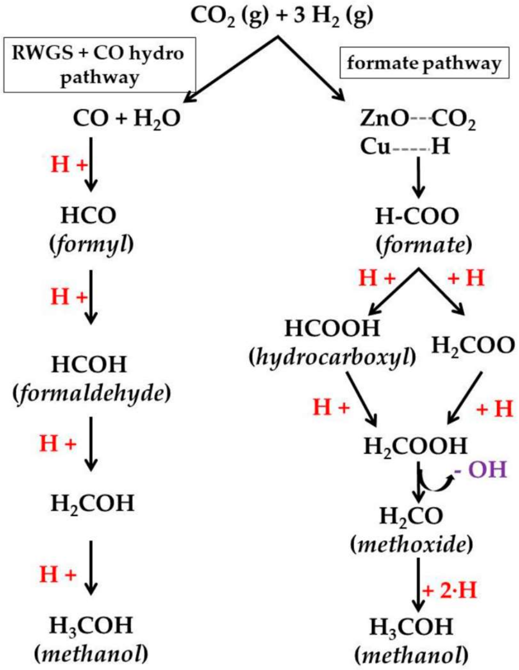

Figure 11 The two mainly proposed mechanisms for CO_2 hydrogenation to methanol. Reprinted from [11] *distributed under the terms and conditions of the Creative Commons Attribution (CC BY) license.*

According to several studies, methanol is mainly produced through the formate path, since the high amount of CO_2 in the reaction environment limits its formation by the RWGS [67]–[69]. With this in mind, and also considering the detrimental effect of the RWGS reaction on the selectivity of the CO_2-to-DME process mentioned above, it can be concluded that the better strategy to develop efficient CO_2 hydrogenation catalysts is to enhance their activity towards methanol formation via the formate route [66]. As can be seen in Figure 12, when Cu-ZnO-based catalysts are used for CO_2 hydrogenation, the two reactive species adsorb on two different active sites; namely, hydrogen adsorbs on Cu-sites while CO_2 is adsorbed on ZnO sites. This is the origin of the synergy between the two species mentioned above. For this reason, an intimate contact between the two species is a key factor to obtain efficient catalysts.

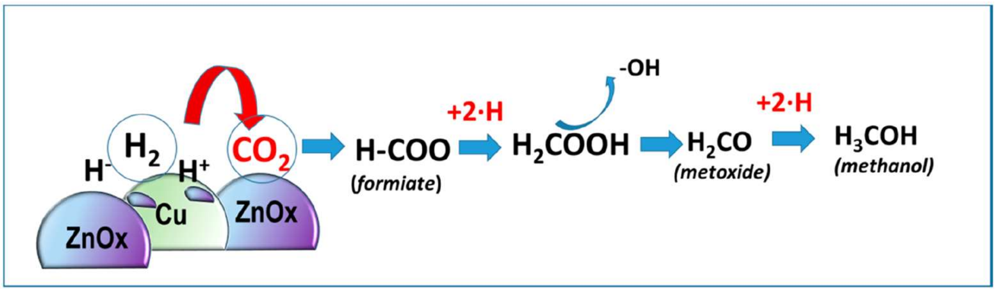

Figure 12 Graphical representation of the Cu-ZnO synergistic effect on methanol formation through the formate pathway. Reprinted from [66] *distributed under the terms and conditions of the Creative Commons Attribution (CC BY) license.*

Since the formate route has been identified as the main reaction pathway for methanol synthesis from CO_2, the design of the catalysts needs to be tailored with the goal of limiting the amount of sites responsible for the RWGS. To optimize the selectivity of the Cu/ZnO-based catalysts for methanol, minimizing the sites responsible for the RWGS reaction, several strategies have been adopted, like the addition of other chemical species as promoters/modifiers, the optimization of the synthesis routes, and also the development of new catalysts not based on Cu [66][11].

Regarding the addition of promoters, Cu/ZnO catalysts are most often paired with Al_2O_3 which increases the thermal and chemical stability of the catalyst, granting more stable performances [6], [15], [61][66]. Furthermore, the presence of Al^{3+} ions favors the formation of the previously mentioned reduced ZnO sites [66]. Typically, Cu/ZnO/Al_2O_3 catalysts feature an amount of Cu ranging from 50 mol% to 70 mol%, 20-50 mol% of ZnO and 5-20% of Al_2O_3 [6][14]. The second most used promoter for Cu/ZnO catalysts is ZrO_2; this modifier is considered superior to Al_2O_3 due to its lower hydrophilicity, that leads to a limited water adsorption, and higher basicity, which favors the adsorption of CO_2, improving methanol formation. ZrO_2 also facilitates the formation of oxygen vacancies in the reduction of the catalyst, increasing the dispersion of Cu and the formation of Cu-ZnO sites [65], [66], [70]. Ga^{3+} has been studied as a modifier through its insertion into the crystal lattice of ZnO and proved to be effective in promoting the formation of Cu-ZnO active sites by favoring the reducibility of ZnO and also facilitating the adsorption of the reaction intermediates [66]. Cu-ZnO active sites are also positively influenced by the addition of Mn^{2+}, which increases Cu dispersion, enhancing its contact with ZnO and lowering its reduction temperature. An increase in hydrogen adsorption was instead observed after the addition of noble metals, but the use of such species is limited due to their high cost [66]. Another system that has been studied to improve the performance and stability of Cu/ZnO-based catalysts is mesostructured silica (SBA-15); this system, indeed, due to the relatively large size of its pores, allow a confinement of the redox catalyst inside its ordered porous matrix in form of nanoparticles, increasing their dispersion, their contact area with the reagents, and their stability [66][71][72]. A high dispersion of Cu/ZnO nanoparticles, leading to a high contact area and improved reducibility was also obtained by using carbon nanotubes, reduced graphene oxide aerogel, and carbonaceous coordination polymers [66].

Regarding the synthesis routes (Figure 13), Cu-based catalysts are most often obtained through coprecipitation processes, consisting in the precipitation of metal hydroxycarbonates or hydroxides obtained by adding a basic solution (usually carbonates or hydroxides) to a solution of the metal precursors (generally nitrates). In this regard, several synthesis parameters such as the order of add of the solutions, the chosen base, the temperature, and the pH can influence the final morphology of the catalyst and thus its catalytic performances. The precipitation of the precursors is usually followed by aging, during which the precipitates transition from an amorphous to a crystalline phase; the precipitates are then washed to eliminate any impurity, mainly consisting in Na^+ and nitrates, detrimental for the final catalyst since they give rise to Cu agglomeration. The precipitates are eventually treated at high temperature to induce the transformation of the precipitated hydroxycarbonates/hydroxides to oxides. The crystalline phases formed during the aging process are crucial to obtain catalysts with good morphological properties, such as a high surface area and a proper contact between Cu and ZnO. Particularly, the ideal crystalline phase to obtain a good redox catalyst is zincian malachite; the presence of the amorphous zincian georgite also proved to be beneficial. This phase, indeed, allows some residual carbonates to survive the calcination process; the presence of such residues favors the maintenance of the textural properties of the catalyst in terms of surface area and porosity. It must be pointed out that, after the synthesis, Cu is always present in its oxide form (CuO); for this reason, all catalysts need to be reduced with hydrogen before being used for CO_2 hydrogenation [6], [11].

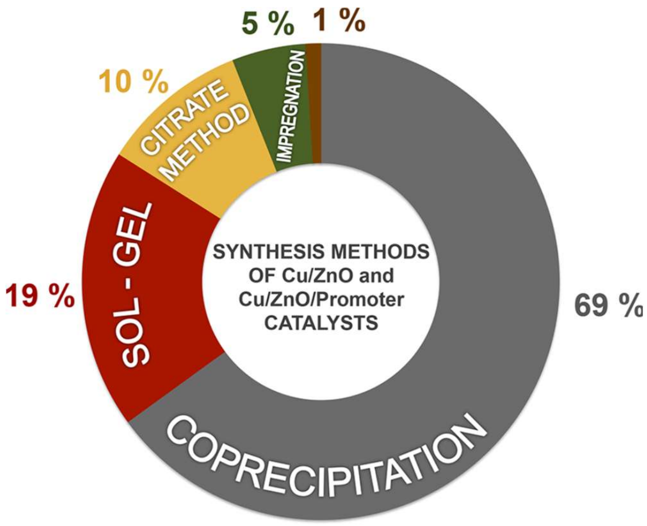

Figure 13 Synthesis processes used to obtain Cu/ZnO-based catalysts. Reprinted from [6] *distributed under the terms and conditions of the Creative Commons Attribution (CC-BY-NC-ND) license Copyright © 2017 American Chemical Society.*

Non-Cu-based catalysts

To overcome the thermodynamic constraints of CO_2 hydrogenation, some researchers have focused on the development of catalysts for methanol synthesis from CO_2 not based on Cu; however, the number of papers about this type of catalysts is really small compared to the literature focused on traditional Cu-based catalysts [66]. The most studied non-Cu-based catalysts are based on noble metals, mainly Pd; particularly, while the use of only Pd nanoparticles promotes the formation of CO through the RWGS reaction, the use of Pd supported on other species, like ZnO, showed high selectivity towards methanol production, due to the formation of the PdZn alloy, acting as active site. Another support that has been studied for Pd-based catalysts is Ga_2O_3; this system does not only form the PdGa alloy, but also the Pd_2Ga intermetallic compound, which shows high activity and methanol selectivity. Pd/In_2O_3 was also studied, showing an improved activity and stability compared to Cu/ZnO-based catalysts [11]. Another noble metal investigated as methanol synthesis catalyst is Au, usually reported in form of nanoparticles supported on a metal oxide; in this context, several metal oxides have been reported as supports, but the most promising ones proved to be ZnO and CeO_2, allowing to obtain highly selective catalysts. Some cases of bimetallic systems, mainly based on Rh and Pt, have also been reported [11]. However, the use of noble metals, despite showing promising performances, have a substantial drawback, consisting in their high cost; for this reason, several researchers have been focusing on catalysts based on non-noble metals. Among these, Co-based catalysts showed high methanol selectivity due to the presence of the CoO phase, which inhibits the RWGS reaction. Ni nanoparticles supported on Ga_2O_3 showed high catalytic activity; the highest values of methanol selectivity were observed for 10.2 nm nanoparticles, due to the improved stabilization and hydrogenation of reaction intermediates, while smaller nanoparticles promoted CO formation [66]. In_2O_3 is another non-Cu catalyst on which the researchers focused on; particularly, it showed an almost complete selectivity to methanol at low values of conversion, inhibiting the RWGS rection, due to the presence of oxygen vacancies, acting as active sites for CO_2 adsorption and for the stabilization of reaction intermediates. The formation of such vacancies was favored by the modification of In_2O_3 with Ga, maximizing methanol yield especially at high temperature (300-400°C). The activity and stability of In_2O_3 were also improved by the addition of ZrO_2 [11], [66].

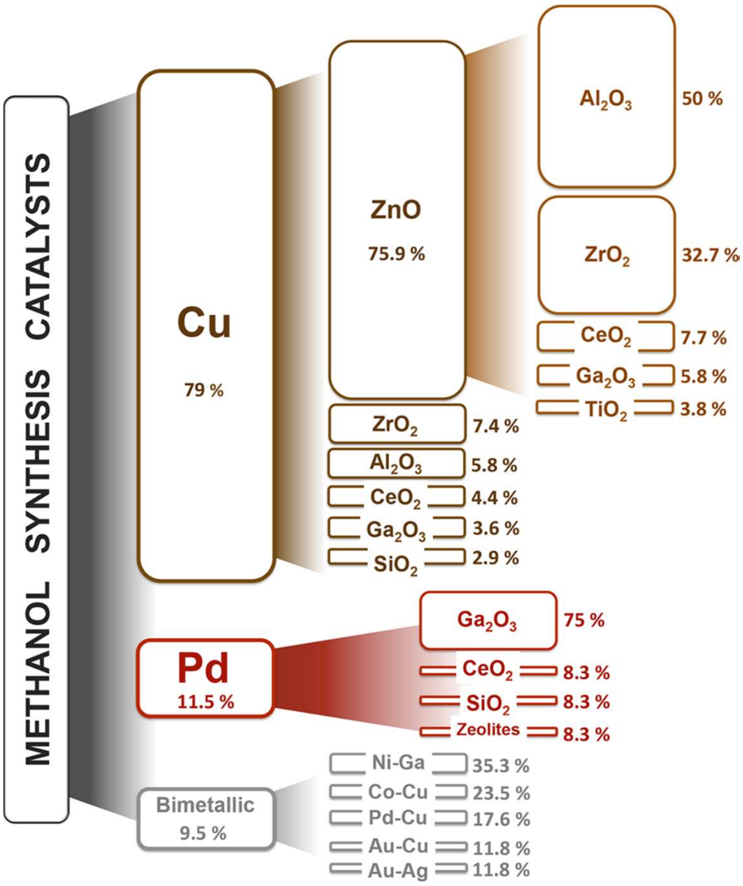

Figure 14 Catalytic systems reported in the literature for the CO2 hydrogenation to methanol. Reprinted from [6] *distributed under the terms and conditions of the Creative Commons Attribution (CC-BY-NC-ND) license Copyright © 2017 American Chemical Society.*

1.4.3 Acidic catalysts for the CO_2-to-DME process

Regarding methanol dehydration to DME, the solid acidic catalysts that have been reported in the literature mainly consist in γ-Al_2O_3 and zeolites, similarly to the catalysts used for the syngas-to-DME process. The advantages of γ-Al_2O_3 mainly consist in its low cost compared to other more active dehydration catalysts, like zeolites, a high surface area, a good thermal stability and the presence of weak and moderate Lewis acid sites on its surface [66][15]. However, as already mentioned for the syngas-to-DME process, γ-Al_2O_3 tends to lose performances over time, due to deactivation of its Lewis acid sites [14], [61]. This downside of γ-Al_2O_3 is particularly problematic for the CO_2-to-DME process due to the formation of water during the hydrogenation of CO_2, for a total of three water molecules for each DME molecule produced. Furthermore, in the CO_2-to-DME process water is also produced by the RWGS reaction; the significant amount of water produced during the process can adsorb on the Lewis acid sites of γ-Al_2O_3, competing with methanol and deactivating the sites. Another disadvantage of γ-Al_2O_3 consists in the fact that, due to its acidic properties, this catalyst needs high reaction temperatures (300-400 °C), incompatible with those required by methanol synthesis (250-300 °C) [15], [66]. In order to overcome the drawback due to deactivation of the acid sites of γ-Al_2O_3, several researchers focused their attention on the modification of its acidic properties by the incorporation of other species, like SiO_2, Cu, Fe_2O_3, Ti, Nb, B and phosphates, mainly in order to decrease the hydrophilicity of the surface of alumina. Despite the promising results obtained, γ-Al_2O_3 is not considered an ideal dehydration catalyst for the CO_2-to-DME process, and the attention of the researchers is currently focused mainly on zeolites [15], [66].

As already mentioned for the syngas-to-DME process, zeolites show a much higher resistance to water adsorption than γ-Al_2O_3, due to both the presence of Brønsted sites and a lower surface hydrophilicity, especially for zeolites with high Si/Al ratios [23], [25]. Zeolites also, compared to γ-Al_2O_3, allow to carry out methanol dehydration at lower temperatures, more compatible with methanol synthesis (250-280 °C) [15]. However, even at relatively low temperatures, the presence of high-strength Brønsted sites, despite showing high activity for methanol dehydration, also give rise to the formation of by-products, as previously explained. Besides the acid strength, the formation of coke and by-products is strongly influenced by the zeolite structural properties, particularly in terms of the size of pore channels and cages. For instance, zeolite beta (BEA) due to the presence of large cages interconnected by a 3D porous network, shows a high activity, but also rapidly deactivates due to coke deposition. On the other hand, ZSM-5 (MFI), featuring a 3D framework but smaller pores, and particularly ferrierite (FER), due to its small 2D pore network, demonstrated to be the best compromise between catalytic activity, selectivity to DME, and resistance to deactivation [66]. It has been observed, indeed, how coke formation, caused by the production of olefins and, particularly, aromatic compounds, is favored not only by strong Brønsted sites but also by the presence of large cages interconnected by relatively small pores organized in a 3D framework. These cavities do not allow the formed by-products to properly exit the pore system, building up and reacting to form carbonaceous deposits, mainly consisting in poly-methylbenzenes [15]. In addition to the Si/Al ratio and the microporous features, crystallite size of zeolites results to be an important factor to obtain good catalytic performances and avoid deactivation; particularly, due to improved mass transfer, zeolites with small crystallites (in the nano-scale) shows improved methanol conversion, DME selectivity and considerably reduced amount of coke deposition, compared with zeolites featured by micro-crystallinity. In both its nano- and micro-crystalline form, ferrierite showed better performances than ZSM-5 [15][61]. Coke deposition is also limited by the presence of mesopores, which facilitates mass transfer avoiding the accumulation of coke precursors; the positive effect of mesoporosity have been observed for zeolites with a hierarchical structure and for a ZSM-5/MCM-41 composite material [15]. Besides the increase in aluminum content, which showed excellent results for FER in terms of activity, the detrimental presence of strong Brønsted acid sites in zeolites can be inhibited by halogenation processes, desilication, impregnation with metals like Na, Mg, Zn, Zr and impregnation with γ-Al_2O_3 [15], [66].

Alongside γ-Al_2O_3 and zeolites, other acidic catalysts like supported heteropolyacids (HPAs), ion exchange resins, silicoaluminophosphates (SAPO) and natural clays have been proposed [15], [66]. Furthermore, some cases of other oxides and mixed oxides such as TiO_2, TiO_2/ZrO_2, ZrO_2 [73][49], sulfated zirconia (SO_4^{2-}/ZrO_2) [74], WO_x/Al_2O_3 [75], WO_x/ZrO_2 [76], WO_x/TiO_2, Nb_2O_5, and Nb-doped TiO_2 [15], [66] have been reported. Due to the peculiar properties of mesoporous and mesostructured materials, like the high surface area and the large pore size, some authors have proposed such systems as methanol dehydration catalysts; some examples include mesoporous/mesostructured γ-Al_2O_3 [77], [78], doped mesoporous/mesostructured silica [79][80], [81] [82] and other oxides and mixed oxides [73]–[76].

1.4.4 Bifunctional/hybrid catalysts for the CO_2-to-DME process

Like in the case of the syngas-to-DME process, when the CO_2-to-DME process is performed through a one-step route it is necessary to include both the redox and the dehydration catalyst into the reactor [15] [14], [66]. In most cases, the two catalysts are simply physically mixed together [83]–[85]. However, the interest of several researchers for bifunctional catalysts, in which the two phases are in an intimate contact, is recently growing and several cases of actual bifunctional catalysts have been reported [86], [87]. Such catalysts, often defined as “hybrid”, are usually obtained through coprecipitation of the redox phase on the acidic catalyst (usually zeolites) used as support; however, other synthesis routes like impregnation and sol-gel approaches have been reported [15]. In this perspective, it is believed that the close proximity of the two type of active sites (redox and acid) would improve the performances of the catalyst, due to a more prompt dehydration of the formed methanol [14], [15]. An important aspect in bifunctional catalysts is the morphology and the homogeneity of the dispersion of the redox phase on the acidic support; namely, Frusteri *et al.* [87] observed how the use of ferrierite as a support allowed to obtain homogeneous dispersion of the redox phase ($Cu/ZnO/ZrO_2$) on its surface due to its lamellar crystals. Other zeolites (ZSM-5 and mordenite) presented less homogeneous dispersion, limiting mass transfer and the acid activity of the support. However, an agreement on the better combination method of the two phases (either physical or chemical mixing) has not been reached so far. Some authors, indeed, observed detrimental effects deriving from the close contact between the two catalytic functions which caused the coverage of the active sites and a decrease in the surface area of the acidic catalyst used to support the methanol synthesis catalyst. Also, bifunctional catalysts often show deactivation phenomena over time, due to sintering of the particles of the redox phase, coke deposition or water adsorption [15][66]. Another detrimental effect observed on bifunctional zeolite-based catalysts can be ascribed to ion-exchange phenomena between the H^+ cations of the zeolite and Cu^{2+} cations from the redox phase, giving rise to deactivation of both catalytic functions [70][65]. Particularly, Bonura *et al.* [65] made a direct comparison of two-function CZZ/H-ZSM-5 catalysts obtained by coprecipitation, dual bed configuration, grinding and physical mixing (Figure 15a).

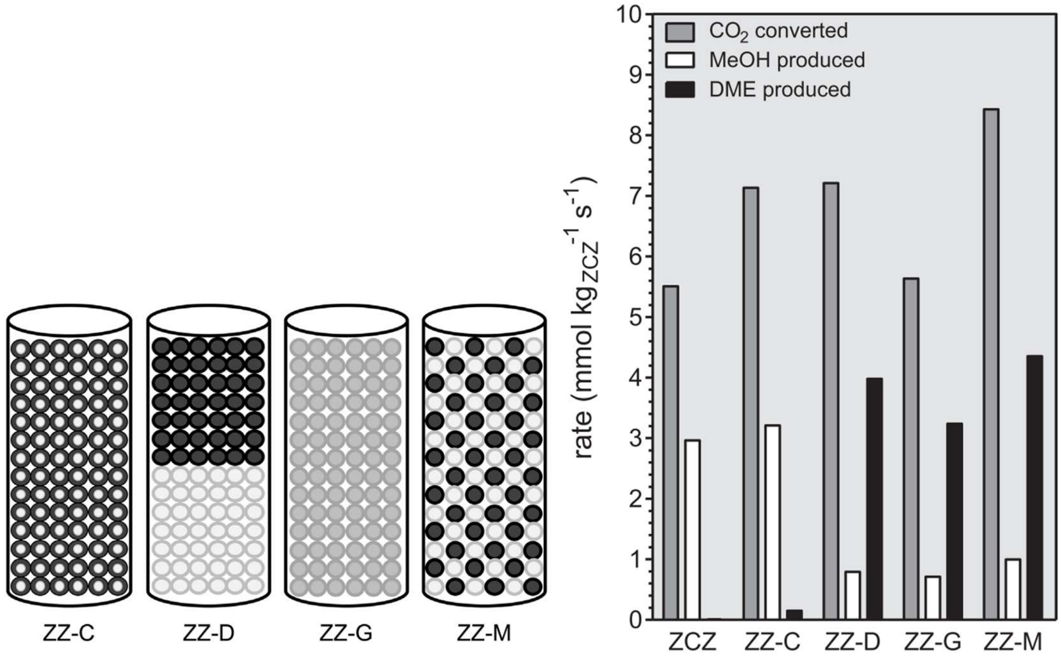

Figure 15 Combination method for redox and acidic catalysts: coprecipitation (ZZ-C), dual-bed (ZZ-D), grinding (ZZ-G), and mixing of pelletized catalysts (ZZ-M) (a). Catalytic results (b). Reprinted with permission from [65] *license number 5470440299719.*

The obtained results (Figure 15b) clearly showed an extremely low amount of DME production rate for the catalyst obtained by coprecipitation, associated with a disappearance of its weak acid sites, caused by the ion-exchange phenomena mentioned above. On the other hand, catalysts obtained without an intimate contact between the redox and the acidic phase did not alter the amount of acid sites of the zeolites and gave rise to the formation of important amounts of DME.

Besides the lack of agreement in the literature about the best combination method for CO_2-to-DME catalysts, the different redox and dehydration catalysts chosen by the authors, the different reaction conditions and the different synthesis methods make a direct comparison of the several types of bifunctional/hybrid catalysts really difficult; most findings, however, seem to suggest that the research on bifunctional catalysts showed promising results, but more studies are required to optimize these systems to avoid deactivation [66][15].

Chapter 2

Siliceous and non-siliceous ordered mesoporous materials: synthesis, features, and possible applications

This chapter is devoted to siliceous and non-siliceous ordered mesoporous (mesostructured) oxides providing a general overview on synthesis methods, their textural properties, and their applications in different fields, as catalysis, sorption, and sensing.

2.1 Porous materials: an overview

According to the International Union of Pure and Applied Chemistry (IUPAC) [88], porous materials are divided in three classes depending on their pore size:

- Microporous (pore size <2 nm)
- Mesoporous (2 nm ≤ pore size ≤ 50 nm)
- Macroporous (pore size > 50 nm)

Although microporous materials show the highest surface area, the small pore size can limit mass transfer when large molecules are involved in the reactions [89]. Zeolites are the most common inorganic members of this class, with a narrow and uniform micropore size distribution, arising from their crystalline structure. Other important members are Metal Organic Frameworks (MOFs), inorganic-organic hybrid materials featuring micropores and ultramicropores and very high surface area, but often suffering of thermal and chemical instabilities at mid- and high temperature.

Mesoporous materials can be considered ideal materials having high surface area but without the intrinsic limits of their microporous counterparts, in terms of diffusion drawbacks or plugging *phenomena*, making them promising candidates for catalysis, adsorption, sensor, lithium-ion batteries, drug delivery, and nanodevices. Among them, ordered mesoporous materials, also known as mesostructured materials, possess an ordered arrangement of the mesoporous channels and extremely high surface area, which allows the maximization of the accessibility and, consequently, the surface reactivity/adsorption ability toward specific species [90]. In addition to these features, the use of these materials as hosting supports for other active phases, by anchoring nanoparticles into the mesopores or by grafting both the inner and external surface with organic molecules, offers the opportunity of developing multifunctional materials that may find applications in a great variety of fields. Silica and aluminosilicates were first developed in form of mesostructured materials [89], due to the geometrical flexibility of the tetrahedral building blocks which provides chemical stability and ease of synthesis. Because of the chemical inertness, silica as pure material finds a limited number of applications, and, therefore, it is mainly used as host material for active species. For these reasons, research is moving toward aluminosilicates and non-siliceous mesostructured materials. The synthetic strategies used for mesoporous silica can be adapted for aluminosilicates while for non-siliceous oxides the development of new approaches is needed. Indeed, non-siliceous precursors are extremely reactive in the hydrolysis processes and can be subjected to side redox reactions, or phase transitions, accompanied by thermal collapse of the mesostructure. For the above reasons, separate paragraphs will be devoted to a description of the synthetic approaches for the synthesis of siliceous and non-siliceous mesostructured oxides.

2.2 Mesoporous siliceous materials

The first synthesis of a mesostructured material was reported in a patent published in 1969, but its importance was not recognized [89], [91], since 1992, when a similar material, Mobil Composition of Matter No. 41 (MCM-41), was obtained in the Mobil Oil Corporation laboratories, making this event as the milestone in the history of mesostructured materials [92]. A highly ordered hexagonal array of the mesochannels with a very narrow pore size distribution, an extremely high surface area and porous volume are its peculiar features. Since then, a large variety of mesostructured materials with different porous structure (two-dimensional (2D) hexagonal, space group *P6mm*, three-dimensional (3D) hexagonal *P63/mmc*, 3D cubic *Pm3m*, *Pm3n*, *Fd3m*, *Fm3m*, *Im3m*, and bicontinuous cubic *Ia3d*) have been developed Figure 16, opening new fields of application.

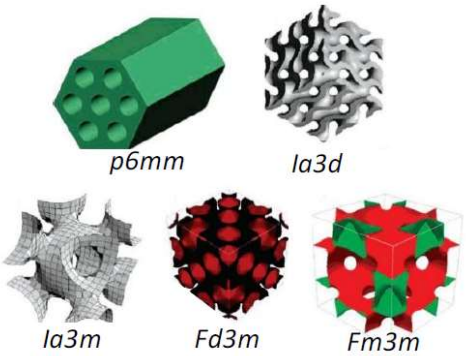

Figure 16 Representation of different mesoporous orders of siliceous materials. Reprinted with permission from [93]*, license number 5483261066899.*

The formation of mesostructured material is based on the assembly between the inorganic species (silica precursor) and the organic templating agents (amphiphilic copolymers, surfactants). The organic-inorganic interactions deriving from weak non-covalent bonds like hydrogen bonds, van der Waals forces, and electro-valent bonds, is the driving force for the assembly. Two main mechanisms, *cooperative self-assembly* and *true liquid-crystal templating processes*, have been hypothesised for the obtainment of mesostructures, as reported in Figure 17. The *cooperative self-assembly* approach involves the interaction between inorganic species and organic molecules before the micelles formation (pathway A), while the *liquid-crystal templating* route is based on the formation of liquids crystals by the assembly of the organic molecules before the interaction with the inorganic species (pathway B) [94]. Then, for both approaches, the condensation of the silica precursor occurs around the organic mesophase. In addition to the inorganic-organic interactions, key factors that make silica particularly suitable for the mesostructure formation are the well-controlled hydrolysis and condensation of the silica precursors (e.g., siliceous alkoxides), and the thermal stability of the silica framework during the removal of the organic molecular templates (calcination).

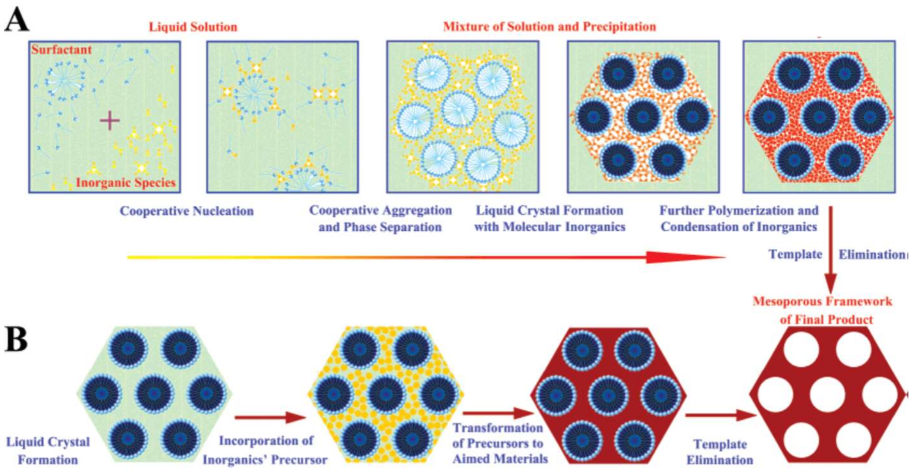

Figure 17 Cooperative self-assembly (A), and true liquid crystal templating process (B) for the synthesis of mesostructured silica-based materials. Reprinted with permission from [95]*. Copyright (2007) American Chemical Society.*

From a thermodynamic point of view, the whole formation of the ordered mesoporous material can be depicted in terms of the free energy [96]:

$$\Delta G = \Delta G_{inter} + \Delta G_{wall} + \Delta G_{intra} + \Delta G_{sol}$$

where ΔG_{inter} is the energy associated with the interaction between the micelles of surfactant and the inorganic walls, ΔG_{wall} is the structural free energy for the inorganic framework, ΔG_{intra} is the van der Waals force and conformational energy of the surfactant, and ΔG_{sol} is the chemical potential associated with the species in solution phase. ΔG_{sol} is usually considered as constant and, therefore, the interaction between the surfactant and inorganic species, such as the matching of the charge density, is the core of the process. The assembly process is favoured by more negative ΔG_{inter}. Detailed investigations on the inorganic-organic interaction were reported in the literature [95]. By changing reaction conditions (pH, chemicals, inorganic precursors, and templating agents), several routes have been developed so far for the syntheses of ordered mesoporous materials Figure 18. The interactions between the charged inorganic phase and the head group of the surfactants in the route (a-d) are mainly of electrostatic nature, while those between neutral inorganic species and non-electrolyte templating molecules are given by hydrogen bonds (e, f) [97], [98].

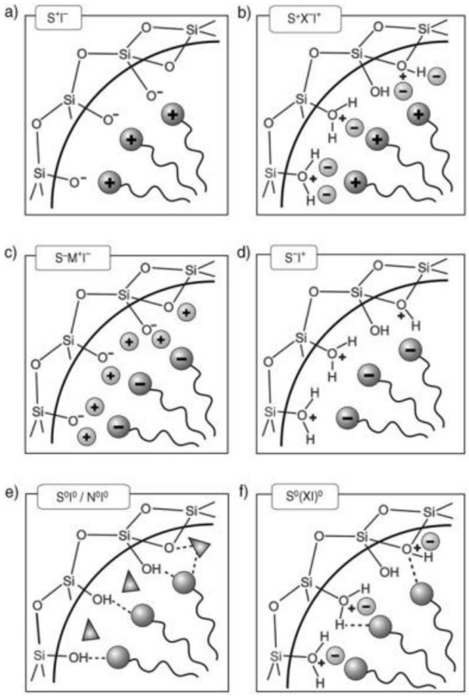

Figure 18 Types of interactions between inorganic species and surfactant head groups in basic (a, c), acidic (b) and neutral (d) media or via hydrogen bonds between uncharged species (e) or ion pairs (f). Reproduced with permission from [99]. *Copyright 2006 WILEY-VCH Verlag GmbH & Co. KGaA, Weinheim, license number 5513611296279.*

The silica is obtained through hydrolysis and condensation reactions as indicated in the following equations.

$$\equiv Si-OR+H_2O \leftrightarrows \equiv Si-OH+ROH \qquad \text{(hydrolysis)}$$

$$\equiv Si-OH+HO-Si\equiv \leftrightarrows \equiv Si-O-Si\equiv +H_2O \qquad \text{(water condensation)}$$

$$\equiv Si-OR+HO-Si\equiv \leftrightarrows \equiv Si-O-Si\equiv +ROH \qquad \text{(alcohol condensation)}$$

2.2.1 Substitution of Si in siliceous mesoporous materials

The same synthetic strategies described for siliceous materials can be used to obtain mesoporous systems in which Si is partially substituted by another species. This approach is of particular interest since it allows an SiO_2-based material, normally chemically inert, to gain peculiar properties. The most common species used to partially substitute Si is Al; in the context of this thesis Al-substituted siliceous materials have a great importance, since the introduction of aluminum in the framework of silica grants acidic properties. Indeed, due to the similar atomic radii of Al^{3+} (0.51 Å) and Si^{4+} (0.42 Å), in aluminosilicates Al replaces Si assuming a tetracoordinated (AlO_4^{5-}) form; consequently, to balance the charge, an -OH group (a Brønsted acid site) is formed [100].

2.3 Mesoporous non-siliceous materials

The success achieved for siliceous mesostructured materials by the soft template approach, have not been similarly obtained for mesoporous non-siliceous oxides. So far, besides the soft template route, additional synthetic pathways have been proposed in the literature for this aim Figure 19:

1. ***Soft template***: based on the adaption of the synthetic method proposed for mesostructured siliceous materials, exploiting the self-assembly phenomena of diverse surfactants or block copolymers as templates or structure-directing agents (SDAs).

2. ***Hard template***: based on the use of preformed scaffold of ordered mesostructured silica or carbon as moulds [101].

3. ***Colloidal crystal template***: based on the formation of a uniform close packing arrangement of organic (polystyrene (PS), poly-(methyl methacrylate) (PMMA)) or inorganic (silica) homogenously-sized spheres and the subsequent filling of the interstitial spaces by inorganic precursors.

4. ***Super lattice***: based on the use of pre-formed capped nanoparticles as building blocks, and the interaction and assembly between the capping agent of the nanoparticles and the surfactant (or block copolymers) used as porogen agent to form the mesoporous structure.

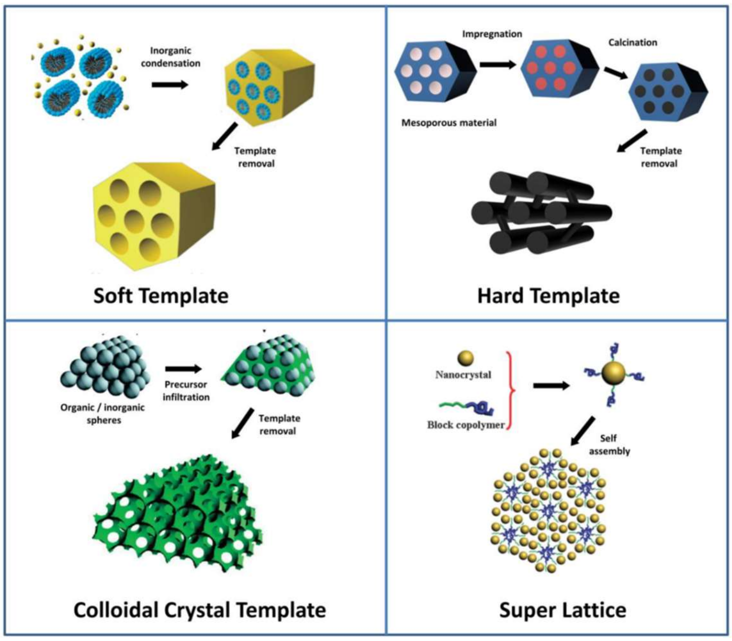

Figure 19 Schematic representation of the four synthetic pathways developed to obtain ordered mesoporous materials. Reprinted from [102]*, Copyright (2017), with permission from Elsevier (Hard template). Adapted with permission from* [103] *copyright (2008) American Chemical Society (Colloidal Crystal Template). Adapted from* [104] *with permission of The Royal Society of Chemistry (Super Lattice).*

The hard template and the colloidal crystal template methods are multistep approaches and their scale-up in industrial processes might be challenging. In the super lattice method, the main limit is related to the selection of proper capping and porogen agents promoting their interaction and the consequent assembly. The soft template methods suffer from the major problem of losing the porous structure after crystallization of the inorganic precursors, but this has been overcome by using amphiphilic block copolymers with higher thermal stability than temperature of crystallization transition, making this method promising in comparison with the others. Therefore, in the following paragraph the attention will be paid on the soft template method.

2.3.1 From soft template methods to evaporation-induced self-assembly (EISA)

As previously mentioned, the application of the soft template method requires the adaptation of the experimental conditions used for the synthesis of mesostructured silicas, due to the faster hydrolysis and condensation reactions of the metal precursors compared to the siliceous counterpart. Indeed, a wormlike porous structure is often obtained without the achievement of the decided mesoporous order. In order to avoid macro-phase separation, the method requires a better control on the hydrolysis-condensation rate, and a strong interaction between the templates and precursor. The first successful synthesis of mesostructured metal oxide other than silica was proposed in 1995 by Antonelli *et al*. [105], leading to the obtainment of amorphous mesostructured TiO_2 but with a poor thermal stability. In 1998, Stucky and co-workers [106], were able to overcome this issue by the use of amphiphilic tri-block copolymers as templates, for the synthesis of both crystalline metal oxides (TiO_2, ZrO_2, Al_2O_3, Nb_2O_5, Ta_2O_5, WO_3, HfO_2, SnO_2) and amorphous mixed oxides ($SiAlO_{3.5}$, $SiTiO_4$, $ZrTiO_4$, Al_2TiO_5 and ZrW_2O_8) (Figure 20). Block copolymers, such as Pluronic-type triblock, are considered to be among the most promising templating agents for the crystal growth of inorganic materials, allowing the obtainment of a robust mesostructure with long-range ordering lengths [94]. Besides the proper selection of the copolymer, a key point is the accurate control of the sol-gel transition through slow evaporation of the solvent. This approach was firstly presented by Bricker's group for mesostructured silica in 1997 [98] and called evaporation-induced self-assembly (EISA) [101]. A focus on this synthetic approach will be given in the next paragraph.

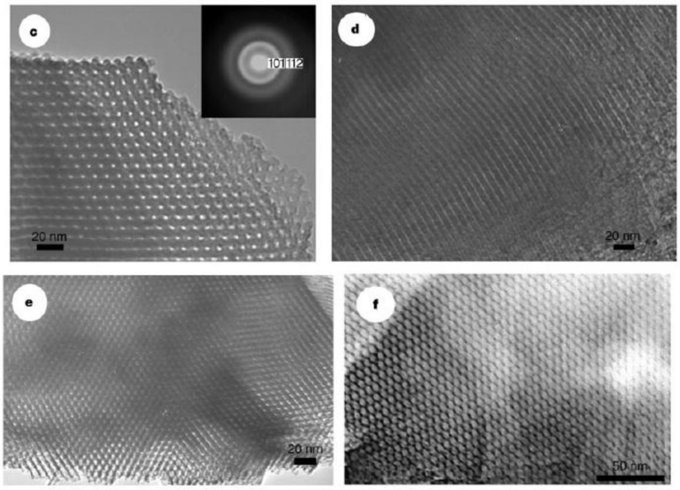

Figure 20 TEM images of ZrO_2 (c, d) and Nb_2O_5 (e, f) mesostructured oxides. Reprinted by permission from Macmillan Publishers Ltd [Nature] [106]*, copyright (1998), license number 5510850181915.*

2.3.2 Evaporation-induced self-assembly (EISA)

After its first use for the synthesis of silica thin films [98], the EISA method was later adapted to prepare mesostructured metal oxides including TiO_2, ZrO_2, Al_2O_3, Nb_2O_5, Ta_2O_5, WO_3, HfO_2, SnO_2, and mixed oxides $SiAlO_{3.5}$, $SiTiO_4$, $ZrTiO_4$, Al_2TiO_5 and ZrW_2O_8 [106]. In this method, a decrease of the hydrolysis and condensation rates of the metal precursors is achieved by using non-aqueous volatile polar solvents (*e.g.*, alcohols or tetrahydrofuran), in which a surfactant and then the inorganic precursors with low polymerization degree are dissolved. At the beginning of the process, the initial concentration of the surfactant in this solution is kept below its critical micelle concentration (CMC). Then, the slow evaporation of the solvent leads to a gradual increase of the surfactant concentration. The surfactant molecules self-assemble and form a liquid-crystal phase, capable to interact with the inorganic species. The cooperative inorganic-organic assembly is generated by a humidity aging process, leading to a robust mesostructure [94]. Post-synthesis treatments, as drying, calcination, pyrolysis, and solvothermal processes, are usually adopted to control the solidification and possible crystallization of the inorganic framework, render the mesostructured more robust, and remove the SDAs (Figure 21).

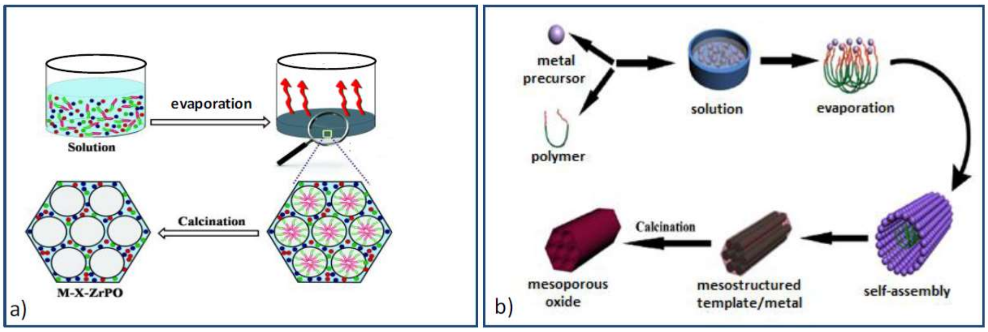

Figure 21 Schematic representation of the EISA synthetic approach. (a) Adapted from [107] *with permission of The Royal Society of Chemistry. (b) Reprinted from* [108] *with permission from Elsevier, license number 5513600777454.*

Sanchez and co-workers [109] by *in situ* small angle X-ray scattering (SAXS) hypothesised a disorder-to-order transition step from an isotropic sol to a worm-like phase, up to an aligned and organized micelle phase, as the mechanism involved in the formation of mesostructured TiO₂. Furthermore, the authors found a second transition induced by the aging, from a cubic to a triclinic porous structure (Figure 22).

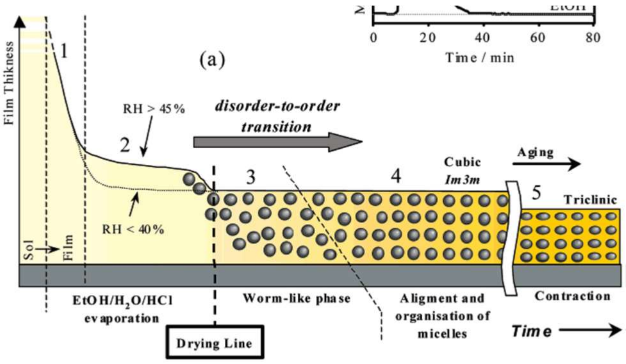

Figure 22 Schematic representation of the stages of mesostructured film formation. Reprinted with permission from [109]. *Copyright (2003) American Chemical Society.*

Since many experimental parameters are involved in the formation and transitions of the mesophase and the inorganic mesostructured, such as reactivity of the metal precursors, humidity, solvents, SDAs, temperature, atmosphere, surface/volume ratio of the sol, a careful control over them is the challenge and the key for the creation of a long-range ordering of the mesoporous structure. Moreover, even if a good control is achieved during the EISA synthesis, post-synthesis treatments, such as the calcination step, might be responsible for retaining or not the porous mesostructure during the amorphous-to-crystalline transition [110]. In order to overcome the mesostructure collapse phenomena during the crystallisation step, a suitable selection of the SDAs was demonstrated to assure the formation of a robust and thermally stable scaffold. Indeed, the SDAs commonly used in the synthesis of mesostructured silica (*e.g.* cetyltrimethylammonium bromide, CTAB) start to decompose at about 200 °C, making them unsuitable for obtainment a stable of non-siliceous mesostructures. Among the different classes of surfactants, block copolymers with excellent self-assembly capacity to construct robust mesostructures (Figure 23a), due to the repellence between the two or more chemically distinct homopolymer subunits (blocks), were selected as ideal candidates [94][111]. Amphiphilic tri-block copolymers, named as Pluronics®, such as poly(ethylene oxide)-poly(propylene oxide)-poly(ethylene oxide) (PEO-PPO-PEO), are the most commonly proposed block copolymers due to their higher thermal stability (from about 300 °C to 400 °C), but still not sufficient for the obtainment of some mesostructured metal oxides [111]. Therefore, two main solutions have been proposed to assure high thermal stability of the scaffold and the preservation of the porous structure: (i) the use of a Pluronic in the presence of sulphuric acid leads to the acid carbonization of the copolymer during the thermal treatment under inert atmosphere, producing a more stable carbon scaffold (Figure 23b) [110]; (ii) the second strategy consists in the *ad hoc* design of block copolymers with improved thermal stability due to the lower oxygen content and higher carbon content (*e.g.* poly(ethylene oxide)-polystyrene (PEO-PS) or poly(ethylene oxide)-polyisoprene (PEO-PI)) (Figure 23c). This latter solution has been referred as Combined Assembly by Soft and Hard (CASH) [112], being a strategy that combines the advantages of soft and hard-templating approaches. The di-block copolymer consists of two units, where one (e.g. PEO) is easily decomposed, whereas the second unit is a more thermally stable (*e.g.* PI) sp^2-carbon-containing hydrophobic block, which can be converted into a more robust amorphous carbon scaffold when thermally treated under an inert atmosphere [112].

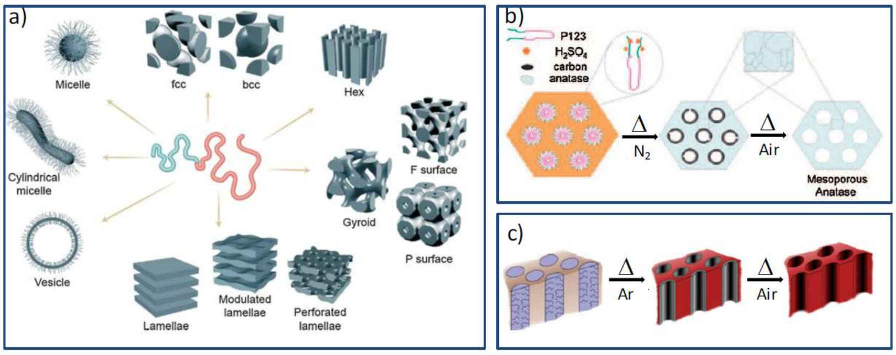

Figure 23 (a) Graphical representation of the various morphologies assumed by block copolymers, including spherical and cylindrical micelles, vesicles, spheres with face-centered cubic (space group: Fm3m) and body-centered cubic (Im3m) packing, hexagonally packed cylinders (p6m), bicontinuous gyroid (Ia3d), F surface (Fd3m), P surfaces (Pm3n, Pn3m, or Pm3m), and lamella. Adapted with permission from ref. [113] *(b) Schematic illustration of the acid carbonization method. Reproduced with permission from* [114]*. Copyright 2010 WILEY-VCH. (c) Schematic representation of CASH method. Reprinted by permission from Macmillan Publishers Ltd: [Nature]* [112]*, copyright (2010).*

2.4 Applications

Mesostructured materials characterized by large specific surfaces and easy pore accessibility find various applications in heterogeneous catalysis, sorption, separation, gas sensing, optoelectronics, host-guest chemistry, molecular electronic devices and medicine [115]. So far, due to the in-depth knowledge about the sol-gel chemistry of siliceous materials and surfactant self-assembly, rational design of ordered mesoporous SiO_2-based materials have been successfully realized [95], and therefore their applications result to be more widespread than those of mesostructured metal oxides. In the following paragraphs, various potential applications of siliceous and non-siliceous metal oxide materials will be described.

2.4.1 Functionalization of the mesostructures by organic and inorganic active phases

Functionalisation of silica with organic active phases

Although SiO_2 is an inert material and is not often used alone, its surface is easily activated by the incorporation of active sites or by deposition of active species. The advantage of using mesostructured silica consists in the presence of relatively large pores, which facilitate mass transfer, together with the very high surface area which allows a high concentration of active sites as a function of the mass of the material [89]. In the literature, many possible pathways have been proposed to modify mesoporous surface with organic molecules or inorganic active phase, both during the synthesis or post-synthesis.

The functionalisation of mesostructured silica with organic molecules follows three main pathways (Figure 24):

- **Grafting**: hybrid organic-inorganic materials are synthesized through a two-steps procedure consisting in the synthesis of the mesostructured material and in the subsequent post-synthesis condensation reaction between Si-OH groups located onto the pore walls and suitable reagents such as chlorosilanes (*e.g.* $ClSiR_3$), alkoxyorganosilanes (*e.g.* $RSi(OR)_3$), aminorganosilanes ($NH_2RSi(OR)_3$ or silane terminated polymers (polymer-$Si(OR)_3$)

- **Co-condensation**: hybrid organic-inorganic materials are synthesized through a one-pot synthesis using the silicon alkoxide together with a trialkoxyorganosilane ($R'Si(OR)_3$) with R' being an active organic functions.

- **Periodic mesoporous organosilicas**: hybrid organic-inorganic materials are synthesized through the use of bridged organosilica precursor of the type $(R'O)_3Si\text{-}R\text{-}Si(OR')_3$.

The approaches here described and widely diffused for silica, can be properly adapted for the non-siliceous materials.

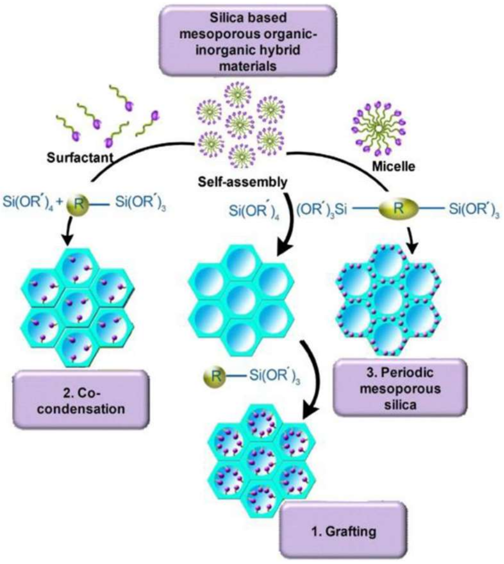

Figure 24 Strategies aimed to obtain organic-inorganic hybrid mesoporous silica: 1. Grafting, 2. Co-condensation or in situ grafting and 3. Periodic mesoporous silica. Reproduced with permission from [99]. *Copyright 2006 WILEY-VCH Verlag GmbH & Co. KGaA, Weinheim, license number 5513611046286.*

These materials can be applied in many fields as pollutant sorbents [116], [117], catalysts at low temperatures [118], and sensors [119], [120].

Functionalization with inorganic active phases

Concerning the functionalisation with inorganic active phases, also in this case one or two steps synthesis routes are possible. In the first case, the metal oxide precursor is directly added during the synthesis of the mesostructured silica while, in the second case, a further step of impregnation with a suitable solution of the metal precursor, has to be performed. However, the integration of a metal oxide precursor during the silica synthesis could cause a loss of order in the porous structure. Hence, the two-step method is preferred.

Impregnation is the most frequently used preparation route. The main advantage of this approach is its simplicity and the production of limited amounts of waste; it consists in putting into contact a solid with a liquid (usually a solution) containing the precursors of the species to be deposited into/over the support. During impregnation several different processes take place at different rates [121]:

- selective adsorption of species (charged or not) by coulomb force, van der Waals forces or H-bonds;
- ion exchange phenomena between the charged surface and the electrolyte;
- polymerization/depolymerization of the species (molecules, ions) bonded to the surface;
- partial dissolution of the surface of the solid.

Usually, during impregnation a suitable support material is put into contact with a solution of the precursor of the active phase. The evaporation of the impregnation solvent (usually water) induced by drying leads the active phase precursor to adhere to the external surface, or to diffuse into the channels of the porous support. Two different impregnation methods are most commonly adopted: the “wet impregnation” and the “incipient wetness impregnation”.

In the wet impregnation approach the amount of precursor solution added to the porous support exceeds its pore volume, determined by N_2 physisorption. Although this is the easiest impregnation method, large fraction of the precursor tends to adhere mainly on the external surface resulting in a heterogeneous or an egg-shell distribution of the guest phase. Such distributions can, on the one hand, favour the accessibility to gaseous or liquid species, since reactant penetration deep inside the catalyst bodies is unnecessary, but, on the other hand, do not hamper sintering phenomena during the further thermal treatments or the use of these materials at mid or high temperature. The irreversibility of the sintering phenomena renders this material not regenerable. For this reason, other impregnation strategy is usually required, such as the incipient wetness impregnation, also known as dry impregnation. In this process the volume of the precursor solution exactly corresponds to the pore volume. However, according to IUPAC definition [121], the volume of the solution can be empirically determined as the value beyond which the catalyst begins to look wet. The use of an amount equal to the pore volume allows to avoid the deposition of metal precursor outside the pores, and the consequent formation of microcrystals after the thermal treatment.

Indeed, after the impregnation process, regardless to the specific adopted method, the impregnated support needs to be thermally treated to allow the precursor to be converted into the final chemical phase. It should be noted that the experimental conditions during drying or calcination can affect the solvent diffusion inside the pores and, consequently, the extent of the homogeneity of the guest phase distribution into/onto the support. Since mesostructured materials with pore sizes below 10 nm offers a relatively large pore volume, impregnation appears to be a suitable method for the incorporation of active phase(s) inside the mesopores. In particular, incipient wetness impregnation is the most appropriate strategy, since it should offer the advantage, at least in principle, to let the guest phase deposit completely inside the pores of the support material.

In the framework of incipient wetness impregnation strategy, the so-called “two-solvent” or “double-solvent” strategy, has attracted a considerable interest [122], [123], [124] since the loading of the pores with a metal precursor solution is facilitated by the use of an apolar solvent (alkane) [125] (Figure 25). It is based on the dispersion of the dried hydrophilic porous support in a first hydrophobic solvent (n-pentane, n-hexane or cyclohexane) followed by the addition of a proper volume of the metal precursor aqueous solution, evaluated on the basis of the porous volume of the support by nitrogen physisorption measurements. The mixture is submitted to a mild temperature (40 °C – 80 °C) treatment up to the complete evaporation of the hydrophobic solvent. An exhaustive study was carried out on the mesoporous silica/hydrophobic solvent/aqueous solution system to understand the processes involved in the double solvent technique [125]. It was proposed that in the presence of a hydrophobic solvent, the water traces are pushed against the hydrophilic silica walls favouring the rehydroxylation of the surface, that then interact with the aqueous solution introduced afterward. Most of the surface groups of dry SBA-15 consist of isolated silanols, accompanied with a smaller contribution of geminal and hydrogen-bonded silanols. The addition of the hydrophobic solvent seems to modify the surface by increasing the amount of geminal and hydrogen-bonded silanol groups, consequently rendering silica more hydrophilic. This should result in an improved dispersion of the metal oxide nanoparticles, obtained after drying and calcination. Concerning these latter steps, it has been also pointed out the crucial importance of the drying step in removing all traces of residual solvent that if present might limit the efficacy of the calcination process. Another study was instead devoted to the effect of the use of different alkane solvents on the incorporation and the dispersion of the particles [125].

The two-solvent incipient impregnation approach was proposed for the effective and homogenous dispersion of ZnO and Fe_2O_3 inside the silica mesochannels in SBA-15 and M41S (MCM-41, MCM-48) to build up sorbents for different environmental applications as the removal of toxic gaseous species from gas mixture and the removal of pollutants from liquid media [126]–[133]. In the case of Fe_2O_3-based systems, the combined use of STEM-EDX chemical mapping, DC magnetometry, and ^{57}Fe Mössbauer spectroscopy allowed to evidence the high homogeneity in both the particle size and the dispersion into the silica mesostructure, together with the presence of very tiny particles (2-5 nm. This confirmed the efficacy of the two-solvent strategy and the action of the silica mesochannels in limiting and controlling the growth of the guest phase.

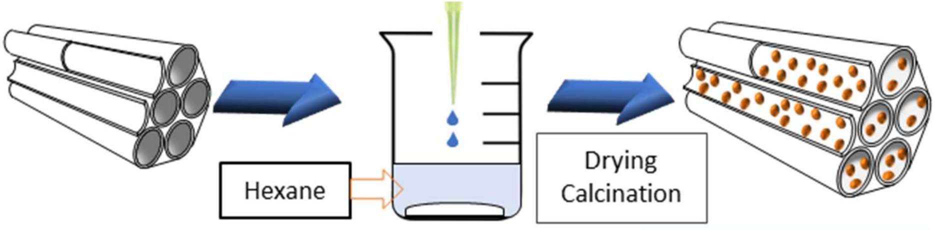

Figure 25 Schematic representation of the two-solvent impregnation strategy on mesostructured materials. Adapted with permission from [134].

Another possible alternative to the two-solvent method is represented by a combination of impregnation with a sol-gel or solution self-combustion process, set up by the Solid State Chemistry and Nanomaterials group of the University of Cagliari. Sol-gel/solution combustion synthesis was first proposed in the mid-1980s and can be described as a complex self-sustained chemical process, occurring in a homogeneous solution of precursors Figure 26.

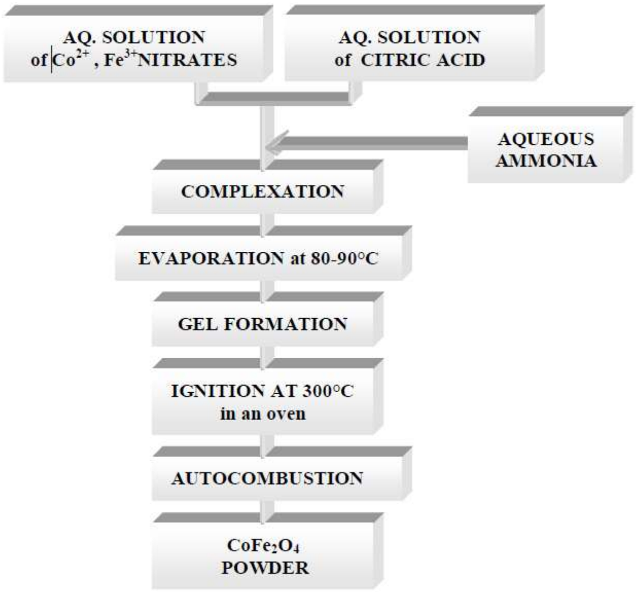

Figure 26 Schematic representation of the sol-gel nitrate/citrate-based self-combustion for the obtainment of $CoFe_2O_4$ nanoparticles; reprinted with permission from [135].

It involves self-propagating exothermic redox reactions deriving by the use of suitable oxidizer and reductant species. Here, we report the most common oxidizers and reductants (fuels) proposed in the literature Table 2.

Table 2 Most commonly used oxidizers and reductants (fuels) for the sol-gel/solution self-combustion process. Reprinted with permission from [136]*, Copyright © 2016 American Chemical Society.*

oxidizer	fuel	solvent
metal nitrates or	urea (CH_4N_2O)	water (H_2O)
nitrate hydrates:	glycine ($C_2H_5NO_2$)	hydrocarbons:
$Me^{\nu}(NO_3)_{\nu}\cdot nH_2O$	sucrose ($C_{12}H_{22}O_{11}$)	kerosene
ν - metal valence	glucose ($C_6H_{12}O_6$)	benzene (C_6H_6)
	citric acid ($C_6H_8O_7$)	alcohols:
ammonium nitrate (NH_4NO_3)	hydrazine-based fuels:	ethanol (C_2H_6O)
	carbohydrazide (CH_6N_4O)	methanol (CH_4O)
	oxalyldihydrazide ($C_2H_6N_4O_2$)	furfuryl alcohol ($C_5H_6O_2$)
nitric acid (HNO_3)	hexamethylenetetramine ($C_6H_{12}N_4$)	2-methoxyethanol ($C_3H_8O_2$)
	acetylacetone ($C_5H_8O_2$)	formaldehyde (CH_2O)

The obtained products are in form of a voluminous powder (Figure 27) and a large amount of non-toxic gas are released. Noteworthy, this approach allows to synthesize a variety of nanoscale materials, such as oxides, metals, alloys, and sulfides, which find important application in several fields [136].

The self-combustion-impregnation strategy involves a first step of impregnation of the metal nitrate (precursor of the desired guest phase) aqueous solution containing the reductant agent on the porous support, followed by a combustion step induced by a sudden ignition. The solution/gel burn in a self-propagating process, quickly converting the precursor mixtures into the voluminous powder product. Citric acid and glycine are most frequently used reductant due to their low temperature decomposition and the good capability to chelate metal cations [137]–[140]. Therefore, some reductants play two important roles: they are at the same time fuels and chelating agent able to prevent the precipitation of hydroxylated compounds. This strategy has been successfully applied for the development of $ZnFe_2O_4$@SBA15 sorbents for removal of H_2S from syngas [126], [127] and $CuO/ZnO/ZrO_2$@SBA15 [72] catalysts for methanol production from CO_2 hydrogenation.

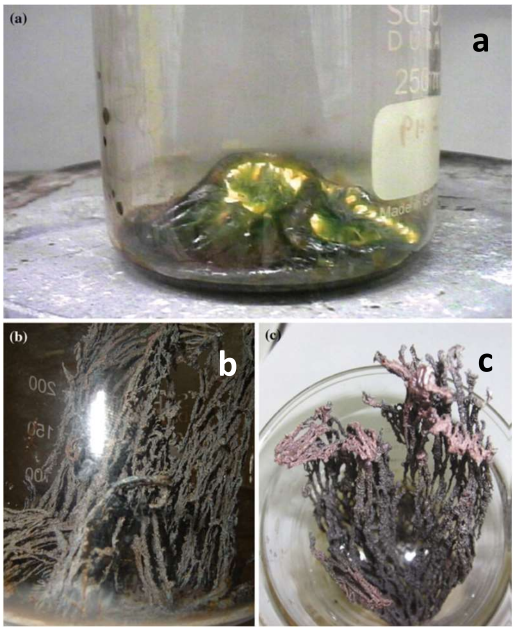

Figure 27 Flameless self-combustion process (volcano) (a) and tree-like structure of the obtained powder (b-c). Reprinted with permission from [141] *license number 5513660814399.*

2.4.2 Application of siliceous and non-siliceous materials

SiO_2-Me_xO_y composites (where Me is a metal) obtained by impregnation strategies are largely used in different fields as catalysts [89], sorbents [128][127][126], and sensors. In the last few years, the design of nano-sized silica particles, showing dimension lower than 100 nm, has opened the way for further applications in biomedical field, especially as drug delivery systems [142]. Up to now, some examples in which SiO_2-based systems have been employed in the industrial field are already present. For instance, in the Catalin Inc. (Albermarle Catilin) a pilot plant has been developed in which mesostructured silica nanoparticles-based catalysts are employed in an environmentally-friendly process for biodiesel production [142]. Regarding Al-substituted mesostructured silica, due to its acidic properties mainly finds application in catalysis for acid-catalyzed reactions like methanol dehydration [79][143], transesterification [144], alkylation, isomerization [145] and cracking [146].

Non-siliceous mesostructured metal oxides have attracted considerable attention due to their diverse, and often unique properties, functionalities, and potential applications, in comparison with their siliceous counterparts. Even though in the last ten years substantial achievements have been made concerning their synthesis and structural characterization [104], just in some cases, the application of the mesostructured metal oxides is presented, due to the fact that the main aim in most of the cases is the presentation of the synthetic pathway able to generate the mesostructure. Moreover, in many types of applications, the mesostructure is often lost during the repeated cycles causing a remarkable drop in the initial performances. However, some examples can be reported. Mesostructured SnO_2 materials have been prepared by using both surfactant [147]–[149] and mesoporous silica [150] as template, and the potential applications as H_2, H_2 and NO_x, CO sensors [147]–[149] and batteries [150] have also been showed. Nanocasted mesoporous cobalt oxide materials showing high surface areas up to 300 m^2g^{-1} have been used as catalysts [151], (50 % of their activity was lost after 4 hours use due to the loss of the surface area) and as negative electrodes in rechargeable lithium-ion batteries [152]. Mesoporous ZnO with a wurtzite-like nanocrystalline framework has been synthesized by using Schiff-base amine as templating agents [153]. The obtained material showed photoconductivity and photoluminescence at room temperature under irradiation with visible light [153]. Nevertheless, due to its unique photocatalytic properties, the availability of its appropriate commercial precursors to generate the mesostructure, as well as its easier handling compared to other metals precursors, mesostructured titanium oxide is the most studied and employed metal oxide. Its applications include photocatalysis, dye-sensitized solar cell, electrochromic and photoelectrochromic devices, chemical energy storage (*e.g.* Li ion batteries [154], [155] and supercapacitor [156]), luminescent devices [156][157], and drug delivery [158]. Another non-siliceous ordered mesoporous oxide that has attracted a considerable interest is Al_2O_3. This system mainly finds application as a catalyst; furthermore, due to its high hydrolytic stability, it is often used as a support to host other phases with various applications in catalysis and adsorption [104][159]. Yuan et al. reported the synthesis of different ordered mesoporous Al_2O_3 samples, obtained with an EISA approach using different non-ionic block copolymers as templating agents, different aluminum precursors and different acidic species as catalysts for the EISA process. The synthesized systems showed high thermal stability up to 1000 °C and were used as supports to host a Ru-based catalyst for various hydrogenation reactions [160]. As reported in Chapter 1, in the context of this thesis, γ-Al_2O_3 finds application not only as an acidic catalyst for methanol dehydration, but also, when obtained in a mesostructured form, as a support to host the redox phase inside its pores [45][46][47].

Chapter 3

Development of TiO_2- $Zr_xTi_{1-x}O_2$- and Al-SiO_2-based mesostructured acidic dehydration catalysts

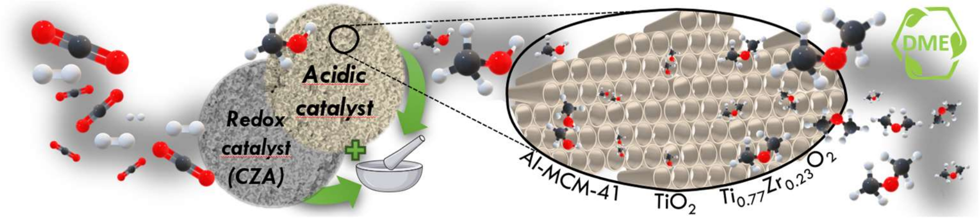

3.1 Introduction

This chapter is focused on the development of mesostructured acidic metal oxides as catalysts for the methanol dehydration physically mixed with a commercial Cu-based redox catalyst (CZA) and tested for the CO_2-to-dimethyl ether (DME) one-pot production. The regular porous structure of mesostructured catalysts, their ideal pore size, and high surface area should in principle render the active sites easily accessible for methanol dehydration. Furthermore, the mesostructured acidic supports should be ideal in terms of pore size to disperse a redox phase inside the mesopores for the development of bifunctional nanocomposite catalysts. Sintering phenomena of the redox phase, due to its incorporation in the mesochannels should thus be prevented and the material made stable and regenerable.

Al-MCM-41, TiO_2 and TiO_2-ZrO_2 with different Ti:Zr molar ratio have been obtained through the sol-gel method in its conventional or EISA (Evaporation-Induced Self-Assembly) approach. Few cases of TiO_2, ZrO_2 and Zr-TiO_2 [49][161] have been reported in the literature, together with some studies on mesostructured aluminosilicates [81][162][79][80][143]. TiO_2, ZrO_2, and Ti-Zr mixed oxides feature only Lewis acidic sites, weaker than those of γ-Al_2O_3 [161], and thus less prone to be deactivated due to water adsorption. Therefore, they are responsible for higher amounts of DME produced, whereas the mesostructured aluminosilicates have shown both Lewis and Brønsted acidity [163][164][165][166]. With the aim of understanding how the different textural and acidic properties of these systems can be correlated with the performances and eventually design efficient dehydration catalysts, a careful study on the acidic sites has been performed by both adsorption microcalorimetry with ammonia and FTIR-monitored adsorption of pyridine. The results of this chapter have been published in [73].

3.2 Synthesis methods

Synthesis of Al-MCM-41

The mesostructured aluminosilicate Al-MCM-41 was synthesized by properly changing the sol-gel strategy reported by Cara *et al.* for the synthesis of MCM-41 [128]. Typically, 0.2314 g of aluminum isopropoxide were dissolved in 3.79 mL of TEOS, while 1 g of the templating agent CTAB was solubilized in 200 g of bi-distilled H_2O into a separate flask by stirring at 300 RPM for 3.5 h at 30 °C. After the addition of 69.1 g of absolute ethanol (EtOH abs), the solution was stirred for other 20 minutes, and then, 21 mL of NH_3 were added. The precursors' solution, previously prepared, was immediately poured into the flask hosting the CTAB solution, and the stirring increased up to 600 RPM and kept for additional 5 minutes, until a milky white mixture was produced. The magnetic stirring was then set back to 300 RPM and the reaction let to continue for 19 h at 30 °C. The obtained material was washed with a 1/1 water/ethanol solution and separated by centrifugation at 4500 RPM for 3 times. Eventually, the solid was dried and calcined at 550 °C to induce the decomposition of CTAB.

Synthesis of mesostructured TiO_2- and $Zr_xTi_{1-x}O_2$-based catalysts

Inspired by the sulfuric acid carbonization approach proposed by Zhao *et al.* for TiO_2 [110], the synthetic process was modified to obtain mixed titania-zirconia oxides having a Ti:Zr molar ratio of 77:23 ($Ti_{0.77}Zr_{0.23}O_2$), 23:77 ($Ti_{0.23}Zr_{0.77}O_2$), and 50:50 ($Ti_{0.50}Zr_{0.50}O_2$). In a typical synthesis, 1 g of Pluronic® P123 was dissolved in 30 g of EtOH abs, 1.4 g of HCl 37 wt% and 0.46 g of H_2SO_4 44 wt% were added under vigorous magnetic stirring (400 RPM) and the mixture heated at 40 °C for 3 h under a N_2. Then, $Ti(OPr)_4$ and $Zr(OBr_4)$ (for the amounts see Table 3) were added dropwise and left for further 20 h at the same temperature. The corresponding sol was poured into a Petri dish and evaporated for two days at 40 °C in air under 50-60% of relative humidity (RH). The resultant film was aged at 100 °C for 2 days. The obtained product was treated at 450 °C (heating rate 1°C min^{-1}) under N_2 for 2 h, and then calcined at 380 °C (2 °C min^{-1}) under air for 2 h. After the N_2 treatment the samples showed a black shining color, suggesting the formation of an amorphous carbon scaffold. Conversely, they appeared light-yellow after calcination.

Table 3 Synthetic details of the sol preparation for mesostructured TiO_2 and mixed oxide $Ti_{0.77}Zr_{0.23}O_2$ $Ti_{0.50}Zr_{0.50}O_2$ and $Ti_{0.23}Zr_{0.77}O_2$ by EISA approach [73].

Sample	Pluronic P 123 (g)	Ethanol (g)	HCl (g)	H_2SO_4 (g)	$Ti(OPr)_4$ (g)	$Zr(OBu)_4$ (g)
TiO_2	1	30	1.4	0.46	3	-
$Ti_{0.77}Zr_{0.23}O_2$	1	30	1.4	0.46	2.180	1.126
$Ti_{0.50}Zr_{0.50}O_2$	1	30	1.4	0.46	1.500	2.455
$Ti_{0.23}Zr_{0.77}O_2$	1	30	1.4	0.46	0.706	3.800

3.3 Structural, textural and morphological characterization

Wide-angle X-ray diffraction (WA-XRD) patterns (Figure 28a, Figure 29a) of the samples Al-MCM-41, TiO_2, and $Ti_{0.77}Zr_{0.23}O_2$, the most promising binary Ti-Zr oxide in terms of degree of mesoporous order (see Figure 29g, Figure 29h, Figure 30e-h) and ferrierite, shown for comparison, are reported in Figure 28a and Figure 29a. Concerning the binary oxides, TEM images (Figure 30) showed a lower degree of mesoporous order for the samples $Ti_{0.23}Zr_{0.77}O_2$ and $Ti_{0.50}Zr_{0.50}O_2$, and, therefore, the attention was focused only on $Ti_{0.77}Zr_{0.23}O_2$. The WA-XRD pattern of the ferrierite sample (PDF card N. 00-039-1382) shows sharp diffraction peaks (Figure 28a), confirming its microcrystalline nature. On the contrary, the sample Al-MCM-41 is amorphous and features a broad band centered at about 23° (2θ). TiO_2 sample is nanocrystalline and, specifically, formed by 4 nm anatase nanocrystals (PDF card N. 00-021-1272). The mean crystallite size was obtained by Scherrer equation, assuming K equal to 0.9, and by fitting the most intense peaks by PseudoVoigt function, through a 1:1 Gaussian: Lorentzian ratio (mu = 0.5). $Ti_{0.77}Zr_{0.23}O_2$ is again amorphous, as confirmed by the two broad bands at about 30° and 55° (Figure 29a). Small angle XRD (SA-XRD, Figure 28b and Figure 29b) showed the presence of a well-defined mesoporous order, for all samples but ferrierite. Nitrogen physisorption analysis further confirmed the mesoporous nature of the three samples, and the microporosity of ferrierite (Figure 28c-d and Figure 29c-d). Table 4 reports the textural properties of the samples: the highest surface area (1246 m^2g^{-1}) was found for the Al-MCM-41, three times higher than that of ferrierite (415 m^2g^{-1}). TiO_2 and $Ti_{0.77}Zr_{0.23}O_2$ show surface areas of 273 and 183 m^2g^{-1}, respectively. The substitution of Ti by Zr caused a decrease in the lattice spacing (d_{100}) and lattice parameter (a_0) of the mesostructure, with a remarkable decrease in the wall thickness (T_w) values, whereas the pore sizes are close (Table 4). Figure 28e-h report representative TEM micrographs of the aluminosilicate samples (ferrierite, Al-MCM-41), with the ferrierite particles showing an elongated morphology, whereas for the Al-MCM-41 spherical particles with a well-defined mesostructure are visible. TEM analyses on the TiO_2 and $Ti_{0.77}Zr_{0.23}O_2$ samples revealed a well-defined honeycomb structure with 4 nm-sized pore (Figure 29e-h).

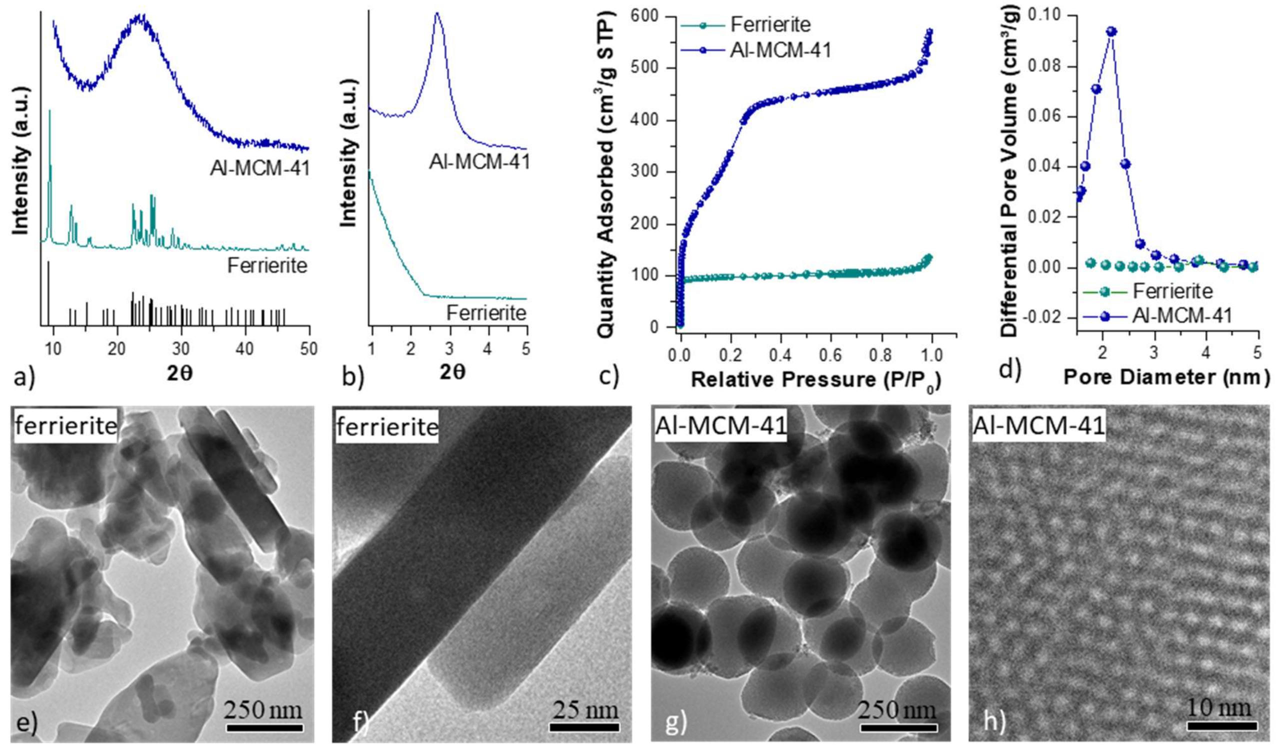

Figure 28. WA-XRD (a) and SA-XRD (b) patterns, nitrogen-physisorption isotherms (c), BJH pore size distributions (d), TEM images of the aluminosilicate samples ferrierite (e,f) and Al-MCM-41 (g,h) [73].

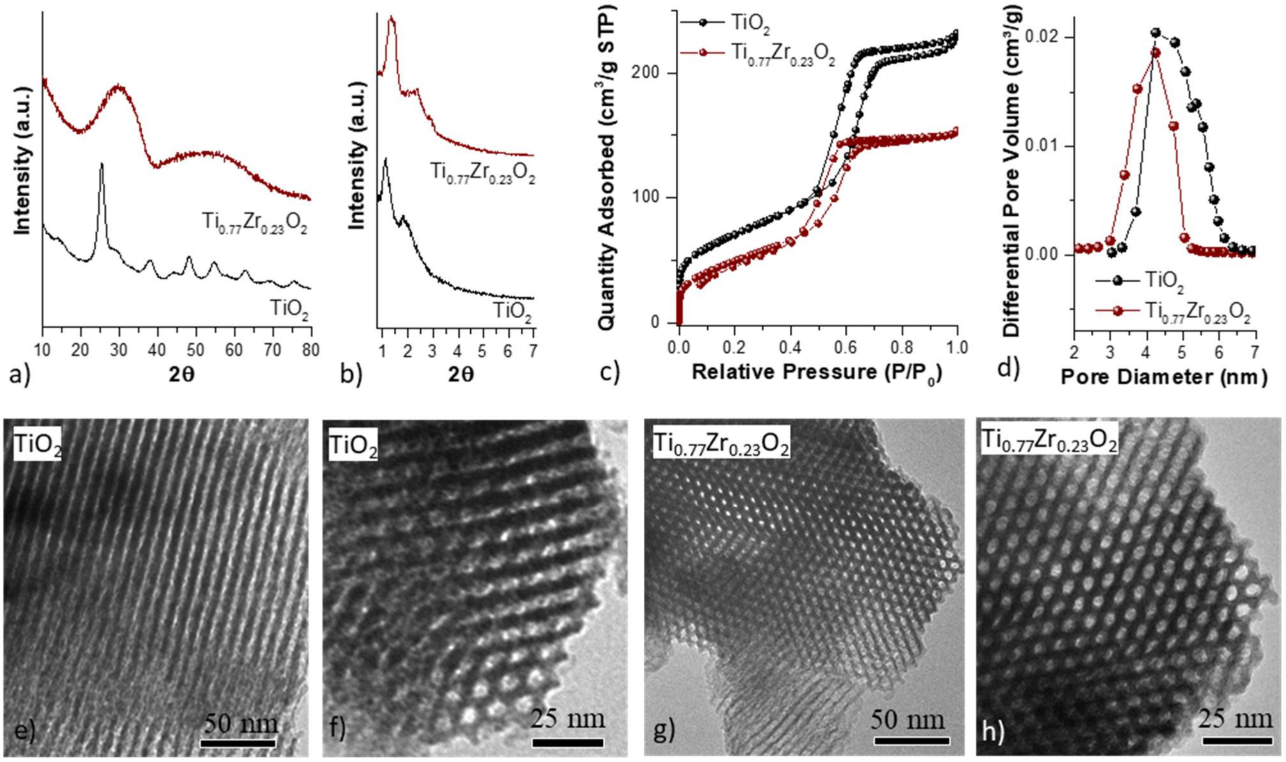

Figure 29. WA-XRD (a) and SA-XRD (b) patterns, nitrogen-physisorption isotherms (c), BJH pore size distributions (d), TEM images of the mesostructured titanium oxide-based samples TiO_2 (e,f) and $Ti_{0.77}Zr_{0.23}O_2$ (g,h) [73].

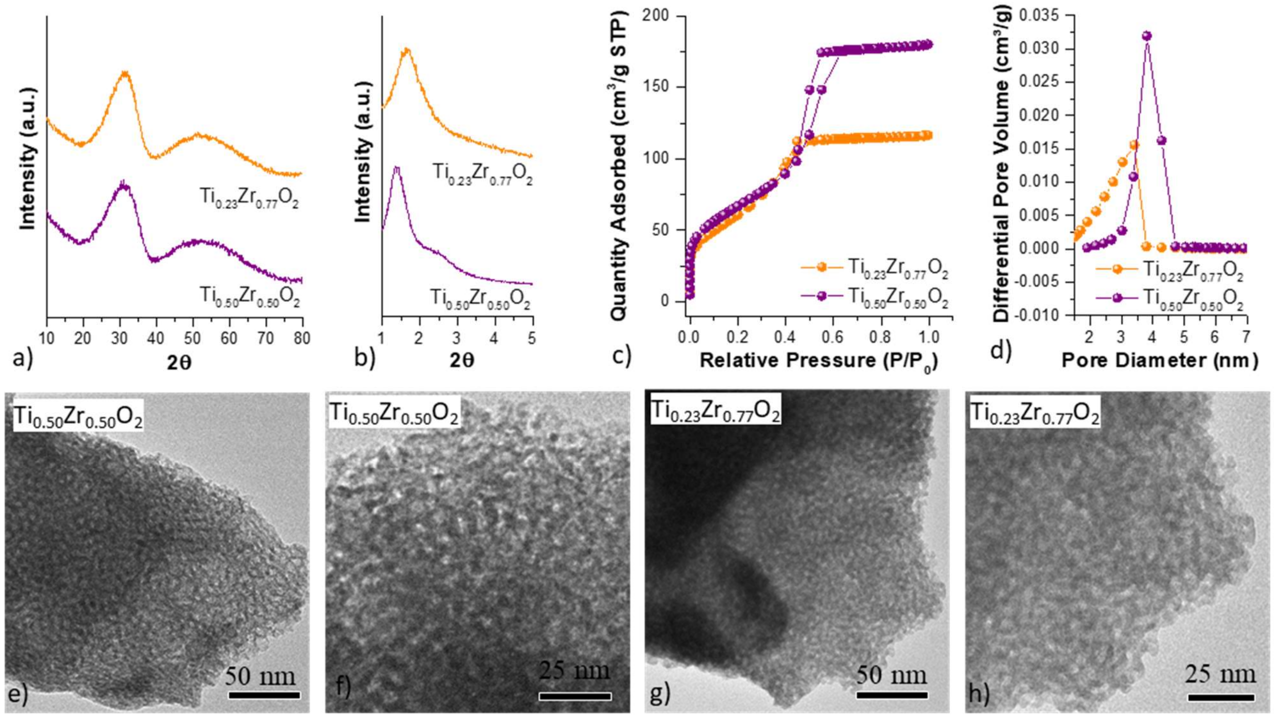

Figure 30 WA-XRD (a) and SA-XRD (b) patterns, nitrogen-physisorption isotherms (c), BJH pore size distributions (d), TEM images of the mesostructured mixed oxides $Ti_{0.23}Zr_{0.77}O_2$ and $Ti_{0.50}Zr_{0.50}O_2$ (e-h) [73].

Table 4. Surface area (SA), pore volume (V_P), pore diameter (D_p), wall thickness (T_w), lattice spacing (d_{100}), and hexagonal unit cell parameter (a_0) for all the samples [73].

Sample	**Typology of isotherm**	**SA ($m^2 g^{-1}$)**	**V_p ($cm^3 g^{-1}$)**	**D_p (nm)**	**T_w (nm)**	**d_{100} (nm)**	**a_0 (nm)**
Ferrierite	I	415	0.1	0.4	-	-	-
Al-MCM-41	IVB	1246	0.7	2.2	1.6	3.3	3.8
TiO_2	IVA	273	0.3	3.9	4.8	7.5	8.7
$Ti_{0.77}Zr_{0.23}O_2$	IVA	183	0.2	4.2	3.6	6.8	7.8
$Ti_{0.23}Zr_{0.77}O_2$	IVA	234	0.2	3.4	2.0	5.4	6.2
$Ti_{0.50}Zr_{0.50}O_2$	IVA	242	0.28	3.8	2.5	6.3	7.3

Relative standard deviation: %RSD(SA)=2.1%; %RSD (V_p)=1.1%; %RSD (D_p)=1.8%. d_{100} and a_0 were obtained from X-ray diffraction data.

Experimental details on the nitrogen physisorption measurements and SA-XRD

The lattice parameter of the mesostructures was calculated from the SA-XRD using the equation $a_0 = \frac{2d_{100}}{\sqrt{3}}$, assuming hexagonal porours structure. T_w was calculated by subtracting the mean pore diameter (D_p), obtained from nitrogen physisorption through BJH method, from the hexagonal cell parameter (a_0).

Prior to the nitrogen physisorption analyses, ferrierite and Al-MCM-41 samples were thermally treated for 12 h under vacuum at 250 °C (heating rate, 1 °C min^{-1}), while the TiO_2/ZrO_2 samples were heated at 120 °C. The Brunauer–Emmett–Teller (BET) specific surface area was calculated from the adsorption data in the P/P_0 range 0.05–0.17 for Al-MCM-41 and 0.05–0.3 for the TiO_2/ZrO_2 samples. Due to the microporous features of ferrierite, the specific surface area was estimate by using the Dubinin-Radushkevich model and the total pore volume and pore size by the Horvath-Kawazoe model. For Al-MCM-41, TiO_2 and $Ti_{0.77}Zr_{0.23}O_2$ the total pore volume (V_p) was calculated at P/P_0 = 0.875, while mean pore diameter was determined by employing the Barrett- Joyner-Halenda (BJH) model to the desorption branch isotherm.

3.4 Study of the acidic properties

As previously mentioned, the ammonia-adsorption microcalorimetry and FTIR-monitored pyridine adsorption were adopted to study the acidic properties of the samples. The calorimetric curves obtained by plotting the differential heat of adsorption (Q_{diff}) *vs.* ammonia coverage (n_A, μmol g^{-1}) are shown in Figure 31. All samples showed high initial values of Q_{diff} (> 230 kJ mol^{-1}), suggesting the existence of a small fraction of very strong acidic sites. A quasi-*plateau* was observed between 150 and 110 kJ mol^{-1} and 87 and 77 kJ mol^{-1} for ferrierite and TiO_2, respectively, indicating the presence of isoenergetic acidic sites. For the other samples, a continuous Q_{diff} decrease was shown with increasing coverage extent. This suggested an energetical heterogeneity of the surface acidic sites. A threshold value between specific and non-specific (physisorption) adsorbent/adsorbate interaction was assumed equal to 70 kJ mol^{-1}, *i.e.*, the initial heat released during NH_3 adsorption experiments on a non-acidic reference sample of pure silica [144]. Therefore, the ammonia uptake corresponding to differential heat values below this cut-off value was neglected in the assessment of the acidic sites concentration n_A. The results are listed in Table 5. The most acidic sample was found to be ferrierite, featuring the highest NH_3 uptake (1539 µmol g^{-1}). Moderately lower amount of total acidic sites was observed for the TiO_2 sample (1168 µmol g^{-1}). Less than halved amounts of total acidic sites were found for $Ti_{0.77}Zr_{0.23}O_2$ (504 µmol g^{-1}), and Al-MCM-41 (416 µmol g^{-1}). Furthermore, the irreversibly adsorbed NH_3 ($n_{A,irr}$) was calculated from the microcalorimetric data (Table 5). TiO_2 showed the highest concentration of $n_{A,irr}$ (934 µmol g^{-1}), which is about the 80% of the total acidic sites, far from the value of 49% calculated for $Ti_{0.77}Zr_{0.23}O_2$. A high percentage of $n_{A,irr}$ (69%) was also observed for Al-MCM-41. Ferrierite was responsible for the lowest percentage of irreversible acidic sites (45%). However, by normalizing the ammonia coverage for the surface area (µmol m^{-2}) (Figure 31b), the values of $n_{A,irr}$ were found in the order TiO_2 (3.42 µmol m^{-2}) > Ferrierite (1.67 µmol m^{-2}) > $Ti_{0.77}Zr_{0.23}O_2$ (1.36 µmol m^{-2}) >> Al-MCM-41 (0.23 µmol m^{-2}). It is worthy to note that the surface concentration of acidic sites on which NH_3 is irreversibly adsorbed for Al-MCM-41 is one order of magnitude lower than that of the other catalysts.

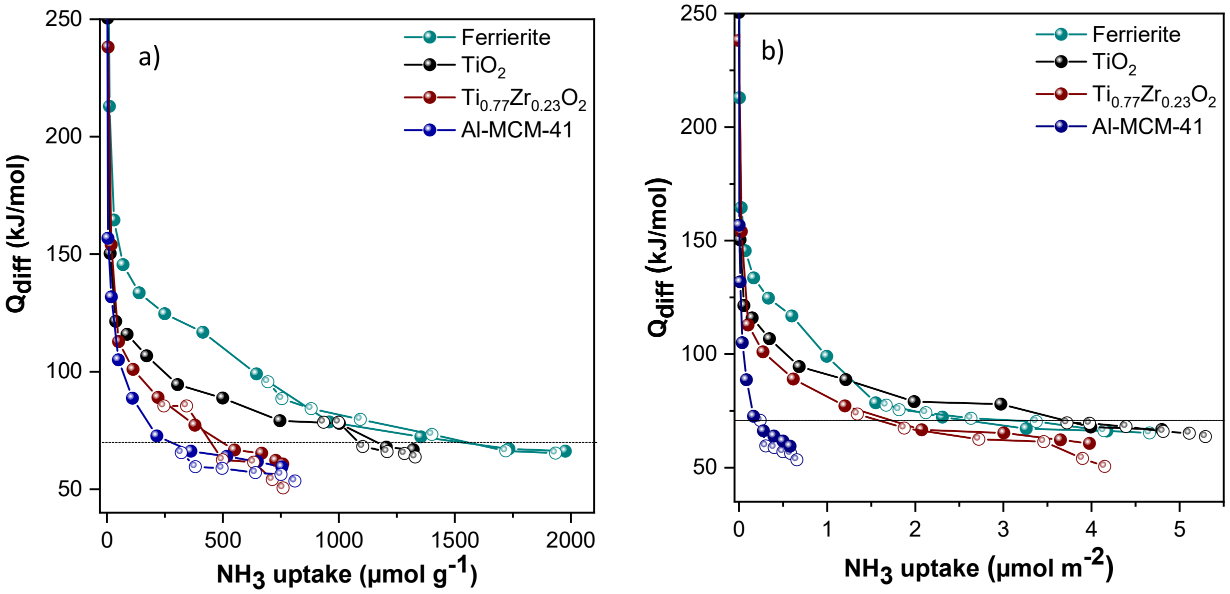

Figure 31. Differential heat (Q_{diff}) vs. uptake for ammonia adsorption expressed in µmol g^{-1} (a) and µmol m^2 (b) for the samples ferrierite, Al-MCM-41, TiO_2 and $Ti_{0.77}Zr_{0.23}O_2$. Open symbols refer to readsorption after overnight evacuation. Dash lines refers to the cut-off value between physisorption and chemisorption (70 kJ mol^{-1}) [73]. *For further details on the analysis setup, see the Appendix.*

Table 5. Ammonia-adsorption microcalorimetric results for the samples ferrierite, Al-MCM-41, TiO_2 and $Ti_{0.77}Zr_{0.23}O_2$ [73].

Sample	$n_{A,tot}$[a] (µmol g^{-1})	$n_{A,tot}$[a] (µmol m^{-2})	$n_{A,irr}$[b] (µmol g^{-1})	$n_{A,irr}$[b] (µmol m^{-2})	$n_{A,irr}$/ $n_{A,tot}$ (%)
Ferrierite	1539	3.71	694	1.67	45
Al-MCM-41	416	0.32	286	0.23	69
TiO_2	1168	4.27	934	3.42	80
$Ti_{0.77}Zr_{0.23}O_2$	504	2.75	248	1.36	49

[a] *Total amount of acidic sites: $Q_{diff} \geq 70$ kJ/mol.*

[b] *Amount of irreversibly adsorbed NH_3.*

The acidic properties of the catalysts were further investigated through FTIR-monitored pyridine (probe molecule) adsorption. The FTIR spectra, recorded in the 1700-1400 cm^{-1} range after a pyridine saturation-desorption run at room temperature, are displayed in Figure 32. Different FTIR signals ascribable to pyridine in its coordinatively bonded (Lewis), pyridinium ion (PyH^+, Brønsted) or hydrogen-bonded form (physisorption) [161], [167] are visible.

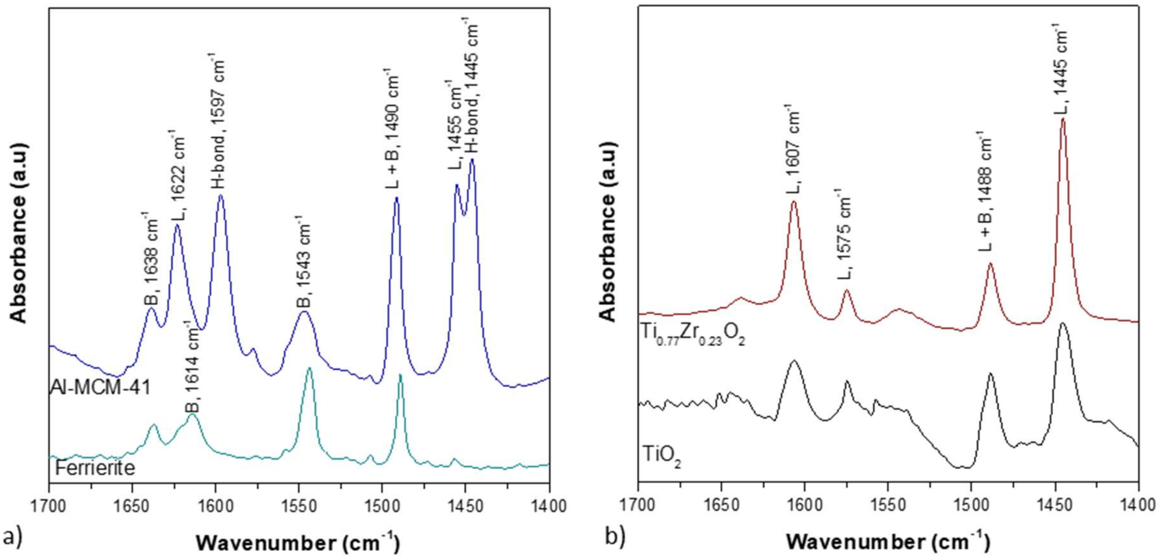

Figure 32. FTIR spectra of the samples after saturation and subsequent desorption: ferrierite and Al-MCM-41 (a); TiO_2 and $Ti_{0.77}Zr_{0.23}O_2$ (b). B, L and H-bond labels are associated with Brønsted acidity, Lewis acidity and hydrogen bonding, respectively [73].

In the case of ferrierite, Brønsted acidity (1543 cm^{-1}), and almost neglectable Lewis acidity (1455 cm^{-1}) were observed (Figure 32a). The quantification of the two contributions was performed according to [168], in which molar extinction coefficients 2.22 and 1.67 cm µmol^{-1} were used for Lewis and Brønsted acidic sites, respectively. As expected, almost all the acidic sites were found to be of Brønsted nature (96%), with only a 4% of Lewis acidity. On the contrary, both Brønsted (1543 cm^{-1}) and Lewis acidity (1455 cm^{-1}) were observable for the sample Al-MCM-41, together with a pronounced H-bond fraction (1445 cm^{-1}) (Figure 32a). To quantify these contributions, the reference [169] was taken into account (excluding H-bond from the quantification and using the previously-mentioned molar extinction coefficients). 66% and 34% of Lewis and Brønsted acidic sites were estimated, in agreement with reference [169]. In the literature, the presence of Brønsted acidic sites in silica-alumina catalysts (zeolites and amorphous aluminosilicates) is usually ascribed to unsaturated tetracoordinated aluminum species. Actually, in the case of amorphous systems, the explanation may become complex if other species are present, such as penta-coordinated aluminum, whose amount, generally low, can be tuned according to the synthetic approach [170]. Concerning zeolites, the presence of extra-framework aluminum oxide or aluminum bonded with less than four SiO_4^{4-} tetrahedra can instead justify the Lewis acidity [169]. Therefore, a high percentage of tetracoordinated aluminum (96% of Brønsted acidic sites) in ferrierite was ensured by its crystal structure, whereas the amorphous nature of Al-MCM-41 led to a high amount (66%) of Lewis acidic sites. Typical bands centered at about 1445, 1575 and 1607 cm^{-1}, ascribable to Lewis acidity, were visible in the FTIR spectra of TiO_2 and $Ti_{0.77}Zr_{0.23}O_2$ (Figure 32b). According to the literature [161], the two intense bands at about 1445 and 1607 cm^{-1} are related to strong Lewis sites, while the band at 1575 cm^{-1} is due to weak Lewis sites. However, the presence of a broad and weak band at about 1540 cm^{-1} does not exclude a minor amount of Brønsted acidic sites, probably due to unsaturated surface metal atoms, bonded to -OH groups [171], [172].

3.5 Study of the catalytic performances

Physical mixtures of CZA with the different acidic dehydration catalysts (ferrierite, Al-MCM-41, mesostructured TiO_2, or mesostructured $Ti_{0.77}Zr_{0.23}O_2$) were tested for the CO_2-to-dimethyl ether (DME) one-pot process. Taking as a reference the CZA alone, similar CO_2 conversion (X_{CO2}) values were obtained for all physical mixtures, but the CZA-TiO_2, which showed a lower X_{CO2} (Figure 33). Ideally, the dehydration catalyst in this system should convert all the produced methanol into DME, further inducing the production of more methanol and lowering the CO production. Indeed, a 10 mol% drop in CO selectivity was observed as a consequence of the addition of ferrierite to CZA (Figure 33), due to the consumption of methanol that on the one hand favors the conversion of CO_2 to further methanol, and on the other hand limits its decomposition to CO over the CuO-based redox phase [173]. Conversely, the mixture with the other acid catalysts did not produce any remarkable change in the CO selectivity. The results in terms of DME formation indicated better performance (S_{DME} = 38 mol%) of the CZA-ferrierite mixture compared to the other physical mixtures (CZA + Al-MCM-41/TiO_2/$Ti_{0.77}Zr_{0.23}O_2$), whose DME selectivity (S_{DME}) was found in the range 7.5 - 10.5 mol%. These results can be explained taking into account the amount, strength, and nature of the acidic sites, and the structural and textural properties of the dehydration catalysts.

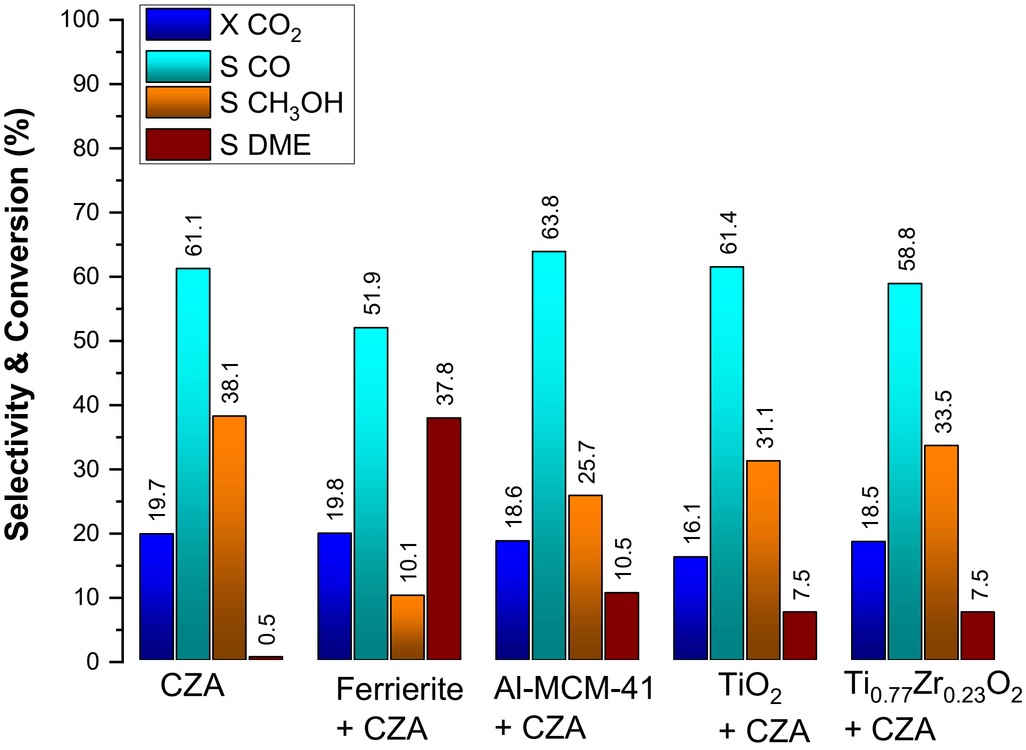

Figure 33. Mean values of CO_2 conversion and selectivity to CO, methanol, and DME after 36 h of test for CZA and physical mixtures (CZA-dehydration catalyst) excluding the first 3h of test. Catalytic conditions: temperature: 250 °C, pressure: 3.0 MPa; GHSV: 12000 Ncm^3 g$_{cat}^{-1}$ h^{-1} in the case of CZA test and 6000 Ncm^3 g$_{cat}^{-1}$ h^{-1} for the physical mixtures tests. Weight Ratio CZA: dehydrant: 1:1 [73].

The higher catalytic performances of the CZA-ferrierite mixture in terms of S_{DME} (37.8 mol%) can be justified due to its acidic site type (Brønsted, Figure 32), their high amount (1539 µmol g^{-1}, Table 5), and the presence of an isoenergetic sites. Although, in the literature, the performances of ferrierite are reported as less affected by the coke formation than those of other zeolites (MFI and MOR), thanks to its 2D pore structure [61], [174]–[176], in our experiments, a slight worsening of the catalytic performances was encountered with a decrease in the S_{DME} from 39.1 mol% (value at 3 h) to 36.5 mol% (value at 36 h), as shown in Figure 35. To exclude the contribution of coke, CHN analyses were performed on the CZA-ferrierite physical mixture before and after the catalytic test, as shown in Table 6. The carbon content (1.19 w/w%) in the CZA-ferrierite mixture can be totally ascribed to the carbon present in CZA, and no coke formation was found, confirming the results from other authors [175]. Therefore, the observed decrease in S_{DME} can be associated with a slight decrease in the surface area and the pore volume, due to the hydrogenation reaction, as highlighted by the comparison of the N_2-physisorption isotherms of the pristine and used mixture (CZA, α-Al_2O_3 and ferrierite, Table 7, Figure 35b).

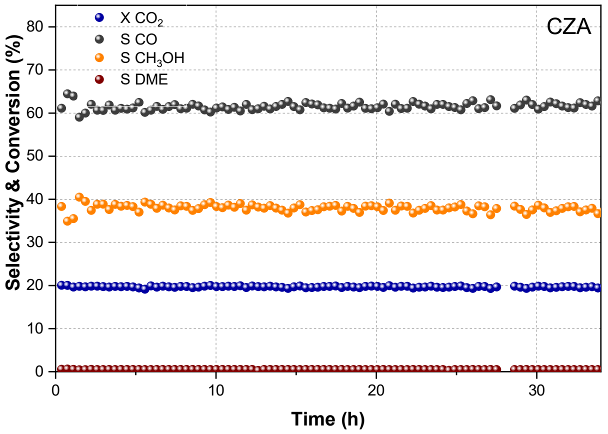

Figure 34. Conversion of CO_2 and selectivity to CO, methanol (MeOH) and dimethyl ether (DME) vs Time for the sample CZA [73].

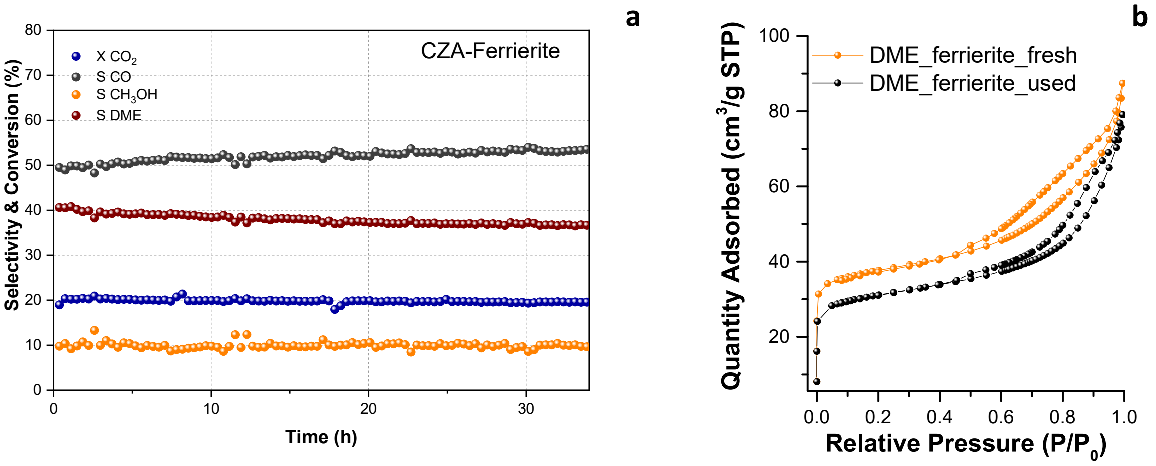

Figure 35. Conversion of CO_2 and selectivity to CO, methanol (MeOH) and dimethyl ether (DME) vs Time for the sample Ferrierite (a). N_2-physisorption isotherms of the mixture CZA/α-Al_2O_3 and ferrierite before (DME_ferrierite_fresh) and after the catalytic test (DME_ferrierite_used (b) [73].

Table 6. CHN analysis on the spent CZA-ferrierite physical mixture and on its components before the catalytic test [73].

Sample	Carbon w/w%	Hydrogen w/w%	Nitrogen w/w%
CZA	3.83	0.20	0.26
α-Al_2O_3	0.11	0.24	0.31
Ferrierite	0.16	0.34	0.35
CZA-ferrierite	1.19	0.07	0.08

Table 7. Surface area (SA), pore volume (V_P), BJH-calculated pore diameter (D_p), of the tested mixture CZA/a-Al_2O_3 and the dehydration catalyst. Fresh stands to the pristine mixture, whereas used indicates the 36 hours used mixture [73].

Sample	S_{BET} (m^2g^{-1})	V_p (cm^3g^{-1})
CZA-ferrierite_fresh	117	0.13
CZA-ferrierite_used	97	0.12
CZA-Al-MCM-41_fresh	781	0.56
CZA-Al-MCM-41_used	597	0.46
CZA-TiO_2_fresh	111	0.14
CZA-TiO_2_used	60	0.11
CZA-$Ti_{0.77}Zr_{0.23}O_2$_fresh	87	0.13
CZA-$Ti_{0.77}Zr_{0.23}O_2$_used	74	0.11
CZA-$Ti_{0.23}Zr_{0.77}O_2$_fresh	83	0.11
CZA-$Ti_{0.23}Zr_{0.77}O_2$_used	68	0.11

Among the mesostructured catalysts, Al-MCM-41 was found to be the best one in terms of DME selectivity, though less selective (10.5 mol% S_{DME}) than ferrierite (37.8 mol% S_{DME}), despite the better textural properties. This is mainly ascribable to the much higher total number of acidic sites and the presence of a group of moderately strong isoenergetic Brønsted sites on the zeolite, arising from its crystal structure. Contrarily, being the Al-MCM-41 amorphous, both the energetic heterogeneity of the acidic sites and the co-presence of Brønsted (66%) and Lewis sites (33%) are reflected in the lower catalytic activity in terms of S_{DME}. Moreover, the progressive deactivation of its Lewis acidic sites, due to the formation of carbonaceous residues and/or to the gradual collapse of its pore structure (Figure 36b, Table 7), can be the reason behind the gradual lowering of the DME production, observed during the first 7 h of test (Figure 36a). However, the occurrence of stable performances during the following 29 h (Figure 36a), in agreement with previous observations [79], [177], revealed the formation of carbonaceous species according to Bedoya *et al.* [177].

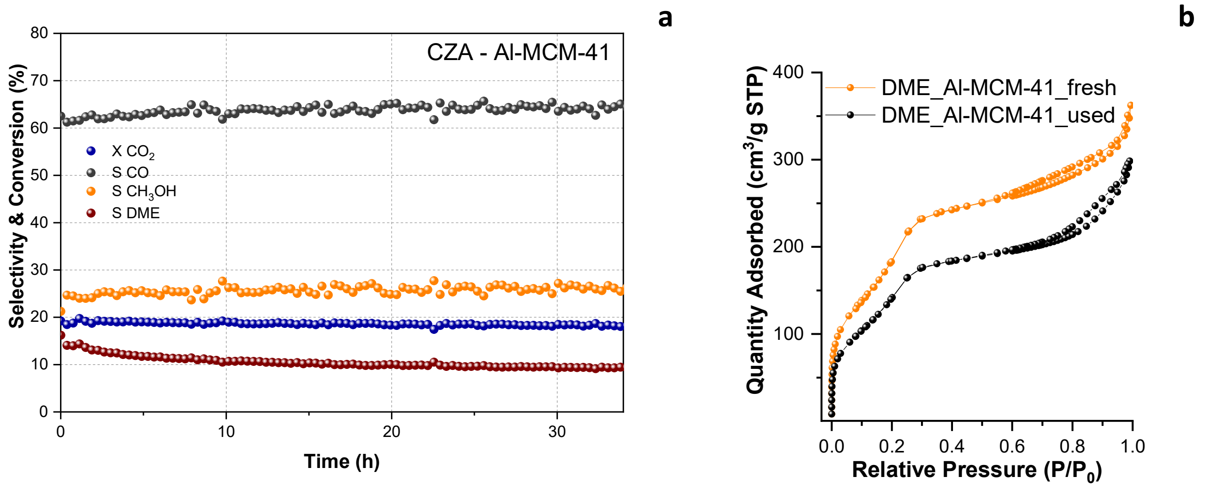

Figure 36. Conversion of CO_2 and selectivity to CO, methanol (MeOH) and dimethyl ether (DME) vs Time for the sample Al-MCM-41 (a). N_2-physisorption isotherms of the mixture CZA/a-Al_2O_3 and Al-MCM-41 before (DME_Al-MCM-41_fresh) and after the catalytic test (DME_ Al-MCM-41_used) (b) [73].

The worst performances were observed for the CZA-TiO_2 mixture. In particular, during the first hours of the test promising catalytic performances were revealed but, then, a remarkable worsening followed in terms of X_{CO2}, from 19.7 mol% to 13.8 mol%, and S_{DME} selectivity, from 16.3 mol% to 5.1 mol%, (Figure 37a). These results are compatible with the significant worsening of the textural properties observed in the mixture after the reaction (Figure 37b, Table 7).

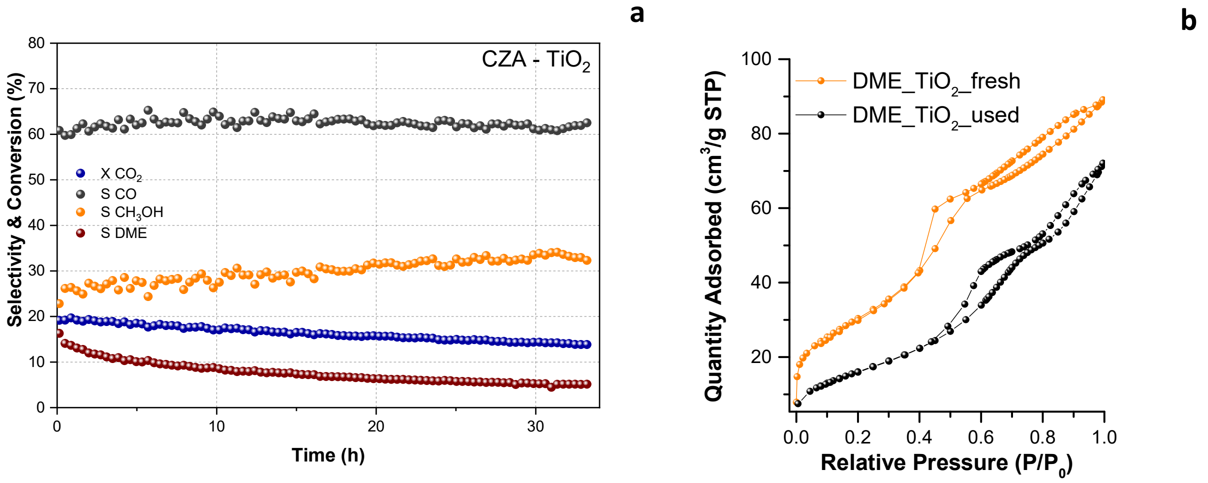

Figure 37. Conversion of CO_2 and selectivity to CO, methanol (MeOH) and dimethyl ether (DME) vs Time for the sample TiO_2 (a). N_2-physisorption isotherms of the mixture CZA/a-Al_2O_3 and TiO_2 before (DME_TiO_2_fresh) and after the catalytic test (DME_ TiO_2_used) (b) [73].

$Ti_{0.77}Zr_{0.23}O_2$ showed steady performances (Figure 38a), a mean value of S_{DME} close to that of TiO_2, and the lowest CO selectivity (58.8 mol%) among all mesostructured catalysts, even slightly lower than that of pure CZA (61.1 mol%). After the test, the textural properties of $Ti_{0.77}Zr_{0.23}O_2$ were not strongly affected (Figure 38b**,** Table 7). Despite the presence of Lewis acidic sites in both TiO_2 and $Ti_{0.77}Zr_{0.23}O_2$, the different behavior of these two catalysts can be associated with the remarkable differences in terms of their amount (1168 and 504 µmol g^{-1} of total acidic sites, respectively) and strength (934 and 248 µmol g^{-1} of irreversible acidic sites, respectively) (Table 5). Indeed, the high amount of total acidic sites can be responsible for the higher initial catalytic activity of TiO_2, but the high percentage of irreversible acidic sites (about 80%), (Table 5), led to a strong deactivation with the water molecules produced during the hydrogenation and dehydration reactions. On the contrary, the initial lower and then steady performances of $Ti_{0.77}Zr_{0.23}O_2$ can be justified in terms of lower amount and percentage of irreversible acidic sites (about 50%) that led to a better water tolerance. This effect might be due to the presence of zirconium, as already reported by other authors [161] for the application of non-mesostructured Ti-ZrO_2 samples in the dehydration of methanol to DME at atmospheric pressure.

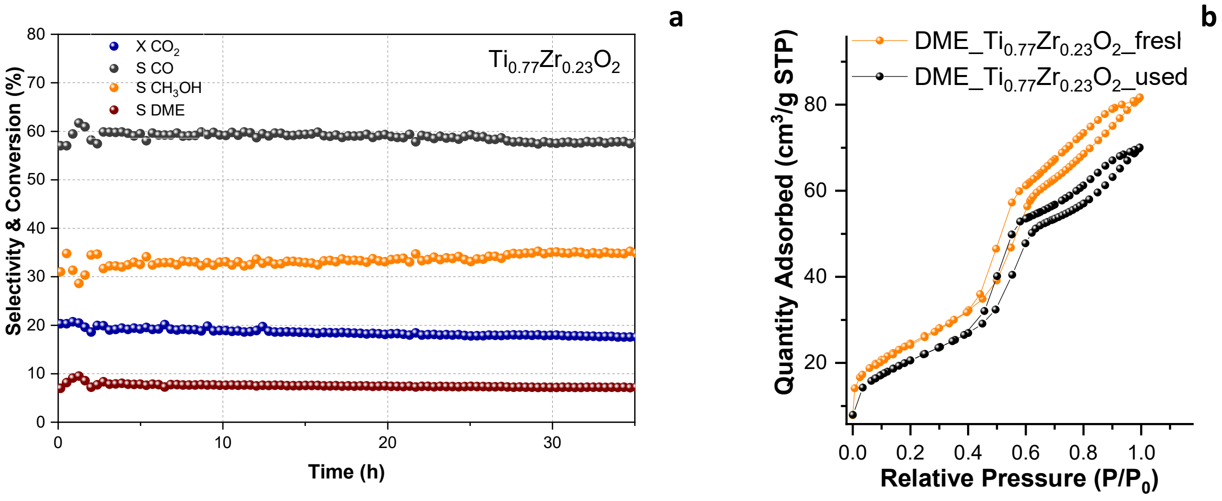

Figure 38. Conversion of CO_2 and selectivity to CO, methanol (MeOH) and dimethyl ether (DME) vs Time for the sample $Ti_{0.77}Zr_{0.23}O_2$ (a). N_2-physisorption isotherms of the mixture CZA/a-Al_2O_3 and $Ti_{0.77}Zr_{0.23}O_2$ before (DME_ $Ti_{0.77}Zr_{0.23}O_2$_fresh) and after the catalytic test (DME_ $Ti_{0.77}Zr_{0.23}O_2$_used) (b) [73].

Based on this discussion, a Ti-Zr mixed oxide with a higher amount of Zr ($Ti_{0.23}Zr_{0.77}O_2$) was tested and as expected, its catalytic performances (Figure 39a) were the most stable. A slight worsening of its textural properties after the reaction, similarly to $Ti_{0.77}Zr_{0.23}O_2$ was observed (Figure 39b).

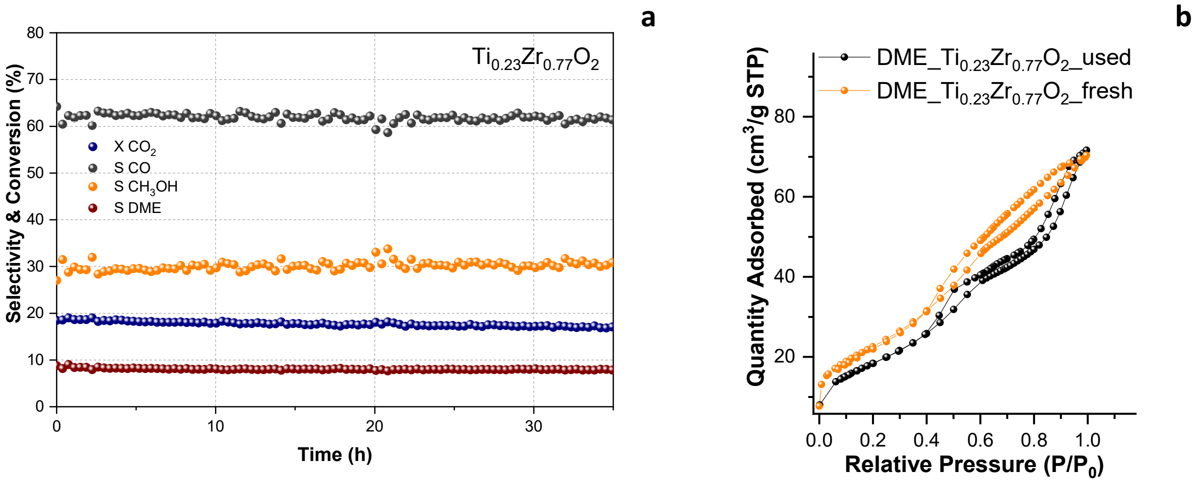

Figure 39. Conversion of CO_2 and selectivity to CO, methanol (MeOH) and dimethyl ether (DME) vs Time for the sample $Ti_{0.23}Zr_{0.77}O_2$. (a). N_2-physisorption isotherms of the mixture CZA/a-Al_2O_3 and $Ti_{0.23}Zr_{0.77}O_2$ before (DME_ $Ti_{0.23}Zr_{0.77}O_2$_fresh) and after the catalytic test (DME_ $Ti_{0.23}Zr_{0.77}O_2$_used) (b) [73].

These findings suggest that several aspects need to be taken into account when evaluating the catalysts, such as: (i) its stability, (ii) CO_2 conversion, (iii) CO, CH_3OH, and DME selectivity, with the last two considered in the yield. Indeed, the yield can be reasonably expressed as both DME yield and DME + CH_3OH yield, being also methanol a valuable product (Table 8). These values reveal that Al-MCM-41 is the catalyst showing the highest DME yield (2.0%), while the highest DME + CH_3OH yield (7.6%) was found for $Ti_{0.77}Zr_{0.23}O_2$, which also accounts for steady performances during the test.

Table 8 DME yield (%) and DME + methanol yield (%) of pure CZA and CZA + dehydration catalyst (Ferrierite, Al-MCM-41, $Ti_{0.77}Zr_{0.23}O_2$, TiO_2) physical mixtures [73].

Sample	DME Yield (%)	DME + CH_3OH Yield (%)
CZA	-	7.5
Ferrierite	7.5	9.5
Al-MCM-41	2.0	6.7
TiO_2	1.2	6.2
$Ti_{0.77}Zr_{0.23}O_2$	1.4	7.6

3.6 Conclusions

In this work, different mesostructured oxides were synthesized, characterized, and tested as dehydration catalysts in mixture with a commercial redox catalyst (CZA) for the one-pot DME production from CO_2. The samples differed for both their chemical composition and textural properties. A commercial dehydration zeolite catalyst (ferrierite) was used as a reference for the comparison of their catalytic performances. In the light of the findings, we can conclude that:

1) The microporous crystalline material (ferrierite) demonstrated much better catalytic performances for methanol dehydration than the mesostructured amorphous aluminosilicate (Al-MCM-41), due to the high amount of isoenergetic Brønsted acidic sites.

2) Although the mesostructured crystalline TiO_2 and the amorphous Ti-Zr oxide $Ti_{0.77}Zr_{0.23}O_2$ feature mostly Lewis acidic sites, with a higher amount for TiO_2, this latter catalyst shows a gradual decrease in its activity, probably due to a higher acidic strength, which causes a deactivation due to irreversible water adsorption. The presence of Zr in the TiO_2 framework ($Ti_{0.77}Zr_{0.23}O_2$) led to less strong acidic sites and, consequently, steady catalytic performances.

3) The comparison between the amorphous Al-MCM-41 and $Ti_{0.77}Zr_{0.23}O_2$, showing different nature (Brønsted *vs.* Lewis) but comparable amount of the acidic sites (416 $\mu mol\ g^{-1}$ *vs* 504 $\mu mol\ g^{-1}$), pointed out a higher activity for Brønsted acidic sites.

Chapter 4

Development of Al-SiO_2- and Al_2O_3-based mesostructured catalysts with different textural properties

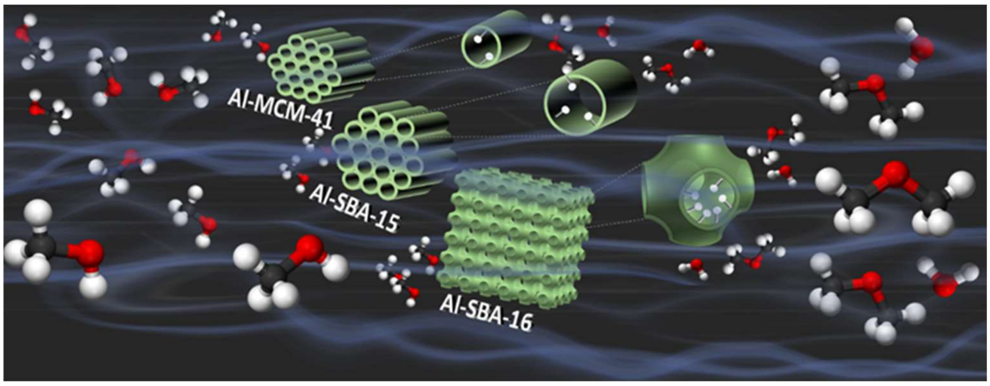

4.1 Introduction

In this chapter, we designed five different mesostructured acidic materials to be used as methanol dehydration catalysts for the one-pot CO_2-to-DME process, as physical mixtures with CZA. The mesostructured acidic catalysts consist in two mesostructured γ-Al_2O_3 samples, different for their pore size, and three mesostructured aluminosilicates with the same Si/Al ratio (= 15) but significantly different textural properties (namely Al-MCM-41, Al-SBA-15, and Al-SBA-16). So far, γ-Al_2O_3 has been widely proposed in the literature as methanol dehydration catalyst due to its low cost, and the presence of Lewis acid sites of moderate strength, which lead to high DME selectivity. On the contrary, strong Brønsted sites, although they show a higher activity in methanol dehydration, lead to a lower selectivity, due to the methanol-to-olefins (MTO) process and a potential deactivation arising from coke formation that generates hydrocarbons [19], [30], [49], [50]. Therefore, γ-Al_2O_3 has been widely reported for the methanol-to-DME [178]–[180], the syngas-to-DME [44], [181], [182], and CO_2-to-DME processes [183]–[185]. Nevertheless, γ-Al_2O_3 performances tend to worsen over time, due to deactivation of its Lewis acid sites caused by the formation of a Lewis acid-base adduct as a consequence of the adsorption of water molecules [14], [61]. This is particularly disadvantageous for the CO_2-to-DME process due to the formation of water molecules in a ratio with respect to DME molecules of 3:1. In the previous chapter, in agreement with the results from other authors [23], [25], Brønsted sites showed much higher water tolerance and better dehydration performances, compared to the Lewis counterparts. In this context, aluminosilicates (mainly zeolites), featuring Brønsted acid sites, have proven to be better catalysts, also due to their lower surface hydrophilicity [23], [25]. Moderate or weak-strength Brønsted acid sites can be considered ideal, to avoid the formation of by-products [23]. Again, in this chapter the attention was paid on the characterization of the acid sites by FTIR-monitored pyridine adsorption and NH_3-microcalorimetry. Some of the results reported in this chapter have been published in [186].

4.2 Synthesis methods

Synthesis of Al-MCM-41

Aluminum-doped MCM-41 (Al-MCM-41) with a Si/Al ratio of 15 was synthesized as reported in Paragraph 3.2.

Synthesis of Al-SBA-16

Al-SBA-16 was synthesized based on the synthesis proposed by Wang *et al*. [187] for Al-SBA-15 and changed for the purpose. The selection of a Si/Al ratio (= 15), not investigated in the original work, led to the obtainment of a cubic SBA-material (SBA-16) instead of a hexagonal one. Namely, to prepare ≈1.5 g of product, 2.36 g of P123 were first dissolved into 45 mL of absolute ethanol into a round-bottom flask under continuous stirring at room temperature. After two hours, the following reactants were added: 5.34 g of TEOS, 0.38 g of $AlCl_3{\cdot}6H_2O$, and 0.5 mL of water. The stirring was kept for 24 h, then the solution was poured into a 21 cm Petri dish and left at room temperature into a controlled-humidity chamber (RI=40%). After 2 days, the as-formed gel was recovered from the Petri dish, heated at 600 °C with a heating ramp of 2 °C/min, and calcined for 5 h.

Synthesis of Al-SBA-15

Al-SBA-15 was synthesized through the solvothermal procedure proposed by Meloni *et al*. [144], [145]. Firstly, a solution of P123 (4 g) and NaCl (6.7 g) into 126 mL of 1M HCl was prepared under continuous stirring at 40 °C. 8.5 g of TEOS were then added dropwise, and the stirring kept for 24 h at 40 °C. Elapsed this time, 1.02 g of $Al(NO)_3{\cdot}9H_2O$ were added and the system left under stirring for other 24 h. The mixture was then poured into the Teflon liner of a 300 mL autoclave, which was subjected to a solvothermal treatment at 100 °C. After 48 h, the autoclave was left to cool down and the pH of the mixture was modified by adding concentrated ammonia (28-30%) till a value of 5 was reached. Then, the autoclave was sealed again and treated for a second solvothermal step under the same conditions (100 °C for 48 h). Once the autoclave was cooled, the obtained solid was separated by centrifugation at 4500 RPM for 10 min, washed twice with distilled water and dried overnight at 60 °C. Then a calcination at 600 °C (4 °C/min) for 5 h was carried out.

Synthesis of mesostructured γ-Al_2O_3

Two samples of Al_2O_3 were synthesized through an EISA method, adapted from [160], using two different templating agents, namely P123 (Al_2O_3_P) and F127 (Al_2O_3_F) in order to induce the formation of a mesostructured with different pore size. Typically, about 1.5 g of mesostructured Al_2O_3 was obtained by dissolving the triblock copolymer (3 g of P123 or F127) in 75 mL of absolute ethanol under continuous stirring at room temperature. After 2 h, 4.8 mL of HNO_3 and 6.24 g of aluminum isopropoxide were added and the resulting solution was kept under stirring at room temperature for 24 h. Then, the sol was then transferred into a Petri dish inside a controlled-humidity chamber (RH≈20%) standing on a heating plate at 70 °C. After 48 h the gel was recovered and first treated at 400 °C (heating ramp of 1 °C/min) in static air for 4 h (Al_2O_3_P_400; Al_2O_3_F_400), to remove the templating agent, and secondly at 900 °C (1 °C/min) for 2 h (Al_2O_3_P_900; Al_2O_3_F_900) for the obtainment of the desired crystalline alumina phase (γ-Al_2O_3).

4.3 Structural, textural, and morphological characterization

This paragraph in focused on the characterization of the mesostructured acidic systems by SA-XRD, WA-XRD, N_2 physisorption, TEM, calorimetry and FTIR spectroscopy with ammonia and pyridine as probe molecules.

SA-XRD patterns, reported in Figure 40a, show a mesoporous order for all samples. A hexagonal mesostructure (p6mm), revealed by the main peak (100) located at 0.9° 2θ value, and two low-intensity peaks (110, 200) located at 1.5° and 1.8°, was obtained for the Al-SBA-15 sample. A cell parameter of 10.8 nm was calculated (Table 9). To the Al-SBA-16, a cubic pore arrangement (Im3m) [100], [188] was inferred due to the presence of a main peak (110) located at 1.2°, associated with a cell parameter of 10.6 nm, and a peak (200) at 1.3°. A significantly smaller cell parameter (3.9 nm was showed by Al-MCM-41, as indicated by a broad peak located at about 2.6°. In this case, the pore arrangement geometry could not be clearly attributed, due to the lack of additional signals. However, a hexagonal arrangement was hypothesized on the basis of the selected synthesis conditions that, in the absence of Al, led to a hexagonal mesostructure (MCM-41) [128].

A mesoporous order was also present in both γ-Al_2O_3 samples (Figure 41a). In the SA-XRD patterns, a main peak located at 2θ values in the range 0.7°-1.1° and a shoulder located at higher values, suggest the formation of a hexagonal mesostructure with a relatively pour mesoporous order. The position of the bands is in agreement with the data presented in the literature for γ-Al_2O_3 with a hexagonal mesoporous structure [160], [189], [190]. The systems obtained with the two Pluronics strongly differ for the cell parameter (Table 9). As expected, a shift towards higher 2θ values was observed for both samples when the synthesis temperature reached 900 °C, indicating that the formation of a crystalline phase is associated with a decrease of the cell parameter of the mesoporous structure. Specifically, a_0 drops from 10.8 nm for Al_2O_3_P_400 to 9.3 nm for Al_2O_3_P_900, and from 14.4 nm to 13.1 nm for the F127 counterparts.

Figure 40b depicts the WA-XRD of the three mesostructured aluminosilicates, with a main broad band located at a 2θ value of about 23°, revealing their amorphous nature.

Also the Al_2O_3 samples thermally treated at 400 °C (Figure 41b) have amorphous nature, whereas the 900 °C treatment induced the formation of a cubic γ-Al_2O_3 phase (PDF card 00-047-1292) in form of very small nanocrystals. The Rietveld refinement (Figure 42a) on the Al_2O_3_P_900 pattern permitted to calculate a mean crystallite size of 5.1(1) nm and a cell parameter of 7.879(4) Å, slightly smaller than that reported in the PDF card (#00-047-1292, a = 7.9448 Å). A similar result in terms of cell parameter (7.886 (4) Å) was obtained for Al_2O_3_F_900 (Figure 42b), together with a slightly smaller mean crystallite size (4.5 (4) nm). The refinement also highlights the presence of two broad bands at about 36° and 63°, ascribable to the presence of a residue of amorphous alumina.

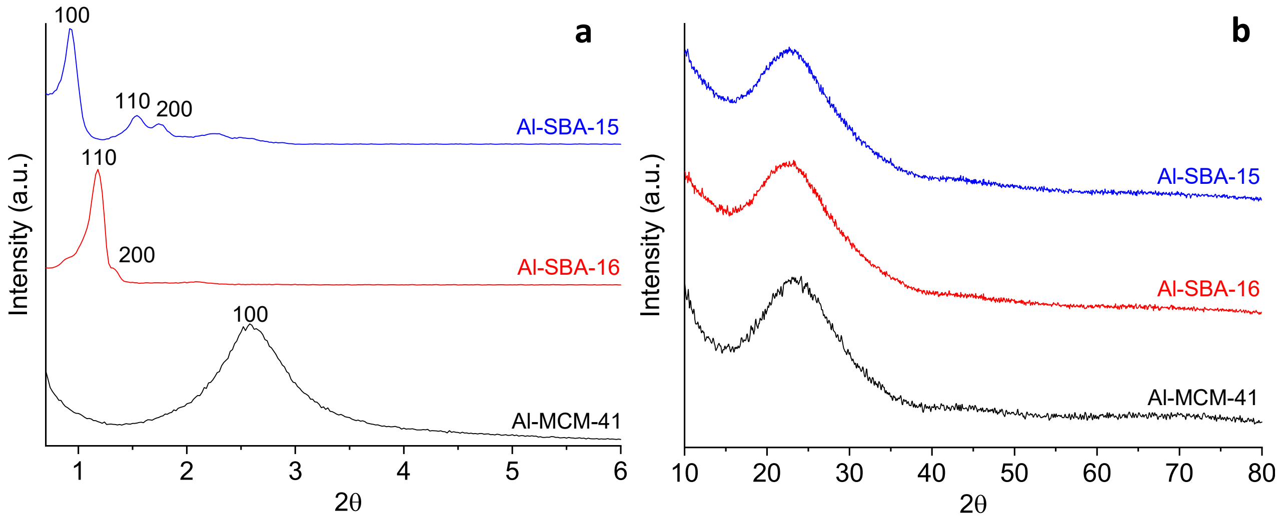

Figure 40 Small-angle (a) and wide-angle (b) X-ray diffraction patterns of the aluminosilicate samples.

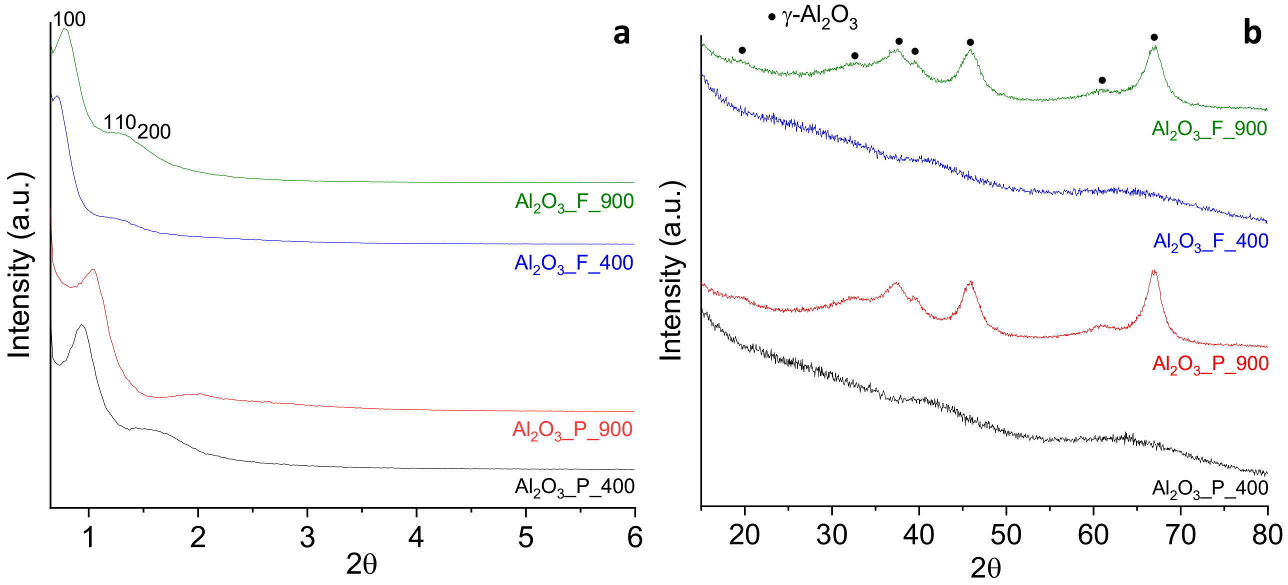

Figure 41 Small-angle (a) and wide-angle (b) X-ray diffraction patterns of the Al_2O_3 samples.

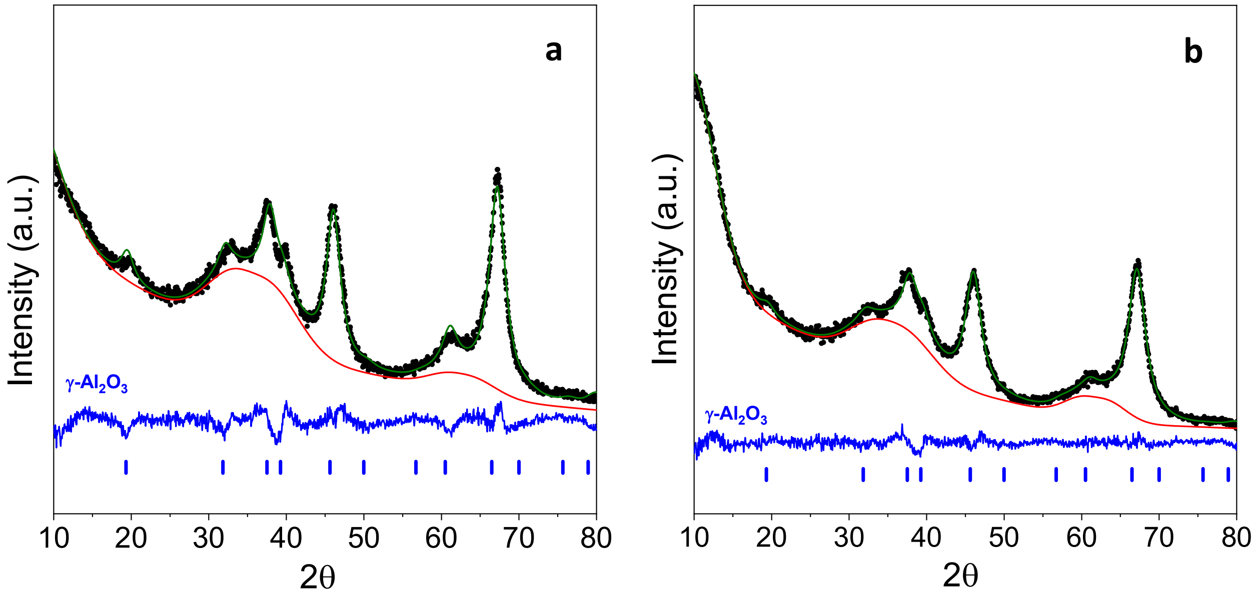

Figure 42 Rietveld refinement of the WA-XRD pattern of Al_2O_3_P_900 (a) and Al_2O_3_F_900 (b).

The mesoporous nature of all samples (Figure 43a, Figure 44a) was confirmed by the shape of the N_2 physisorption isotherms, featuring a capillary condensation branch. Furthermore, for all aluminosilicates, a multilayer adsorption is preceded by a microporous contribution. The capillary condensation branch of Al-MCM-41 sample (type IVb isotherm), located at the lowest value of relative pressure (<0.3) among all samples, indicates a smaller mean pore diameter (2.1 nm). The two Al-SBA samples show IVa isotherms located at 0.5-0.6 for Al-SBA-16 and 0.7-0.8 for Al-SBA-15, indicating pore sizes larger than those of Al-MCM-41. A narrow hysteresis with very steep and perpendicular branches (type H1, according to IUPAC classification) was obtained for the Al-SBA-15, indicating a narrow pore size distribution and a well-defined arrangement of the mesochannels [145], [146]. On the contrary, Al-SBA-16 showed an H2 hysteresis type according to IUPAC, with a less steep adsorption branch, typical of SBA-16 materials [188], [191], [192]. The textural properties of the samples are listed in Table 9. Al-SBA-15 showed the highest pore volume (1.07 cm^3/g) and pore diameter (6.9 nm). Al-MCM-41showed the highest surface area (1262 m^2/g) and the lowest pore diameter (2.1 nm). For all the aluminosilicate mesostructures, a narrow pore size distribution calculated with BJH method (Figure 43b) was found. Finally, Al-SBA-16 features an intermediate mean pore size of 4.6 ± 0.5 nm.

The series of F127-Al_2O_3 samples shows type IV isotherms with a steep capillary condensation and parallel hysteresis branches, followed by a *plateau* (Figure 44a). The P123 systems presented less steep capillary condensation curves and no *plateau* (Figure 44a), suggesting a lower degree of mesoporous order and a possible macroporous contribution with inter-particle capillary condensation [193]–[195]. As expected, the 900 °C treatment caused a partial mesostructure collapse, highlighted by a decrease in the surface area (from 274 to 197 m^2/g for Al_2O_3_P and from 309 to 194 m^2/g for Al_2O_3_F) and pore volume (from 0.76 to 0.57 cm^3/g for Al_2O_3_P and from 0.83 to 0.57 cm^3/g for Al_2O_3_F). In addition, a gradual decrease in the mean pore size was observed as a consequence of the thermal treatment at 900 °C: the mean pore diameter decreased from 7.8 nm to 5.6 nm for the samples obtained with P123, and from 9.3 nm to 8.7 nm, for the samples obtained using F127.

Table 9 BET surface area (SA), pore volume (V_p), cell parameter (a_0), mean BJH pore diameter (D_p) and wall thickness (T_w) of the samples.

Sample	SA (m^2/g)	V_p (cm^3/g)	a_0 (nm)	D_p (nm)	T_w (nm)
Al-MCM-41	1262	0.77	3.9	2.1 ± 0.7	1.7
Al-SBA-16	437	0.52	10.6	4.6 ± 0.5	4.6
Al-SBA-15	673	1.07	10.8	6.9 ± 0.5	3.8
Al_2O_3_P_400	274	0.76	10.8	7.8 ± 1.9	3.0
Al_2O_3_P_900	197	0.57	9.3	5.6 ± 1.7	3.9
Al_2O_3_F_400	309	0.83	14.4	9.3 ± 1.0	5.1
Al_2O_3_F_900	194	0.57	13.1	8.7 ± 2.7	4.4

Relative standard deviation: %RSD (SA) = 2.1%; %RSD (V_p) = 1.1%; %RSD (D_p) = 1.8%.

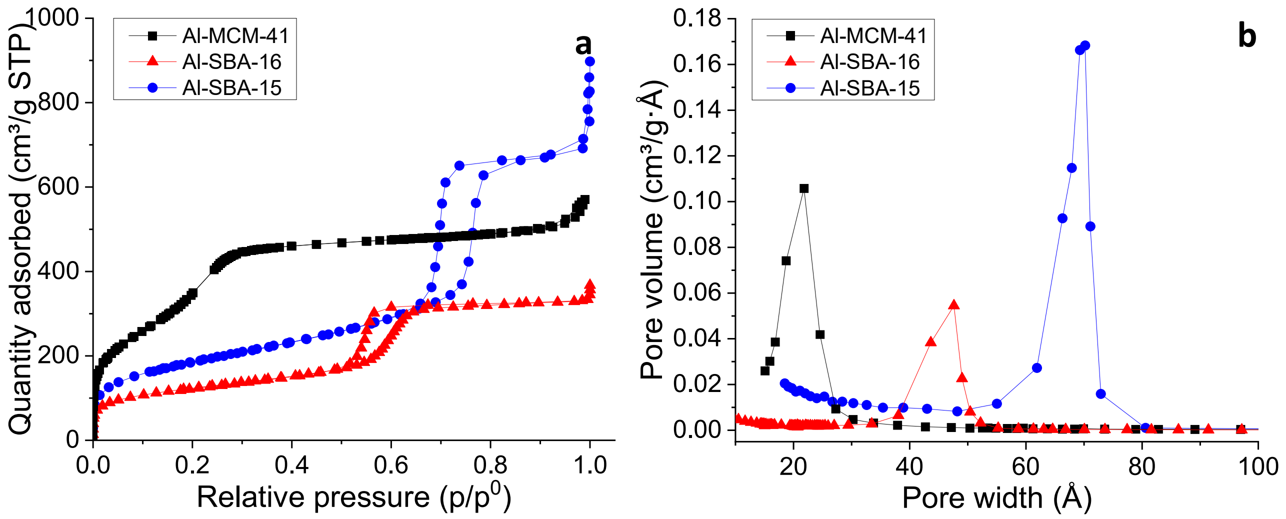

Figure 43 Nitrogen physisorption isotherms (a) and BJH pore size distribution (b) for the aluminosilicate samples.

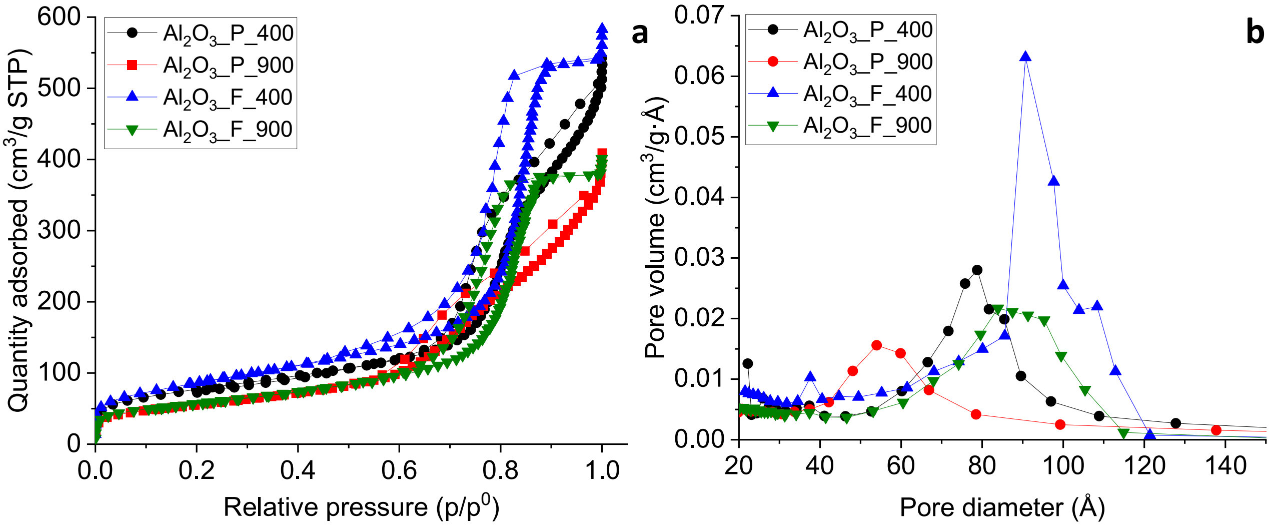

Figure 44 Nitrogen physisorption isotherms (a) and BJH pore size distribution (b) for Al_2O_3 samples.

Experimental details on the nitrogen physisorption measurements and SA-XRD

The lattice parameter of the mesostructures was calculated using the equation $a_0 = \frac{2d_{100}}{\sqrt{3}}$, for the samples that showed a hexagonal pore structure (Al-MCM-41, Al-SBA-15 and all Al_2O_3 samples) [128], [196]; the formula $a_0 = d_{110}\sqrt{2}$ was used for Al-SBA-16, that showed a cubic porous structure [191], [197].

Prior to the nitrogen physisorption analyses all samples were thermally treated for 12 h under vacuum at 250 °C (heating rate, 1 °C min^{-1}). The Brunauer–Emmett–Teller (BET) specific surface area (SA) was calculated from the adsorption data in the P/P_0 range 0.05-0.17 for Al-MCM-41 and 0.05-0.25 for the other samples. The total pore volume (V_p) was calculated at P/P_0 = 0.9975, while mean pore diameter (D_p) was determined by applying the Barrett–Joyner–Halenda (BJH) model to the desorption branch isotherm for all samples except for Al-SBA-16 for which the adsorption branch was used [197]. The pore wall thickness (T_w) was calculated using the formula $T_w = a_0 - D_p$ for the samples with a hexagonal mesostructure and $T_w = a_0 \frac{\sqrt{3}}{2} - D_p$ for Al-SBA-16 [188], [198]. Rietveld refinement was carried out on the XRD pattern of γ-Al_2O_3 using the software MAUD [199]. LaB_6 from NIST was used as standard reference for determining the instrumental parameters. The CIF structure used for the refinement was 1200015 from Crystallography Open Database [200].

TEM analyses proved the presence of an ordered mesoporous structure for all samples (Figure 45, Figure 46). Al-MCM-41 featured spherical particles (Figure 45a-c) of about 250 ± 20 nm in size (Figure 47) and the smallest pore diameter (Figure 45d). Significantly higher pore diameter can be detected in the TEM micrographs of Al-SBA-15 and Al-SBA-16. Al-SBA-16 shows a cubic mesopore arrangement (Figure 45e-h). Although electron microscopy in transmission mode can lead to an underestimation of the pore size and an overestimation of the wall thickness, due to the thickness of the sample, mean pore diameter was estimated for all samples but Al-MCM-41. For the SBA-16, a narrow distribution with a pore diameter of 3.0 ± 0.3 nm was estimated by TEM micrographs (Figure 45h). This value was lower than that calculated with BJH method (4.6 nm), probably due to the intrinsic limit mentioned above, and/or by the cubic porous structure with large cages interconnected by smaller channels. Since the cages are hidden by the pore walls and only the interconnecting channels are visible, the pore size estimated by the TEM micrographs results to be lower. In some TEM micrographs (Figure 45h), thanks to a low thickness of the sample in that zone, the presence of the cages interconnected by pore channels are clearly visible, with the size of the cages estimated as 5.2 ± 0.4 nm. The value of wall thickness was 4.5 ± 0.5 nm, in very good agreement with the data obtained from the cell parameter and BHJ pore diameter (4.6 nm). Al-SBA-15 featured a mesostructure with a hexagonal arrangement, visible as honeycomb-like structure and a parallel arrangement of the channels in the TEM micrographs (Figure 45i-l). It also exhibited the highest pore diameter of 6.7 ± 0.8 nm and an associated wall thickness of 4.1 ± 0.5 nm, in agreement with the nitrogen physisorption data. The slight mismatching between the data obtained by the two techniques can be ascribed, besides the above-mentioned intrinsic limit of TEM microscopy, to the fact that the electron beam is not perfectly aligned with the C_6 axis of symmetry [201].

All Al_2O_3 samples also show a hexagonal mesoporous structure (Figure 46), but with a degree of mesoporous order much lower than that showed by Al-SBA-15: some areas with a disordered mesoporosity are visible. This finding agreed with the observations based on nitrogen physisorption. The comparison of the micrographs acquired before (Figure 46a,b,e,f) and after the thermal treatment at 900 °C (Figure 46c,d,g,h) highlighted the retainment of the mesostructure. The mean pore size for Al_2O_3_P_900 was 5.0 ± 0.5 nm with a wall thickness of 4.1 ± 0.5 nm, close to the values calculated by N_2 physisorption and SA-XRD (D_p=5.6 nm, T_w=3.9 nm, Table 9). Moreover, the calculated wall thickness is also in good agreement with the crystallite size of about 5 nm obtained by Rietveld refinement.

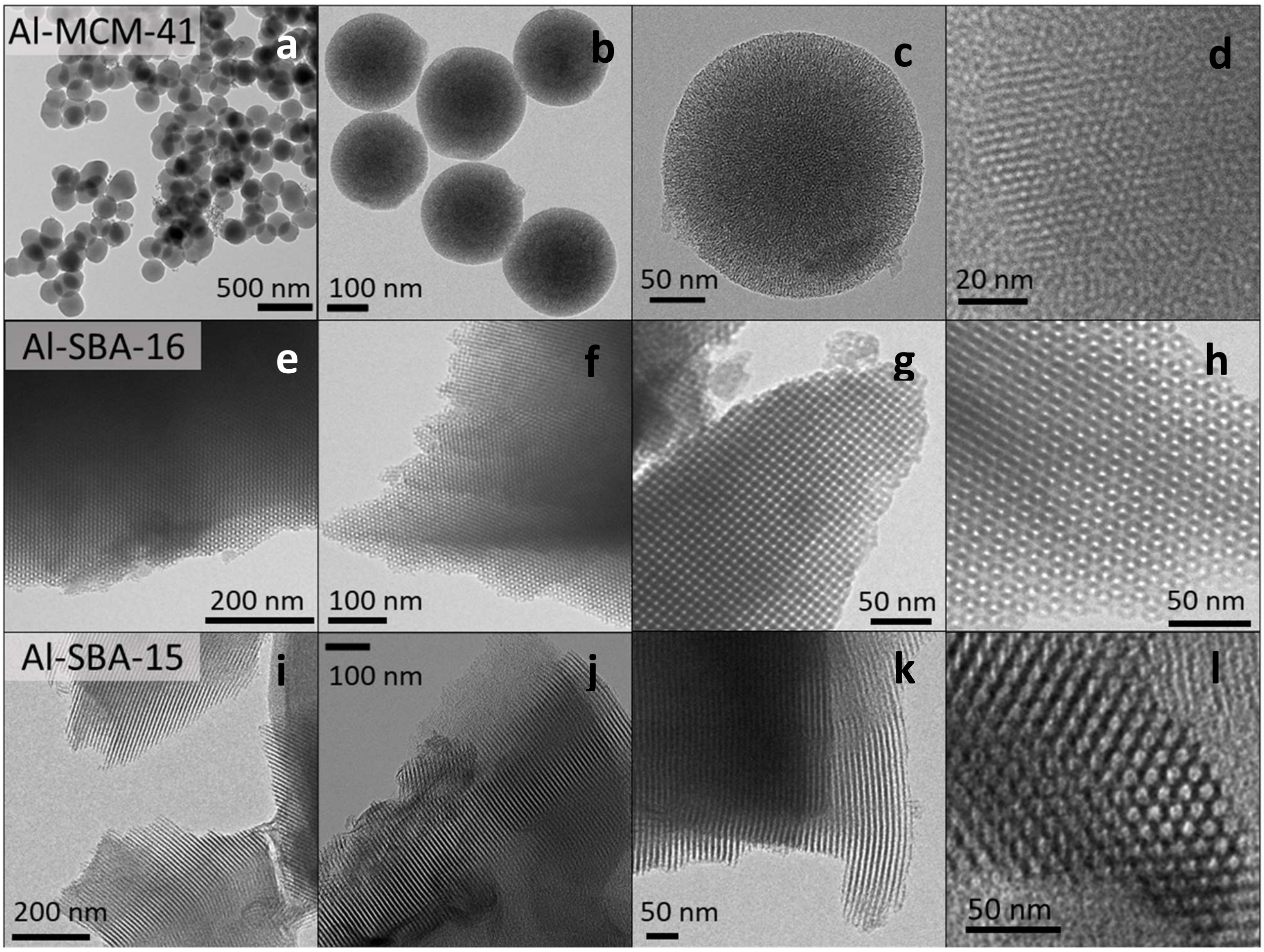

Figure 45 TEM images of Al-MCM-41 (a-d), Al-SBA-16 (e-h), Al-SBA-15 (i-l).

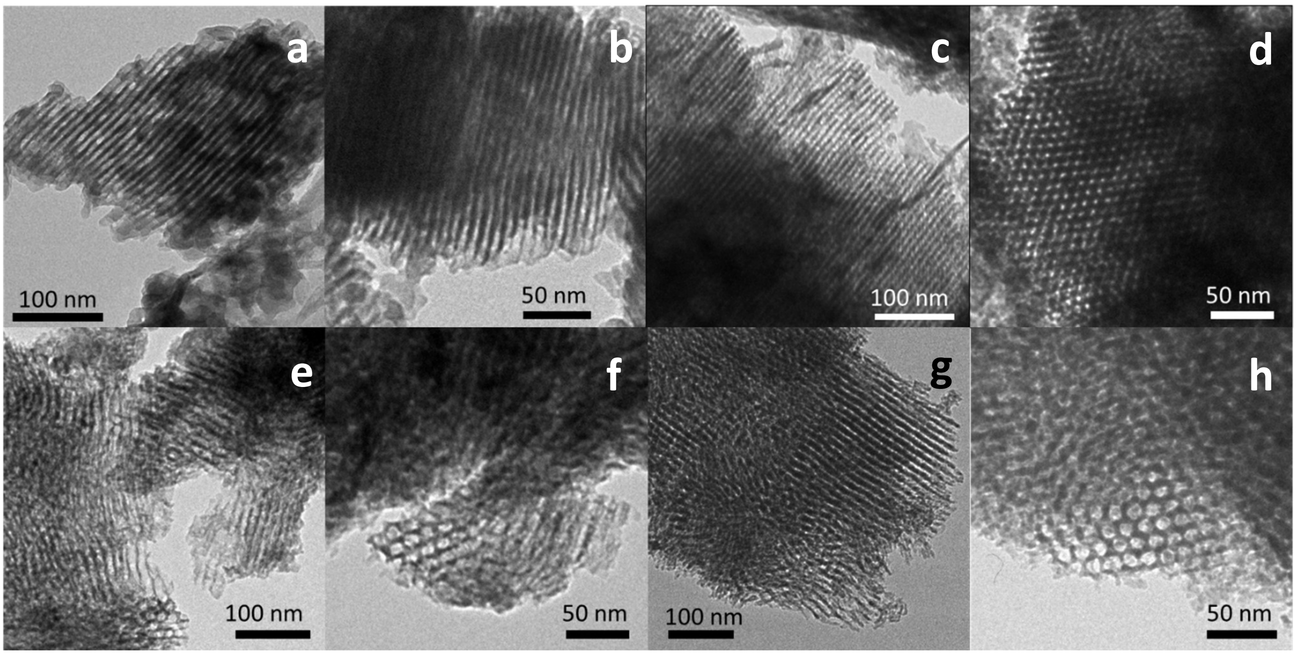

Figure 46 TEM images of Al_2O_3_P_400 (a,b), Al_2O_3_P_900 (c,d), Al_2O_3_F_400 (e,f), Al_2O_3_F_900 (g,h).

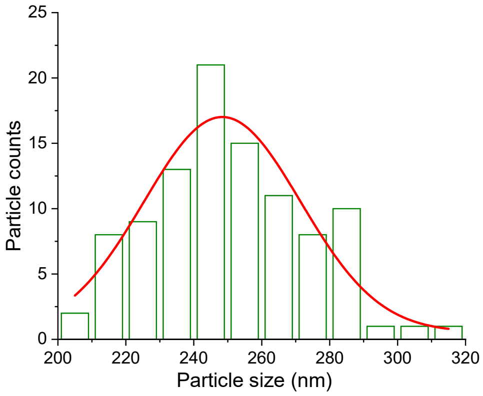

Figure 47 Particle size distribution of Al-MCM-41 obtained from transmission electron microscopy.

EDX chemical mapping (Figure 48), performed on the three aluminosilicate samples, revealed a homogeneous distribution of Si and Al atomic species throughout the samples. Semi-quantitative analysis performed by EDX points out a Si/Al ratio of 15±1 for all samples, confirming the theoretical ratio used in the synthesis processes.

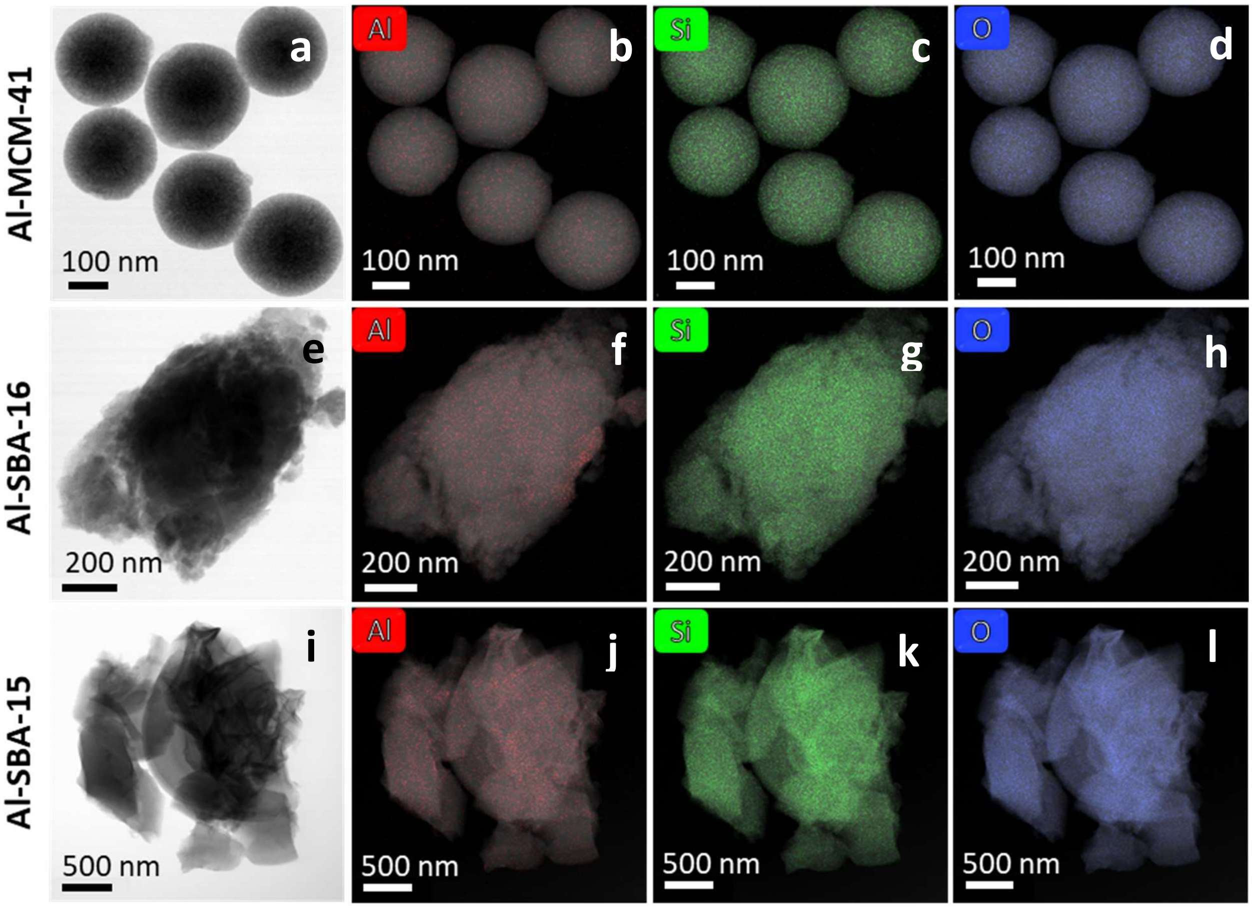

Figure 48 EDX chemical mapping of Al-MCM-41 (a-d), Al-SBA-16 (e-h), and Al-SBA-15 (i-l).

4.4 Study of the acidic properties

All the mesostructured systems presented in this chapter were subjected to characterization of the acid sites with FT-IR spectroscopy using pyridine as probe molecule (Py-FTIR). In the literature FTIR spectroscopy with a probe molecule is a widely used characterization technique that allows to assess the typology of the acid sites present in the investigated samples; however, quantification, despite being possible, is not always performed [202]. Furthermore, the few systematic works usually focus on the investigation of the same type of material (*e.g.* Al-SBA-15 [146], [164], [165], [202] or Al-MCM-41 [203]) with different Si/Al ratios or on the comparison of very different materials as amorphous *vs* crystalline aluminosilicates (zeolites) *vs.* γ-Al_2O_3 [165], [204], [205]. In agreement with what previously observed for Al-MCM-41 [73] in Chapter 3 and for Al-SBA-15 samples [164], [169], [202], all aluminosilicate samples show the presence of both Lewis and Brønsted acid sites (Figure 49a-c, Figure 50a-c).

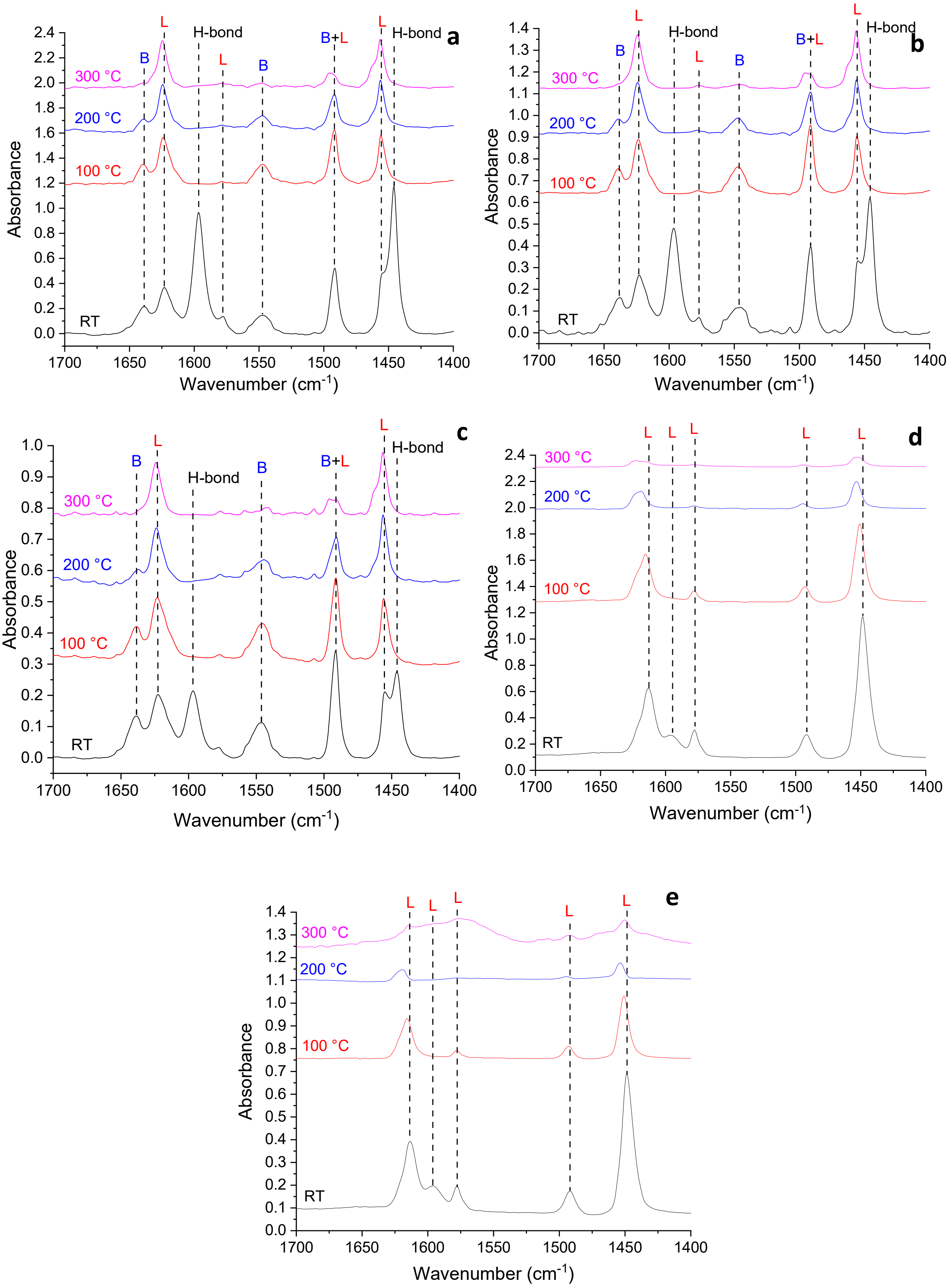

Figure 49 FTIR spectra of adsorbed pyridine for Al-MCM-41 (a), Al-SBA-15 (b), Al-SBA-16 (c), Al_2O_3_P_900 (d), and Al_2O_3_F_900 (e).

The RT spectra point out the presence of pyridine molecules physically adsorbed on silanol groups by H-bond, with their weak nature testified by their disappearance at 100 °C. A gradual decrease in the intensity of the signals related to both Lewis and Brønsted acid sites was observed by increasing the temperature from 25 to 300 °C (Figure 50a-c, Table 10, Table 11, Table 12), due to a progressive desorption of pyridine from both types of acid sites but prominent for Brønsted sites. Indeed, the Brønsted/Lewis ratio (Figure 50a-c, Figure 51a, Table 10, Table 11, Table 12) progressively decreases, clearly suggesting that Lewis sites are remarkably stronger than Brønsted ones, in agreement with previous studies on samples featuring only Lewis sites [14], [61]. The progressive decrease of Brønsted/Lewis ratio with an increase in temperature was also observed by Occelli *et al*. [203], who, however, found that not all investigated samples showed that trend, as it really depends on the synthesis method and the precursors used. An opposite trend of the Brønsted/Lewis sites ratio along with increasing temperature was instead observed by other authors for Al-SBA-15 [164]. In the present work, for all investigated temperatures, the value of Brønsted/Lewis ratio and the total amount of acid sites (Brønsted + Lewis) expressed in terms of μmol/m^2 increase in the order Al-SBA-16 > Al-SBA-15 > Al-MCM-41 (Figure 51a, Table 10, Table 11, Table 12). An inverse behavior is observed for the total amount of acid sites in terms of μmol/g at RT: Al-MCM-41 (210 μmol/g) > Al-SBA-15 (164 μmol/g) > Al-SBA-16 (143 μmol/g). However, this trend is almost exclusively ascribed to the decrease in the number of Lewis sites (from 108 μmol/g for Al-MCM-41 to 72 μmol/g for Al-SBA-15 and 55 μmol/g for Al-SBA-16), being the amount of Brønsted sites almost constant (94 ± 7 μmol/g). This fact suggests that, for the same Si/Al ratio, the remarkable differences in the textural properties mainly affect the amount of Lewis sites. This trend was also observed at 100 °C, temperature at which the presence of physisorbed pyridine is excluded. At 100 °C, the amount of Brønsted sites was almost constant (84 ± 7 μmol/g) among the three aluminosilicates while the number of Lewis sites decreases from 85 μmol/g (Al-MCM-41) to 53 μmol/g (Al-SBA-16). Even at higher temperatures, no remarkable differences in the amount of Brønsted sites were detected. To conclude, these data highlighted that Brønsted sites of similar strength are present on the different samples. With regards to the γ-Al_2O_3 samples, FTIR spectra only show bands ascribable to Lewis acid sites (Figure 49d), in agreement with previous findings [206]–[208]. The use of the Pluronic P123 instead of the F127 one led to a significantly higher amount of acidic sites (Al_2O_3_P_900 *vs*. Al_2O_3_F_900). Interestingly, in this case, an increase in the desorption temperature from 25 to 300 °C caused a progressive shift from 1448 cm^{-1} to 1453 cm^{-1}. This fact can be attributed to the desorption of pyridine from either weak Lewis sites or surface hydroxyl groups. Analogous shift is also observable for the Lewis band located at 1613 cm^{-1} at RT, associated with the disappearance of the band at 1596 cm^{-1}, that different authors attributed either to H-bonded pyridine [209] or weak Lewis sites [207]. With this in mind, we can presumably conclude that the amount of Lewis sites at RT is overestimated. Moreover, from the quantitative analysis, it can be pointed out that the Lewis sites present on γ-Al_2O_3, indeed, show a much more remarkable decrease of their number with the increase in temperature (Figure 50d, Table 13, Table 14) than that shown by aluminosilicates, suggesting that the Lewis sites on γ-Al_2O_3 are much weaker than those of the aluminosilicates, in agreement with the literature [165].

Table 10 FTIR results of adsorbed pyridine for Al-MCM-41.

Al-MCM-41	Brønsted sites (μmol/g)	Lewis sites (μmol/g)	Total sites (μmol/g)	Total sites (μmol/m^2)	Brønsted/Lewis
RT	102	108	210	0.166	0.94
100 °C	91	85	176	0.139	1.07
200 °C	53	79	132	0.105	0.67
300 °C	13	73	86	0.068	0.18

Table 11 FTIR results of adsorbed pyridine for Al-SBA-15.

Al-SBA-15	Brønsted sites (μmol/g)	Lewis sites (μmol/g)	Total sites (μmol/g)	Total sites (μmol/m^2)	Brønsted/Lewis
RT	92	72	164	0.244	1.28
100 °C	77	66	143	0.212	1.17
200 °C	38	55	93	0.138	0.69
300 °C	11	48	59	0.088	0.23

Table 12 FTIR results of adsorbed pyridine for Al-SBA-16.

Al-SBA-16	Brønsted sites (μmol/g)	Lewis sites (μmol/g)	Total sites (μmol/g)	Total sites (μmol/m^2)	Brønsted/Lewis
RT	88	55	143	0.327	1.60
100 °C	83	53	136	0.311	1.57
200 °C	42	52	94	0.215	0.81
300 °C	12	45	57	0.130	0.27

Table 13 FTIR results of adsorbed pyridine for Al_2O_3*_P_900.*

Al_2O_3_P_900	Brønsted sites (µmol/g)	Lewis sites (µmol/g)	Total sites (µmol/g)	Total sites (µmol/m^2)	Brønsted/Lewis
RT	-	359	359	1.822	-
100 °C	-	171	171	0.868	-
200 °C	-	56	56	0.284	-
300 °C	-	28	28	0.142	-

Table 14 FTIR results of adsorbed pyridine for Al_2O_3_F_900.

Al_2O_3_F_900	Brønsted sites (µmol/g)	Lewis sites (µmol/g)	Total sites (µmol/g)	Total sites (µmol/m^2)	Brønsted/Lewis
RT	-	197	197	1.015	-
100 °C	-	72	72	0.371	-
200 °C	-	15	15	0.077	-
300 °C	-	-	-	-	-

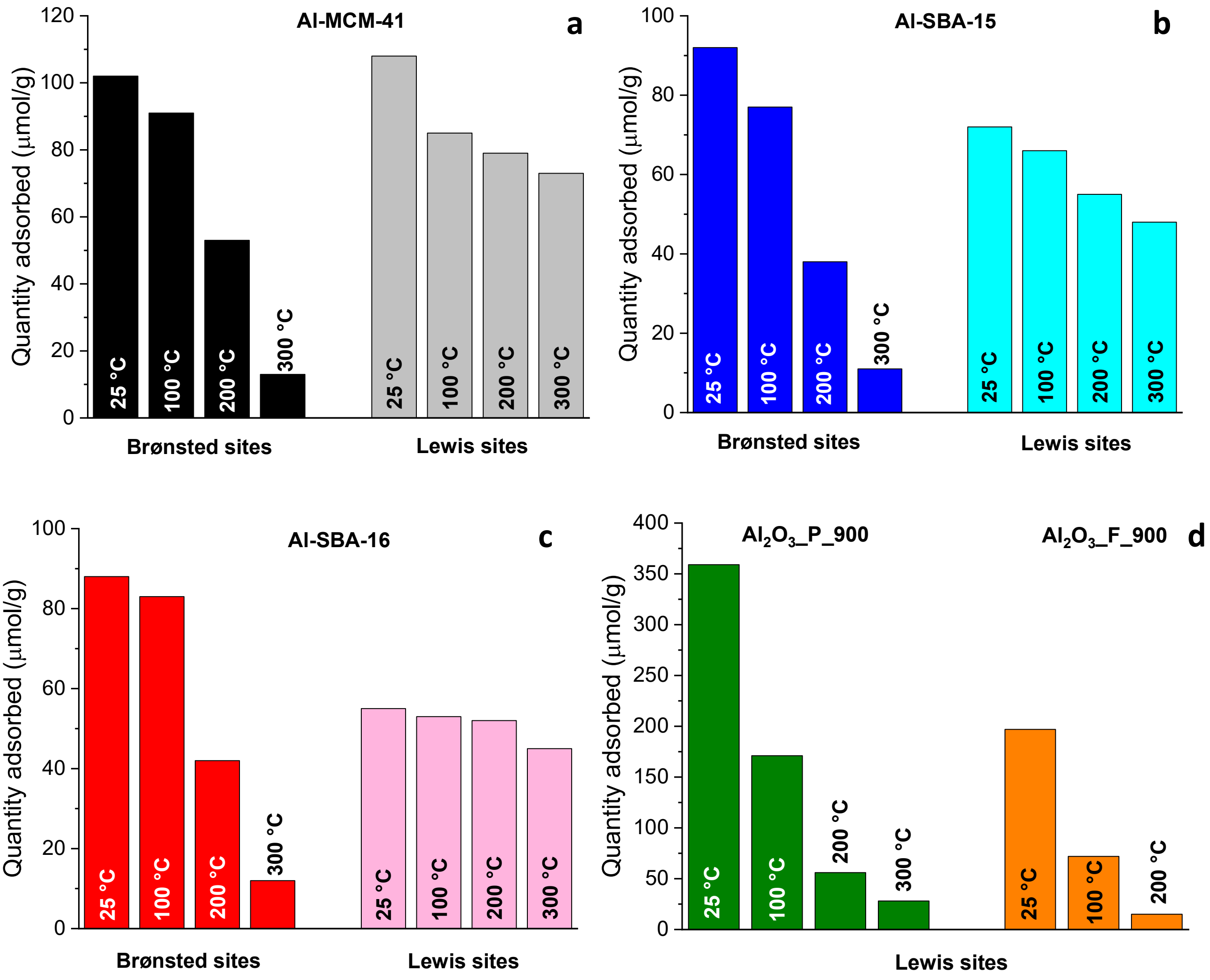

Figure 50 Amount of Brønsted and Lewis acid sites determined with Py-FTIR on Al-MCM-41 (a), Al-SBA-15 (b), Al-SBA-16 (c). Amount of Lewis acid sites determined with Py-FTIR on Al_2O_3_P_900 and Al_2O_3_F_900 (d).

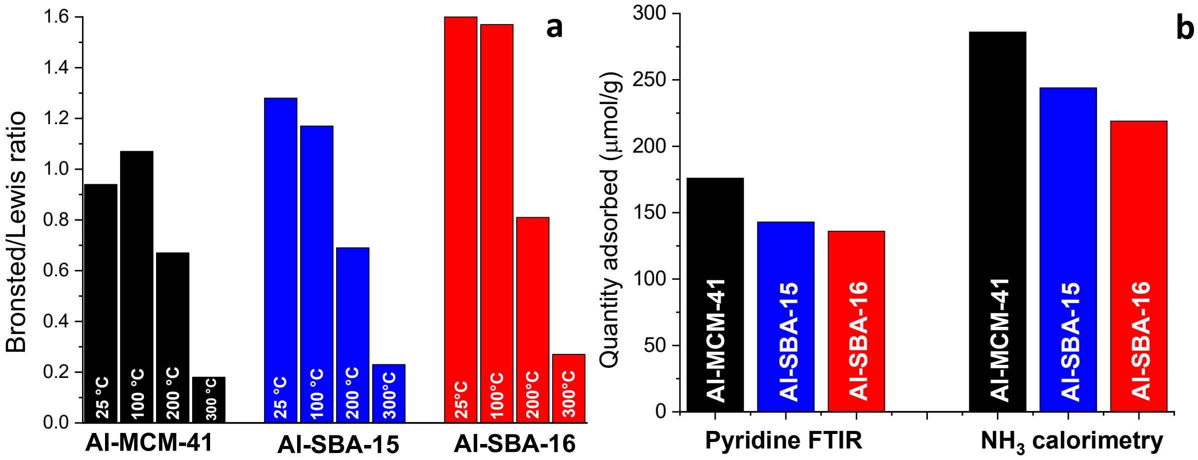

Figure 51 Brønsted/Lewis ratio determined on aluminosilicate samples with Py-FTIR at different temperatures (a). Comparison between the amount of total acid sites determined at 100 °C on aluminosilicate samples with Py-FTIR and the amount of irreversible acid sites determined with NH_3 adsorption calorimetry (b).

The acidic properties were also investigated by ammonia-adsorption microcalorimetry (Figure 52, Figure 53, Figure 54, Table 15), a technique widely reported for acidic samples such as aluminosilicates and γ-Al_2O_3 [144], [210]–[212]. Similar amounts of acid sites on all aluminosilicates, namely 420, 446, and 422 µmol/g were obtained for Al-MCM-41, Al-SBA-15, and Al-SBA-16, respectively, reasonably due to the selection of the same Si/Al ratio (=15). Interestingly, the amount of acid sites on which NH_3 is irreversibly adsorbed at 80 °C shows the same trend (Al-MCM-41 > Al-SBA-15 > Al-SBA-16, see Figure 52a) observed for the total amount of acid sites (Brønsted + Lewis) determined by FTIR-monitored pyridine adsorption at 100 °C. The higher amount of irreversible acid sites on Al-MCM-41 and Al-SBA-15 can be ascribed to a higher number of Lewis sites, since they appeared to be stronger than Brønsted sites by FTIR measurements. Al-MCM-41 and Al-SBA-16 showed the highest and the lowest percentage or irreversible acid sites (68% and 52%, Table 15), respectively. Noteworthy, the quantitative data obtained on the acid sites by the two different techniques are comparable (Figure 51b) despite the experimental differences in terms of basic strength and steric hindrance of the probe molecule (pyridine *vs.* NH_3) and the different temperature (100 °C *vs.* 80 °C). As expected, since the three aluminosilicates feature remarkably different surface area values, an opposite trend is shown by the surface density of total acid sites, *i.e.* the amount of acid sites expressed as $\mu mol/m^2$ (Figure 52b, Table 15), which decreases in the order Al-SBA-16 > Al-SBA-15 > Al-MCM-41. In particular, for Al-SBA-16 a significantly higher acid site surface density of 0.97 $\mu mol/m^2$ was obtained because of its relatively low surface area. On the other hand, Al-MCM-41 showed the lowest surface density of acid sites (0.33 $\mu mol/m^2$). As expected, the same trend is observed for the surface density of irreversible acid sites (Figure 52b, Table 15). Lower amounts of irreversible acid sites were found for the two γ-Al_2O_3 samples (Al_2O_3_P_900 and Al_2O_3_F_900), confirming the presence of much weaker Lewis acid sites compared to those of the aluminosilicate samples, as indicated by FTIR. Since the calorimetric measurements are carried out at 80 °C, we can deduce that, at this temperature, a large portion of acid sites is not strong enough for ammonia to be adsorbed on them. These samples exhibited very high initial Q_{diff} values (>> 150 kJ/mol, generally taken as the threshold for highly strong acid sites), indicating the presence of a small amount of very strong sites. However, a sharp and progressive Q_{diff} decrease with increasing ammonia uptake is then observed, indicating a more energetically heterogeneous surface, with respect to the aluminosilicates. In agreement with the Py-FTIR measurements, the results showed that the sample Al_2O_3_F_900 has slightly lower acidity than the Al_2O_3_P_900, in terms of numbers of total sites (n_{tot}) and sites responsible for an irreversible ammonia adsorption

(n_{irr}) (Table 15). The values of n_{tot} agree with those reported in previous works [213], [214]. Previous FTIR studies on the NH_3-adsorption microcalorimetry on alumina proved that only Lewis acid sites are present [165], [215]. This feature was confirmed by our pyridine-FTIR measurements and by several works reported in the literature [165], [204], [208]. Accordingly, it can be assumed that NH_3 is coordinatively adsorbed on unsaturated Al^{3+} cations (Lewis sites) also in the present case. Due to their low surface area, γ-Al_2O_3 samples show the highest surface density of total acid sites.

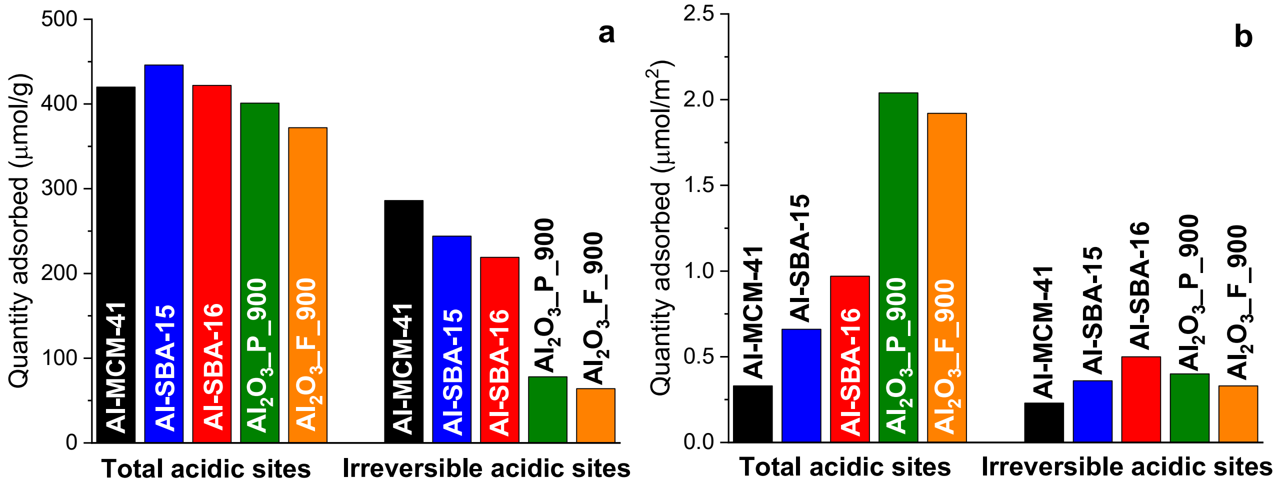

Figure 52 Amount of total and irreversible acid sites determined with NH_3-adsorption microcalorimetry for all samples in terms of µmol/g (a) and µmol/m² (b).

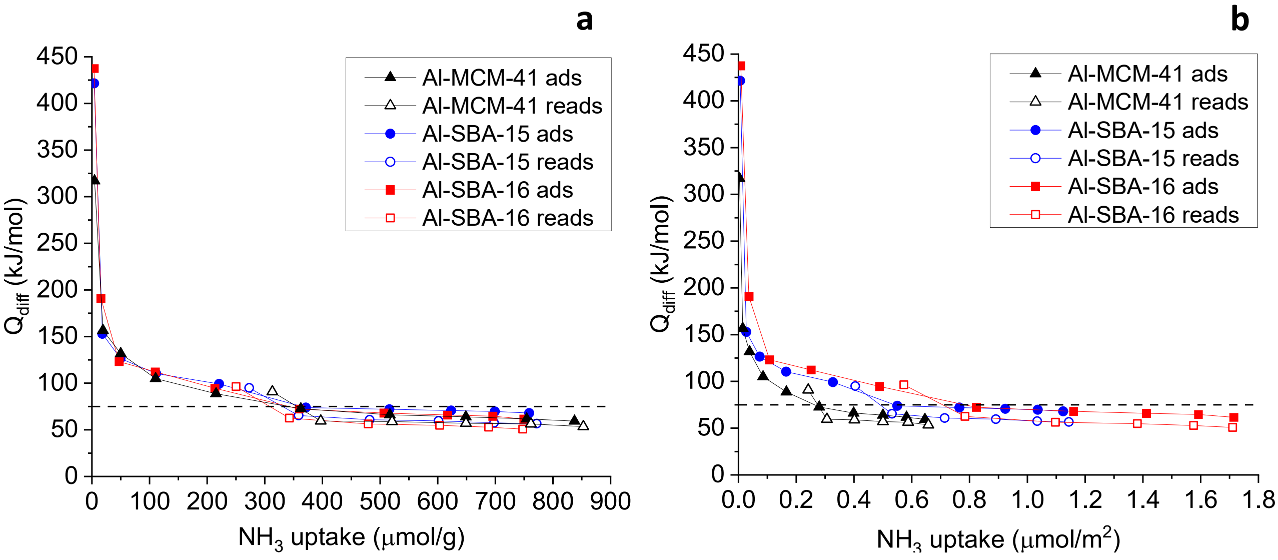

Figure 53 Differential heat (Q_{diff}) vs. uptake for ammonia adsorption expressed in µmol/g (a) and µmol/m² (b) for all samples. Open symbols refer to re-adsorption after overnight evacuation. Dash lines refers to the cut-off value between physisorption and chemisorption (75 kJ/mol).

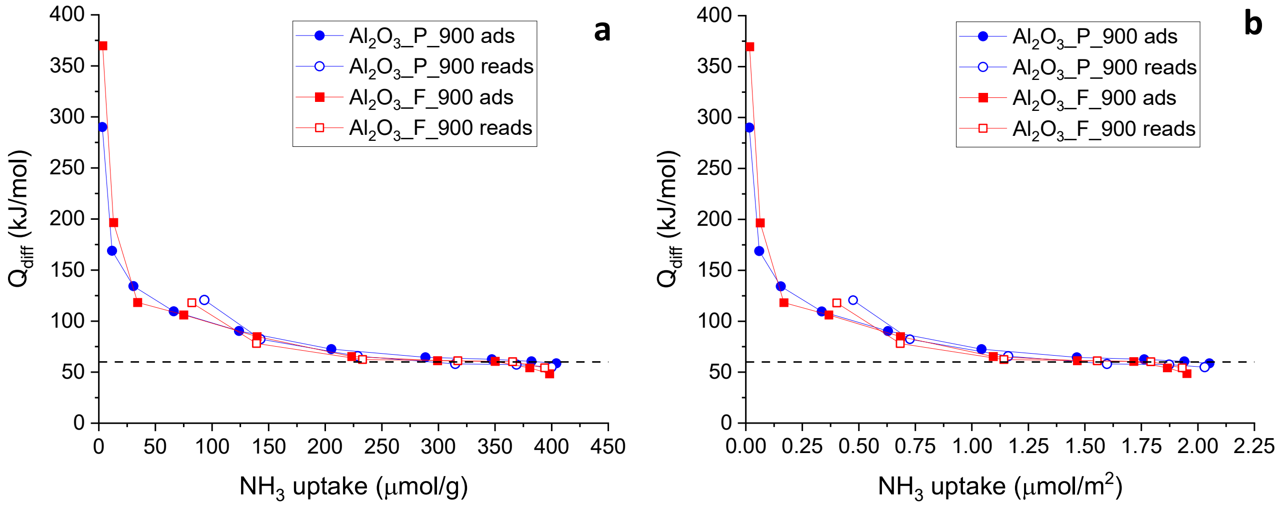

Figure 54 Differential heat (Q_{diff}) vs. uptake for ammonia adsorption expressed in μmol/g (a) and μmol/m^2 (b) for Al_2O_3_P_900 and Al_2O_3_F_900. Open symbols refer to re-adsorption after overnight evacuation. Dash lines refers to the cut-off value between physisorption and chemisorption (60 kJ/mol).

Table 15 Ammonia adsorption microcalorimetric results for all samples.

Sample	$n_{A,tot}$ (μmol/g)	$n_{A,irr}$ (μmol/g)	% $n_{A,irr}$	$n_{A,tot}$ (μmol/m^2)	$n_{A,irr}$ (μmol/m^2)	BET surface area (m^2/g)
Al-MCM-41	420	286	68%	0.333	0.227	1262
Al-SBA-15	446	244	55%	0.663	0.363	673
Al-SBA-16	422	219	52%	0.966	0.501	437
Al_2O_3_P_900	401	78	20%	2.04	0.40	197
Al_2O_3_F_900	372	64	17%	1.92	0.33	194

4.5 Study of the catalytic performances

The results of the catalytic tests for methanol dehydration in the CO_2-to-DME process for all the acid catalysts in the form of physical mixtures with a commercial $CuO/ZnO/Al_2O_3$-based redox catalyst (CZA) are depicted in Figure 55 and Figure 56. The catalytic tests were performed using 0.2 g of dehydration catalyst mixed with 0.05 g of CZA and 3.2 g of α-Al_2O_3, an inert material, to reach a total bed volume of ≈3 cm^3. The gas hourly space velocity (GHSV) was 48000 Ncm^3 g_{cat}^{-1} h^{-1}. Physical mixtures were reduced inside the reactor in a stream of a H_2/N_2 mixture (H_2, 15 vol% in N_2) at 250 °C for 2 h under atmospheric pressure. The reaction was carried out at 250 °C, 3.0 MPa with a H_2 and CO_2 (molar ratio of 3:1) mixture for 36 h.

The catalysts show comparable CO_2 conversion values (5.1 ± 0.2%), as a consequence of the use of the same redox catalyst, which is the main responsible for the production of methanol by hydrogenation reaction of CO_2, catalyzed by Cu. A first important difference is observed for the CO selectivity, an undesired by-product deriving from the RWGS reaction. Indeed, Al-SBA-16 can be considered the best methanol dehydration catalyst, since it shows a significantly lower CO selectivity (38.7%) with respect to the other catalysts (42.6-45.2%) and the highest value of DME selectivity (26.6% *vs.* <12%). Consequently, it also shows the lowest value of selectivity to methanol (34.7%). The worst performances are shown by γ-Al_2O_3, featuring a DME selectivity of about 2% associated by the highest methanol and CO selectivity values (45.2% and 53.1% for Al_2O_3_P_900, 46.1% and 51.8% for Al_2O_3_F_900, respectively).

The comparison between the catalytic performances and the acidic properties highlights the absence of correlation between the dehydration activity (Al-SBA-16 >> Al-SBA-15 ≈ Al-MCM-41 >> γ-Al_2O_3) and the total amount of sites (sites with $Q_{diff} \geq 75$ kJ mol^{-1}) determined with NH_3-microcalorimetry (Figure 52, Table 15). Furthermore, although the total number of acid sites determined by Py-FTIR at 100°C (temperature at which the contribution of physisorbed pyridine can be excluded) increases in the order γ-Al_2O_3 ≈ Al-MCM-41 > Al-SBA-15 > Al-SBA-16, the DME selectivity shows an opposite trend (Figure 50, Figure 55). In the literature [73], it was demonstrated that the dehydration activity is related to the amount and strength of Brønsted acid sites, being the Lewis sites strongly affected by deactivation due to water adsorption. Accordingly, the lower activity of Lewis sites is presumably the reason behind the worse performances of γ-Al_2O_3, as evidenced by Py-FTIR measurements, indicating the exclusive presence of Lewis sites (Figure 49d-e, Figure 50d). On the contrary, the dehydration activity of aluminosilicates was not directly justified based on the amount of Brønsted sites, being similar in the three samples at all temperatures, presumably due to the same Si/Al ratio.

The obtained DME selectivity values could instead be associated with the surface density of acid sites. Indeed, the methanol dehydration involves two molecules of methanol, and the acid sites proximity might promote the reaction, allowing faster kinetics. Particularly, the two mechanisms for methanol dehydration described in Chapter 1 cannot be considered to justify this finding, since they involve either a single acid site or an acid site with an adjacent oxygen site. However, it is important to point out that a variant of the L-H model hypothesized for zeolites has been proposed for sulfonic ion exchange resins, featuring Brønsted sites [27], [216], [217]. This mechanism, involving the adsorption of two different methanol molecules on two adjacent Brønsted acid sites, could be also proposed in our case, justifying the increase of methanol dehydration performances due to the proximity of Brønsted sites. However, to hypothesize a different mechanism involving two Brønsted acid sites, further studies and a careful characterization would be required, also considering the lack of agreement in the literature about the mechanism of methanol dehydration on aluminosilicate systems. Taking into account our assumption on the proximity of the acid sites, being Al-SBA-16 the aluminosilicate with the lowest surface area and the best activity, we can conclude that a surface area maximization is detrimental. The data determined from Py-FTIR at 100 °C and NH_3-microcalorimetry, reported in Table 16, point out that the Al-SBA-16 is the sample with the highest Brønsted acid sites surface density (0.19 μmol/m^2 *vs.* 0.11 μmol/m^2 for Al-SBA-15 and 0.07 μmol/m^2 for Al-MCM-41), and the highest surface density of the sites on which ammonia is irreversibly adsorbed (0.501 μmol/m^2 vs. 0.363 μmol/m^2 for Al-SBA-15 and 0.227 μmol/m^2 for Al-MCM-41). The trend for Brønsted acid sites is also confirmed at higher temperatures (Table 10-Table 14). Accordingly, Al-SBA-16 has the highest surface density of its Brønsted acid sites, and therefore acts as the best methanol dehydration catalyst.

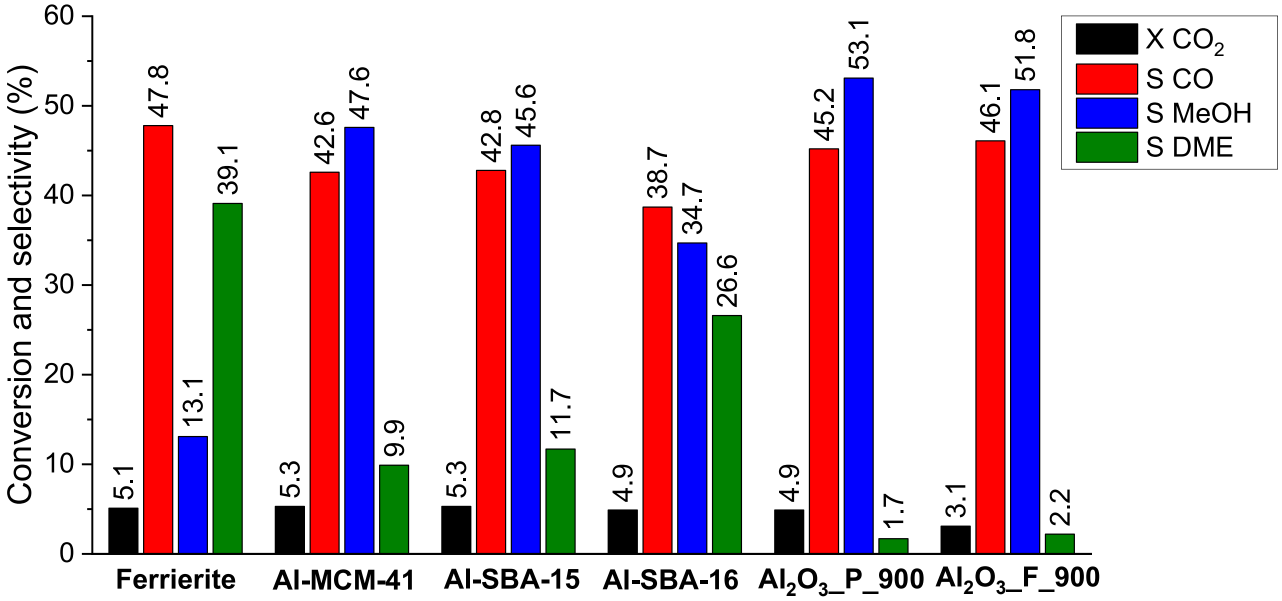

Figure 55 Mean values of CO_2 conversion and selectivity to CO, methanol, and DME for catalytic tests on CZA-dehydration catalyst physical mixtures.

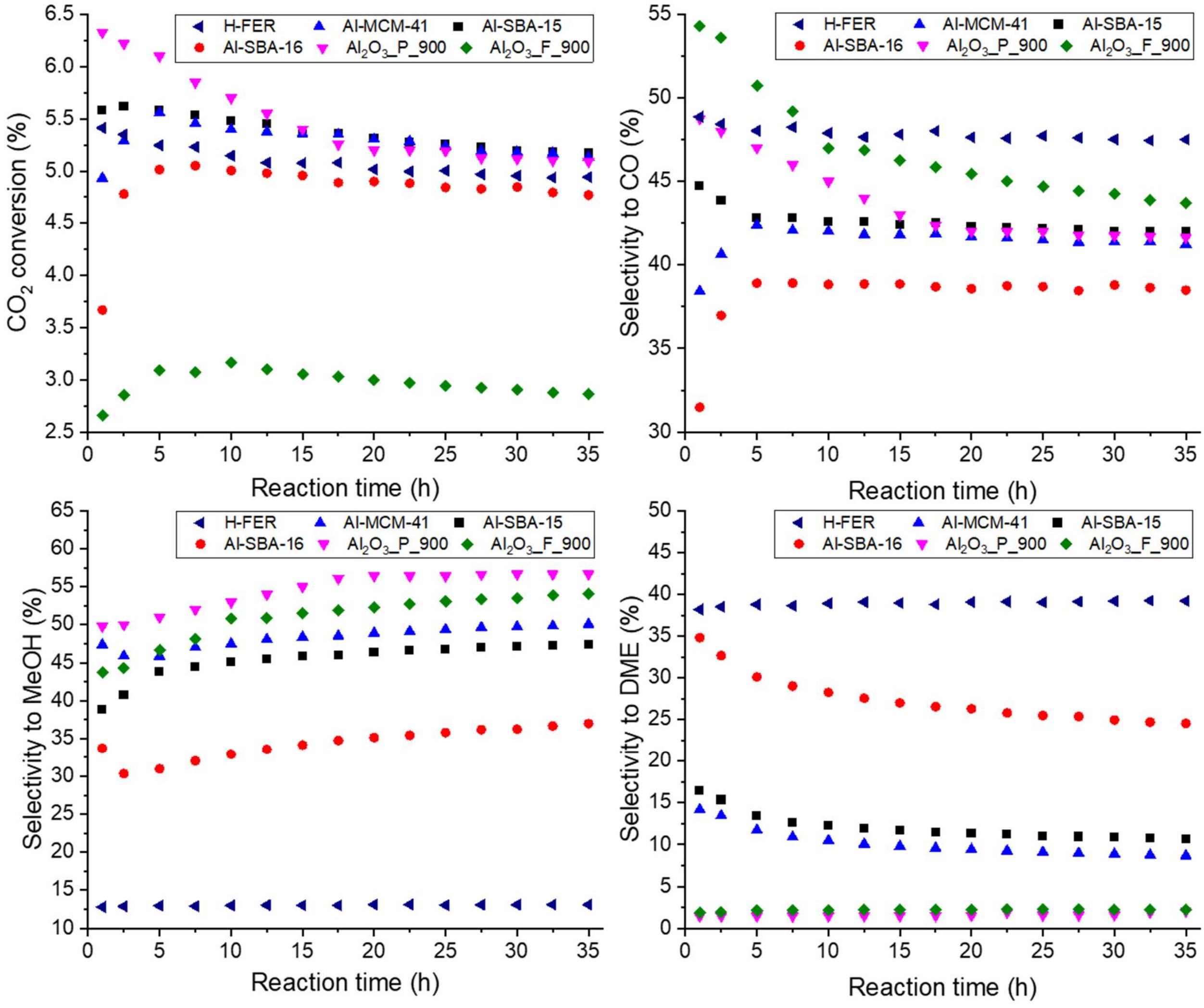

Figure 56 Values over time of CO_2 conversion and selectivity to CO, methanol, and DME for catalytic tests on CZA-dehydration catalyst physical mixtures.

Table 16 Correlation of the acidic features of the samples with the catalytic performances.

Sample	**Py-FTIR** **tot. sites at 100 °C (μmol/m^2)**	**Py-FTIR** **Brønst. sites at 100 °C (μmol/m^2)**	**NH_3-Cal** **Vtot (μmol/m^2)**	**NH_3-Cal** **Virr (μmol/m^2)**	**S_{DME} (mol%)**
Al-MCM-41	0.139	0.072	0.333	0.227	9.9
Al-SBA-15	0.212	0.114	0.663	0.363	11.7
Al-SBA-16	0.311	0.190	0.966	0.501	26.6
Al_2O_3_P_900	0.868	-	2.04	0.40	1.7
Al_2O_3_F_900	0.371	-	1.92	0.33	2.2

In order to gather information about possible differences between the used and fresh catalytic mixtures, WA-XRD, Thermo-Gravimetric Analysis (TGA) and FTIR analysis were carried out on all spent catalytic mixtures, as well as nitrogen physisorption on both the fresh and the spent physical mixture of Al-SBA-16 (i.e. 0.05 g CZA + 0.2 g Al-SBA-16 + 3.2 g α-Al_2O_3).

The characterization of the used physical mixtures is affected by the fact that the main component of the mixture is the inert material (α-Al_2O_3), accounting for 92.8% of the total weight of the physical mixture, while only 7.2% of its weight consists of the actual catalyst (1.4% CZA + 5.8% dehydration catalyst). Furthermore, due to the fine mixing of the three materials, it is not possible to separate the actual catalysts from the inert material. This problem is particularly relevant for XRD; in the first case, indeed, α-Al_2O_3 not only is, by far, the most abundant phase, but also present much sharper and intense diffraction peaks than CZA. Regarding dehydration catalysts, aluminosilicates do not present diffraction peaks, being they amorphous materials, and γ-Al_2O_3, being it a nanocrystalline material, features much less sharp peaks than α-Al_2O_3. For these reasons, the XRD patterns of the spent mixtures (not reported) only show the signals attributable to α-Al_2O_3, giving no information about the catalyst itself. A similar issue affects TG analysis (not reported); in this case a weight loss of only about 1-1.5% is observed for all samples, with a gradual decrease which does not give any information about any thermal decomposition or crystalline transition. This finding is due to the inertness of α-Al_2O_3 in the investigated temperature range (25-900 °C), and, again, to the fact that it is the main component of the mixture. FTIR characterization (Figure 57) on spent mixtures, as expected, shows a main contribution located at wavenumber values lower than 870 cm^{-1}, attributed to the Al-O stretching of α-Al_2O_3, the main component of the mixture, indicated by the black arrows. All spent mixtures (except for CZA+Al_2O_3_P_Used and CZA+Al_2O_3_F_Used) also show a contribution attributed to the aluminosilicate (900-1300 cm^{-1}, red arrows), as clearly evincible from the comparison with the FTIR spectra of the aluminosilicates, added as references. The bands attributed to aluminosilicates in the spent mixtures do not show any significant difference with those present in the spectra of the aluminosilicates, suggesting that the dehydration catalysts are not affected by the reaction process. The spectra of the γ-Al_2O_3 samples (Al_2O_3_P_900 and Al_2O_3_F_900) do not show any significant difference with that of α-Al_2O_3; consequently, the spent mixtures CZA+Al_2O_3_P_Used and CZA+Al_2O_3_F_Used present spectra similar to those of Al_2O_3_P_900 and Al_2O_3_F_900. The signals attributed to CZA (1260-1600 cm^{-1}) are not visible in the spectra of the spent mixtures, reasonably due to the low amount of CZA in the mixtures (1.4%).

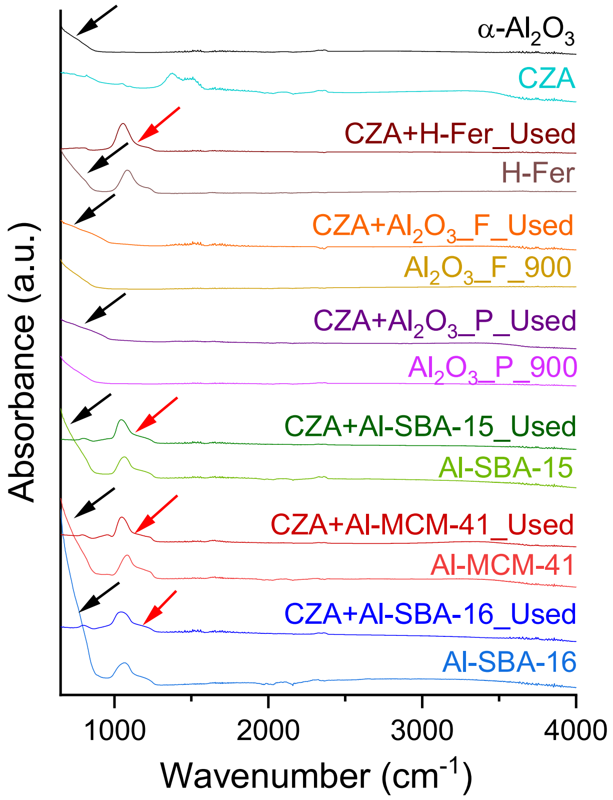

Figure 57 FTIR characterization on the physical mixtures after the reaction and on their corresponding components.

Nitrogen physisorption measurements were carried out on the spent and fresh mixtures based on CZA and Al-SBA-16, in order to assess any difference in terms of textural properties due to the reaction process. The physisorption isotherms and the pore size distribution curves are reported in Figure 58, the results for CZA have been reported in separate graphs (Figure 59) due to significant differences in terms of scale; the textural properties (i.e. BET surface area and pore volume) are reported in Table 17. As can be seen by the comparison of the textural properties of the fresh and the spent mixture, no significant differences can be seen before and after the reaction; particularly, the values of pore volume are identical, and the values of surface area are within the 3% experimental error associated with the measurement. The values of surface area and pore volume are significantly lower than those showed by CZA and Al-SBA-16 due to the presence of α-Al_2O_3, which is the main component of the mixture and features extremely low values of surface area and pore volume. The presence of Al-SBA-16 in the mixtures, however, is still visible from the presence of a capillary condensation branch, with an associated hysteresis cycle.

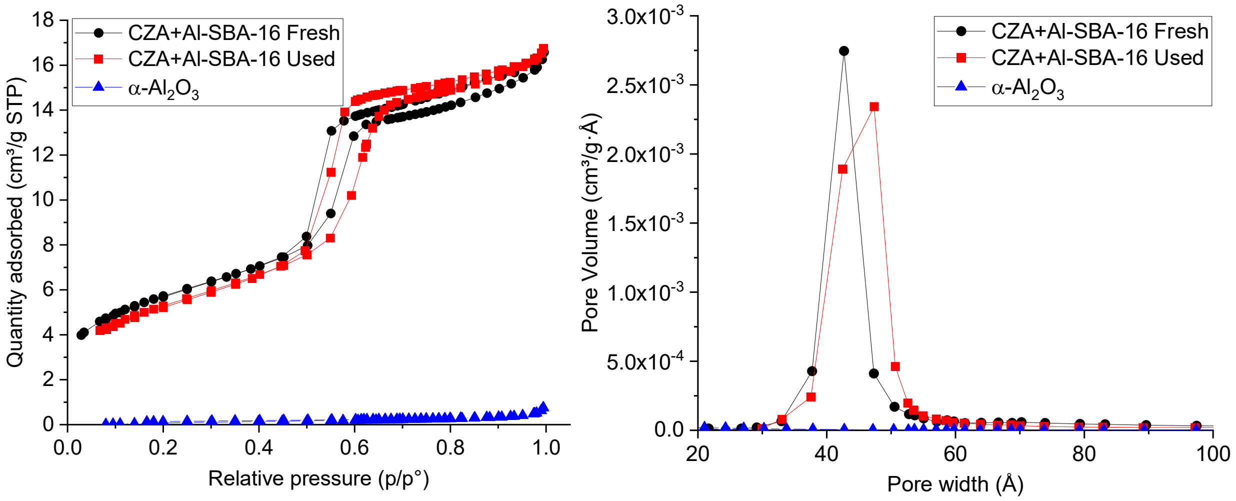

Figure 58 Nitrogen physisorption isotherms (a) and BJH pore size distribution (b) of the fresh and used Al-SBA-16-based physical mixtures (i.e. 0.05 g CZA + 0.2 g Al-SBA-16 + 3.2 g α-Al_2O_3) and of α-Al_2O_3.

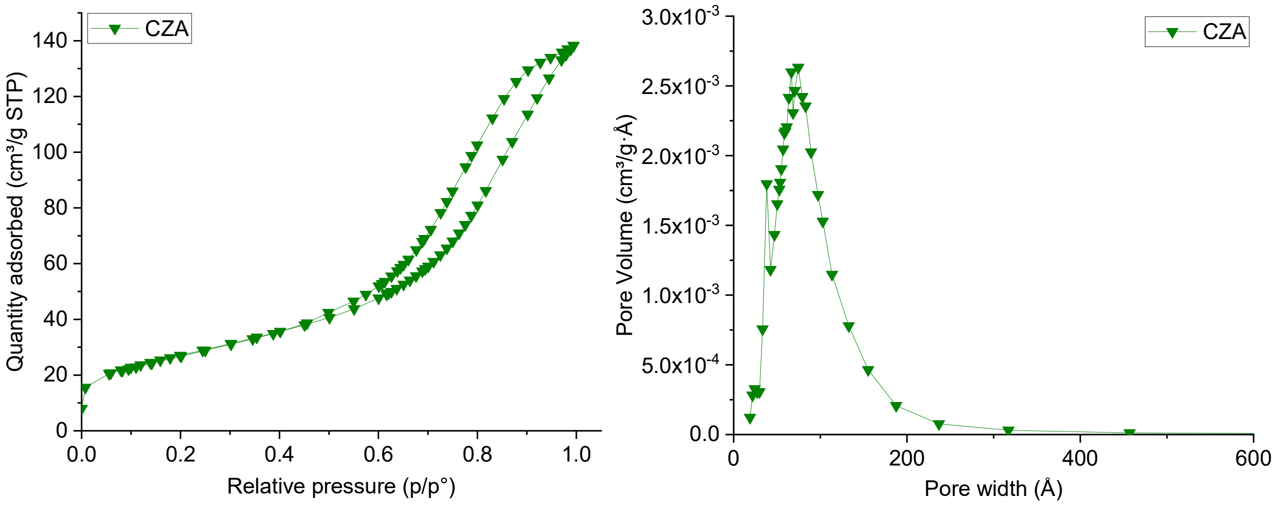

Figure 59 Nitrogen physisorption isotherms (a) and BJH pore size distribution (b) of CZA.

Table 17 BET surface area (SA) and pore volume (V_p) of the fresh and used Al-SBA-16-based physical mixtures (i.e. 0.05 g CZA + 0.2 g Al-SBA-16 + 3.2 g α-Al_2O_3), Al-SBA-16, α-Al_2O_3 and CZA.

Sample	BET surface area (m^2/g)	Pore volume (cm^3/g)
CZA+Al-SBA-16_Fresh	19.8	0.026
CZA+Al-SBA-16_Used	18.6	0.026
CZA	97.7	0.214
Al-SBA-16	437	0.52
α-Al_2O_3	0.5	0.001

On the basis of the characterization performed, mainly nitrogen physisorption and FTIR, can be inferred that the catalytic physical mixtures do not undergo any significant textural and/or structural transformation during the reaction process.

4.6 Conclusions

In this chapter three mesostructured aluminosilicates, featuring different textural properties but the same Si/Al ratio (= 15), were synthesized, characterized, and tested for the CO_2-to-DME one-pot process in form of physical mixture with a commercial redox catalyst (CZA), and compared with two γ-Al_2O_3 samples, with the aim of correlating their textural and acidic properties (amount, strength and typology of the acid sites) with their catalytic performances for methanol dehydration to dimethyl ether. To sum up, the following conclusions can be stated:

(i) Catalysts bearing Brønsted sites (*i.e.* the aluminosilicates, S_{DME} = 9.9 – 26.6%), as expected, show better performances than those with Lewis sites (*i.e.* γ-Al_2O_3, S_{DME} = 1.7-2.2%). On the same sample, Py-FTIR also pointed out how Lewis sites have an overall higher strength than Brønsted sites, with consequently a higher water resistance of the latter ones.

(ii) Surface density of acid sites is the key feature on which the synthesis should act to improve the methanol dehydration performances. The three aluminosilicates, despite providing similar amounts of Brønsted sites, show significantly different catalytic performances (S_{DME} = 9.9 – 26.6%), with the Al-SBA-16 found to be the best methanol dehydration catalyst (S_{DME} = 26.6%), thanks to the highest surface density of acid sites.

Chapter 5
Development of mesostructured composites as bifunctional catalysts for the one-pot CO_2-to-DME process

5.1 Introduction

This chapter is focused on the development of composite bifunctional catalysts (chemical mixtures) for the one-pot conversion of CO_2 to DME and on the comparison of their performances with those of physical mixtures. The focus has been put on mesostructured acid systems since the large size of mesopores should lead to an efficient impregnation of the dehydration catalysts, allowing the deposition of redox catalyst nanoparticles inside the pores, consequently maximizing the contact area. Furthermore, the impregnation inside the mesopores, should hamper growth phenomena of the redox phase particles, keeping their size in the nano-range. Impregnation on zeolites, conversely, would lead to a deposition of the redox phase only on the surface of the support, due to the small size of micropores, leading to a lower contact area and also not allowing the confinement of the redox phase particles inside the pores, putting no limit to their growth during the functionalization process of the support.

All the Al_2O_3- and aluminosilicate-based mesostructured acidic systems described in the previous chapter were used as supports for functionalization with a CuO-, CuO/ZnO- or CuO/ZnO/ZrO_2 (CZZ)-based redox phase. With the aim of obtaining composites with a homogeneous dispersion of the redox phase inside the mesochannels of the acidic catalysts supports, two different impregnation approaches were investigated. The first one consists of a two-solvent impregnation, while the second one is based on a proper combination of an impregnation strategy and a self-combustion process. Different parameters, such as loading, redox species and their molar ratio were explored.

The mesostructured nanocomposites presenting the most homogeneous dispersion of the redox phase and the best textural and morphological features were tested and compared with physical mixtures made up of the selected acidic support and a CuO/ZnO/ZrO_2-based redox phase (CZZ) prepared with the same synthetic strategy but in the absence of the support. Some of the results reported in this chapter have been published in [186].

5.2 Development of mesostructured composites on Al-MCM-41 and Al-SBA-16 using a two-solvent impregnation route

The first attempt to obtain bifunctional composite catalysts was performed using a two-solvent impregnation technique on Al-MCM-41 and Al-SBA-16. The two-solvent impregnation (see also Paragraph 2.4.1) consists in the initial dispersion of the pre-dried siliceous support into a non-polar solvent such as n-hexane, cyclohexane or n-pentane. An aqueous solution of the precursors is then added to the support dispersed into the non-polar solvent; to allow the complete incorporation of the precursors inside the pores, the volume of the solution is chosen to be equal to the pore volume of the support, assessed by nitrogen physisorption measurement. The subsequent evaporation of the non-polar solvent should favor the diffusion of the aqueous solution into the mesopores and the final composites were obtained by a proper thermal treatment. The two-solvent method was previously used to develop nanocomposites on MCM-41 and SBA-15, by impregnating them with a metal oxide phase [126]–[128] [131]. The choice of this particular impregnation method, rather than other more common routes, like the wet impregnation and the incipient wetness impregnation, comes from previous results on ZnO@SBA-15 composites, which showed a significantly improved dispersion of the metal oxides inside the mesochannels [126]. The better results obtained with this route have been ascribed to the presence of the non-polar solvent, which pushes the aqueous phase inside the pores against the siliceous pore walls, causing a rehydroxylation of the surface [125].

5.2.1 Synthesis of Al-MCM-41- and Al-SBA-16-based composites by two-solvent impregnation method

In a typical synthesis, the support (Al-MCM-41 or Al-SBA-16) was firstly dried in an oven at 120°C overnight in order to almost completely eliminate the adsorbed water; 0.25 g of material were then submerged in 20 mL of a non-polar solvent, namely hexane, into a covered beaker and kept under stirring at 450 RPM for 2 h; then an appropriate amount of a metal nitrate solution corresponding to the pore volume of the support was added drop-wise and the stirring was increased to 500 RPM. The concentration of the precursor solution was established keeping in mind that a volume of solution corresponding to the pore volume of the support must contain the amount of metal precursors necessary to obtain the desired final wt% loading. After 1.5 h the beaker was uncovered and the temperature was raised to 80°C, to allow the evaporation of the hexane; when almost all the solvent had evaporated, the beaker was put into an oven at 80°C overnight. Eventually, the obtained powder was calcined at 500°C for 2 h with a 2°C/min ramp.

5.2.2 Characterization of Al-MCM-41-based composites obtained by two-solvent impregnation

Five different Al-MCM-41-based composites with various loadings (10-20%) in terms of CuO and CuO/ZnO wt% were prepared following the procedure described in paragraph 4.2.1. as reported in Table 18. The 2/1 Cu/Zn ratio was chosen since ratios close to this value have been reported as the most promising ones for methanol synthesis catalysts [218], [219][220].

Table 18 Al-MCM-41-based composites synthesized by the two-solvent impregnation method.

Sample	Redox phase	Loading (wt%)	Cu/Zn molar ratio
Cu10@Al-MCM-41_TS	CuO	10%	-
Cu20@Al-MCM-41_TS	CuO	20%	-
CuZn10@Al-MCM-41_TS	CuO/ZnO	10%	2/1
CuZn15@Al-MCM-41_TS	CuO/ZnO	15%	2/1
CuZn20@Al-MCM-41_TS	CuO/ZnO	20%	2/1

Wide-angle XRD (WA-XRD) (Figure 60a) measurements point out, besides the amorphous band of Al-MCM-41, the presence of narrow and intense peaks for both the samples functionalized with Cu (Cu 10% and Cu 20%); indicating that CuO (tenorite; PDF card 00-045-0937) crystallized in form of particles much larger than the size of the mesopores (2-3 nm), necessarily located outside the mesoporous structure. On the other hand, CuZn 10% does not show any crystalline reflections, indicating that both metal oxides were dispersed onto the support in form of small nanoparticles, presumably inside the mesopores. CuZn 15% shows two weak peaks between 30° and 40°, where main peaks of CuO (002 and 111) are located, indicating that, with a 15% loading, at least a fraction of CuO starts to crystallize outside the pores. At a 20% loading (CuZn 20%) the peaks of tenorite are much more intense, and the other minor peaks are visible, pointing out the crystallization of a significant amount of CuO outside the mesoporous structure. In all cases, no signal attributed to ZnO are visible, suggesting the formation of an amorphous phase or a crystalline phase consisting of either very small nanoparticles or a very thin layer. This finding was previously observed on

ZnO@SBA-15 composites and ascribed to the high affinity of ZnO for the silica surface [127][126], as confirmed by XPS and ^{29}Si MAS NMR studies [127][221], that suggest the deposition of ZnO inside the pores as an amorphous thin layer. Other authors [220] observed a similar phenomenon on CuO/ZnO. Considering the XRD measurements on CuZn 15% and comparing them with the pattern of Cu 10%, since they have about the same amount of CuO it can be inferred that the homogeneous distribution of ZnO inside the pores also favors the dispersion of CuO in form of small nanoparticles. The deposition of ZnO inside the pores is also confirmed by small-angle XRD (SA-XRD) measurements (Figure 60b); a gradual decrease in intensity of the 100 mesostructure signal, associated with an increase in loading, is indeed observed for the samples impregnated with CuO/ZnO. This trend, on the other hand, in not observed for the samples only functionalized with CuO.

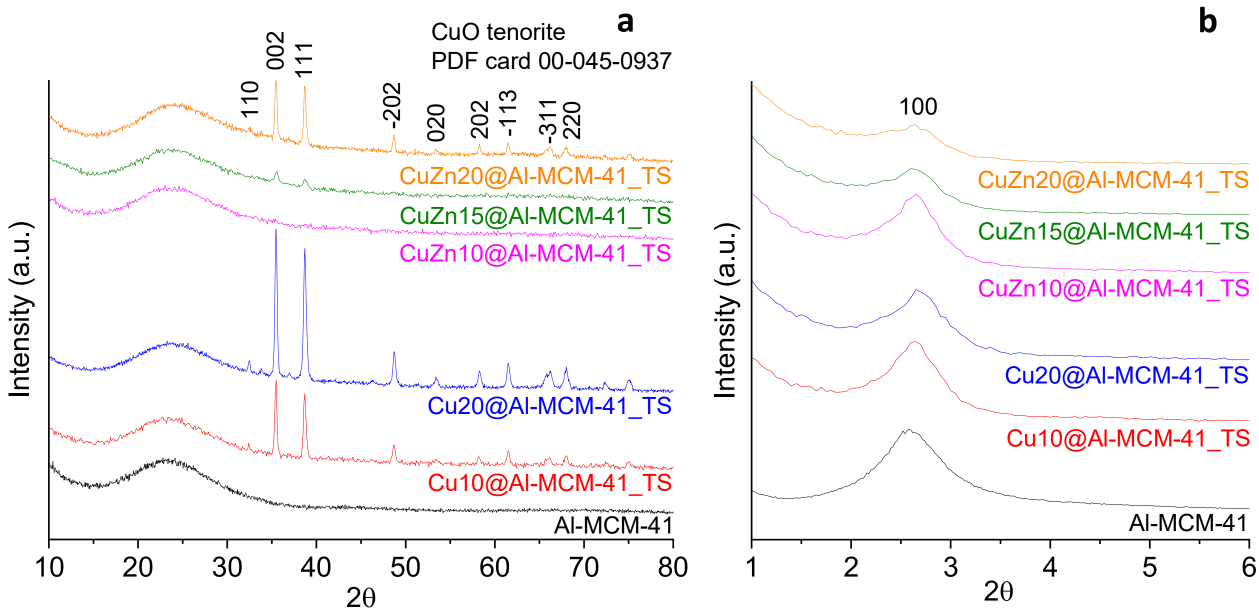

Figure 60 WA-XRD (a) and SA-XRD (b) patterns of Al-MCM-41-based composites synthesized by two-solvent method.

5.2.3 Characterization of Al-SBA-16-based composites obtained by two-solvent impregnation

The two-solvent impregnation process was subsequently used on Al-SBA-16, as it demonstrated to be the most promising mesostructured acidic system in terms of catalytic performances for the dehydration of methanol (Chapter 3). Four different Al-SBA-16-based composites with two loadings (10-15%) in terms of CuO and CuO/ZnO wt% were prepared following the procedure described in paragraph 4.2.1. as reported in Table 19. The 2/1 Cu/Zn ratio, as previously reported, was selected on the basis of the literature data [218], [219][220], while the loading was kept below 20% according to the previous results on Al-MCM-41 composites shown in Paragraph 4.2.2.

Table 19 Al-SBA-16-based composites synthesized by the two-solvent impregnation method.

Sample	**Redox phase**	**Loading (wt%)**	**Cu/Zn molar ratio**
Cu10@Al-SBA-16_TS	CuO	10%	-
Cu15@Al-SBA-16_TS	CuO	15%	-
CuZn10@Al-SBA-16_TS	CuO/ZnO	10%	2/1
CuZn15@Al-SBA-16_TS	CuO/ZnO	15%	2/1

As can be seen from Figure 61a, all wide-angle XRD patterns show the clear presence of sharp and intense diffraction peaks, attributable to CuO in its crystalline phase tenorite (PDF card: 00-045-0937), with increasing intensity by increasing the loading. The presence of narrow peaks suggests that the redox phase (CuO, CuO/ZnO) is partially or completely deposited onto the surface of the mesoporous support, even at the lowest loading (10%). All small-angle XRD patterns (Figure 61b) show the clear presence of a 110 main peak, together with a 200 peak, indicating that the mesoporous order was maintained after the functionalization process; no differences with the loading are observed, confirming that most of the redox phase crystallized outside the pores. The different behavior with respect to Al-MCM-41-based systems, clearly evincible from the comparison between the two composites with a 10% CuO/ZnO loading (CuZn10@Al-MCM-41 vs. CuZn10@Al-SBA-16), can be ascribed to the lower surface area and pore volume of Al-SBA-16 (Table 9).

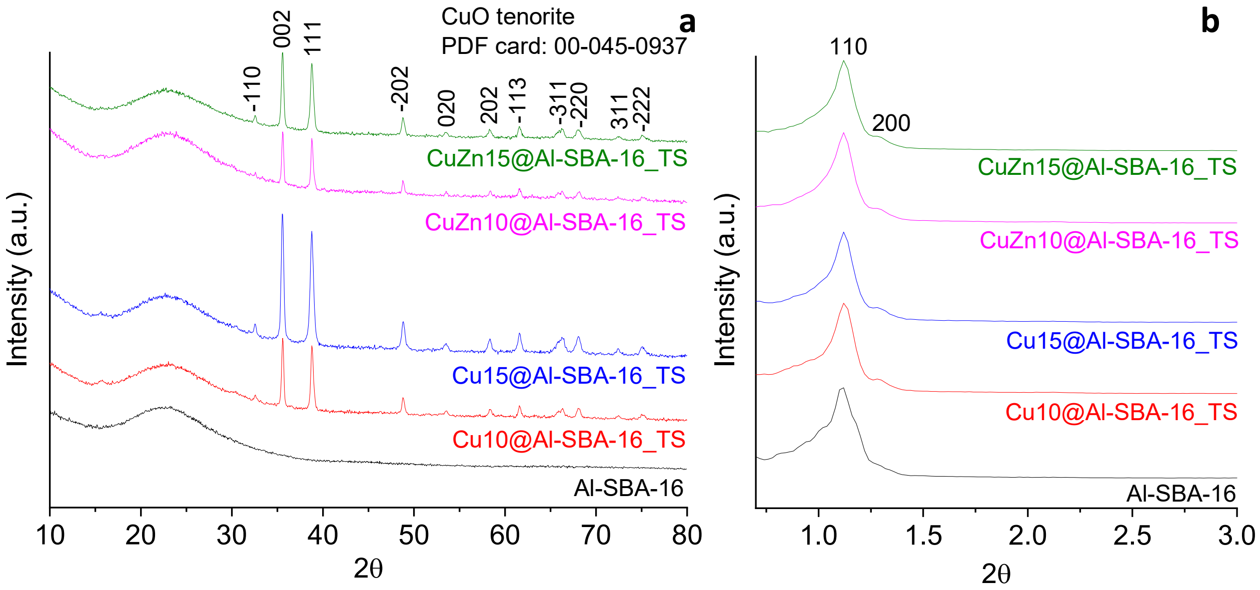

Figure 61 WA-XRD (a) and SA-XRD (b) patterns of Al-SBA-16-based composites synthesized by two-solvent method.

TEM analysis confirms the findings gathered from XRD data about the presence of particles of redox phase outside the mesoporous aluminosilicate matrix. As an example we report, in a panel related to CuZn15@Al-SBA-16_TS (Figure 62), two bright-field images showing the presence of large dark particles near the mesostructured support (black arrows); the high contrast given by these particles suggests a different phase contrast, and consequently a different (namely more dense) chemical composition. EDX chemical mapping confirmed that these particles are composed of CuO and ZnO; CuO is completely absent in the mesostructured aluminosilicate matrix, whether a small amount of ZnO has been detected, indicating that ZnO has a greater affinity than CuO for the support. The interplanar distance determined for CuO particles from HR-TEM images shows a value of 2.50 Å, very close to the value associated to the [002] crystal planes (2.53 Å).

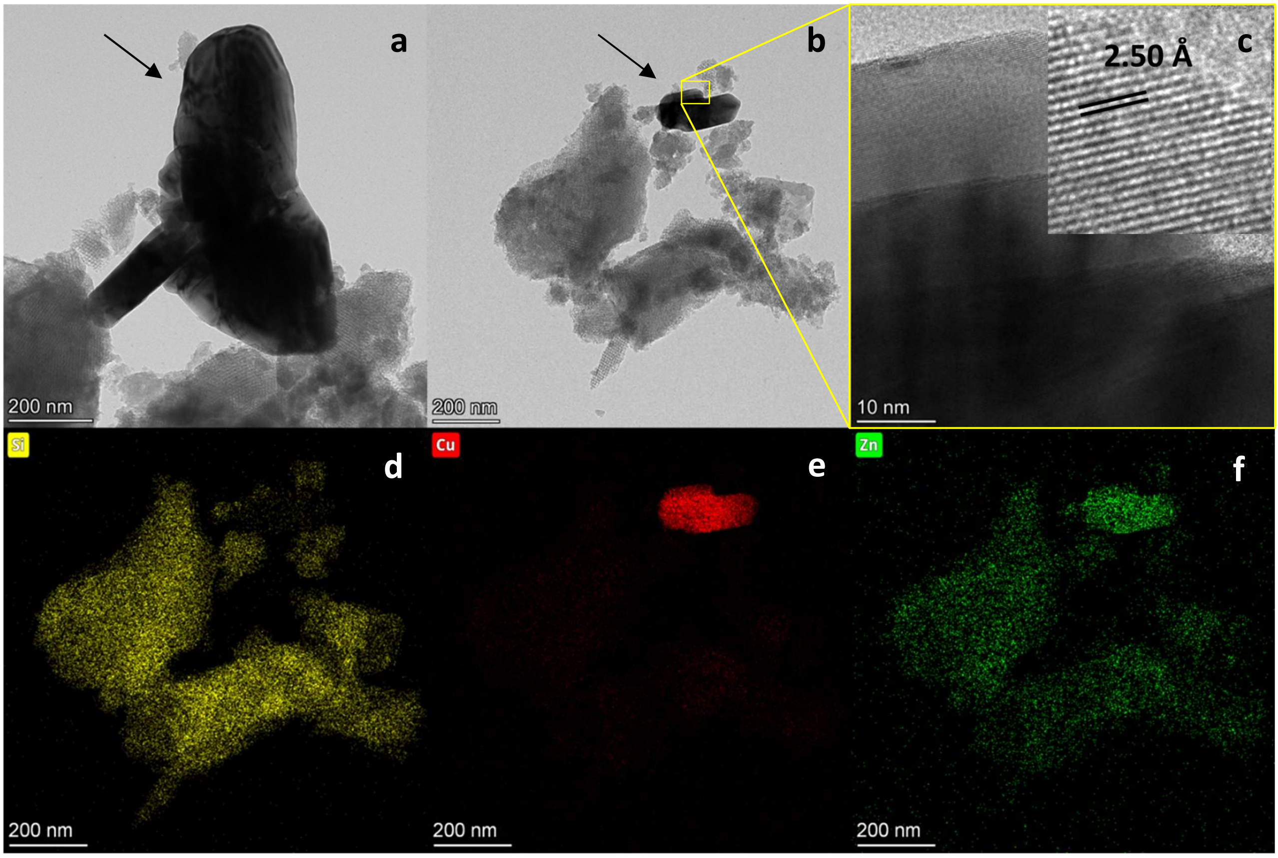

Figure 62 TEM (a,b), HR-TEM (c) micrographs and EDX chemical mapping of CuZn15@Al-SBA-16_TS (d-f).

5.3 Development of mesostructured composites on Al-SBA-16 using a self-combustion impregnation route

Since the two-solvent impregnation technique did not show promising results for the development of composite materials with a homogeneously dispersed redox phase, a second attempt was done using an impregnation technique based on a self-combustion reaction [72], [136], [140], [222], [223]. This approach consists in the dispersion of the pre-dried support into an aqueous solution of the metal nitrates and glycine; in this context, glycine acts both as a complexing agent, by bonding to the metal ions with its carboxyl group, and as a reducing agent. Differently from the two-solvent impregnation described above, in this case the transformation of the nitrates to oxides does not consists in a thermal decomposition of the nitrates, but in an auto-propagating oxidation-reduction reaction between the nitrates (oxidating agent) and glycine (reducing agent). Due to the exothermic nature of the reaction, nitrates are rapidly converted into crystalline oxides. The "glycine-nitrate" method was previously reported for CuO@SBA-15 [224], Fe_2O_3@SBA-15 [225], LaCoO@SBA-15 [226] and, in the context of CO_2 hydrogenation, for Cu-based methanol synthesis catalysts dispersed onto SBA-15 support [72] but, to the best of our knowledge, never on other mesostructured materials or acidic aluminosilicates.

5.3.1 Synthesis method of the Al-SBA-16-based composites.

To obtain Al-SBA-16-based composites with the self-combustion glycine-nitrate approach, the method described in [72] was followed. In a typical synthesis, 1 g of the mesostructured support, previously dried overnight at 120 °C, was submerged with 10 mL of the precursor solution containing the metal nitrates ($Cu(NO_3)_2*2.5H_2O$, $Zn(NO_3)_2*6H_2O$ and $ZrO(NO_3)_2$) and glycine into a beaker under vigorous stirring. The concentration of metal nitrates depends on the weight loading of the composite and the amount of glycine is determined from the amount of metal ions in the solution, according to a glycine/metal ions molar ratio of 1.44. Water was then let evaporate until a viscous gel was obtained. The resulting gel was then sonicated for 5 minutes and eventually submitted to a sudden temperature raise at 300°C, by putting it into a pre-heated oven.

Since higher amounts of redox phase allow to obtain higher values of CO_2 conversion, for these composites a weight loading of 20% was chosen. Namely, three different composites were prepared, with a Cu/Zn loading of 20%, two different Cu/Zn ratios (1/1 and 2/1) and the effect of the presence of Zr was investigated. The parameters used for the impregnation are reported in Table 20.

Table 20 Al-SBA-16-based composites synthesized by the self-combustion impregnation method.

Sample	Redox phase	Cu/Zn loading (wt %)	Cu/Zn(/Zr) molar ratio
$Cu_1Zn_1$20@Al-SBA-16_SC	CuO/ZnO	20%	1/1
$Cu_2Zn_1$20@Al-SBA-16_SC	CuO/ZnO	20%	2/1
$Cu_2Zn_1$20_Zr@Al-SBA-16_SC	CuO/ZnO/ZrO_2	20%	2/1/1.3

5.3.2 Structural and morphological characterization

Wide-angle XRD measurements (Figure 63a), do not show any crystalline peaks attributable to any copper- or zinc-based phase, unlike what was observed for the composites obtained through the two-solvent impregnation described in Paragraph 4.2. Only in the patterns of $Cu_2Zn_1$20@Al-SBA-16_SC and $Cu_2Zn_1$20_Zr@Al-SBA-16_SC, the ones with the highest amount of copper, a weak and broad band located at 2θ values between 30° and 40° was noticed, corresponding to the two main peaks (002; 111) of the tenorite (CuO) phase. These findings highlight that the redox phase has been deposited onto the support in form of small nanoparticles, not observable from XRD measurements, or as an amorphous phase. Like in the case of the composites obtained with the two-solvent impregnation, the ordered mesoporous structure was maintained after the functionalization process, as can be evinced from the small-angle X-ray patterns (Figure 63b). In this case, however, an evident decrease in terms of intensity of the mesostructure 110 and 200 signals was observed for the composites compared to the support, suggesting that the redox phase has been incorporated into the mesopores. This intensity decrease, on the other hand, was not observed for the composites obtained on the same support (Al-SBA-16) with the two-solvent impregnation, since this approach did not lead to a proper dispersion of the redox phase inside the pores, as evidenced in Paragraph 4.2.3. Furthermore, a slight shift (0.02°) of the mesostructure 110 signal towards higher values of 2θ is observable for the composites obtained with the self-combustion approach (Figure 63b). This shift can be ascribed to a decrease of the mean pore diameter as a consequence of the impregnation process, suggesting that the redox phase has been deposited inside the pores in form of a thin layer or very small nanoparticles.

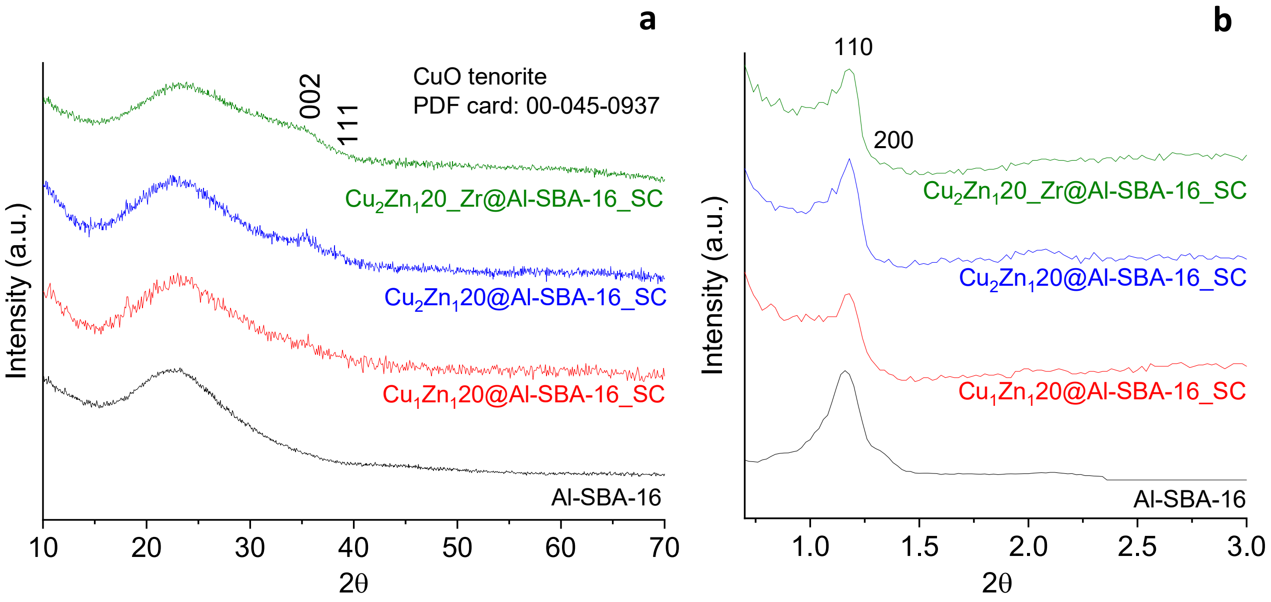

Figure 63 WA-XRD (a) and SA-XRD (b) patterns of Al-SBA-16-based composites synthesized by self-combustion method.

TEM micrographs point out that the mesostructure was maintained after the impregnation process, as already evidenced by SA-XRD patterns; furthermore, differently from the composites obtained with the two-solvent impregnation technique TEM images do not show the presence of large dark particles ascribed to the redox phase outside the pores. The absence of these large particles is also confirmed by EDX mapping, which, on the contrary evidenced a homogeneous dispersion of the elements of the redox phase (Cu, Zn and Zr) throughout the whole support for all three samples (Figure 64). The absence of large crystalline particles of redox phase was also highlighted by the lack of bright spots in the SAED pattern (insets in Figure 64a, d, and g).

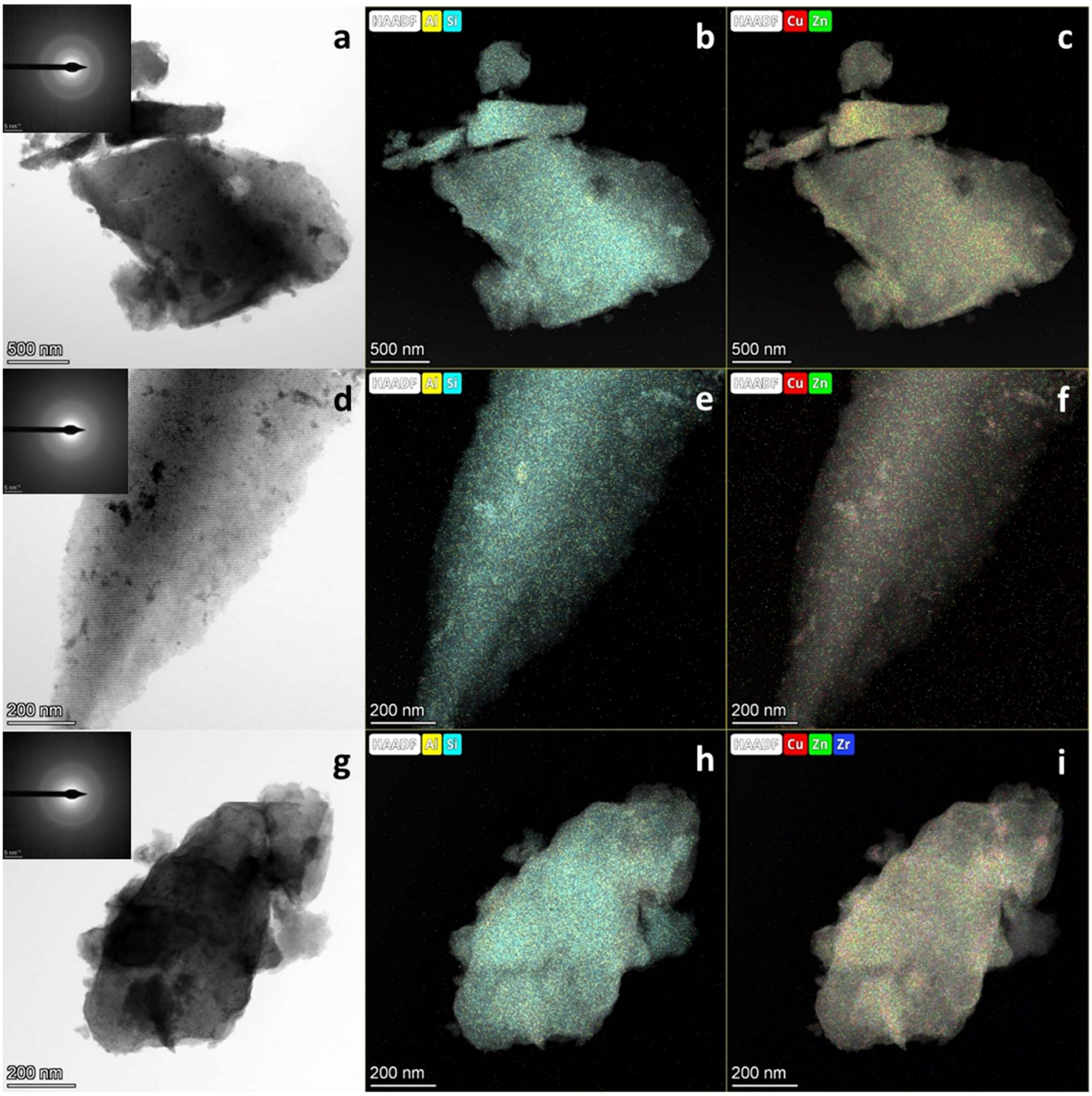

Figure 64 EDX chemical mapping of Cu_1Zn_120@Al-SBA-16_SC (a-c), Cu_2Zn_120@Al-SBA-16_SC (d-e), and Cu_2Zn_120_Zr@Al-SBA-16_SC (g-i) composites.

5.3.3 Study of the catalytic performances

All the three composites obtained through the self-combustion impregnation technique were tested for the direct synthesis of dimethyl ether from CO_2 and H_2. The catalytic tests on composite catalysts were performed using 0.25 g of catalyst mixed with 3.2 g of α-Al_2O_3, an inert material, to reach a total bed volume of ≈3 cm^3. The resulting gas hourly space velocity (GHSV) resulted to be 48000 $Ncm^3\ g_{cat}^{-1}\ h^{-1}$. Composite catalysts were reduced inside the reactor in a stream of a H_2/N_2 mixture (H_2, 15 vol% in N_2) at 300 °C for 2 h under atmospheric pressure. The reaction was carried out at 250 °C, 3.0 MPa with a H_2 and CO_2 (molar ratio of 3:1) mixture for 36 h.

Since important considerations about the stability of the catalysts over time have to be made the values of CO_2 conversion (Figure 65a) and selectivity to CO (Figure 65b), methanol (Figure 65c) and DME (Figure 65d), as well as DME yield (Figure 66a), are here reported in form of activity vs time plots; furthermore, the histograms of mean values are also reported (Figure 66b).

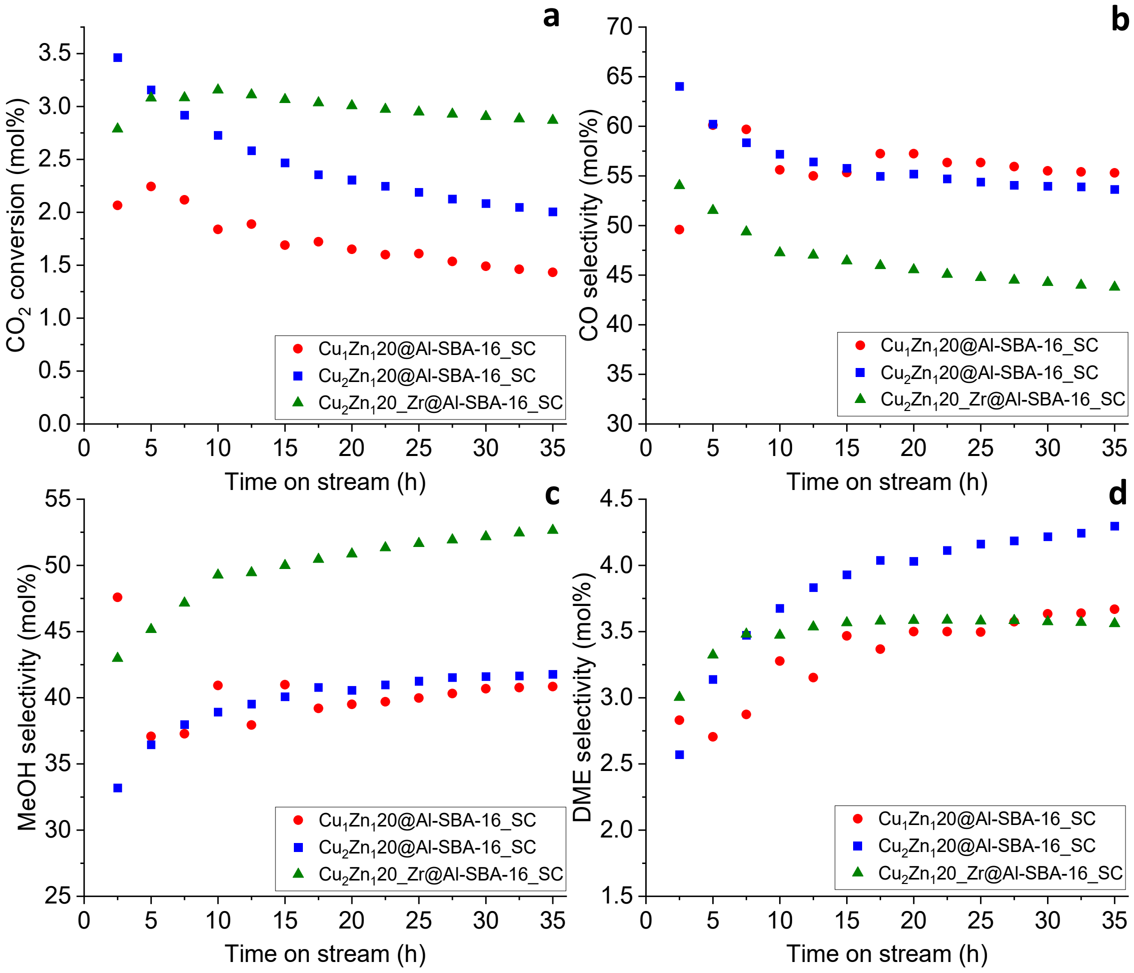

Figure 65 Values of CO_2 conversion (a) and selectivity to CO (b), methanol (c) and DME (d) over time for the composites obtained with self-combustion process on Al-SBA-16.

In terms of CO_2 conversion, a first important comparison can be made between $Cu_1Zn_1$20@Al-SBA-16_SC and $Cu_2Zn_1$20@Al-SBA-16_SC; these two composites have the same wt% loading of redox phase (20%) but different Cu/Zn ratios, 1/1 and 2/1 respectively. As can be seen from the X CO_2 values (Figure 65, Figure 66b), $Cu_2Zn_1$20@Al-SBA-16_SC showed a higher value of CO_2 conversion (2.4%) than $Cu_1Zn_1$20@Al-SBA-16_SC (1.7%), as expected according to the literature, suggesting that a Cu/Zn ratio of 2/1 is more effective than a 1/1 ratio, being Cu^0 the actual active phase of the catalyst. It is also important to notice that both CuZn-based catalysts showed a gradual decrease in terms of CO_2 conversion, as can be clearly seen from the plot (Figure 65). On the contrary, this decreasing trend was not observed for $Cu_2Zn_1$20_Zr@Al-SBA-16_SC, suggesting that the presence of Zr could contribute to significantly increase the stability of the catalyst over time, as suggested in the literature, in which a third phase (usually Al_2O_3 or, like in our case, ZrO_2) in redox catalysts is proposed to increase the thermal and chemical stability of the systems. Another significant difference ascribable to the addition of Zr is the improvement in terms of selectivity to methanol, associated to a decrease in selectivity to CO (Figure 65, Figure 66b), as already observed in the literature [72]. $Cu_2Zn_1$20_Zr@Al-SBA-16_SC shows indeed values of MeOH and CO selectivity of 50.3% and 46.2%; on the other hand, the two other catalysts show values of methanol (≈40%) and CO selectivity (≈56%) very similar to each other, but significantly different from those of $Cu_2Zn_1$20_Zr@Al-SBA-16_SC. In terms of selectivity to DME, $Cu_2Zn_1$20_Zr@Al-SBA-16_SC shows the more stable values Figure 65; on the other hand, the two other catalysts show values of DME selectivity gradually increasing over time. This finding can be presumably attributed to the significant decrease in terms of CO_2 conversion described above for these two catalysts; lower values of conversion, indeed, lead to an overestimation of molecules like DME and an underestimation of species like CO by the gas chromatographic system. The increasing trend in DME selectivity showed by $Cu_1Zn_1$20@Al-SBA-16_SC and $Cu_2Zn_1$20@Al-SBA-16_SC could be thus attributed to an overestimation of this value, rather than an actual increase in dehydration activity of the catalysts. DME yield values reported in Figure 66a suggest that the better catalyst in terms of DME production is $Cu_2Zn_1$20_Zr@Al-SBA-16_SC, which shows an initial DME yield similar to that of $Cu_2Zn_1$20@Al-SBA-16_SC but a better stability.

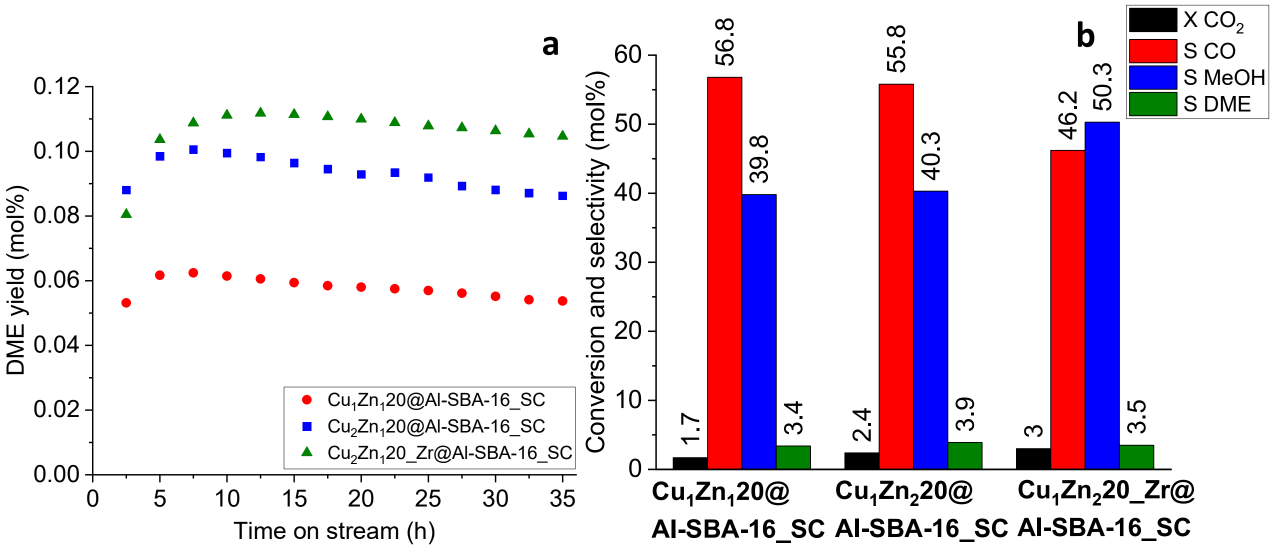

Figure 66 Values of DME yield over time (a) and mean values of CO_2 conversion and selectivity to CO, methanol and DME (b) for the composites obtained with self-combustion process on Al-SBA-16.

5.4 Development of composites on different mesostructured supports (Al-MCM-41, Al-SBA-15, Al-SBA-16, γ-Al_2O_3) using self-combustion impregnation

Since the self-combustion impregnation demonstrated to be much more effective than the two-solvent impregnation for the aim of obtaining composite bifunctional catalysts with the redox phase homogeneously dispersed inside the mesopores of the acidic catalyst, we chose to use this impregnation technique to synthesize bifunctional catalysts by impregnating all the five different mesostructured supports showed in Chapter 3. Considering the results obtained in Paragraph 5.3, since a Cu/Zn ratio of 2/1 proved to be more efficient than a Cu/Zn ratio of 1/1, and the presence of zirconium demonstrated to increase the stability of the catalyst over time, all the supports were impregnated chosing the same parameters used for $Cu_2Zn_1$20_Zr@Al-SBA-16_SC. Since there are no differences in the redox phase of the composite systems prepared in this paragraph, for brevity the redox phase is here indicated as CZZ; all information is reported in Table 21.

Table 21 Composites synthesized on different mesostructured acidic supports by the self-combustion impregnation method.

Sample	Support	Redox phase	Cu/Zn loading (wt %)	Cu/Zn/Zr molar ratio
CZZ@Al-MCM-41_SC	Al-MCM-41	$CuO/ZnO/ZrO_2$	20%	2/1/1.3
CZZ@Al-SBA-16_SC	Al-SBA-16	$CuO/ZnO/ZrO_2$	20%	2/1/1.3
CZZ@Al-SBA-15_SC	Al-SBA-15	$CuO/ZnO/ZrO_2$	20%	2/1/1.3
CZZ@Al_2O_3_P_SC	Al_2O_3_P_900	$CuO/ZnO/ZrO_2$	20%	2/1/1.3
CZZ@Al_2O_3_F_SC	Al_2O_3_F_900	$CuO/ZnO/ZrO_2$	20%	2/1/1.3

5.4.1 Structural, textural, and morphological characterization

Wide-angle X-ray patterns (Figure 67, Figure 68) for all composites do not show any sharp diffraction peak attributable to the redox phase; as already seen in Paragraph 5.3.2, only a broad and weak band attributable to CuO at 2θ values between 30° and 40° is observed, the range where the main diffraction peaks (002 and 111) of tenorite are located. No other contributions attributed to the redox phase are observed, pointing out that the redox phase is in form of very small nanocrystals. Comparing the aluminosilicate-based composites to each other (Figure 67), this band appears to be more visible for CZZ@Al-SBA-16_SC, presumably due to the lower pore volume of the support Al-SBA-16, compared to Al-MCM-41 and Al-SBA-15. In the case of γ-Al_2O_3-bases composites (Figure 68) the CuO band overlaps with the signals of γ-Al_2O_3, resulting in a single wide band located between 25° and 40°.

As expected from the previously reported XRD data on Al-SBA-16-based composites, SA-XRD (Figure 67, Figure 68) proved that the mesostructure was maintained after the impregnation process in all cases, as demonstrated by the presence, of the same bands present in the patterns of the mesostructured supports. A decrease in the intensity of the main signal of the mesostructure and a slight shift towards higher values of 2θ was observed for all composites compared to their corresponding supports.

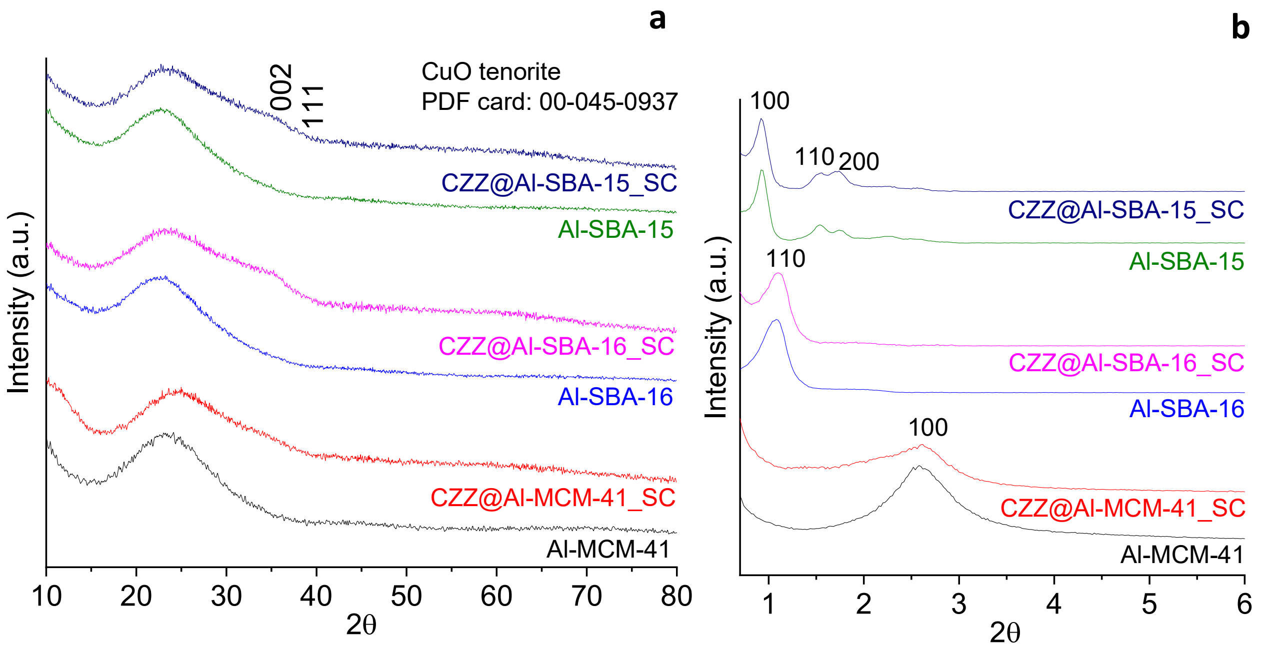

Figure 67 WA-XRD (a) and SA-XRD (b) patterns of composites synthesized by self-combustion method on Al-MCM-41, Al-SBA-16 and Al-SBA-15 compared with the corresponding mesostructured acidic supports.

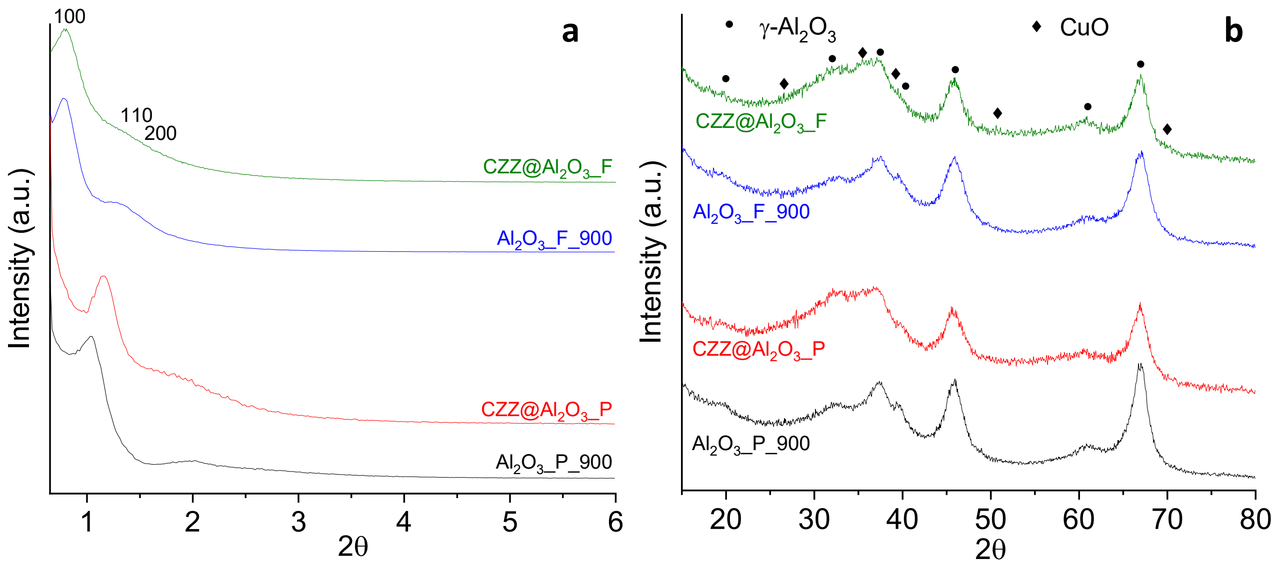

Figure 68 WA-XRD (a) and SA-XRD (b) patterns of composites synthesized by self-combustion method on Al_2O_3_P_900 and Al_2O_3_P_900.

Textural properties data, extrapolated by the nitrogen physisorption measurements, are reported in Table 22. Nitrogen physisorption measurements showed a significant decrease of both surface area and pore volume for all samples (Table 22 Figure 69-Figure 73), after functionalization with the redox phase, as clearly indicated by the drop of the physisorption isotherms to much lower values of adsorbed volume. Also, a minor decrease in terms of mean pore diameter was observed, attributable to the deposition of the redox phase on the inner walls of mesopores.

Table 22 BET surface area (SA), pore volume (V_p), and mean BJH pore diameter (D_p) of all the mesostructured supports and their composites obtained by self-combustion impregnation.

Sample	SA (m^2/g)	V_p (cm^3/g)	D_p (nm)
Al-MCM-41	1262	0.77	2.2
CZZ@Al-MCM-41_SC	586	0.31	1.7
Al-SBA-16	437	0.52	4.6
CZZ@Al-SBA-16_SC	260	0.33	4.3
Al-SBA-15	673	1.07	7.0
CZZ@Al-SBA-15_SC	376	0.68	6.7
Al_2O_3_P_900	197	0.57	5.6
CZZ@Al_2O_3_P_900_SC	161	0.35	5.0
Al_2O_3_F_900	194	0.57	8.7
CZZ@Al_2O_3_F_900_SC	153	0.34	6.7

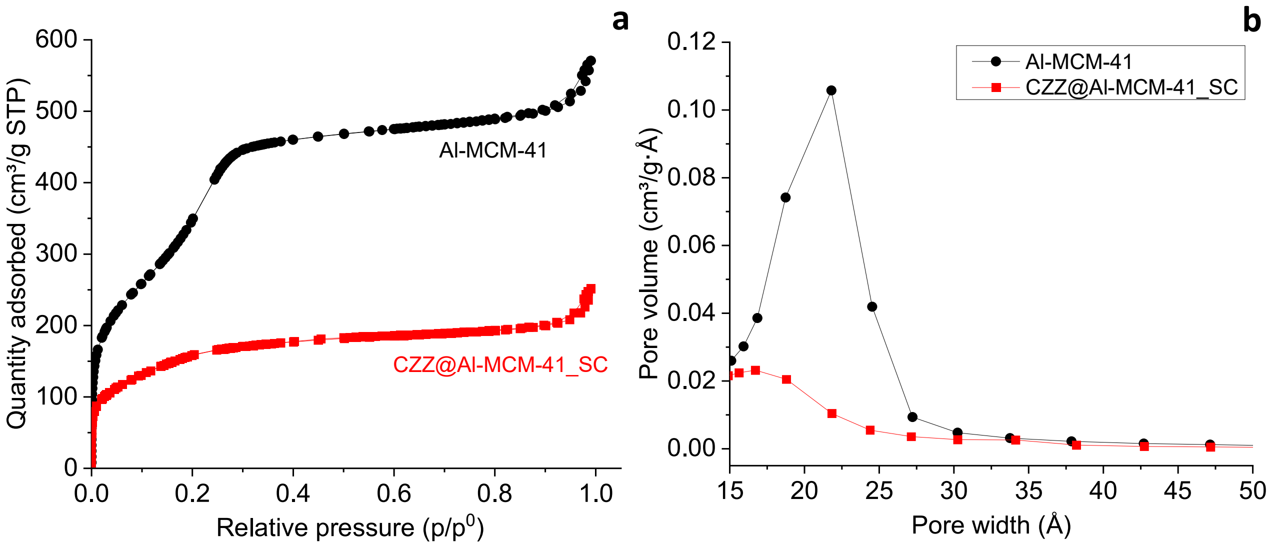

Figure 69 Nitrogen physisorption isotherms (a) and BJH pore size distribution (b) of CZZ@Al-MCM-41_SC and its support.

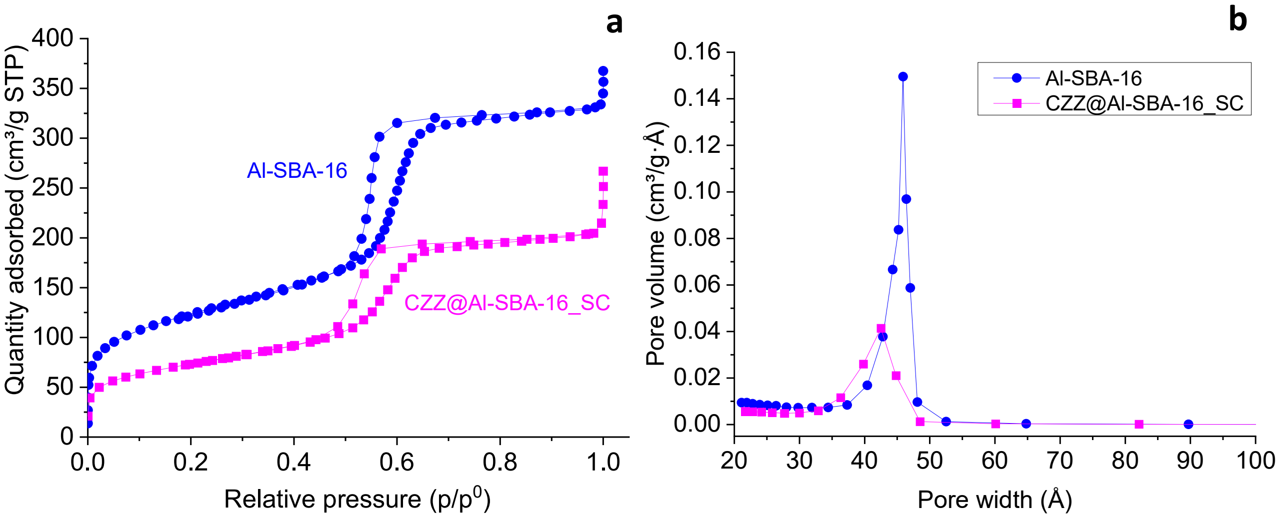

Figure 70 Nitrogen physisorption isotherms (a) and BJH pore size distribution (b) of CZZ@Al-SBA-16_SC and its support.

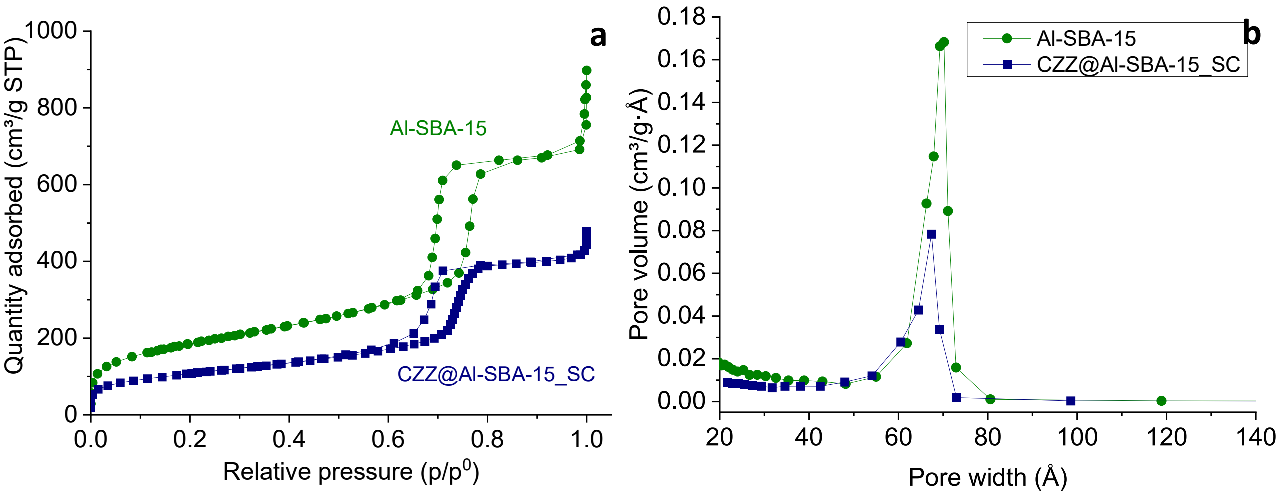

Figure 71 Nitrogen physisorption isotherms (a) and BJH pore size distribution (b) of CZZ@Al-SBA-15_SC and its support.

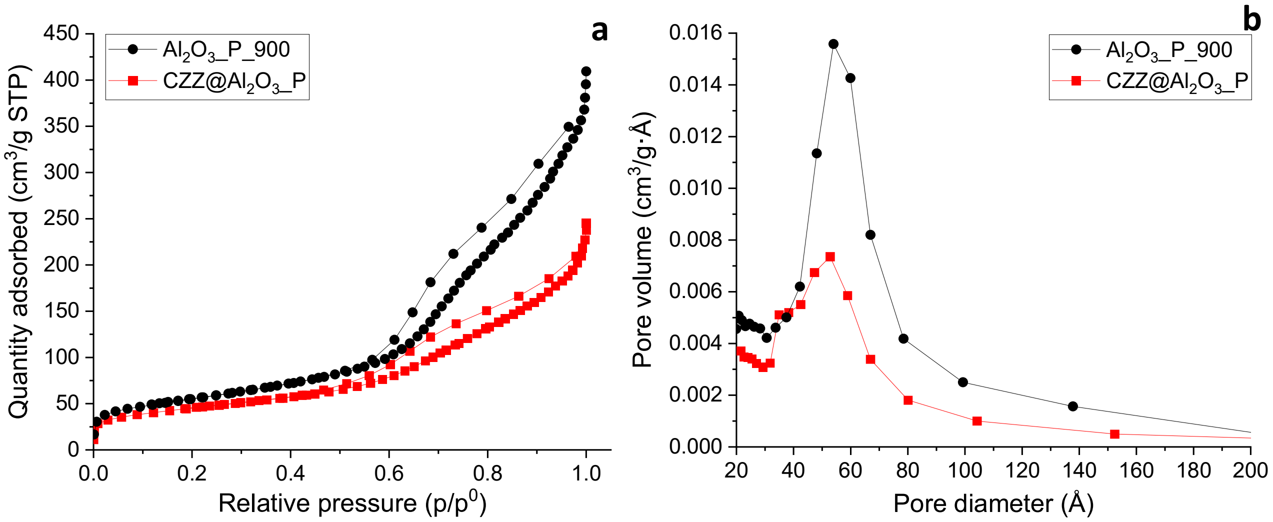

Figure 72 Nitrogen physisorption isotherms (a) and BJH pore size distribution (b) of CZZ@Al_2O_3_P_SC and its support.

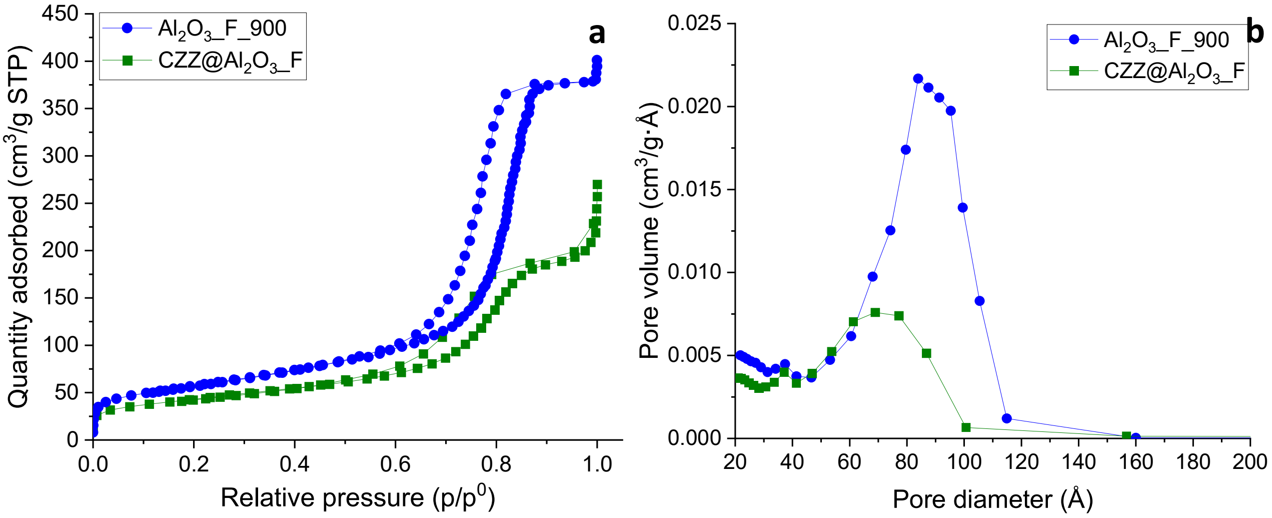

Figure 73 Nitrogen physisorption isotherms (a) and BJH pore size distribution (b) of CZZ@Al_2O_3_F_SC and its support.

TEM imaging (Figure 74, Figure 76), EDX chemical mapping (Figure 75, Figure 77) and EDX linear profile (Figure 78) evidenced, as expected from the previous results obtained for the composites on Al-SBA-16, the overall homogeneity of distribution of the redox phase throughout the mesostructured matrix for all samples. The ordered mesoporous structure was maintained after the functionalization process, as can be seen from the TEM micrographs; the process, also did not give rise to any separation of Al_2O_3 particles for aluminosilicates. The impregnation route, as can be seen from EDX chemical mapping of Cu, Zn and Zr, resulted in a homogeneous functionalization; the lack of large particles attributable to the redox phase outside the mesopores of the supports, together with the absence of diffraction peaks in the low angle XRD patterns, suggests that the redox phase has been homogeneously dispersed inside the pores in form of small nanoparticles. The particles of the redox phase (CuO, ZnO and ZrO_2) are not visible in TEM images since these species are finely dispersed onto the support in form of either very small nanoparticles or as a homogeneous layer, as already suggested by WA-XRD measurements. Only a slight difference in TEM micrographs can be seen in terms of lower contrast between pore and pore walls, indicating the presence of the redox phase within the mesochannels (white circles in Figure 76).

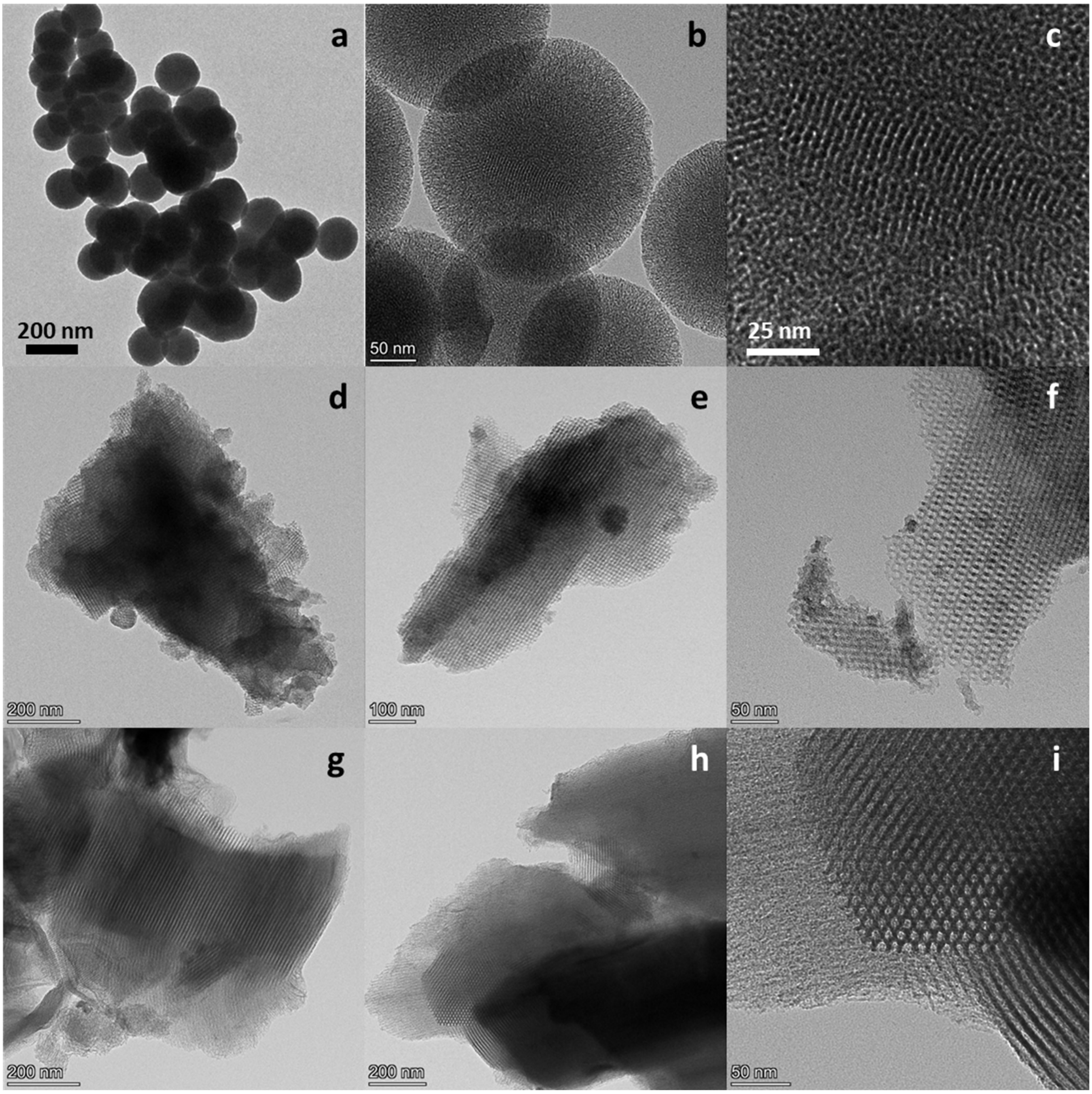

Figure 74 TEM micrographs of CZZ@Al-MCM-41_SC (a-c), CZZ@Al-SBA-16_SC (d-e), and CZZ@Al-SBA-15_SC (g-i) composites.

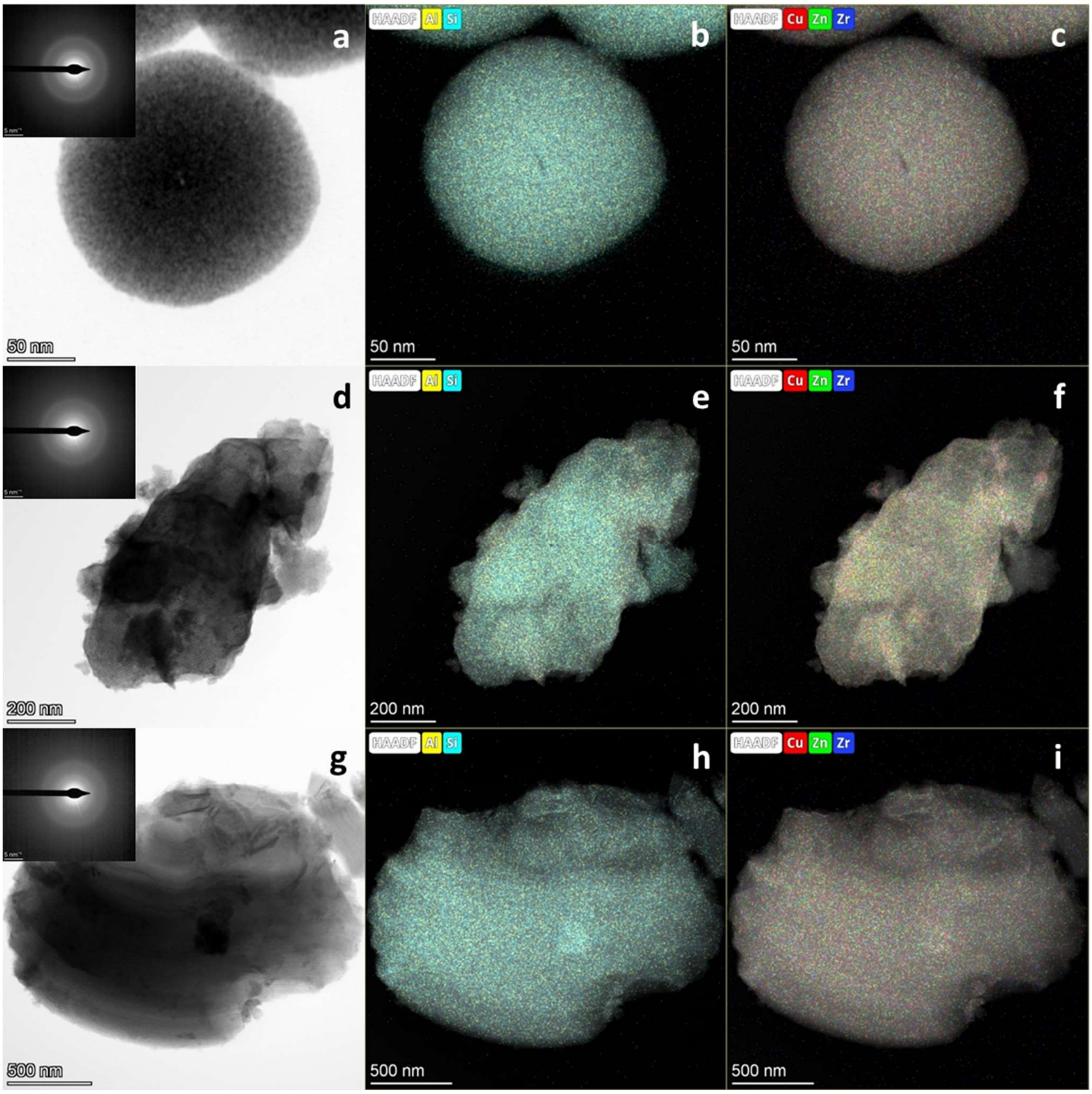

Figure 75 EDX chemical mapping of CZZ@Al-MCM-41_SC (a-c), CZZ@Al-SBA-16_SC (d-e), and CZZ@Al-SBA-15_SC (g-i) composites.

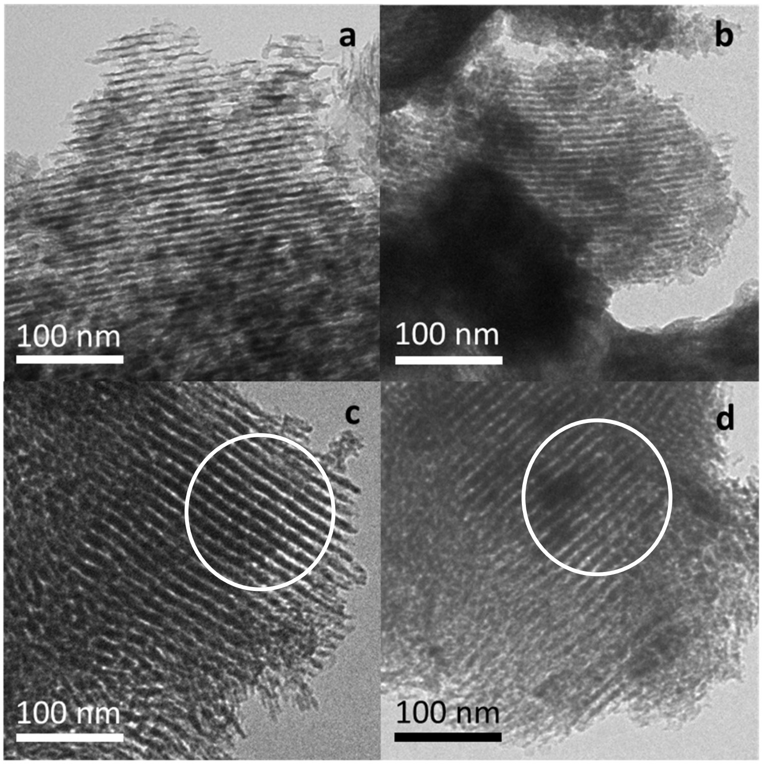

Figure 76 TEM micrographs of Al_2O_3_P_900 (a) CZZ@Al_2O_3_P_SC (b), Al_2O_3_F_900 (c), and CZZ@Al_2O_3_F_SC [186].

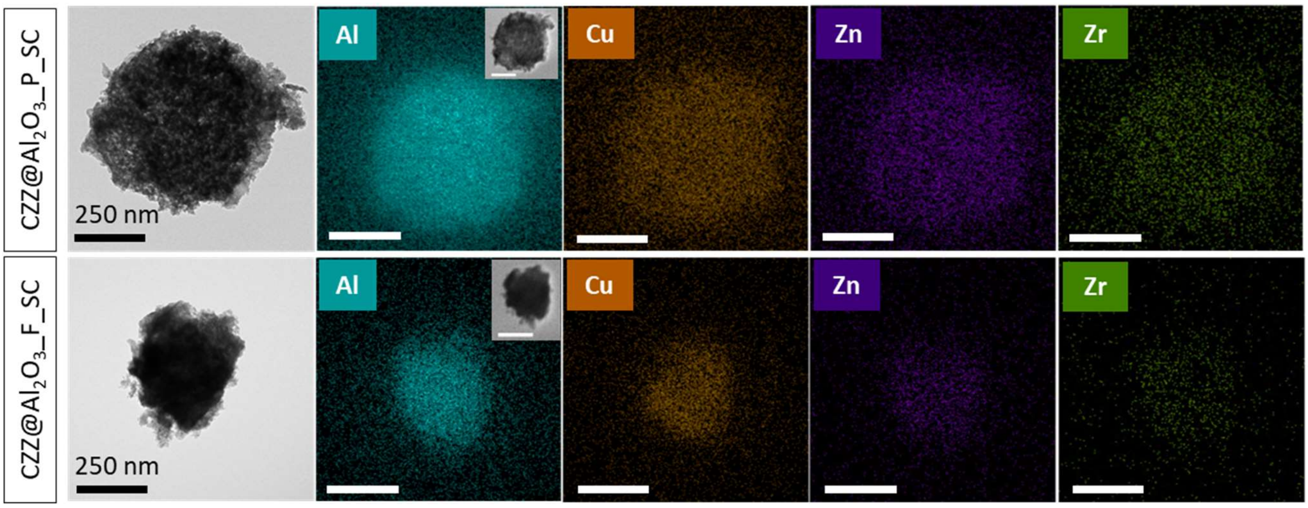

Figure 77 EDX chemical mapping of CZZ@Al_2O_3_P_SC (top row) and CZZ@Al_2O_3_F_SC (bottom row) composites [186].

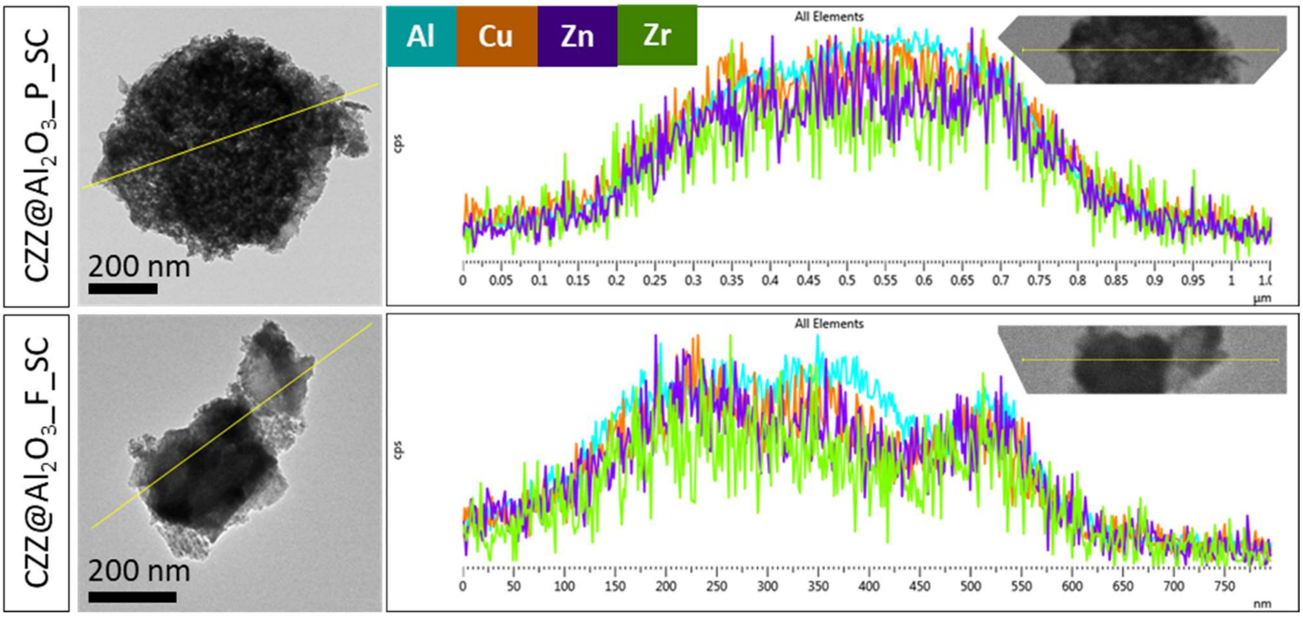

Figure 78 EDX linear profile of CZZ@Al$_2$O$_3$_P_SC (top) and CZZ@Al$_2$O$_3$_F_SC (bottom) composites [186].

5.4.2 Synthesis and characterization of the CZZ redox catalyst

Besides synthesis of the composites, an unsupported CuO/ZnO/ZrO$_2$ (molar ratio of 2/1/1.3) redox catalyst with the same composition of the redox phase incorporated into the acidic mesostructures, named CZZ, was synthetized also by employing the same self-combustion method described in Paragraph 5.3.1 for the synthesis of composite catalysts; however, in this case, no support was used during the self-combustion process, leading to the formation of an unsupported redox catalyst, in form of a black powder. The CZZ pure redox catalyst was synthesized in order to test it in form of physical mixtures with the acidic supports used in this Paragraph (Al-MCM-41, Al-SBA-16, Al-SBA-15, and γ-Al$_2$O$_3$). The catalytic tests of these physical mixtures, alongside with those of the composite bifunctional catalysts, will allow to perform a direct comparison between the physical and the chemical mixing methods, leading to a better understanding of the effect of the intimate contact between the two phases in composite catalysts.

Figure 79 reports the wide-angle X-ray diffraction pattern of the CZZ redox catalyst; as can be seen, the pattern clearly shows the presence of several diffraction peaks, attributable to different crystalline phases. The phase identification points out that each atomic species of the redox catalyst (namely Cu, Zn and Zr) gave rise to the formation of phases with different crystal structure and different oxidation state. Particularly, Cu was present as metallic copper (Cu), cuprite (Cu$_2$O) and tenorite (CuO), zinc was only present in its zincite form (ZnO) and Zr was present as Baddeleyite (monoclinic ZrO_2) and cubic ZrO_2. A Rietveld refinement of the pattern was performed in order to quantify the phases and the results of the analysis are reported in Table 23).

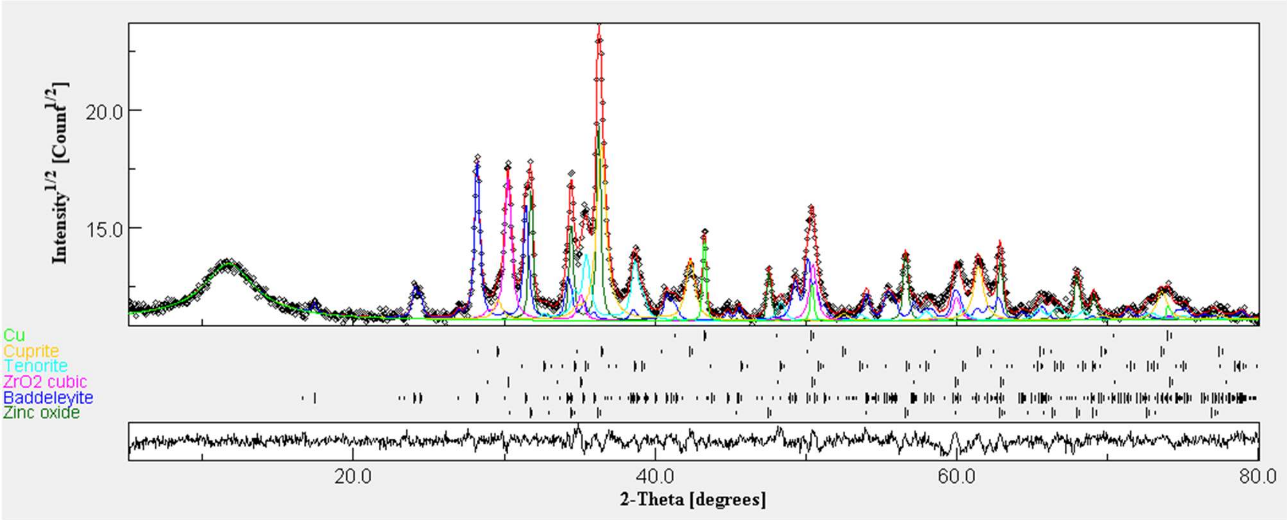

Figure 79 Rietveld analysis on the wide-angle XRD pattern of the unsupported CZZ redox catalyst.

Table 23 Weight composition of the crystalline phases present in the unsupported CZZ redox catalyst determined by Rietveld analysis.

Phase	**Cu**	**Cu_2O**	**CuO**	**ZnO**	**Monoclinic ZrO_2**	**Cubic ZrO_2**
Amount (wt%)	3.2 ± 0.1	28 ± 2	14.2 ± 0.8	19.0 ± 0.0	19.2 ± 0.9	15.6 ± 0.9

Figure 80 depicts the TEM images and EDX chemical mapping of unsupported CZZ redox catalyst. As can be seen, the self-combustion reaction carried out without using a support gave rise to the formation of large particles of irregular shape and also caused a clear separation of the phases, leading to an inhomogeneous dispersion of the redox species into each other.

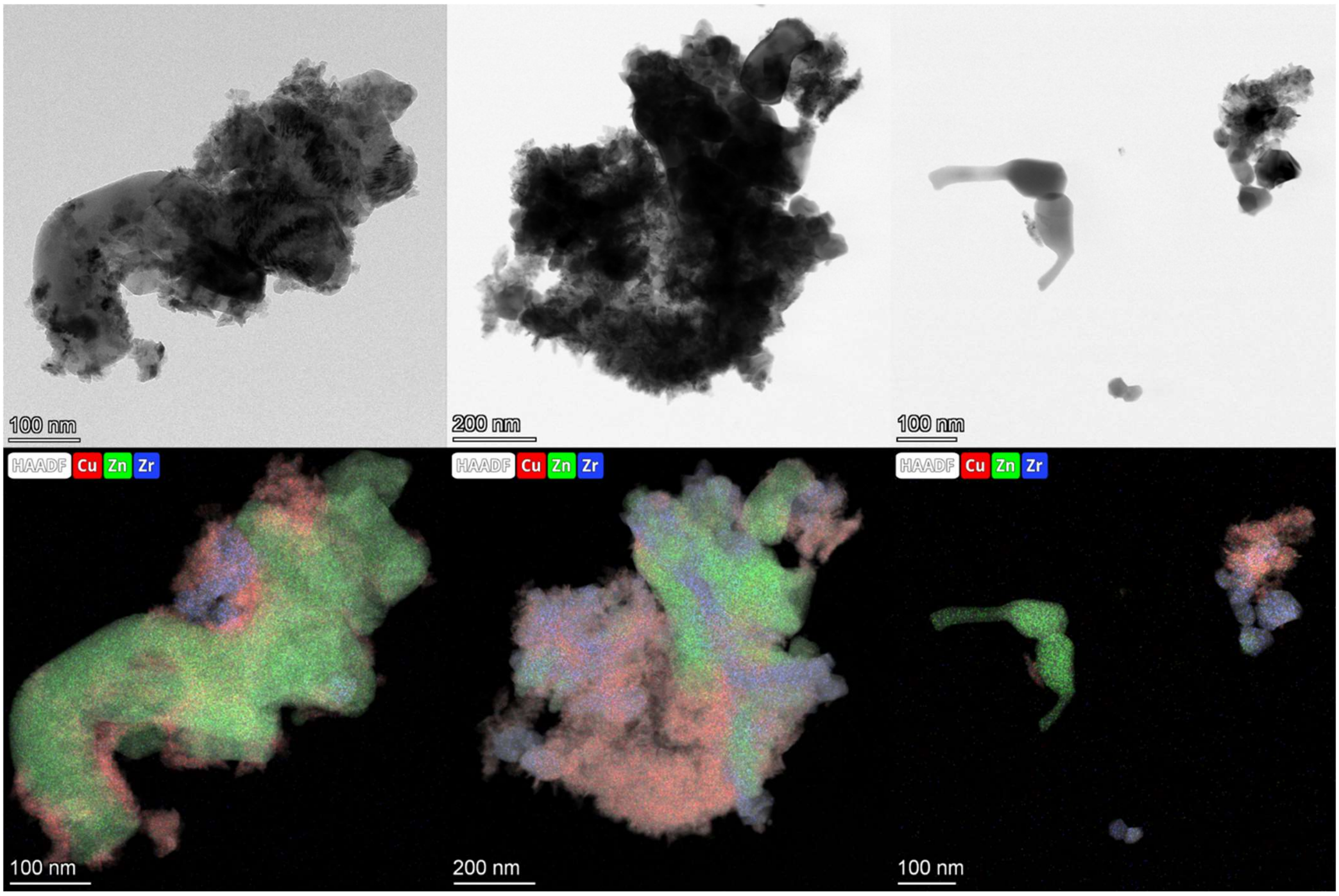

Figure 80 EDX chemical mapping of the unsupported CZZ redox catalyst.

5.4.3 Study of the catalytic performances

The catalytic performances of aluminosilicate-based composites for the one-pot CO_2-to-DME process have been evaluated and compared with the performances of physical mixtures consisting in the mesostructured acidic supports together with CZZ, a pure redox catalyst obtained with the same self-combustion process used for the functionalization of the supports, as described in Paragraph 5.4.2. This comparison allowed to understand how the catalytic performances are influenced by the nature of the contact between the two phases (either physical, in the case of physical mixtures, or chemical contact, in the case of bifunctional composite catalysts). The catalytic tests on composite catalysts were performed using 1 g of catalyst; the tests on physical mixtures were performed using 0.333 g of unsupported CZZ redox catalyst and 0.667 g of mesostructured dehydration catalyst. 2.5 g of α-Al_2O_3, an inert material, were added to the catalytic systems in order to have a total bed volume of $\approx$3 cm^3. The resulting gas hourly space velocity (GHSV) was 12000 $Ncm^3\ g_{cat}^{-1}\ h^{-1}$. Both composite catalysts and physical mixtures were reduced inside the reactor in a stream of a H_2/N_2 mixture (H_2, 15 vol% in N_2) at 300 °C for 2 h under atmospheric pressure. The reaction was carried out at 250 °C, 3.0 MPa with a H_2 and CO_2 (molar ratio of 3:1) mixture for 36 h.

As can be seen from the data reported in Figure 81 and Figure 82, all the composites showed a higher value of CO_2 conversion compared to the corresponding physical mixtures, presumably due to the superior dispersion of the $Cu/ZnO/ZrO_2$-based redox phase. In the first case, indeed, the redox phase is dispersed in form of small nanoparticles inside the mesopores of the support, giving rise to high dispersion and thus a high contact area of the active sites of the redox catalyst with the reactants. In the second case, on the other hand, being the CZZ redox catalyst obtained without a previous impregnation into a support, the active phase results to be much less dispersed and consists in much larger particles, as evidenced by XRD and TEM data, hence giving rise to a lower area of contact with the reactants and, consequently, a lower CO_2 conversion. Particularly, the composite catalyst CZZ@Al-SBA-15_SC showed the highest value of CO_2 conversion among the three composites, presumably as a consequence of the high pore volume of the support, that allows a better dispersion of the redox phase. All composite catalysts, however, showed lower values of selectivity and yield to DME, compared to their corresponding physical mixtures (Figure 81, Figure 82, Figure 83) and, consequently, higher values of methanol selectivity. The cause of this drop in S_{DME} can be ascribed to the coverage of the acidic sites of the supports due to the functionalization process; after this process, the acid sites present on the surface of the supports, which are responsible for the methanol dehydration to DME, are covered by the deposition of the nanoparticles of redox phase, being consequently no longer able to adsorb methanol molecules. This hypothesis is further confirmed by the fact that the composite catalyst that showed the highest S_{DME} is CZZ@Al-MCM-41_SC, likely due to its very high surface area, that allows to have a higher amount of uncovered acidic sites after the impregnation process. Besides the coverage of the acid sites, ion-exchange phenomena between the redox phase and the Brønsted sites present on aluminosilicate supports cannot be excluded. On this regard, very low performances in terms of DME production rate were also observed by Bonura *et al.* [65] for a bifunctional catalyst obtained by a coprecipitation method from H-ZSM-5 and $Cu/ZnO/ZrO_2$; the authors attributed this behavior to an ion-exchange phenomenon between the zeolite and the metal cations of the redox phase, which caused the disappearance of the Brønsted acid sites of H-ZSM-5 with moderate strength, only leaving strong sites, unable to promote methanol dehydration [65][227]. Other authors observed a performance drop over time due to the intimate contact between the redox and acidic phase in H-

ZSM-5 physically mixed by grinding with a $Cu/ZnO/Al_2O_3$-based redox phase for the syngas-to-DME process; this fact was attributed to sintering of the redox phase particles, their oxidation and also the ion-exchange phenomena with the zeolite mentioned above, which led to a deactivation of the acidic sites of the dehydration catalyst [59]. Similar results, associated with a decrease in the number of Brønsted acid sites, were also observed when H-ZSM-5 was put into contact with the dehydration catalyst through mechanical mixing (grinding) and liquid phase mixing (slurry), resulting in a performance drop; this negative effect was not observed, on the other hand, when the two catalysts were separately pelletized and then mixed together [62]. This difference in DME selectivity also shows effects on CO selectivity, which is higher for composite catalysts. This is probably due to equilibrium effects; the subtraction of methanol from the reaction environment due to its dehydration to DME, pushes the equilibrium of the reaction towards the formation of more methanol, thus lowering the CO selectivity. In the case of composite catalyst, having a low S_{DME}, methanol remains in the reaction environment and S_{CO}, thus, results to be higher. Due to their significantly higher selectivity to DME, all tested physical mixtures showed higher DME yields than their corresponding composites. As expected, the bifunctional catalyst with the highest Y_{DME} is CZZ@Al-MCM-41_SC.

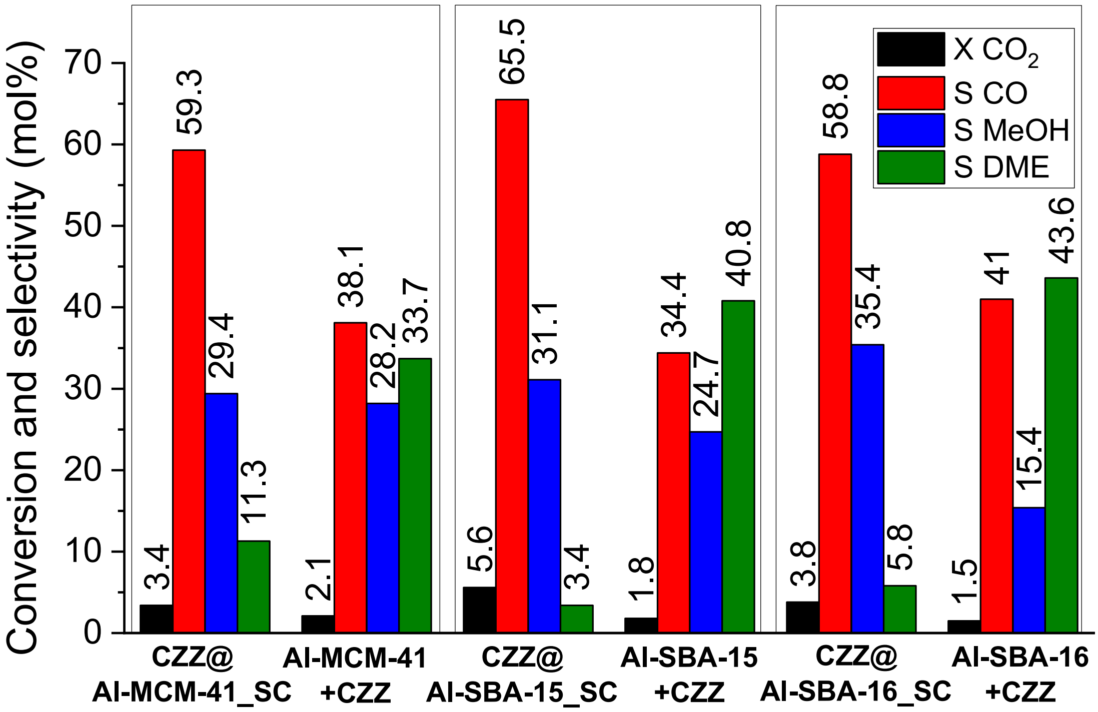

Figure 81 Mean values of CO_2 conversion and selectivity to CO, methanol and DME (b) for the composites and physical mixtures based on aluminosilicates

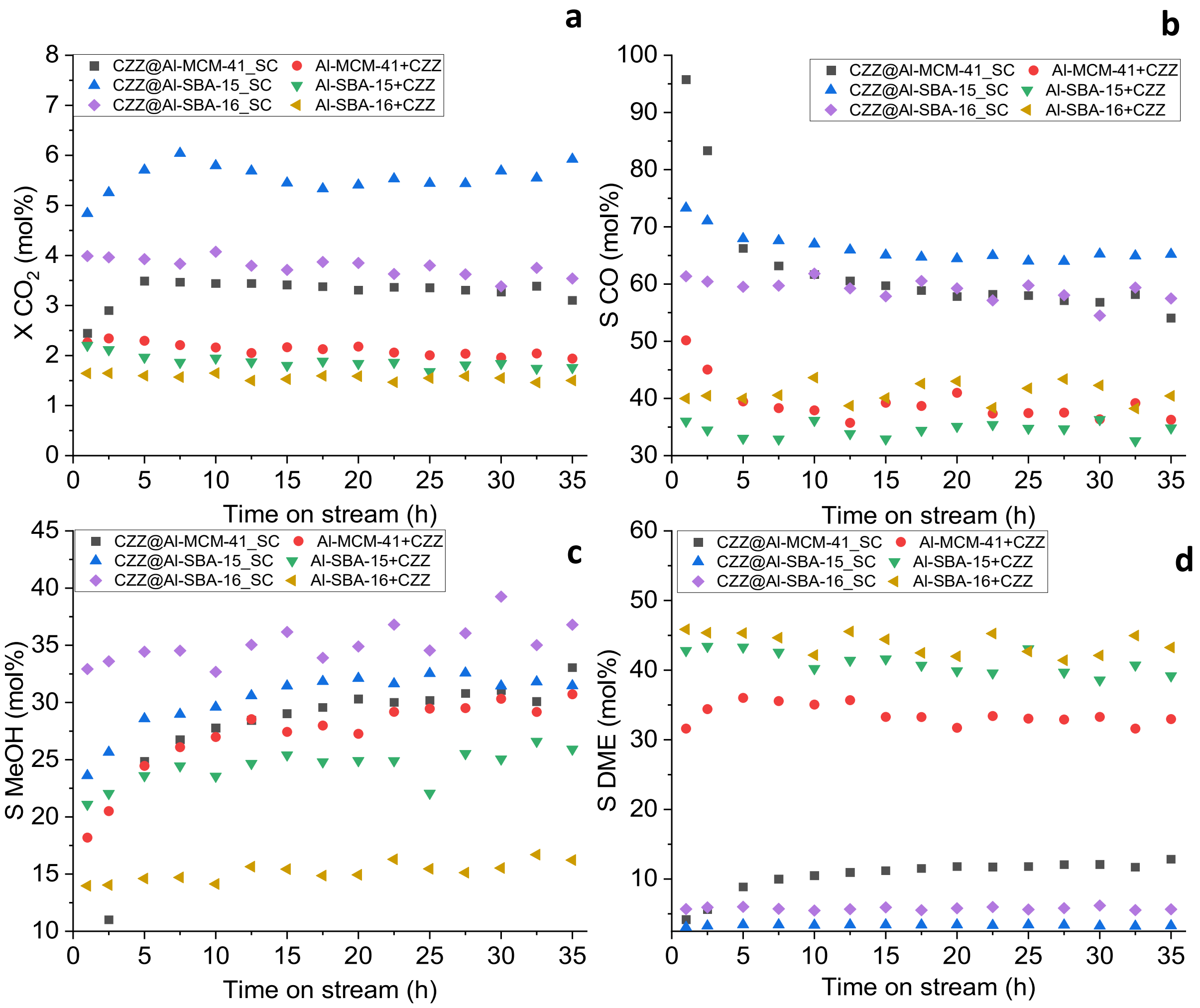

Figure 82 Values of CO_2 conversion (a) and selectivity to CO (b), methanol (c) and DME (d) over time for the composites and physical mixtures based on aluminosilicates.

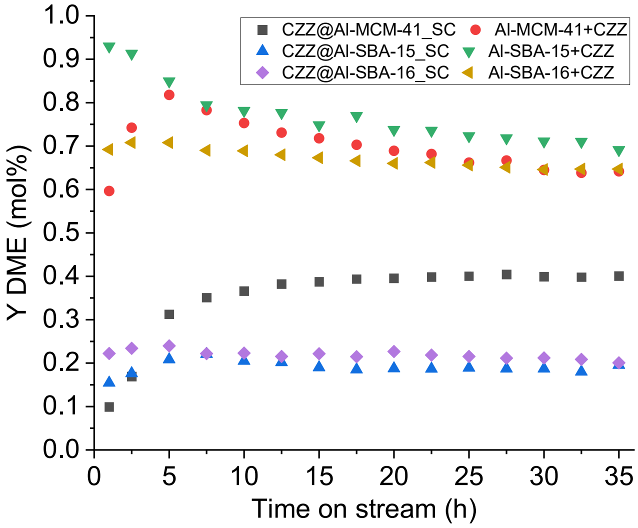

Figure 83 Values of DME yield over time for the composites and physical mixtures based on aluminosilicates.

Like previously done with aluminosilicate-based composites, γ-Al_2O_3-based composite catalysts were tested and their performances were compared with those of physical mixtures consisting of the mesostructured γ-Al_2O_3 support and the unsupported CZZ redox catalyst. The catalytic tests on composite catalysts were performed using 0.25 g of catalyst; the tests on physical mixtures were performed using 0.083 g of CZZ redox catalyst and 0.167 g of mesostructured dehydration catalyst. 3.2 g of α-Al_2O_3, an inert material, were added to the catalytic systems in order to have a total bed volume of ≈3 cm^3. The resulting gas hourly space velocity (GHSV) resulted to be 48000 $Ncm^3\ g_{cat}^{-1}\ h^{-1}$. Both composite catalysts and physical mixtures were reduced inside the reactor in a stream of a H_2/N_2 mixture (H_2, 15 vol% in N_2) at 300 °C for 2 h under atmospheric pressure. The reaction was carried out at 250 °C, 3.0 MPa with a H_2 and CO_2 (molar ratio of 3:1) mixture for 36 h. Also in this case, composite catalysts show significantly higher values of CO_2 conversion than the corresponding physical mixtures with CZZ (Figure 84a, Figure 85b), suggesting a positive effect deriving from the dispersion of the redox phase inside the mesopores in form of small nanoparticles. It can be observed that the CZZ@Al_2O_3_P_SC catalyst shows a higher conversion (4.5 mol%) and methanol selectivity (43.8 mol%) compared to CZZ@Al_2O_3_F_SC (X_{CO_2} = 3.4 mol% and S_{MeOH} = 40.4 mol%). Despite the same redox phase loading and the similar textural properties in terms of surface area and pore volume (Table 22) of the two composite catalysts, the different values of CO_2 conversion could be ascribed to the differences in pore size and pore size distribution, that may lead to a different dispersion of the redox phase inside the mesopores. Taking into account that the pore size of both the composite catalysts is significantly larger than that of the molecules involved in the reaction, the difference in terms of pore size should not affect the mass transfer phenomena, which can therefore be neglected. Due to the lower CO_2 conversion, both physical mixtures show fluctuating values of selectivity towards CO, methanol and DME; on the other hand, composite catalysts feature more stable selectivity values. Similarly to what was observed for aluminosilicate-based composites, γ-Al_2O_3-based bifunctional catalysts show lower values of DME selectivity and yield (Figure 84d, Figure 85) than their physically mixed counterparts. Also in this case, this finding could be explained considering that the accessibility of the acidic sites of the walls of mesostructured γ-Al_2O_3 to methanol molecules is hampered due to the deposition of the CZZ redox phase by the post-synthesis self-combustion impregnation process, thus hampering the dehydration reaction. Considering the combined results of XRD, TEM and nitrogen physisorption characterization, it can be assumed that the CZZ phase is homogeneously dispersed inside the mesopores as a thin layer rather than as nanoparticles. In this case, the deactivation of acid sites due to ion-exchange phenomena observed by other authors [65] can be excluded, since γ-Al_2O_3 only presents Lewis acid sites; therefore, the very low performances in terms of DME selectivity of the composite catalysts can be attributed to the coverage of the acid sites of the dehydration catalyst.

A direct comparison between the γ-Al_2O_3-based composite catalysts here reported with other γ-Al_2O_3-based catalysts proposed in the literature may be difficult due to the important differences in terms of reactions conditions (*e.g.* GHSV, redox/acid phase ratio, pressure, temperature, and type of reactor). Nevertheless, it can be observed how γ-Al_2O_3, in comparison with other acidic catalysts like zeolites, does not show good performances in terms of DME selectivity, due to the previously mentioned deactivation of Lewis acid sites caused by water adsorption. In this regard, some authors [184] tested two different physical mixtures made up of a redox catalyst ($CuO/ZnO/Al_2O_3$) together with γ-Al_2O_3 and H-ZSM-5 as dehydration catalysts, respectively. The physical mixture with γ-Al_2O_3 showed a very low DME yield (0.4%); this value is better than the ones obtained in this thesis (0.02% for CZZ@Al_2O_3_P_SC), but it is worth of note that this is probably due to the significantly lower value of GHSV used by the authors (3000 NmL/g * h) compared to ours (48,000 NmL/g * h). Regarding bifunctional composite catalysts reported in the literature, da Silva et al. [183] developed composite catalysts based on non-mesoporous alumina with interesting results. The authors proposed two composite bifunctional catalysts synthesized by impregnating a γ-Al_2O_3 support with a CuO/ZnO redox phase using either a precipitation or a wet impregnation method. The catalyst synthesized by the precipitation approach did not show any methanol dehydration activity; on the other hand, at the same values of temperature and pressure used in this thesis (250 °C, 30 bar), the catalyst synthesized by impregnation showed a DME selectivity of 35%. Also in this case, however, the significantly lower value of GHSV used by da Silva et al. (12,000 NmL/g * h) and the lower loading of redox phase (6.9 wt%) make a direct comparison in terms of DME selectivity difficult. As regards composite bifunctional catalysts based on mesostructured γ-Al_2O_3, only four works deal with this type of materials; however, three of them focus on the DME synthesis from syngas, and only one concerns the CO_2-to-DME process [77]. The Cu/γ-Al_2O_3 bifunctional catalyst presented in [77] was tested at two different GHSV values, namely 2000 and 4000 NmL/g*h. At 2000 NmL/g*h, the catalyst showed a DME selectivity of 12.6% but at GHSV = 4000 NmL/g*h this value decreased to about 2%, strongly indicating an effect of GHSV on product selectivity, consequently explaining the low values of S_{DME} obtained on our catalysts using a much higher GHSV value (48,000 NmL/g * h).

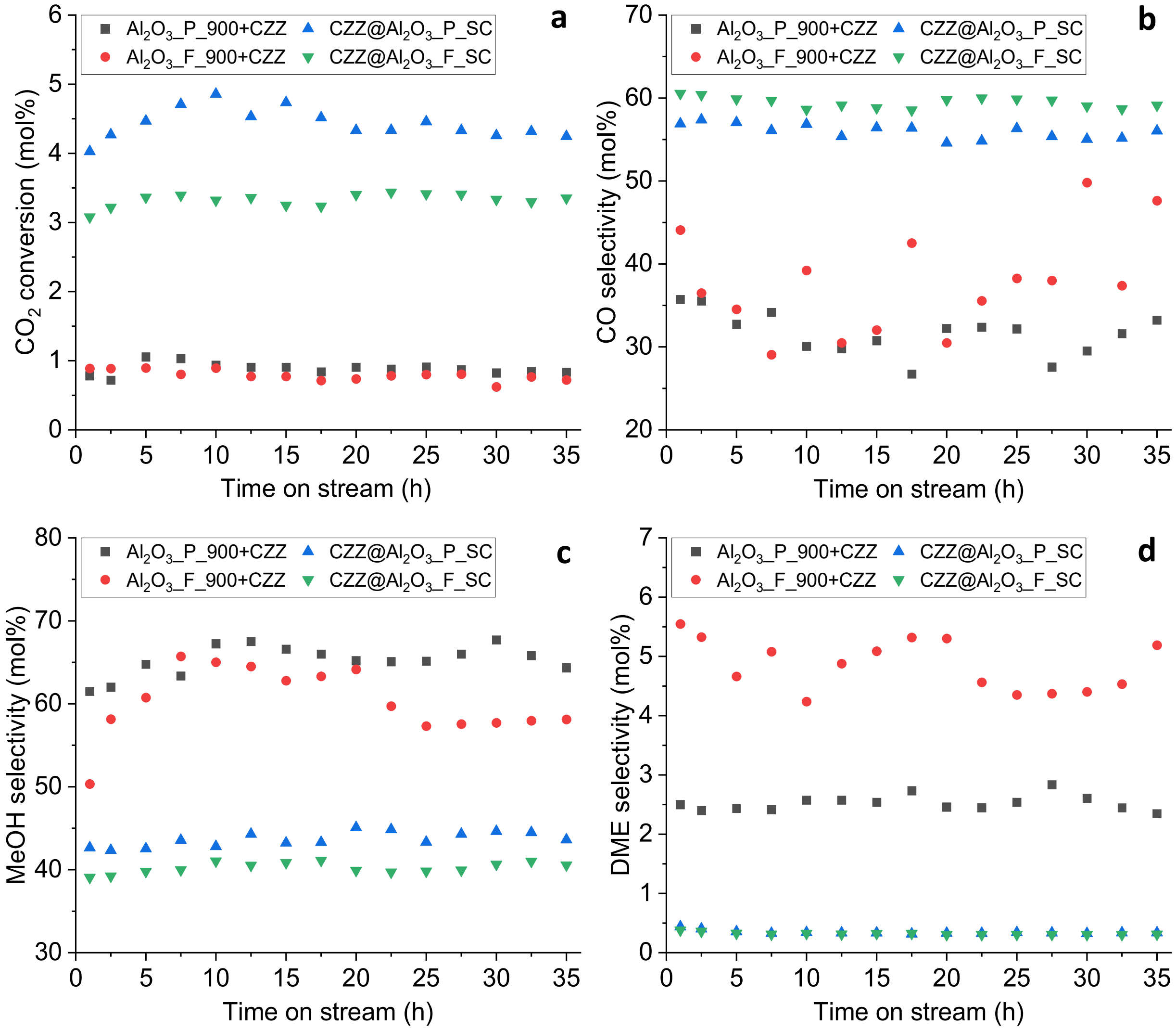

Figure 84 Values of CO_2 conversion (a) and selectivity to CO (b), methanol (c) and DME (d) over time for the composites and physical mixtures based on γ-Al_2O_3.

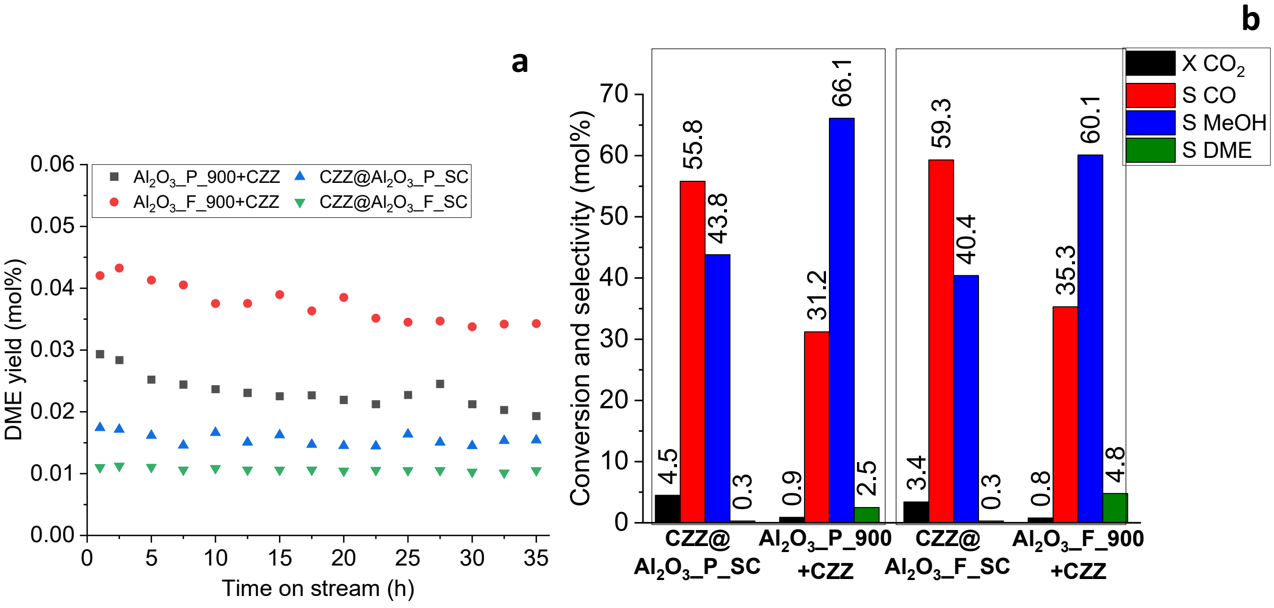

Figure 85 Values of DME yield over time (a) and mean values of CO_2 conversion and selectivity to CO, methanol and DME (b) for the composites and physical mixtures based on γ-Al_2O_3.

5.5 Conclusions

In this chapter two different impregnation approaches have been used with the aim of synthesizing bifunctional composite catalysts for the CO_2-to-DME reaction by dispersing a redox phase onto the supports described in Chapter 4. A first attempt, performed using a two-solvent impregnation on both Al-MCM-41 and Al-SBA-16, has not given promising results, since it led to the formation of large particles of redox phase outside the pores of the support material, according to XRD and TEM data. An impregnation route based on a self-combustion reaction has been applied to Al-SBA-16, by testing different loadings; in all cases this method gave rise to a homogeneous dispersion of the redox phase throughout the mesoporous structure, suggesting that the redox phase is deposited in form of a thin layer or very small nanoparticles, as indicated by the lack of diffraction peaks in WA-XRD patterns and by TEM and EDX measurements, maximizing the intimate contact between the two functions (redox-acidic). The catalytic results point out that, regarding the redox phase, a Cu/Zn ratio of 2/1 is more active than a 1/1 ratio and the addition of ZrO_2 grants a better stability of the catalyst over time.

The most promising redox phase has been than used to load mesostructured aluminosilicates and γ-Al_2O_3 supports. All the three mesostructured aluminosilicates (Al-MCM-41, Al-SBA16, Al-ABA15), as well as γ-Al_2O_3 obtained by two different Pluronics proved to be good supports, in terms of well-defined porous structure (hexagonal or cubic and narrow pore size distribution), high surface area, dispersion of aluminum into the silica network, for the dispersion of a Cu/ZnO/ZrO_2-based redox phase inside the mesopores by a self-combustion reaction.

Composite bifunctional catalysts have been compared with physical mixtures consisting of the corresponding support mixed with the unsupported CZZ redox catalyst. Composite catalysts show a higher CO_2 conversion but a lower DME selectivity if compared with the corresponding physical mixtures. The first fact can be attributed to the higher dispersion of the redox phase in form of nanoparticles, which allows a higher area of contact with the reagents and thus a higher conversion. The second finding can be ascribed to the coverage of the acidic sites of the mesostructured supports after the functionalization process with the redox phase, which decreases the ability of the system to adsorb and dehydrate methanol.

Conclusions and future perspectives

This thesis aims to contribute to the field of carbon capture and use (CCU) technologies by developing, synthesizing, and carefully characterizing new porous catalysts with well-designed features on the mesoscale for the one pot CO_2-to-DME conversion. Particular attention has been paid on the development of acidic mesostructured materials to be used as dehydration catalysts or bifunctional catalysts when coupled with a redox phase incorporated (chemical mixture) or in simple contact (physical mixture). By changing the chemical composition and textural properties of the diverse mesostructures it has been possible to correlate the material features, the acidic properties, and the catalytic activities with the aim of understanding how catalytic performances are affected by the nature of the contact between the redox and the acidic functions and determining the key-parameters governing the entire process.

A first comparison has been done between a commercial zeolite ferrierite (microporous crystalline aluminosilicate), the most promising methanol dehydration catalyst to date, and three different mesostructured acidic catalysts, namely an aluminosilicate (Al-MCM-41, prepared with a room temperature sol-gel route), a TiO_2 in anatase phase, and a Zr-TiO_2 mixed oxide (both synthesized with an EISA approach). The characterization of acid sites, performed by the combined use of ammonia-adsorption microcalorimetry and FTIR-monitored pyridine adsorption, evidences the presence of only Brønsted acidic sites in ferrierite; TiO_2 and Zr-TiO_2, on the other hand, only feature Lewis acidic sites, while Al-MCM-41 presents both the typologies of sites. Due to the high amount of isoenergetic Brønsted sites, as a consequence of its crystalline nature, the zeolite ferrierite shows the best catalytic performances in terms of selectivity to DME. Al-MCM-41 and Zr-TiO_2, both amorphous oxides, have very similar amounts of acid sites, but Zr-TiO_2 features only Lewis sites, while Al-MCM-41 has also Brønsted sites. Since Al-MCM-41 shows better performances than Zr-TiO_2, the higher activity has been attributed to the presence of Brønsted sites that, also according to the literature, have demonstrated to be much more active than Lewis sites for methanol dehydration. Regarding TiO_2, it shows a very high amount of Lewis sites and most of the sites feature a high strength; on the other hand, Zr-TiO_2 shows a much lower amount of sites and also a lower acidic strength, indicating how the substitution of Ti by Zr in TiO_2 causes a decrease in both the number and the strength of acid sites. While the two oxides show comparable mean values of DME selectivity, TiO_2 gradually loses performance over time, presumably due to the deactivation of its Lewis sites as a consequence of water adsorption, more prominent in the case of strong Lewis sites.

Zr-TiO_2, on the other hand, shows stable performances, suggesting a higher water resistance of the moderate and weak Lewis sites than the strong ones.

Since Al-MCM-41 has demonstrated to be the most promising mesostructured acidic catalyst, a second study has been focused on different aluminosilicates with the same Si/Al ratio (=15) and different textural properties. The studied systems are Al-MCM-41 (synthesized by a sol-gel route), Al-SBA-16 (prepared with an EISA approach), and Al-SBA-15 (obtained with a solvothermal sol-gel method). These systems have been compared with two mesostructured γ-Al_2O_3 samples, obtained by two different Pluronics (P123, F127). The characterization of the acid sites points out that the aluminosilicates show the presence of both Brønsted and Lewis acid sites, while γ-Al_2O_3 only shows Lewis sites. As expected from the previous results, the aluminosilicates show much higher activity towards methanol dehydration than γ-Al_2O_3, thanks to the presence of Brønsted sites. The three aluminosilicates show similar amounts of Brønsted sites, but important differences can be observed for Lewis sites; particularly Al-MCM-41 shows the highest number of Lewis sites, while Al-SBA-16 shows the lowest amount. Despite this difference, Al-SBA-16 features the highest DME selectivity among all mesostructured aluminosilicates, also showing a global DME + MeOH selectivity higher than that of ferrierite, thanks to its low selectivity to CO. Al-SBA-16 also shows the highest surface density of acid sites (*i.e.* the amount of sites as a function of the surface area of the catalyst) among all aluminosilicates. These results suggest that the key factor to obtain good dehydration catalysts is the surface density of acid sites, rather than their number; indeed, being methanol dehydration a bimolecular reaction, it can be assumed that the proximity of acid sites plays a fundamental role in promoting this reaction.

The aluminosilicates and the γ-Al_2O_3 samples have been used as supports to prepare bifunctional composite catalysts by incorporating a Cu-based redox phase onto them. First, a two-solvent impregnation route has been used on both Al-MCM-41 and Al-SBA-16; this method, however, has not shown promising results, since a heterogeneous composite has been obtained with the redox phase in form of large particles outside the pores. More interesting results have been obtained using an impregnation process based on a self-combustion reaction, which allowed to obtain a homogeneous dispersion of the redox phase in form of either an amorphous layer or small nanoparticles inside the mesopores. Catalytic tests on bifunctional composites based on Al-SBA-16 have pointed out that a CuO/ZnO ratio of 2/1 shows a higher CO_2 conversion than a 1/1 ratio and that the addition of ZrO_2 to the redox phase enhances the stability of the catalyst. The self-combustion impregnation has then been used on all the three mesostructured aluminosilicates and on the two mesostructured γ-Al_2O_3 samples; all of them have proved to be good supports for the homogeneous dispersion of a Cu/ZnO/ZrO_2-based (CZZ) redox phase inside the mesopores. All the composite bifunctional catalysts (chemical mixtures) have been tested and compared with physical mixtures consisting of the CZZ redox phase (obtained by a sol-gel self-combustion procedure in the absence of the support) and the acidic mesostructured catalyst. Composite catalysts show a higher CO_2 conversion if compared with the corresponding physical mixtures. This finding can be attributed to the higher dispersion of the redox phase in form of nanoparticles in the case of composites, which leads to a higher area of contact with the reactants and thus a higher conversion. However, composite catalysts also show a lower DME selectivity; this result can be ascribed to the coverage of the acid sites of the mesostructured supports after the functionalization process, which decreases the ability of the system to adsorb and dehydrate methanol.

With the aim of improving the acidic properties and, consequently, the catalytic performances of the acidic supports, a study on the effect of the Si/Al ratio, varying the amount of Al precursor to obtain Si/Al ratios ranging from 10 to 20 on Al-MCM-41, Al-SBA-15 and Al-SBA-16 is currently in progress.

In light of the above, future experiments will involve an optimization of the loading of the composite catalysts, in order to reduce the coverage of the acid sites which lower the methanol dehydration activity. Also, the use of non-acidic mesostructured supports (MCM-41, SBA-15) may be the ideal condition to disperse a redox phase, obtaining highly active redox catalysts to be used in form of physical mixtures with dehydration catalysts, not leading to the coverage of acid sites. Furthermore, to lower the costs of the synthesis of the mesostructured silicas, sustainable synthetic routes involving the use of waste as silicon precursor and the recovering of the SDAs will be considered, taking into account the recent results obtained for MCM-41 from hexafluorosilicic acid [130], a waste from the fertilizers industrial chain. Considering the high dehydration activity of zeolites, future attempts will be focused also on the synthesis of zeolites using silicon and aluminum industrial wastes. As new future perspectives, this thesis is the starting point for the development of mesostructured catalysts for other CO_2 conversion processes. Preliminary results have pointed out that mesostructured silica as well as mesostructured alumina can be successfully used as supports to obtain very promising CO_2 methanation catalysts (high CO_2 conversion and high stability over time), consisting of Ni- and Ni/CeO_2-based composites prepared with the impregnation strategies selected in this thesis.

Appendix

Chemicals, characterization techniques, methods, and experimental setup

This section is devoted to the details on the chemicals, instruments, characterization techniques and scale-lab plant to test the materials for CO_2 conversion to DME employed during the PhD work.

A1. Chemicals

All chemicals employed were used as received without further purification. Hexadecyltrimethylammonium bromide (CTAB, 98%), poly(ethylene glycol)-block-poly(propylene glycol)-block-poly(ethylene glycol) (PEG-PPG-PEG, Average MW=5800 g·mol−1, Pluronic® P-123), ethanol (EtOH, azeotropic 95.6% and EtOH, absolute >99.8%), titanium (IV) isopropoxide $Ti(OPr)_4$, 97%, tetraethyl orthosilicate (TEOS, 98%), ammonia solution (28–30% wt% of NH_3 in H_2O), hydrochloric acid (HCl, 36.5–38.0% wt%), Nitric acid (HNO_3) ≥65% (Honeywell Fluka), sulfuric acid (H_2SO_4, 95.0–98.0 wt%) were purchased from Sigma-Aldrich. Aluminum chloride hexahydrate ($AlCl_3·6H_2O$) 99% (Alfa Aesar), aluminum isopropoxide >98% (Alfa Aesar), aluminum nitrate nonahydrate ($Al(NO_3)_3·9H_2O$) >98% (VWR BDH Chemicals), zirconium (IV) tert-butoxide $Zr(OBu)_4$, 97%. Copper-based methanol synthesis catalyst (CZA), and zeolite ferrierite with molar ratio SiO_2:Al_2O_3 20:1 were supplied by Alpha Aesar. Copper nitrate ($Cu(NO_3)_2$ $2.5H_2O$, Aldrich, 98%) zinc nitrate ($Zn(NO_3)_2$ $6H_2O$, 98%), $ZrO(NO_3)_2$ xH_2O (Aldrich, 99%), glycine (Aldrich, 99%) were used for the self-combustion based-synthesis.

A2. Small-Angle (SA-XRD) and Wide-angle (WA-XRD) Powder X ray diffraction

The mesostructured supports were studied by **Small-Angle XRD (SA-XRD)** to get information about the ordering of the mesoporous channels and the active phase incorporated or deposited into/onto the porous supports. For this reason, the X-ray scattering phenomena have been exploited in the "small-angle mode": the X-rays are collimated towards the sample in the 0.4°-6 angular range paying attention to the use of proper slits in order to avoid any damage of the detector. Indeed, in this angular range, according to the Bragg's equation, it is possible to investigate distances in the 1.5 - 10 nm range, which is the magnitude order of magnitude of the d-spacings in the hexagonal and cubic porous lattices of mesostructured SBA15, SBA16 and MCM-41. The lattice parameter of the mesostructured was calculated using the equations $a_0 = \frac{2d_{100}}{\sqrt{3}}$ and $a_0 = d_{110}\sqrt{2}$ for the samples featuring a hexagonal structure (Al-MCM-41, Al-SBA-15, TiO_2, $Ti_xZr_yO_2$ and γ-Al_2O_3) and a cubic one (Al-SBA-16), respectively.

Small-angle (SA-XRD, 2θ = 0.7° – 6°) X-ray diffraction patterns were collected on a Seifert X3000 instrument with a θ−θ geometry and a Cu anode.

Wide-angle X-ray diffraction (WA-XRD, 2θ = 10°- 80°) patterns were recorded using a PANalytical X'pert Pro (Malvern PANalytical, Malvern, UK) equipped with Cu Kα radiation (1.5418 Å). WA-XRD measurements were employed to verify the effectiveness of the impregnation process, i.e. to check the presence of the reflections typical of metal phases guest into/over the support, to get information about their crystallinity and, whether it is possible, to identify the specific crystalline phase and to estimate the crystallite size. Particle size is calculated by Scherrer's equation:

$$< D_{XRD} >= \frac{K \cdot \lambda}{\beta \cdot cos\theta}$$

where K, is a constant taking into account the crystallite shape, λ is the wavelength of the X-rays and β is the half-maximum line breadth of the peak. The crystallite size of mesostructured titania were calculated by using Scherrer equation.

Rietveld refinement were carried out on the XRD pattern of mesostructured γ-Al_2O_3 and unsupported CZZ using the software MAUD [199]. LaB_6 from NIST was used as standard reference for determining the instrumental parameters.

A3. N_2-physisorption

The textural properties as surface area, pore volume, mean pore diameter and pore size distribution have been obtained by N_2-physisorption. All nitrogen adsorption–desorption isotherms have been obtained at 77 K by means of a Micromeritics 2020 system. Prior to the nitrogen physisorption analyses, ferrierite and Al-MCM-41, Al-SBA15, Al-SBA16 and the corresponding composites were thermally treated for 12 h under vacuum at 250 °C (heating rate, 1 °C min^{-1}), while TiO_2 and TiO_2/ZrO_2 samples were heated at 120 °C. The Brunauer–Emmett–Teller (BET) specific surface area (SA) was determined from the adsorption data in the 0.05-0.25 P/P_0 range for Al-SBA-15, Al-SBA16, γ–Al_2O_3-based samples, in the 0.05-0.17 P/P_0 range for those based on Al-MCM-41 and in the 0.05–

0.3 for the TiO_2/ZrO_2 samples. The total pore volume (V_p) was calculated at $P/P_0 = 0.9975$, and the Barrett–Joyner–Halenda (BJH) model was applied to the desorption branch isotherm to determine the mean pore diameter (D_p) for all samples but Al-SBA-16 for which the adsorption branch was used instead. The pore wall thickness (T_w) was calculated as the difference $T_w = a_0 - D_p$ or $T_w = a_0 \frac{\sqrt{3}}{2} - D_p$ for the samples with a hexagonal meso-order or a cubic one, respectively [188], [198]

Due to the microporous features of ferrierite, the specific surface area was estimate by using the Dubinin-Radushkevich model and the total pore volume and pore size by the Horvath-Kawazoe model.

A4. Transmission electron microscopy (TEM)

The morphology, the textural properties, the microanalysis and the distribution of the different phases in the composites were studied by TEM. TEM images were obtained on a JEOL JEM 1400-PLUS microscope operating at an accelerating voltage of 120 kV equipped with EDX detector and and on a field emission gun FEI TALOS F200S microscope at an acceleration voltage of 200 kV. The FEI TALOS F200S instrument is equipped with an integrated EDS system with two silicon drift detectors, for qualitative and semi-quantitative chemical analysis. Finely ground powders of the samples were first dispersed in n-octane and sonicated. The resulting suspensions were dropped onto 200 mesh carbon-coated copper (Cu-free samples) or nickel grids (Cu-bearing samples).

A5. FTIR-monitored pyridine adsorption

The nature (Lewis or Brønsted) and the amount of acidic acid sites of the materials were studied by Fourier Transform Infrared spectroscopy (FT-IR) measurements in the presence of a probe molecule, namely pyridine (Py-FTIR) employing a Nicolet iS50 spectrometer manufactured by Thermo Fischer Scientific. The spectrometer was equipped with a custom-made glass cell (Figure 86); the sample can be positioned in two different sections of the cell, to be either thermally treated or to undergo the acquisition of the FTIR spectrum. The cell was kept under high vacuum ($<1.3\cdot10^{-3}$ Pa) by a rotative pump and a turbomolecular pump. FT-IR spectra were acquired with a range between 1700 cm^{-1} and 1400 cm^{-1}. Before the analysis, 15-20 mg of each sample were pressed with a hydraulic press (2500-3000 kg for 2-3 minutes) to form a circular self-supported pellet with a diameter of 13 mm, inserted into the cell and then subjected to a thermal treatment at 250 °C for 1 h (with a 7.5 °C/min ramp) under high vacuum in order to ensure a total desorption of the water molecules previously adsorbed on the sample. The sample was subsequently put in the measurement position, let to cool down to room temperature constantly keeping it under high vacuum, and its spectrum was acquired as a background. The sample was subsequently brought to saturation, bringing the whole cell at a pressure of about 267 Pa with pyridine for about 10 min. After evacuating the cell at room temperature, the spectrum of the sample was acquired; the spectrum of the sample was subsequently acquired again after heating the sample at various temperatures (100 °C, 200 °C, 300 °C) under high vacuum. After each thermal treatment, the sample was let to cool down to room temperature before acquiring the spectrum. The thermal treatments performed at increasing values of temperature allowed to quantify the progressive desorption of pyridine from the acid sites of the sample. The areas of IR signals corresponding to each type of acid sites were used to determine the quantity of acid sites still occupied by pyridine at each temperature. Namely, the band located at about 1455 cm^{-1} was used to determine the amount of Lewis acid sites, using an Integrated Molar Extinction Coefficient (IMEC) of 2.22 cm/μmol; the band located at about 1545 cm^{-1} was used to quantify the Brønsted acid sites, with an IMEC of 1.67 cm/μmol [168].

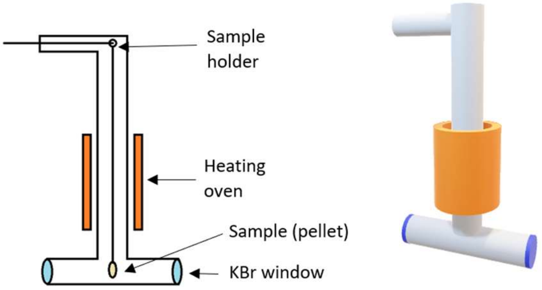

Figure 86 Glass cell used for FTIR-monitored pyridine adsorption.

A6. NH_3 adsorption microcalorimetry

A Tian-Calvet heat flow calorimeter (Setaram) equipped with a volumetric vacuum line was employed for the ammonia microcalorimetric measurements. Each sample (0.1 g, 40-80 mesh) were thermally pre-treated for 12h at 300 °C under vacuum (1 Pa) prior to the introduction of successive small amounts of the probe gas (ammonia). The equilibrium pressure relative to each adsorbed amount was measured by means of a differential pressure gauge (Datametrics) and the thermal effect recorded. The run was stopped at a final equilibrium pressure of ca. 133 Pa. The adsorption temperature was maintained at 80 °C in order to limit physisorption phenomena. After overnight outgassing at 80°C, a second run was carried out. The adsorption and calorimetric isotherms were obtained from each adsorption run. The adsorption isotherm (relating the amount of probe gas with the corresponding equilibrium pressure) and the calorimetric isotherm (relating the integral heat of adsorption with the corresponding equilibrium pressure) were obtained from each adsorption run. The overall uptake of the probe gas on the solid was assessed from the first isotherm ($n_{A,tot}$); the amount of the probe gas irreversibly adsorbed ($n_{A,irr}$) was calculated by subtracting the second isotherm, obtained after outgassing the sample, from the first one. Combining the adsorption and calorimetric data, a plot of the differential heat of adsorption as a function of the adsorbed amount was drawn, which gave information on the influence of the surface coverage on the energetics of the adsorption.

A7. Catalytic Tests

The DME synthesis experiments were carried out in a customized Microactivity Effi (PID Eng&Tech) bench-scale plant Figure 88, employing a high-pressure fixed-bed stainless steel reactor (length 304.8 mm, inner diameter 9.1 mm). A porous plate (made of Hastelloy C, 20 µm) and quartz wool were used to support the catalytic bed inside the isothermal temperature zone of the reactor.

When the catalytic tests were carried out using physical mixtures of catalysts both the redox and the dehydration catalysts were first separately ground into an agate mortar to obtain fine powders, and then mixed together with the inert α-Al_2O_3 using a steel spatula inside a Teflon weighing boat.

To exclude any possible effect of the inert material on catalytic tests, a blank test was performed, pointing out the lack of any catalytic activity for α-Al_2O_3 (Figure 87). The test was carried out using 3.2 g of α-Al_2O_3 at 250 °C, 30 bar.

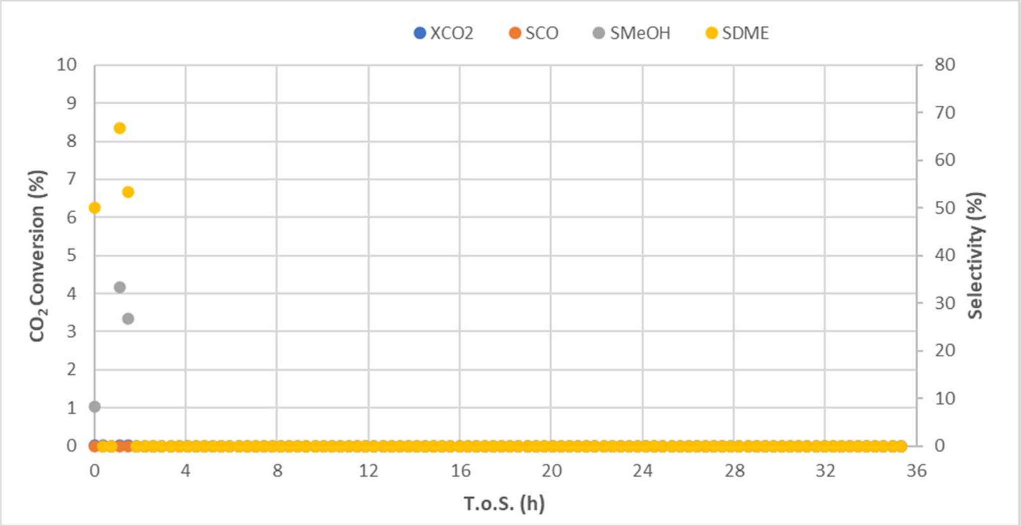

Figure 87 Blank catalytic test on the inert material α-Al_2O_3.

Before the catalytic tests, all fresh catalysts were reduced *in-situ* in a stream of a H_2/N_2 mixture (H_2, 15 vol% in N_2) at 250-300 °C for 2 h under atmospheric pressure. Upon completion of the reduction process, the system was brought at 250 °C, and the reaction gas mixture containing H_2 and CO_2 (molar ratio of 3:1) and 10 vol% of N_2 (used as internal standard for gas chromatographic analysis) was fed and the pressure was allowed to reach 3.0 MPa. After allowing the system to reach the steady state in 1 h on stream, analysis was periodically performed within the run. Runs were carried out for at least 36 h. The reaction stream was analyzed by a 7890B (Agilent) gas chromatograph equipped with a flame ionized detector (FID) for carbon-containing compounds and with a thermal conductivity detector (TCD) for permanent gases. Two columns connected in series were used to identify the components of the outlet gas mixture. In particular, CO_2, methanol, DME, ethane, and propane were separated by a HP-PLOT Q (Agilent) column (length 30 m, inner diameter 0.53 mm, film thickness 40 μm), while a HP-PLOT Molesieve (Agilent) column (length 30 m, inner diameter 0.53 mm, film thickness 50 μm) was used for H_2, N_2, CH_4, and CO. To avoid condensation of condensable products, the connection lines between the plant gas outlet and gas chromatograph inlet were heated at 180 °C. CO_2 conversion (X_{CO2}), products selectivity (S_P, with P: CH_3OH, DME, or CO), and products yield (Y_P, with P: CH_3OH or DME), were calculated as follows:

$$X_{CO_2}\,(\text{mol\%}) = \frac{\left(\frac{\dot{n}_{CO_2}}{\dot{n}_{N_2}}\right)_{in} - \left(\frac{\dot{n}_{CO_2}}{\dot{n}_{N_2}}\right)_{out}}{\left(\frac{\dot{n}_{CO_2}}{\dot{n}_{N_2}}\right)_{in}} \cdot 100$$

$$S_{\mathrm{P}}(\mathrm{mol\%}) = \frac{\nu_{\mathrm{CO_2}}}{\nu_{\mathrm{P}}} \cdot \frac{\left(\frac{\dot{n}_{\mathrm{p}}}{\dot{n}_{\mathrm{N_2}}}\right)_{\mathrm{out}}}{\left(\frac{\dot{n}_{\mathrm{CO_2}}}{\dot{n}_{\mathrm{N_2}}}\right)_{\mathrm{in}} - \left(\frac{\dot{n}_{\mathrm{CO_2}}}{\dot{n}_{\mathrm{N_2}}}\right)_{\mathrm{out}}} \cdot 100$$

$$Y_{\mathrm{P}}(\mathrm{mol\%}) = \frac{\nu_{CO_2}}{\nu_{P}} \cdot \frac{\left(\frac{\dot{n}_{\mathrm{p}}}{\dot{n}_{\mathrm{N_2}}}\right)_{\mathrm{out}}}{\left(\frac{\dot{n}_{\mathrm{CO_2}}}{\dot{n}_{\mathrm{N_2}}}\right)_{\mathrm{in}}} \cdot 100$$

where $\dot{n}_{i,in}$ and $\dot{n}_{i,out}$ are the number of moles of the *i*-th species in the feed or in the gas mixture exiting from the reactor, respectively, and v_i is the stoichiometric coefficient of the *i*-th species in the corresponding balanced equation.

Feed mixture preparation (consisting in a certificate gas bottle mixture) is carried out with a dedicated mass flow controller: Bronkhorst “Mini Cori Flow” with an accuracy of ± 0.2%. The pressure control is based on a high-speed precision servo-controlled valve with an accuracy of ± 0.1 bar. In order to provide a correct measurement of uncertainty (designed to combine uncertainties from multiple variables, *i.e.* gas-chromatographic analysis and flowrates), the propagation of error has been carefully evaluated. The calculated uncertainty of the experimental flow rates together with that related to the gas-chromatographic reading of CO_2, CH_3OH, CH_3OCH_3, CO gives a value not exceeding 2%.

In order to assess the error associated with the catalytic tests, a catalytic run using commercial catalysts was performed three times obtaining a relative standard deviation in the 2-5% range for both conversion and selectivity [228].

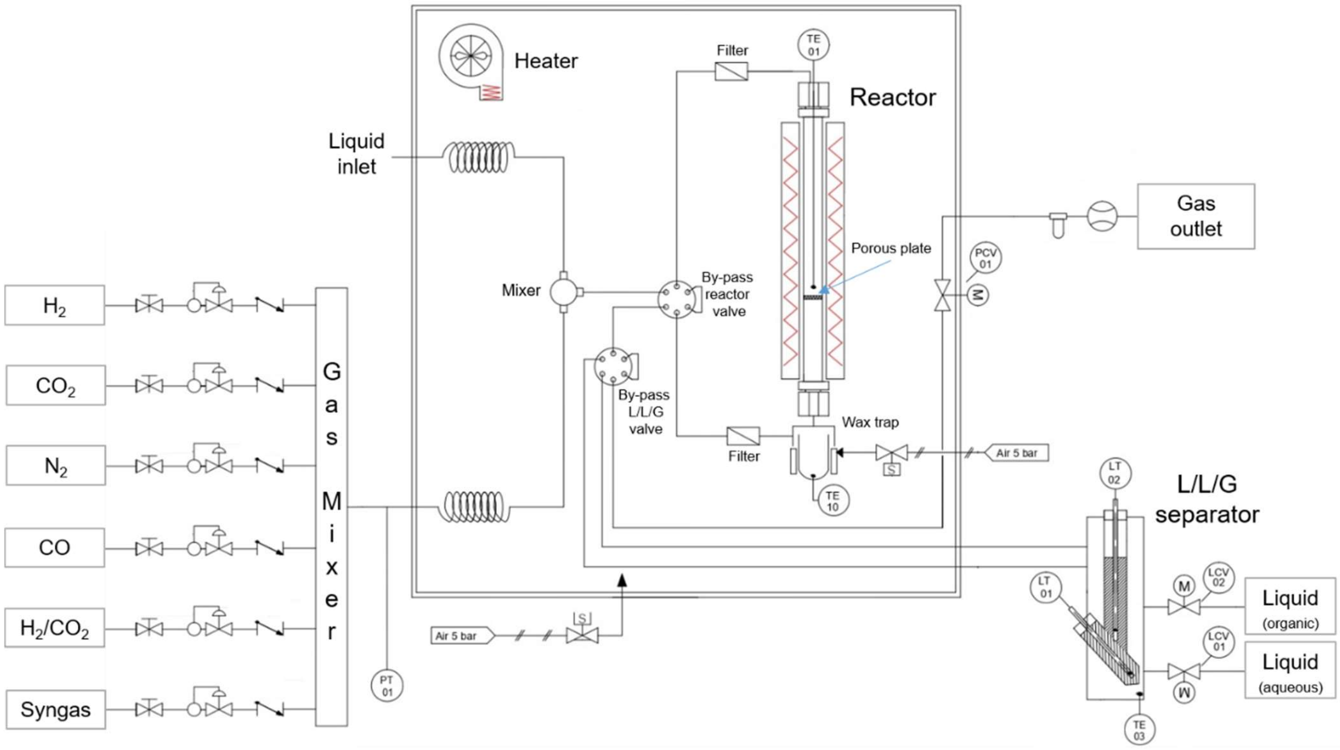

Figure 88 Schematic representation of the Microactivity Effi bench-scale plant.

References

[1] M. T. Dvorak, K. C. Armour, D. M. W. Frierson, C. Proistosescu, M. B. Baker, and C. J. Smith, "Estimating the timing of geophysical commitment to 1.5 and 2.0 °C of global warming," *Nat. Clim. Chang.*, vol. 12, no. 6, pp. 547–552, Jun. 2022.

[2] "Climate Change 2022: Impacts, Adaptation and Vulnerability," *Climate Change 2022: Impacts, Adaptation and Vulnerability*. Intergovernmental Panel on Climate Change, 2022.

[3] F. M. Baena-Moreno, M. Rodríguez-Galán, F. Vega, B. Alonso-Fariñas, L. F. Vilches Arenas, and B. Navarrete, "Carbon capture and utilization technologies: a literature review and recent advances," *Energy Sources, Part A Recover. Util. Environ. Eff.*, vol. 41, no. 12, pp. 1403–1433, 2019.

[4] H. Mikulčić *et al.*, "Flexible Carbon Capture and Utilization technologies in future energy systems and the utilization pathways of captured CO2," *Renew. Sustain. Energy Rev.*, vol. 114, no. August, 2019.

[5] I. Ghiat and T. Al-Ansari, "A review of carbon capture and utilisation as a CO2abatement opportunity within the EWF nexus," *J. CO2 Util.*, vol. 45, no. November 2020, p. 101432, 2021.

[6] A. Álvarez *et al.*, "Challenges in the Greener Production of Formates/Formic Acid, Methanol, and DME by Heterogeneously Catalyzed CO 2 Hydrogenation Processes," *Chem. Rev.*, vol. 117, no. 14, pp. 9804–9838, 2017.

[7] J. Wu and X. D. Zhou, "Catalytic conversion of CO2 to value added fuels: Current status, challenges, and future directions," *Cuihua Xuebao/Chinese J. Catal.*, vol. 37, no. 7, pp. 999–1015, 2016.

[8] A. Raza, R. Gholami, R. Rezaee, V. Rasouli, and M. Rabiei, "Significant aspects of carbon capture and storage – A review," *Petroleum*, vol. 5, no. 4, pp. 335–340, 2019.

[9] M. Aghaie, N. Rezaei, and S. Zendehboudi, "A systematic review on CO2 capture with ionic liquids: Current status and future prospects," *Renew. Sustain. Energy Rev.*, vol. 96, no.

March, pp. 502–525, 2018.

[10] L. Fu *et al.*, “Research progress on CO2 capture and utilization technology,” *J. CO2 Util.*, vol. 66, no. July, p. 102260, 2022.

[11] R. Guil-López *et al.*, “Methanol synthesis from CO2: A review of the latest developments in heterogeneous catalysis,” *Materials (Basel).*, vol. 12, no. 23, 2019.

[12] C. Mebrahtu, F. Krebs, S. Abate, S. Perathoner, G. Centi, and R. Palkovits, *CO 2 Methanation: Principles and Challenges*, 1st ed., vol. 178. Elsevier B.V., 2019.

[13] C. Liu and Z. Liu, “Perspective on CO2 Hydrogenation for Dimethyl Ether Economy,” *Catalysts*, vol. 12, no. 11, p. 1375, 2022.

[14] E. Catizzone, C. Freda, G. Braccio, F. Frusteri, and G. Bonura, “Dimethyl ether as circular hydrogen carrier: Catalytic aspects of hydrogenation/dehydrogenation steps,” *J. Energy Chem.*, vol. 58, pp. 55–77, 2021.

[15] E. Catizzone, G. Bonura, M. Migliori, F. Frusteri, and G. Giordano, “CO2 recycling to dimethyl ether: State-of-the-art and perspectives,” *Molecules*, vol. 23, no. 1, pp. 1–28, 2018.

[16] T. A. Semelsberger, R. L. Borup, and H. L. Greene, “Dimethyl ether (DME) as an alternative fuel,” *J. Power Sources*, vol. 156, no. 2, pp. 497–511, 2006.

[17] R. A. Sills, “DME as a diesel alternative in North America,” no. February, pp. 1–7, 2017.

[18] M. De Falco *et al.*, “Exergetic Analysis of DME Synthesis from CO2 and Renewable Hydrogen,” *Energies*, vol. 15, no. 10, p. 3516, May 2022.

[19] K. Saravanan, H. Ham, N. Tsubaki, and J. W. Bae, “Recent progress for direct synthesis of dimethyl ether from syngas on the heterogeneous bifunctional hybrid catalysts,” *Appl. Catal. B Environ.*, vol. 217, pp. 494–522, 2017.

[20] W. H. Chen, B. J. Lin, H. M. Lee, and M. H. Huang, “One-step synthesis of dimethyl ether from the gas mixture containing CO2 with high space velocity,” *Appl. Energy*, vol. 98, pp. 92–101, 2012.

[21] S. Bhattacharya, K. B. Kabir, and K. Hein, “Dimethyl ether synthesis from Victorian brown

coal through gasification - Current status, and research and development needs," *Prog. Energy Combust. Sci.*, vol. 39, no. 6, pp. 577–605, 2013.

[22] I. Wender, "Reactions of synthesis gas," *Fuel Process. Technol.*, vol. 48, no. 3, pp. 189–297, 1996.

[23] Y. Fu, T. Hong, J. Chen, A. Auroux, and J. Shen, "Surface acidity and the dehydration of methanol to dimethyl ether," *Thermochim. Acta*, vol. 434, no. 1–2, pp. 22–26, 2005.

[24] Y. Tai, "Lignin Fast Pyrolysis : Towards Enhanced Product Selectivities by Varying Particle Sizes of H-ZSM5 Zeolites," 2017.

[25] E. Catizzone, M. Migliori, A. Purita, and G. Giordano, "Ferrierite vs. Γ-Al2O3: The superiority of zeolites in terms of water-resistance in vapour-phase dehydration of methanol to dimethyl ether," *J. Energy Chem.*, vol. 30, pp. 162–169, 2019.

[26] A. Ghorbanpour, J. D. Rimer, and L. C. Grabow, "Computational Assessment of the Dominant Factors Governing the Mechanism of Methanol Dehydration over H-ZSM-5 with Heterogeneous Aluminum Distribution," *ACS Catal.*, vol. 6, no. 4, pp. 2287–2298, 2016.

[27] S. Hosseininejad, A. Afacan, and R. E. Hayes, "Catalytic and kinetic study of methanol dehydration to dimethyl ether," *Chem. Eng. Res. Des.*, vol. 90, no. 6, pp. 825–833, 2012.

[28] J. Li, X. Zhang, and T. Inui, : "E Improvement in the catalyst activity for direct synthesis of dimethyl ether from synthesis gas through enhancing the dispersion of CuO / ZnO / T-A1203 in hybrid catalysts," vol. 147, pp. 23–33, 1996.

[29] S. P. Naik, H. Wan, S. Bali, J. Miller, and W. W. Zmierczak, "A comparative study of ZnO-CuO-Al2O3 /SiO2-Al2O3 composite and hybrid catalysts for direct synthesis of dimethyl ether from syngas," *ACS Natl. Meet. B. Abstr.*, no. 3, pp. 9791–9794, 2009.

[30] T. Takeguchi, K. I. Yanagisawa, T. Inui, and M. Inoue, "Effect of the property of solid acid upon syngas-to-dimethyl ether conversion on the hybrid catalysts composed of Cu-Zn-Ga and solid acids," *Appl. Catal. A Gen.*, vol. 192, no. 2, pp. 201–209, 2000.

[31] S. H. Lima, A. M. S. Forrester, L. A. Palacio, and A. C. Faro, "Niobia-alumina as methanol dehydration component in mixed catalyst systems for dimethyl ether production from

syngas," *Appl. Catal. A Gen.*, vol. 488, pp. 19–27, 2014.

[32] J. Xia, D. Mao, B. Zhang, Q. Chen, Y. Zhang, and Y. Tang, "Catalytic properties of fluorinated alumina for the production of dimethyl ether," *Catal. Commun.*, vol. 7, no. 6, pp. 362–366, 2006.

[33] D. Mao, W. Yang, J. Xia, B. Zhang, and G. Lu, "The direct synthesis of dimethyl ether from syngas over hybrid catalysts with sulfate-modified γ-alumina as methanol dehydration components," *J. Mol. Catal. A Chem.*, vol. 250, no. 1–2, pp. 138–144, 2006.

[34] R. Montesano and D. Chadwick, "Combined methanol and dimethyl ether synthesis from CO/H2: Phosphorus mediated deactivation," *Catal. Commun.*, vol. 29, pp. 137–140, 2012.

[35] S. H. Kang, J. W. Bae, H. S. Kim, G. M. Dhar, and K. W. Jun, "Enhanced catalytic performance for dimethyl ether synthesis from syngas with the addition of Zr or Ga on a Cu-ZnO-Al2O3/γ-Al2O3 bifunctional catalyst," *Energy and Fuels*, vol. 24, no. 2, pp. 804–810, 2010.

[36] A. Venugopal, J. Palgunadi, J. K. Deog, O. S. Joo, and C. H. Shin, "Dimethyl ether synthesis on the admixed catalysts of Cu-Zn-Al-M (M = Ga, La, Y, Zr) and γ-Al2O3: The role of modifier," *J. Mol. Catal. A Chem.*, vol. 302, no. 1–2, pp. 20–27, 2009.

[37] F. Song, Y. Tan, H. Xie, Q. Zhang, and Y. Han, "Direct synthesis of dimethyl ether from biomass-derived syngas over Cu-ZnO-Al2O3-ZrO2(x)/γ-Al 2O3 bifunctional catalysts: Effect of Zr-loading," *Fuel Process. Technol.*, vol. 126, pp. 88–94, 2014.

[38] Y. Tan, H. Xie, H. Cui, Y. Han, and B. Zhong, "Modification of Cu-based methanol synthesis catalyst for dimethyl ether synthesis from syngas in slurry phase," *Catal. Today*, vol. 104, no. 1, pp. 25–29, 2005.

[39] J. Palgunadi, I. Yati, and K. D. Jung, "Catalytic activity of Cu-Zn-Al-Mn admixed with gamma-alumina for the synthesis of DME from syngas: Manganese effect or just method of preparation?," *React. Kinet. Mech. Catal.*, vol. 101, no. 1, pp. 117–128, 2010.

[40] M. H. Huang, H. M. Lee, K. C. Liang, C. C. Tzeng, and W. H. Chen, "An experimental study on single-step dimethyl ether (DME) synthesis from hydrogen and carbon monoxide under various catalysts," *Int. J. Hydrogen Energy*, vol. 40, no. 39, pp. 13583–13593, 2015.

[41] Z. Li, J. Li, M. Dai, Y. Liu, D. Han, and J. Wu, “The effect of preparation method of the Cu-La2O 3-ZrO2/γ-Al2O3 hybrid catalysts on one-step synthesis of dimethyl ether from syngas,” *Fuel*, vol. 121, pp. 173–177, 2014.

[42] S. Asthana, C. Samanta, A. Bhaumik, B. Banerjee, R. K. Voolapalli, and B. Saha, “Direct synthesis of dimethyl ether from syngas over Cu-based catalysts: Enhanced selectivity in the presence of MgO,” *J. Catal.*, vol. 334, pp. 89–101, 2016.

[43] Q. Zhang, Y. Z. Zuo, M. H. Han, J. F. Wang, Y. Jin, and F. Wei, “Long carbon nanotubes intercrossed Cu/Zn/Al/Zr catalyst for CO/CO2 hydrogenation to methanol/dimethyl ether,” *Catal. Today*, vol. 150, no. 1–2, pp. 55–60, 2010.

[44] H. W. Ham, M. H. Jeong, H. M. Koo, C. H. Chung, and J. W. Bae, “The role of the acidity of alumina prepared by aluminum-carbon black composite for CO hydrogenation to dimethyl ether on hybrid Cu-ZnO-Al2O3/alumina,” *React. Kinet. Mech. Catal.*, vol. 116, no. 1, pp. 173–189, 2015.

[45] H. Ham, J. Kim, S. J. Cho, J. H. Choi, D. J. Moon, and J. W. Bae, “Enhanced Stability of Spatially Confined Copper Nanoparticles in an Ordered Mesoporous Alumina for Dimethyl Ether Synthesis from Syngas,” *ACS Catal.*, vol. 6, no. 9, pp. 5629–5640, 2016.

[46] H. Jiang, H. Bongard, W. Schmidt, and F. Schüth, “One-pot synthesis of mesoporous Cu-γ-Al 2O 3 as bifunctional catalyst for direct dimethyl ether synthesis,” *Microporous Mesoporous Mater.*, vol. 164, pp. 3–8, 2012.

[47] Y. Wang *et al.*, “One-step synthesis of dimethyl ether from syngas on ordered mesoporous copper incorporated alumina,” *J. Energy Chem.*, vol. 25, no. 5, pp. 775–781, 2016.

[48] A. García-Trenco and A. Martínez, “Direct synthesis of DME from syngas on hybrid CuZnAl/ZSM-5 catalysts: New insights into the role of zeolite acidity,” *Appl. Catal. A Gen.*, vol. 411–412, pp. 170–179, 2012.

[49] M. Xu, J. H. Lunsford, D. W. Goodman, and A. Bhattacharyya, “Synthesis of dimethyl ether (DME) from methanol over solid-acid catalysts,” *Appl. Catal. A Gen.*, vol. 149, no. 2, pp. 289–301, 1997.

[50] J. Sun *et al.*, “Fabrication of active Cu-Zn nanoalloys on H-ZSM5 zeolite for enhanced dimethyl ether synthesis via syngas,” *J. Mater. Chem. A*, vol. 2, no. 23, pp. 8637–8643, 2014.

[51] D. Mao and X. Guo, “Dimethyl Ether Synthesis from Syngas over the Admixed Cu/ZnO/Al2O3 Catalyst and Alkaline Earth Oxide-Modified HZSM-5 Zeolite,” *Energy Technol.*, vol. 2, no. 11, pp. 882–888, 2014.

[52] Q. L. Xu, P. Lan, S. P. Zhang, T. C. Li, and Y. J. Yan, “Effect of modified zeolite on one-step process of DME synthesis,” *Pet. Sci. Technol.*, vol. 29, no. 5, pp. 439–448, 2011.

[53] D. Mao, J. Xia, B. Zhang, and G. Lu, “Highly efficient synthesis of dimethyl ether from syngas over the admixed catalyst of CuO-ZnO-Al2O3 and antimony oxide modified HZSM-5 zeolite,” *Energy Convers. Manag.*, vol. 51, no. 6, pp. 1134–1139, 2010.

[54] S. H. Kang, J. W. Bae, K. W. Jun, and H. S. Potdar, “Dimethyl ether synthesis from syngas over the composite catalysts of Cu-ZnO-Al2O3/Zr-modified zeolites,” *Catal. Commun.*, vol. 9, no. 10, pp. 2035–2039, 2008.

[55] J. Xia, D. Mao, B. Zhang, Q. Chen, and Y. Tang, “One-step synthesis of dimethyl ether from syngas with Fe-modified zeolite ZSM-5 as dehydration catalyst,” *Catal. Letters*, vol. 98, no. 4, pp. 235–240, 2004.

[56] Q. Xie *et al.*, “Single-step synthesis of DME from syngas on CuZnAl-zeolite bifunctional catalysts: The influence of zeolite type,” *RSC Adv.*, vol. 5, no. 33, pp. 26301–26307, 2015.

[57] L. Wang, Y. Qi, Y. Wei, D. Fang, S. Meng, and Z. Liu, “Research on the acidity of the double-function catalyst for DME synthesis from syngas,” *Catal. Letters*, vol. 106, no. 1–2, pp. 61–66, 2006.

[58] J. H. Kim, M. J. Park, S. J. Kim, O. S. Joo, and K. D. Jung, “DME synthesis from synthesis gas on the admixed catalysts of Cu/ZnO/Al 2O3 and ZSM-5,” *Appl. Catal. A Gen.*, vol. 264, no. 1, pp. 37–41, 2004.

[59] V. V. Ordomsky *et al.*, “The role of external acid sites of ZSM-5 in deactivation of hybrid CuZnAl/ZSM-5 catalyst for direct dimethyl ether synthesis from syngas,” *Appl. Catal. A Gen.*, vol. 486, pp. 266–275, 2014.

[60] M. Cai *et al.*, “Direct dimethyl ether synthesis from syngas on copper-zeolite hybrid catalysts with a wide range of zeolite particle sizes Dedicated to Professor Jean-Pierre Gilson on the occasion of his 60th birthday.,” *J. Catal.*, vol. 338, pp. 227–238, 2016.

[61] E. Catizzone *et al.*, “MFI vs. FER zeolite during methanol dehydration to dimethyl ether: The crystal size plays a key role,” *Catal. Commun.*, vol. 149, p. 106214, 2021.

[62] A. García-Trenco, A. Vidal-Moya, and A. Martínez, “Study of the interaction between components in hybrid CuZnAl/HZSM-5 catalysts and its impact in the syngas-to-DME reaction,” *Catal. Today*, vol. 179, no. 1, pp. 43–51, 2012.

[63] R. Montesano, A. Narvaez, and D. Chadwick, “Shape-selectivity effects in syngas-to-dimethyl ether conversion over Cu/ZnO/Al2O3 and zeolite mixtures: Carbon deposition and by-product formation,” *Appl. Catal. A Gen.*, vol. 482, pp. 69–77, 2014.

[64] P. S. Sai Prasad, J. W. Bae, S. H. Kang, Y. J. Lee, and K. W. Jun, “Single-step synthesis of DME from syngas on Cu-ZnO-Al2O3/zeolite bifunctional catalysts: The superiority of ferrierite over the other zeolites,” *Fuel Process. Technol.*, vol. 89, no. 12, pp. 1281–1286, 2008.

[65] G. Bonura *et al.*, “Catalytic behaviour of a bifunctional system for the one step synthesis of DME by CO2 hydrogenation,” *Catal. Today*, vol. 228, pp. 51–57, 2014.

[66] N. Mota, E. M. Ordoñez, B. Pawelec, J. L. G. Fierro, and R. M. Navarro, “Direct synthesis of dimethyl ether from co2: Recent advances in bifunctional/hybrid catalytic systems,” *Catalysts*, vol. 11, no. 4, 2021.

[67] H. Lei, R. Nie, G. Wu, and Z. Hou, “Hydrogenation of CO2 to CH3OH over Cu/ZnO catalysts with different ZnO morphology,” *Fuel*, vol. 154, pp. 161–166, 2015.

[68] E. L. Kunkes, F. Studt, F. Abild-Pedersen, R. Schlögl, and M. Behrens, “Hydrogenation of CO2 to methanol and CO on Cu/ZnO/Al2O3: Is there a common intermediate or not?,” *J. Catal.*, vol. 328, pp. 43–48, 2015.

[69] C. Tisseraud *et al.*, “The Cu-ZnO synergy in methanol synthesis from CO2, Part 2: Origin of the methanol and CO selectivities explained by experimental studies and a sphere contact quantification model in randomly packed binary mixtures on Cu-ZnO coprecipitate

catalysts," *J. Catal.*, vol. 330, pp. 533–544, 2015.

[70] I. Miletto *et al.*, "In situ FT-IR characterization of CuZnZr/ferrierite hybrid catalysts for one-pot CO2-to-DME conversion," *Materials (Basel).*, vol. 11, no. 11, 2018.

[71] G. Prieto, J. Zečević, H. Friedrich, K. P. De Jong, and P. E. De Jongh, "Towards stable catalysts by controlling collective properties of supported metal nanoparticles," *Nat. Mater.*, vol. 12, no. 1, pp. 34–39, 2013.

[72] M. Mureddu, F. Ferrara, and A. Pettinau, "Highly efficient CuO/ZnO/ZrO2@SBA-15 nanocatalysts for methanol synthesis from the catalytic hydrogenation of CO2," *Appl. Catal. B Environ.*, vol. 258, no. March, 2019.

[73] C. Cara *et al.*, "On the design of mesostructured acidic catalysts for the one-pot dimethyl ether production from CO2," *J. CO2 Util.*, vol. 62, no. April, p. 102066, 2022.

[74] C. Temvuttirojn *et al.*, "Development of SO42−–ZrO2 acid catalysts admixed with a CuO-ZnO-ZrO2 catalyst for CO2 hydrogenation to dimethyl ether," *Fuel*, vol. 241, no. September 2018, pp. 695–703, 2019.

[75] Y. Suwannapichat *et al.*, "Direct synthesis of dimethyl ether from CO2 hydrogenation over novel hybrid catalysts containing a Cu–ZnO–ZrO2 catalyst admixed with WOx/Al2O3 catalysts: Effects of pore size of Al2O3 support and W loading content," *Energy Convers. Manag.*, vol. 159, no. January, pp. 20–29, 2018.

[76] T. Witoon, P. Kidkhunthod, M. Chareonpanich, and J. Limtrakul, "Direct synthesis of dimethyl ether from CO2 and H2 over novel bifunctional catalysts containing CuO-ZnO-ZrO2 catalyst admixed with WOx/ZrO2 catalysts," *Chem. Eng. J.*, vol. 348, no. May, pp. 713–722, 2018.

[77] H. Ham, S. W. Baek, C. H. Shin, and J. W. Bae, "Roles of Structural Promoters for Direct CO 2 Hydrogenation to Dimethyl Ether over Ordered Mesoporous Bifunctional Cu/M-Al 2 O 3 (M = Ga or Zn)," *ACS Catal.*, vol. 9, no. 1, pp. 679–690, 2019.

[78] C. Niamnuy *et al.*, "Synthesis of Dimethyl Ether via CO2 Hydrogenation: Effect of the Drying Technique of Alumina on Properties and Performance of Alumina-Supported Copper

Catalysts," *ACS Omega*, vol. 5, no. 5, pp. 2334–2344, 2020.

[79] S. P. Naik, V. Bui, T. Ryu, J. D. Miller, and W. Zmierczak, "Al-MCM-41 as methanol dehydration catalyst," *Appl. Catal. A Gen.*, vol. 381, no. 1–2, pp. 183–190, 2010.

[80] Y. Sang, H. Li, M. Zhu, K. Ma, Q. Jiao, and Q. Wu, "Catalytic performance of metal ion doped MCM-41 for methanol dehydration to dimethyl ether," *J. Porous Mater.*, vol. 20, no. 6, pp. 1509–1518, 2013.

[81] Y. Xu, P. Yang, H. Zhang, and Z. Deng, "Atomic layer deposition synthesis of alumina-modified SBA-15 and its catalytic reactivity toward methanol dehydration," *Synth. React. Inorganic, Met. Nano-Metal Chem.*, vol. 41, no. 8, pp. 1033–1038, 2011.

[82] Q. Jiang, Y. Liu, T. Dintzer, J. Luo, K. Parkhomenko, and A. C. Roger, "Tuning the highly dispersed metallic Cu species via manipulating Brønsted acid sites of mesoporous aluminosilicate support for CO2 hydrogenation reactions," *Appl. Catal. B Environ.*, vol. 269, no. January, p. 118804, 2020.

[83] S. Ren *et al.*, "Enhanced catalytic performance of Zr modified CuO/ZnO/Al2O3 catalyst for methanol and DME synthesis via CO2 hydrogenation," *J. CO2 Util.*, vol. 36, no. October 2019, pp. 82–95, 2020.

[84] X. An, Y. Z. Zuo, Q. Zhang, D. Z. Wang, and J. F. Wang, "Dimethyl ether synthesis from CO2 hydrogenation on a CuO-ZnO-Al2O3-ZrO2/HZSM-5 bifunctional catalyst," *Ind. Eng. Chem. Res.*, vol. 47, no. 17, pp. 6547–6554, 2008.

[85] S. Ren, S. Li, N. Klinghoffer, M. Yu, and X. Liang, "Effects of mixing methods of bifunctional catalysts on catalyst stability of DME synthesis via CO2 hydrogenation," *Carbon Resour. Convers.*, vol. 2, no. 1, pp. 85–94, 2019.

[86] G. Bonura *et al.*, "Acidity control of zeolite functionality on activity and stability of hybrid catalysts during DME production via CO2 hydrogenation," *J. CO2 Util.*, vol. 24, no. March, pp. 398–406, 2018.

[87] F. Frusteri *et al.*, "Direct CO2-to-DME hydrogenation reaction: New evidences of a superior behaviour of FER-based hybrid systems to obtain high DME yield," *J. CO2 Util.*, vol. 18, pp.

353–361, 2017.

[88] M. A. T. and M. T. S. Lowell, J. E. Shields, *Characterization of porous solids and powders: surface area, pore size, and density*, vol. 16, no. 09. Springer Netherlands, 2004.

[89] A. Taguchi and F. Schüth, “Ordered mesoporous materials in catalysis,” *Microporous Mesoporous Mater.*, vol. 77, no. 1, pp. 1–45, Jan. 2005.

[90] B. Zhou, B. Shi, D. Jin, and X. Liu, “Controlling upconversion nanocrystals for emerging applications,” *Nat. Nanotechnol.*, vol. 10, no. 11, pp. 924–936, Nov. 2015.

[91] F. Di Renzo, H. Cambon, and R. Dutartre, “A 28-year-old synthesis of micelle-templated mesoporous silica,” *Microporous Mater.*, vol. 10, no. 4–6, pp. 283–286, 1997.

[92] J. S. Beck *et al.*, “A new family of mesoporous molecular sieves prepared with liquid crystal templates,” *J. Am. Chem. Soc.*, vol. 114, no. 27, pp. 10834–10843, Dec. 1992.

[93] L. Wang, W. Ding, and Y. Sun, “The preparation and application of mesoporous materials for energy storage,” *Mater. Res. Bull.*, vol. 83, pp. 230–249, Nov. 2016.

[94] J. H. Pan, X. S. Zhao, and W. I. Lee, “Block copolymer-templated synthesis of highly organized mesoporous TiO2-based films and their photoelectrochemical applications,” *Chem. Eng. J.*, vol. 170, no. 2–3, pp. 363–380, Jun. 2011.

[95] Y. Wan and Zhao, “On the Controllable Soft-Templating Approach to Mesoporous Silicates,” *Chem. Rev.*, vol. 107, no. 7, pp. 2821–2860, Jul. 2007.

[96] Q. Huo *et al.*, “Organization of Organic Molecules with Inorganic Molecular Species into Nanocomposite Biphase Arrays,” *Chem. Mater.*, vol. 6, no. 8, pp. 1176–1191, 1994.

[97] B. Samiey, C.-H. Cheng, and J. Wu, “Organic-Inorganic Hybrid Polymers as Adsorbents for Removal of Heavy Metal Ions from Solutions: A Review,” *Materials (Basel).*, vol. 7, no. 2, pp. 673–726, Jan. 2014.

[98] Y. Lu *et al.*, “Continuous formation of supported cubic and hexagonal mesoporous films by sol–gel dip-coating,” *Nature*, vol. 389, no. 6649, pp. 364–368, Sep. 1997.

[99] F. Hoffmann, M. Cornelius, J. Morell, and M. Fröba, “Silica-Based Mesoporous Organic–

Inorganic Hybrid Materials," *Angew. Chemie Int. Ed.*, vol. 45, no. 20, pp. 3216–3251, May 2006.

[100] D. Zhao, Y. Wan, and W. Zhou, *Ordered Mesoporous Materials*. Wiley-VCH, 2013.

[101] C. J. Brinker, Y. Lu, A. Sellinger, and H. Fan, "Evaporation-Induced Self-Assembly: Nanostructures Made Easy," *Adv. Mater.*, vol. 11, no. 7, pp. 579–585, 1999.

[102] M. Chen, H. Xuan, X. Zheng, J. Liu, X. Dong, and F. Xi, "N-doped mesoporous carbon by a hard-template strategy associated with chemical activation and its enhanced supercapacitance performance," *Electrochim. Acta*, vol. 238, pp. 269–277, 2017.

[103] A. Stein, F. Li, and N. R. Denny, "Morphological Control in Colloidal Crystal Templating of Inverse Opals, Hierarchical Structures, and Shaped Particles," *Chem. Mater.*, vol. 20, no. 3, pp. 649–666, Feb. 2008.

[104] D. Gu and F. Schüth, "Synthesis of non-siliceous mesoporous oxides," *Chem. Soc. Rev.*, vol. 43, no. 1, pp. 313–344, 2014.

[105] D. M. Antonelli and J. Y. Ying, "Synthesis of Hexagonally Packed Mesoporous TiO2 by a Modified Sol–Gel Method," *Angew. Chemie Int. Ed. English*, vol. 34, no. 18, pp. 2014–2017, Oct. 1995.

[106] P. D. Yang, D. Y. Zhao, D. I. Margolese, B. F. Chmelka, and G. D. Stucky, "Generalized syntheses of large-pore mesoporous metal oxides with semicrystalline frameworks," *Nature*, vol. 396, no. 6707, pp. 152–155, Nov. 1998.

[107] Z. Miao, H. Zhao, J. Yang, J. Zhao, H. Song, and L. Chou, "One-pot synthesis of ordered mesoporous transition metal–zirconium oxophosphate composites with excellent textural and catalytic properties," *New J. Chem.*, vol. 39, no. 2, pp. 1322–1329, 2015.

[108] N. Pal and A. Bhaumik, "Soft templating strategies for the synthesis of mesoporous materials: Inorganic, organic-inorganic hybrid and purely organic solids," *Adv. Colloid Interface Sci.*, vol. 189–190, pp. 21–41, 2013.

[109] E. L. Crepaldi, G. J. de A. A. Soler-Illia, D. Grosso, F. Cagnol, F. Ribot, and C. Sanchez, "Controlled Formation of Highly Organized Mesoporous Titania Thin Films: From

Mesostructured Hybrids to Mesoporous Nanoanatase TiO 2," *J. Am. Chem. Soc.*, vol. 125, no. 32, pp. 9770–9786, Aug. 2003.

[110] R. Zhang, B. Tu, and D. Zhao, "Synthesis of highly stable and crystalline mesoporous anatase by using a simple surfactant sulfuric acid carbonization method," *Chem. - A Eur. J.*, vol. 16, no. 33, pp. 9977–9981, 2010.

[111] D. Grosso *et al.*, "Fundamentals of Mesostructuring Through Evaporation-Induced Self-Assembly," *Adv. Funct. Mater.*, vol. 14, no. 4, pp. 309–322, Apr. 2004.

[112] J. Lee, M. Christopher Orilall, S. C. Warren, M. Kamperman, F. J. DiSalvo, and U. Wiesner, "Direct access to thermally stable and highly crystalline mesoporous transition-metal oxides with uniform pores," *Nat. Mater.*, vol. 7, no. 3, pp. 222–228, Mar. 2008.

[113] D. G. Bucknall and H. L. Anderson, "Polymers Get Organized," *Science (80-.).*, vol. 302, no. 5652, pp. 1904–1905, Dec. 2003.

[114] R. Zhang, B. Tu, and D. Zhao, "Synthesis of Highly Stable and Crystalline Mesoporous Anatase by Using a Simple Surfactant Sulfuric Acid Carbonization Method," *Chem. - A Eur. J.*, vol. 16, no. 33, pp. 9977–9981, Sep. 2010.

[115] G. J. de A. A. Soler-Illia, C. Sanchez, B. Lebeau, and J. Patarin, "Chemical Strategies To Design Textured Materials: from Microporous and Mesoporous Oxides to Nanonetworks and Hierarchical Structures," *Chem. Rev.*, vol. 102, no. 11, pp. 4093–4138, Nov. 2002.

[116] R. Sanz, G. Calleja, A. Arencibia, and E. S. Sanz-Pérez, "Development of high efficiency adsorbents for CO2 capture based on a double-functionalization method of grafting and impregnation," *J. Mater. Chem. A*, vol. 1, no. 6, p. 1956, 2013.

[117] R. Sanz, G. Calleja, A. Arencibia, and E. S. Sanz-Pérez, "Amino functionalized mesostructured SBA-15 silica for CO2 capture: Exploring the relation between the adsorption capacity and the distribution of amino groups by TEM," *Microporous Mesoporous Mater.*, vol. 158, pp. 309–317, Aug. 2012.

[118] S.-Y. Chen *et al.*, "Synthesis and catalytic activity of amino-functionalized SBA-15 materials with controllable channel lengths and amino loadings," *J. Mater. Chem.*, vol. 22, no. 5, pp.

2233–2243, 2012.

[119] I. G. Shenderovich *et al.*, “Pyridine- 15 N A Mobile NMR Sensor for Surface Acidity and Surface Defects of Mesoporous Silica,” *J. Phys. Chem. B*, vol. 107, no. 43, pp. 11924–11939, Oct. 2003.

[120] Y. Zhu, H. Li, Q. Zheng, J. Xu, and X. Li, “Amine-Functionalized SBA-15 with Uniform Morphology and Well-Defined Mesostructure for Highly Sensitive Chemosensors To Detect Formaldehyde Vapor,” *Langmuir*, vol. 28, no. 20, pp. 7843–7850, May 2012.

[121] J. Haber, J. H. Block, and B. Delmon, “Manual of methods and procedures for catalyst characterization (Technical Report),” *Pure Appl. Chem.*, vol. 67, no. 8–9, pp. 1257–1306, Jan. 1995.

[122] I. Lopes, N. El Hassan, H. Guerba, G. Wallez, and A. Davidson, “Size-Induced Structural Modifications Affecting Co 3 O 4 Nanoparticles Patterned in SBA-15 Silicas,” *Chem. Mater.*, vol. 18, no. 25, pp. 5826–5828, Dec. 2006.

[123] M. Imperor-Clerc, D. Bazin, M.-D. Appay, P. Beaunier, and A. Davidson, “Crystallization of β-MnO 2 Nanowires in the Pores of SBA-15 Silicas: In Situ Investigation Using Synchrotron Radiation,” *Chem. Mater.*, vol. 16, no. 9, pp. 1813–1821, May 2004.

[124] F. Boubekr, A. Davidson, S. Casale, and P. Massiani, “Ex-nitrate Co/SBA-15 catalysts prepared with calibrated silica grains: Information given by TPR, TEM, SAXS and WAXS,” *Microporous Mesoporous Mater.*, vol. 141, no. 1–3, pp. 157–166, May 2011.

[125] J. Van Der Meer, I. Bardez-Giboire, C. Mercier, B. Revel, A. Davidson, and R. Denoyel, “Mechanism of metal oxide nanoparticle loading in SBA-15 by the double solvent technique,” *J. Phys. Chem. C*, vol. 114, no. 8, pp. 3507–3515, 2010.

[126] M. Mureddu *et al.*, “ZnO/SBA-15 composites for mid-temperature removal of H 2S: Synthesis, performance and regeneration studies,” *Fuel*, vol. 102, pp. 691–700, 2012.

[127] M. Mureddu *et al.*, “MeO x /SBA-15 (Me = Zn, Fe): highly efficient nanosorbents for mid-temperature H 2 S removal,” *J. Mater. Chem. A*, vol. 2, no. 45, pp. 19396–19406, Sep. 2014.

[128] C. Cara *et al.*, “MCM-41 support for ultrasmall γ-Fe2O3 nanoparticles for H2S removal,” *J.*

Mater. Chem. A, vol. 5, no. 41, pp. 21688–21698, 2017.

[129] C. Cara *et al.*, “γ-Fe 2 O 3 -M41S Sorbents for H 2 S Removal: Effect of Different Porous Structures and Silica Wall Thickness,” *J. Phys. Chem. C*, vol. 122, no. 23, pp. 12231–12242, Jun. 2018.

[130] M. A. Vacca *et al.*, “Hexafluorosilicic Acid (FSA): from Hazardous Waste to Precious Resource in Obtaining High Value-Added Mesostructured Silica,” *ACS Sustain. Chem. Eng.*, vol. 8, no. 38, pp. 14286–14300, Sep. 2020.

[131] C. Cara *et al.*, “Anchoring ultrasmall FeIII-based nanoparticles on silica and titania mesostructures for syngas H2S purification,” *Microporous Mesoporous Mater.*, vol. 298, no. October 2019, 2020.

[132] M. Sanna Angotzi *et al.*, “Meso- and macroporous silica-based arsenic adsorbents: effect of pore size, nature of the active phase, and silicon release,” *Nanoscale Adv.*, vol. 3, no. 21, pp. 6100–6113, 2021.

[133] M. Sanna Angotzi *et al.*, “As(III, V) Uptake from Nanostructured Iron Oxides and Oxyhydroxides: The Complex Interplay between Sorbent Surface Chemistry and Arsenic Equilibria,” *Nanomaterials*, vol. 12, no. 3, p. 326, Jan. 2022.

[134] C. Cara, “Siliceous and non-siliceous mesostructured iron oxide nanocomposites for H2S removal from syngas.”

[135] D. Peddis, “Sintesi mediante metodo di autocombustione e caratterizzazione strutturale e magnetica di materiali nanostrutturati.”

[136] A. Varma, A. S. Mukasyan, A. S. Rogachev, and K. V. Manukyan, “Solution Combustion Synthesis of Nanoscale Materials,” *Chem. Rev.*, vol. 116, no. 23, pp. 14493–14586, 2016.

[137] J. Schäfer, W. Sigmund, S. Roy, and F. Aldinger, “Low temperature synthesis of ultrafine Pb(Zr, Ti)O3 powder by sol-gel combustion,” *J. Mater. Res.*, vol. 12, no. 10, pp. 2518–2521, 1997.

[138] L. R. Pederson, G. D. Maupin, W. J. Weber, D. J. McReady, and R. W. Stephens, “Combustion synthesis of YBa2Cu3O7-x: glycine/metal nitrate method,” *Mater. Lett.*, vol. 10, no. 9–10,

pp. 437–443, 1991.

[139] A. Chakraborty, P. S. Devi, S. Roy, and H. S. Maiti, “Low-temperature synthesis of ultrafine La 0.84 Sr 0.16 MnO 3 powder by an autoignition process,” *J. Mater. Res.*, vol. 9, no. 4, pp. 986–991, Apr. 1994.

[140] C. Cannas, A. Musinu, D. Peddis, and G. Piccaluga, “New synthesis of ferrite-silica nanocomposites by a sol-gel auto-combustion,” *J. Nanoparticle Res.*, vol. 6, no. 2, pp. 223–232, Jun. 2004.

[141] C. Cannas, A. Ardu, D. Niznansky, D. Peddis, G. Piccaluga, and A. Musinu, “Simple and fast preparation of pure maghemite nanopowders through sol-gel self-combustion,” *J. Sol-Gel Sci. Technol.*, vol. 60, no. 3, pp. 266–274, 2011.

[142] S.-H. Wu, C.-Y. Mou, and H.-P. Lin, “Synthesis of mesoporous silica nanoparticles,” *Chem. Soc. Rev.*, vol. 42, no. 9, p. 3862, 2013.

[143] P. Rocha-Sánchez and M. G. Cárdenas-Galindo, “Theoretical Study on the Brønsted Acidity of Al Doped SBA-15 for Methanol Dehydration as a Reaction Analog for the Transformation of Pectin to Furfural,” *Top. Catal.*, vol. 65, no. 13–16, pp. 1482–1494, 2022.

[144] D. Meloni, D. Perra, R. Monaci, M. G. Cutrufello, E. Rombi, and I. Ferino, “Transesterification of Jatropha curcas oil and soybean oil on Al-SBA-15 catalysts,” *Appl. Catal. B Environ.*, vol. 184, pp. 163–173, 2016.

[145] A. Ungureanu *et al.*, “Effect of aluminium incorporation by the ‘pH-adjusting’ method on the structural, acidic and catalytic properties of mesoporous SBA-15,” *Microporous Mesoporous Mater.*, vol. 163, pp. 51–64, 2012.

[146] J. Socci, A. Osatiashtiani, G. Kyriakou, and T. Bridgwater, “The catalytic cracking of sterically challenging plastic feedstocks over high acid density Al-SBA-15 catalysts,” *Appl. Catal. A Gen.*, vol. 570, no. November 2018, pp. 218–227, 2019.

[147] T. Wagner, C.-D. Kohl, M. Fröba, and M. Tiemann, “Gas Sensing Properties of Ordered Mesoporous SnO2,” *Sensors*, vol. 6, no. 4, pp. 318–323, Apr. 2006.

[148] T. Hyodo, S. Abe, Y. Shimizu, and M. Egashira, “Gas-sensing properties of ordered

mesoporous SnO2 and effects of coatings thereof," *Sensors Actuators B Chem.*, vol. 93, no. 1–3, pp. 590–600, Aug. 2003.

[149] T. Hyodo, N. Nishida, Y. Shimizu, and M. Egashira, "Preparation and gas-sensing properties of thermally stable mesoporous SnO2," *Sensors Actuators B Chem.*, vol. 83, no. 1–3, pp. 209–215, Mar. 2002.

[150] H. Kim and J. Cho, "Hard templating synthesis of mesoporous and nanowire SnO2 lithium battery anode materials," *J. Mater. Chem.*, vol. 18, no. 7, p. 771, 2008.

[151] H. Tüysüz, M. Comotti, and F. Schüth, "Ordered mesoporous Co3O4 as highly active catalyst for low temperature CO-oxidation," *Chem. Commun.*, no. 34, p. 4022, 2008.

[152] K. M. Shaju, F. Jiao, A. Débart, and P. G. Bruce, "Mesoporous and nanowire Co 3 O 4 as negative electrodes for rechargeable lithium batteries," *Phys. Chem. Chem. Phys.*, vol. 9, no. 15, pp. 1837–1842, 2007.

[153] D. Chandra, S. Mridha, D. Basak, and A. Bhaumik, "Template directed synthesis of mesoporous ZnO having high porosity and enhanced optoelectronic properties," *Chem. Commun.*, no. 17, p. 2384, 2009.

[154] J. M. Szeifert *et al.*, "Ultrasmall Titania Nanocrystals and Their Direct Assembly into Mesoporous Structures Showing Fast Lithium Insertion," *J. Am. Chem. Soc.*, vol. 132, no. 36, pp. 12605–12611, Sep. 2010.

[155] D. Fattakhova-Rohlfing, M. Wark, T. Brezesinski, B. M. Smarsly, and J. Rathouský, "Highly Organized Mesoporous TiO2 Films with Controlled Crystallinity: A Li-Insertion Study," *Adv. Funct. Mater.*, vol. 17, no. 1, pp. 123–132, Jan. 2007.

[156] T. Brezesinski, J. Wang, J. Polleux, B. Dunn, and S. H. Tolbert, "Templated Nanocrystal-Based Porous TiO 2 Films for Next-Generation Electrochemical Capacitors," *J. Am. Chem. Soc.*, vol. 131, no. 5, pp. 1802–1809, Feb. 2009.

[157] D. Grosso *et al.*, "Periodically ordered nanoscale islands and mesoporous films composed of nanocrystalline multimetallic oxides," *Nat. Mater.*, vol. 3, no. 11, pp. 787–792, Nov. 2004.

[158] A. A. Ayon *et al.*, "Drug loading of nanoporous TiO 2 films," *Biomed. Mater.*, vol. 1, no. 4, pp.

L11–L15, Dec. 2006.

[159] W. Cai, J. Yu, C. Anand, A. Vinu, and M. Jaroniec, "Facile Synthesis of Ordered Mesoporous Alumina and Alumina-Supported Metal Oxides with Tailored Adsorption and Framework Properties," *Chem. Mater.*, vol. 23, no. 5, pp. 1147–1157, Mar. 2011.

[160] Q. Yuan *et al.*, "Facile synthesis for ordered mesoporous γ-aluminas with high thermal stability," *J. Am. Chem. Soc.*, vol. 130, no. 11, pp. 3465–3472, 2008.

[161] V. Vishwanathan, H.-S. S. Roh, J.-W. W. Kim, and K.-W. W. Jun, "Surface Properties and Catalytic Activity of TiO 2 –ZrO 2 Mixed Oxides in Dehydration of Methanol to Dimethyl Ether," *Catal. Letters*, vol. 96, no. 1/2, pp. 23–28, Jul. 2004.

[162] A. Gharibi Kharaji, M. Beheshti, S. Tangestani-nejad, O. Görke, and H. R. Godini, "Adjusting acidity and porosity of Al-SBA-15 catalyst for methanol to dimethyl ether reaction," *Asia-Pacific J. Chem. Eng.*, vol. 15, no. 6, 2020.

[163] M. Gómez-Cazalilla, J. M. Mérida-Robles, A. Gurbani, E. Rodríguez-Castellón, and A. Jiménez-López, "Characterization and acidic properties of Al-SBA-15 materials prepared by post-synthesis alumination of a low-cost ordered mesoporous silica," *J. Solid State Chem.*, vol. 180, no. 3, pp. 1130–1140, 2007.

[164] S. Xing *et al.*, "Direct synthesis and characterization of pore-broadened Al-SBA-15," *Microporous Mesoporous Mater.*, vol. 239, pp. 316–327, 2017.

[165] K. Góra-Marek, M. Derewiński, P. Sarv, and J. Datka, "IR and NMR studies of mesoporous alumina and related aluminosilicates," *Catal. Today*, vol. 101, no. 2, pp. 131–138, 2005.

[166] J. Wang, L. Huang, H. Chen, and Q. Li, "Acid function of Al-MCM-41 supported platinum catalysts in hydrogenation of benzene, toluene and o-xylene," *Catal. Letters*, vol. 55, no. 3–4, pp. 157–163, 1998.

[167] E. P. Parry, "An infrared study of pyridine adsorbed on acidic solids. Characterization of surface acidity," *J. Catal.*, vol. 2, no. 5, pp. 371–379, 1963.

[168] C. A. EMEIS, "Determination of Integrated Molar Extinction Coefficients for IR Absorption Bands of Pyridine Adsorbed on Solid Acid Catalysts.," *J. Catal.*, vol. 141, no. 38, pp. 347–354,

Aug. 1993.

[169] J. M. R. Gallo, C. Bisio, G. Gatti, L. Marchese, and H. O. Pastore, “Physicochemical characterization and surface acid properties of mesoporous [Al]-SBA-15 obtained by direct synthesis,” *Langmuir*, vol. 26, no. 8, pp. 5791–5800, 2010.

[170] Z. Wang, Y. Jiang, A. Baiker, and J. Huang, “Pentacoordinated aluminum species: New frontier for tailoring acidity-enhanced silica−alumina catalysts,” *Acc. Chem. Res.*, 2020.

[171] H. Zou and Y. S. Lin, “Structural and surface chemical properties of sol-gel derived TiO 2-ZrO2 oxides,” *Appl. Catal. A Gen.*, vol. 265, no. 1, pp. 35–42, 2004.

[172] K. T. Li, I. Wang, and J. C. Wu, “Surface and Catalytic Properties of TiO 2-ZrO 2 Mixed Oxides,” *Catalysis Surveys from Asia*, vol. 16, no. 4. pp. 240–248, 2012.

[173] F. Arena, G. Mezzatesta, G. Zafarana, G. Trunfio, F. Frusteri, and L. Spadaro, “Effects of oxide carriers on surface functionality and process performance of the Cu-ZnO system in the synthesis of methanol via CO2 hydrogenation,” *J. Catal.*, vol. 300, pp. 141–151, 2013.

[174] E. Catizzone, A. Aloise, M. Migliori, and G. Giordano, “Dimethyl ether synthesis via methanol dehydration: Effect of zeolite structure,” *Appl. Catal. A Gen.*, vol. 502, pp. 215–220, 2015.

[175] M. Migliori *et al.*, “New insights about coke deposition in methanol-to-DME reaction over MOR-, MFI- and FER-type zeolites,” *J. Ind. Eng. Chem.*, vol. 68, pp. 196–208, 2018.

[176] E. Catizzone, A. Aloise, M. Migliori, and G. Giordano, “From 1-D to 3-D zeolite structures: performance assessment in catalysis of vapour-phase methanol dehydration to DME,” *Microporous Mesoporous Mater.*, vol. 243, pp. 102–111, 2017.

[177] J. C. Bedoya, R. Valdez, L. Cota, M. A. Alvarez-Amparán, and A. Olivas, “Performance of Al-MCM-41 nanospheres as catalysts for dimethyl ether production,” *Catal. Today*, no. January, pp. 1–8, 2021.

[178] A. R. Keshavarz, M. Rezaei, and F. Yaripour, “Preparation of nanocrystalline γ-Al2O3 catalyst using different procedures for methanol dehydration to dimethyl ether,” *J. Nat. Gas Chem.*, vol. 20, no. 3, pp. 334–338, 2011.

[179] D. Liu, C. Yao, J. Zhang, D. Fang, and D. Chen, “Catalytic dehydration of methanol to

dimethyl ether over modified γ-Al2O3 catalyst,” *Fuel*, vol. 90, no. 5, pp. 1738–1742, 2011.

[180] S. M. Kim, Y. J. Lee, J. W. Bae, H. S. Potdar, and K. W. Jun, “Synthesis and characterization of a highly active alumina catalyst for methanol dehydration to dimethyl ether,” *Appl. Catal. A Gen.*, vol. 348, no. 1, pp. 113–120, 2008.

[181] M. Stiefel, R. Ahmad, U. Arnold, and M. Döring, “Direct synthesis of dimethyl ether from carbon-monoxide-rich synthesis gas: Influence of dehydration catalysts and operating conditions,” *Fuel Process. Technol.*, vol. 92, no. 8, pp. 1466–1474, 2011.

[182] I. Sierra, J. Ereña, A. T. Aguayo, J. M. Arandes, M. Olazar, and J. Bilbao, “Co-feeding water to attenuate deactivation of the catalyst metallic function (CuO-ZnO-Al2O3) by coke in the direct synthesis of dimethyl ether,” *Appl. Catal. B Environ.*, vol. 106, no. 1–2, pp. 167–173, 2011.

[183] R. J. Da Silva, A. F. Pimentel, R. S. Monteiro, and C. J. A. Mota, “Synthesis of methanol and dimethyl ether from the CO2 hydrogenation over Cu·ZnO supported on Al2 and Nb2,” *J. CO2 Util.*, vol. 15, pp. 83–88, 2016.

[184] S. P. Naik, T. Ryu, V. Bui, J. D. Miller, N. B. Drinnan, and W. Zmierczak, “Synthesis of DME from CO2/H2 gas mixture,” *Chem. Eng. J.*, vol. 167, no. 1, pp. 362–368, 2011.

[185] J. Ereña, I. Sierra, A. T. Aguayo, A. Ateka, M. Olazar, and J. Bilbao, “Kinetic modelling of dimethyl ether synthesis from (H2+CO2) by considering catalyst deactivation,” *Chem. Eng. J.*, vol. 174, no. 2–3, pp. 660–667, 2011.

[186] F. Secci *et al.*, “Mesostructured γ-Al2O3-Based Bifunctional Catalysts for Direct Synthesis of Dimethyl Ether from CO2,” *Catalysts*, vol. 13, no. 3, p. 505, Feb. 2023.

[187] J. Wang and Q. Liu, “A simple method to directly synthesize Al-SBA-15 mesoporous materials with different Al contents,” *Solid State Commun.*, vol. 148, no. 11–12, pp. 529–533, 2008.

[188] P. Van Der Voort, M. Benjelloun, and E. F. Vansant, “Rationalization of the synthesis of SBA-16: Controlling the micro- and mesoporosity,” *J. Phys. Chem. B*, vol. 106, no. 35, pp. 9027–9032, 2002.

[189] G. L. Seah *et al.*, “Ordered Mesoporous Alumina with Tunable Morphologies and Pore Sizes for CO2Capture and Dye Separation,” *ACS Appl. Mater. Interfaces*, vol. 13, no. 30, pp. 36117–36129, 2021.

[190] Q. Yuan *et al.*, “Homogeneously dispersed ceria nanocatalyst stabilized with ordered mesoporous alumina,” *Adv. Mater.*, vol. 22, no. 13, pp. 1475–1478, 2010.

[191] G. F. Andrade, D. C. F. Soares, R. K. D. S. Almeida, and E. M. B. Sousa, “Mesoporous silica SBA-16 functionalized with alkoxysilane groups: Preparation, characterization, and release profile study,” *J. Nanomater.*, vol. 2012, 2012.

[192] R. M. Grudzien, B. E. Grabicka, and M. Jaroniec, “Adsorption and structural properties of channel-like and cage-like organosilicas,” *Adsorption*, vol. 12, no. 5–6, pp. 293–308, 2006.

[193] Q. Wu, F. Zhang, J. Yang, Q. Li, B. Tu, and D. Zhao, “Synthesis of ordered mesoporous alumina with large pore sizes and hierarchical structure,” *Microporous Mesoporous Mater.*, vol. 143, no. 2–3, pp. 406–412, 2011.

[194] K. Niesz, P. Yang, and G. A. Somorjai, “Sol-gel synthesis of ordered mesoporous alumina,” *Chem. Commun.*, no. 15, pp. 1986–1987, 2005.

[195] and G. D. S. Peidong Yang, Dongyuan Zhao, David I. Margolese, Bradley F. Chmelka, “Block Copolymer Templating Syntheses of Mesoporous Metal Oxides with Large Ordering Lengths and Semicrystalline Framework,” *Chem. Mater.*, vol. 1536, no. 11, pp. 2813–2826, 1999.

[196] H. Ding, H. Sun, and Y. Shan, “Preparation and characterization of mesoporous SBA-15 supported dye-sensitized TiO2 photocatalyst,” *J. Photochem. Photobiol. A Chem.*, vol. 169, no. 1, pp. 101–107, 2005.

[197] V. Palos-Barba *et al.*, “SBA-16 Cage-Like Porous Material Modified with APTES as an Adsorbent for Pb2+ Ions Removal from Aqueous Solution,” *Materials (Basel).*, vol. 13, no. 927, pp. 1–15, 2020.

[198] L. Wang *et al.*, “Synthesis and characterization of small pore thick-walled SBA-16 templated by oligomeric surfactant with ultra-long hydrophilic chains,” *Microporous Mesoporous Mater.*, vol. 67, no. 2–3, pp. 135–141, 2004.

[199] L. Lutterotti and P. Scardi, “Simultaneous structure and size-strain refinement by the rietveld method,” *J. Appl. Crystallogr.*, vol. 23, no. 4, pp. 246–252, 1990.

[200] K. SHIRASUKA, H. YANAGIDA, and G. YAMAGUCHI, “The Preparation of η Alumina and its Structure,” *J. Ceram. Assoc. Japan*, vol. 84, no. 976, pp. 610–613, 1976.

[201] P. Carta, C. Cara, C. Cannas, and M. A. Scorciapino, “Experiments-Guided Modeling of MCM-41: Impact of Pore Symmetry on Gas Adsorption,” *Adv. Mater. Interfaces*, vol. 9, no. 34, p. 2201591, Dec. 2022.

[202] Y. Li *et al.*, “Direct synthesis of Al-SBA-15 mesoporous materials via hydrolysis-controlled approach,” *J. Phys. Chem. B*, vol. 108, no. 28, pp. 9739–9744, 2004.

[203] M. L. Occelli, S. Biz, A. Auroux, and G. J. Ray, “Effects of the nature of the aluminum source on the acidic properties of some mesostructured materials,” *Microporous Mesoporous Mater.*, vol. 26, no. 1–3, pp. 193–213, 1998.

[204] J. N. Kondo, R. Nishitani, E. Yoda, T. Yokoi, T. Tatsumi, and K. Domen, “A comparative IR characterization of acidic sites on HY zeolite by pyridine and CO probes with silica-alumina and γ-alumina references,” *Phys. Chem. Chem. Phys.*, vol. 12, no. 37, pp. 11576–11586, 2010.

[205] Y. Matsunaga, H. Yamazaki, T. Yokoi, T. Tatsumi, and J. N. Kondo, “IR characterization of homogeneously mixed silica-alumina samples and dealuminated y zeolites by using pyridine, CO, and propene probe molecules,” *J. Phys. Chem. C*, vol. 117, no. 27, pp. 14043–14050, 2013.

[206] Y. F. Shen, S. L. Suib, M. Deeba, and G. S. Koermer, “Luminescence and IR characterization of acid sites on alumina,” *Journal of Catalysis*, vol. 146, no. 2. pp. 483–490, 1994.

[207] M. R. Gafurov, I. N. Mukhambetov, B. V. Yavkin, G. V. Mamin, A. A. Lamberov, and S. B. Orlinskii, “Quantitative Analysis of Lewis Acid Centers of γ-Alumina by Using EPR of the Adsorbed Anthraquinone as a Probe Molecule: Comparison with the Pyridine, Carbon Monoxide IR, and TPD of Ammonia,” *J. Phys. Chem. C*, vol. 119, no. 49, pp. 27410–27415, 2015.

[208] X. Liu and R. E. Truitt, "DRFT-IR studies of the surface of γ-Alumina," *J. Am. Chem. Soc.*, vol. 119, no. 41, pp. 9856–9860, 1997.

[209] M. I. Zaki, M. A. Hasan, F. A. Al-sagheer, and L. Pasupulety, "In situ FTIR spectra of pyridine adsorbed on SiO2–Al2O3, TiO2, ZrO2 and CeO2: general considerations for the identification of acid sites on surfaces of finely divided metal oxides," *Colloids and Surfaces*, vol. 190, pp. 261–274, 2001.

[210] N. Cardona-Martinez and J. A. Dumesic, "Applications of Adsorption Microcalorimetry to the Study of Heterogeneous Catalysis," *Adv. Catal.*, vol. 38, no. C, pp. 149–244, 1992.

[211] B. Dragoi, A. Gervasini, E. Dumitriu, and A. Auroux, "Calorimetric determination of the acidic character of amorphous and crystalline aluminosilicates," *Thermochim. Acta*, vol. 420, no. 1-2 SPEC. ISS., pp. 127–134, 2004.

[212] B. SPIEWAK, B. HANDY, S. SHARMA, and J. DUMESIC, "Microcalorimetric studies of ammonia adsorption on γ-Al203, HNa-Y zeolite, and H-mordenite," *Catal. Letters*, vol. 23, pp. 207–213, 1994.

[213] J. Shen, R. D. Cortright, Y. Chen, and J. A. Dumesic, "Microcalorimetric and infrared spectroscopic studies of γ-Al2O3 modified by tin oxides," *Catal. Letters*, vol. 26, no. 3–4, pp. 247–257, 1994.

[214] J. Le Bars, J. C. Védrine, A. Auroux, S. Trautmann, and M. Baerns, "Microcalorimetric and infrared studies of the acid-base properties of V2O5/γ-Al2O3 catalysts," *Appl. Catal. A, Gen.*, vol. 119, no. 2, pp. 341–354, 1994.

[215] D. Stoilova, K. Cheshkova, and R. Nickolov, "Ftir spectroscopy of NH3 and NO adsorption on copper-on-Alumina catalysts," *React. Kinet. Catal. Lett.*, vol. 68, no. 2, pp. 331–337, 1999.

[216] B. C. Gates and L. N. Johanson, "Langmuir-hinshelwood kinetics of the dehydration of methanol catalyzed by cation exchange resin," *AIChE J.*, vol. 17, no. 4, pp. 981–983, Jul. 1971.

[217] B. C. Gates and L. N. Johanson, "The dehydration of methanol and ethanol catalyzed by polystyrene sulfonate resins," *J. Catal.*, vol. 14, no. 1, pp. 69–76, May 1969.

[218] H. Zhan, X. Shi, B. Tang, G. Wang, B. Ma, and W. Liu, “The performance of Cu/Zn/Zr catalysts of different Zr/(Cu+Zn) ratio for CO2 hydrogenation to methanol,” *Catal. Commun.*, vol. 149, no. October 2020, p. 106264, 2021.

[219] M. Sadeghinia, A. Nemati Kharat Ghaziani, and M. Rezaei, “Component ratio dependent Cu/Zn/Al structure sensitive catalyst in CO2/CO hydrogenation to methanol,” *Mol. Catal.*, vol. 456, no. March, pp. 38–48, 2018.

[220] A. García-Trenco and A. Martínez, “A simple and efficient approach to confine Cu/ZnO methanol synthesis catalysts in the ordered mesoporous SBA-15 silica,” *Catal. Today*, vol. 215, pp. 152–161, 2013.

[221] C. Cannas, M. Casu, A. Lai, A. Musinu, and G. Piccaluga, “XRD, TEM and 29 Si MAS NMR study of sol–gel ZnO–SiO 2 nanocomposites,” pp. 1765–1769, 1999.

[222] M. S. Pereira *et al.*, “Characterization of CoFe 2 O 4 , NiFe 2 O 4 , and ZnFe 2 O 4 Nanoparticles Synthesized by a Proteic Sol-gel Method,” *J. Supercond. Nov. Magn.*, vol. 34, no. 11, pp. 2845–2853, 2021.

[223] C. Cannas *et al.*, “Magnetic properties of cobalt ferrite-silica nanocomposites prepared by a sol-gel autocombustion technique,” *J. Chem. Phys.*, vol. 125, no. 16, 2006.

[224] X. Zhong, J. Barbier, D. Duprez, H. Zhang, and S. Royer, “Modulating the copper oxide morphology and accessibility by using micro-/mesoporous SBA-15 structures as host support: Effect on the activity for the CWPO of phenol reaction,” *Appl. Catal. B Environ.*, vol. 121–122, pp. 123–134, 2012.

[225] L. Xiang, S. Royer, H. Zhang, J. M. Tatibouët, J. Barrault, and S. Valange, “Properties of iron-based mesoporous silica for the CWPO of phenol: A comparison between impregnation and co-condensation routes,” *J. Hazard. Mater.*, vol. 172, no. 2–3, pp. 1175–1184, 2009.

[226] D. Sellam *et al.*, “Simple approach to prepare mesoporous silica supported mixed-oxide nanoparticles by in situ autocombustion procedure,” *Catal. Today*, vol. 157, no. 1–4, pp. 131–136, 2010.

[227] G. Bonura, M. Cordaro, L. Spadaro, C. Cannilla, F. Arena, and F. Frusteri, “Hybrid Cu-ZnO-

ZrO2/H-ZSM5 system for the direct synthesis of DME by CO2 hydrogenation," *Appl. Catal. B Environ.*, vol. 140–141, pp. 16–24, 2013.

[228] G. Lombardelli *et al.*, "CO2hydrogenation to methanol with an innovative Cu/Zn/Al/Zr catalyst: Experimental tests and process modeling," *J. CO2 Util.*, vol. 65, no. June, p. 102240, 2022.

Acknowledgements

There are many people that I would like to thank for supporting and encouraging me during this wonderful experience. First of all, I want to thank my supervisor, Prof. Carla Cannas, for believing in me and for supporting, accompanying and guiding me during my whole career, from my bachelor's thesis work to the end of my PhD. I also would like to thank all the other member of my research group "Solid State Chemistry and Nanomaterials" of the University of Cagliari, namely Dr. Valentina Mameli, for the fundamental help and support she gave me for my thesis work, Dr. Andrea Ardu, for the awesome TEM images he acquired on my materials, and finally Dr. Claudio Cara, Dr. Marco Sanna Angotzi, Dr. Mirko Antonio Vacca and Nicoletta Rusta for all the help they gave me. I would also like to give a special thanks to Prof. Anna Musinu, the former head of our group, for her kindness and for introducing me to the world of nanomaterials. A special thanks goes to the "Industrial Chemistry" research group for the precious collaboration and the priceless contribution they gave to my research work. Particularly, I would like to thank Prof. Elisabetta Rombi, for the help she gave me for the interpretation of my catalytic data, Prof. Maria Giorgia Cutrufello, for introducing me to nitrogen physisorption measurements, Dr. Daniela Meloni, for sharing with me a lot of useful tips and tricks, and, last but not least, Franca Sini, for her infinite kindness and for the time she spent for the analysis of my samples. I would also like to thank Dr. Mauro Mureddu, Dr. Sarah Lai and the whole staff of Sotacarbo SpA for the catalytic tests on my systems and for the support for data interpretation. A special thanks also goes to Prof. Nicola Pinna, Dr. Patricia Russo, Christoph Erdmann and their research group at the Humboldt University in Berlin for allowing me to spend five months in their department (and in the most beautiful city in the world) and for all the precious data I gathered during my stay. I also want to say thanks to my fellow PhD colleagues (also former ones) for sharing with me happy and sad moments during this three-year journey; in particular, I want to thank my former and current office mates Giada Mannias, Paola Carta, Davide Tocco, Monica Mura, and Antonella Ibba. A final special thanks goes to my beloved family and my friends Alessandro, Matteo and Fabio.

We acknowledge the CeSAR (Centro Servizi di Ateneo per la Ricerca) of the University of Cagliari, Italy for the TEM analyses performed with Jeol JEM 1400 Plus and Dr. Andrea Ardu.

Programma Operativo Nazionale "Ricerca e Innovazione" 2014-2020 (PONRI) is acknowledged for my PhD grant.

List of publications produced during the PhD:

- As$^{(III, V)}$ Uptake from Nanostructured Iron Oxides and Oxyhydroxides: The Complex Interplay between Sorbent Surface Chemistry and Arsenic Equilibria.

  Marco Sanna Angotzi, Valentina Mameli, Alessandra Fantasia, Claudio Cara, **Fausto Secci**, Stefano Enzo, Marianna Gerina, Carla Cannas.

  Nanomaterials 2022, *12*(3), 326.

  Author's contribution: Data curation, Formal analysis, Investigation, Visualization.

  Published 20/01/2022 https://doi.org/10.3390/nano12030326
- On the design of mesostructured acidic catalysts for the one-pot dimethyl ether production from CO_2.

  Claudio Cara[1], **Fausto Secci[1]**, Sarah Lai, Valentina Mameli, Kai Skrodczky, Patricia A. Russo, Francesca Ferrara, Elisabetta Rombi, Nicola Pinna, Mauro Mureddu, Carla Cannas ([1] Equal contribution).

  Journal of CO_2 Utilization 62 (2022) 102066.

  Author's contribution (co-first author with equal contribution with first author): Conceptualization, Data curation, Formal analysis, Investigation, Methodology, Visualization, Writing.

  Published 1/06/2022 https://doi.org/10.1016/j.jcou.2022.102066
- Mesostructured γ-Al_2O_3-Based Bifunctional Catalysts for Direct Synthesis of Dimethyl Ether from CO_2.

  Fausto Secci, Marco Sanna Angotzi, Valentina Mameli, Sarah Lai, Patricia A. Russo, Nicola Pinna, Mauro Mureddu, Elisabetta Rombi, Carla Cannas.

  Catalysts 2023, *13*(3), 505.

  Author's contribution (first author): Conceptualization, Data curation, Formal analysis, Investigation, Methodology, Visualization, Writing.

  Published 28/02/2023 https://doi.org/10.3390/catal13030505
- On the role of the nature and density of acid sites on mesostructured aluminosilicates dehydration catalysts for dimethyl ether production from CO_2.

  Fausto Secci, Valentina Mameli, Elisabetta Rombi, Sarah Lai, Marco Sanna Angotzi, Patrícia A. Russo, Nicola Pinna, Mauro Mureddu, Carla Cannas.

  Author's contribution (first author): Conceptualization, Data curation, Formal analysis, Investigation, Methodology, Visualization, Writing.

Submitted to *Journal of Environmental Chemical Engineering* on 28/01/2023; accepted with revisions on 22/02/2023; revisions submitted on 16/03/2023.

- Soft-templated NiO-CeO_2 mixed oxides for biogas upgrading by direct CO_2 methanation.

  Luciano Atzori, Maria Giorgia Cutrufello, Daniela Meloni, **Fausto Secci**, Carla Cannas, Elisabetta Rombi.

  Author's contribution: Data curation, Investigation, Visualization, Writing.

  Accepted for publication on *International Journal of Hydrogen Energy* on 27/03/2023.

La borsa di dottorato è stata cofinanziata con risorse del
Programma Operativo Nazionale Ricerca e Innovazione 2014-2020 (CCI 2014IT16M2OP005),
Fondo Sociale Europeo, Azione I.1 “Dottorati Innovativi con caratterizzazione Industriale”

UNIONE EUROPEA
Fondo Sociale Europeo

Ministero dell'Università
e della Ricerca

PON
RICERCA
E INNOVAZIONE
2014 - 2020